Targeting miR-21 to inhibit the inflammatory response following ischaemic kidney injury

Emily Katerina Glover

Doctor of Philosophy

Translational and Clinical Research Institute, Medical School, Newcastle University

December 2024

Abstract

Targeting ischaemia-reperfusion injury (IRI) in kidney transplantation has the potential to improve transplant survival, thereby benefiting recipients. MicroRNAs (miR) are potential targets through which to modulate these injury pathways and rodent studies suggested a protective effect from blocking miR-21-5p in kidney IRI. I have delivered a miR-21-5p inhibitor (antimiR-21) to human kidney *in vitro* and ex vivo models of IRI to explore the potential of antimiR-21 as a therapeutic target in this context.

Proximal tubule epithelial cells (PTEC) were isolated from human kidneys declined for transplantation and characterised with immunofluorescence, light microscopy and electron microscopy. Endothelial and mesenchymal cell contamination was determined with flow cytometry. PTEC were shown to express miR-21 and HIF1α stabilisation was confirmed on incubation in 1% oxygen to model ischaemia.

PTEC took up antimiR without the use of transfection reagents. Macropinocytosis was a dominant uptake mechanism as uptake was reduced by a macropinocytosis inhibitor but unaffected by blocking megalin-mediated uptake.

The response of PTEC to antimiR-21 treatment from reoxygenation was explored with bulk RNA sequencing and liquid chromatography mass spectrometry-based (LCMS-based) proteomics. 24 hours after antimiR-21 treatment, miR-21 targets were upregulated relative to control treated PTEC. Ingenuity pathway analysis predicts antimiR-21 treatment activates cell survival and blood vessel formation pathways during reoxygenation.

A 24-hour normothermic machine perfusion model was optimised for the circuit used at Newcastle University and used to deliver antimiR-21 or control antimiR to pairs of human kidneys. The response was assessed with TUNEL stain for apoptosis, perfusate cytokine concentrations and LCMS-based proteomics on biopsies.

In summary, PTEC isolated from human kidneys are a valuable *in vitro* model for exploring the effects of antimiR-21 treatment without transfection reagents. *In vitro*, antimiR-21 treatment during reoxygenation appears to be beneficial and in the whole organ model, antimiR-21 could effectively reduce miR-21 expression by 24 hours.

Acknowledgements

I am enormously grateful for the support, encouragement and advice of the large number of individuals and departments that have been essential in supporting the work in this thesis and making my PhD such an enjoyable and stimulating 3 years.

Firstly, I would like thank my main supervisor, Neil Sheerin, for his guidance, encouragement and analytic eye during and leading up to my PhD. I have been provided with a plethora of opportunities to go alongside my thesis project and I have really appreciated the support to explore these. His focus and pragmatic approach has been key in keeping my project progressing.

My wider supervisory team of Simi Ali, Rachel Lennon, Laura Denby and Gary Reynolds have all been crucial support and I have really benefited from having so many people invested in my project. I would particularly like to thank Rachel and Laura for making me feel so welcome on my visits to Manchester and Edinburgh. It has been brilliant to join the Lennon group meetings and am I grateful to Mychel Morais for his time and patience with my almost endless questions and Bernard Davenport and Emily Williams for ensuring my visits went smoothly.

The Biomedical Mass Spectrometry Facility at the University of Manchester have provided me with excellent support both for processing the samples and guiding me through the analysis process and I would like to mention Stacey Warwood, Julian Selley and David Knight in particular. Also in Manchester, Martin Lowe was generous in contributing his expertise in endocytosis to my project.

The bioinformatics aspects of my work have been supported by Gary Reynolds, the Bioinformatics team broadly and Graham Smith in particular. This was a daunting project to embark on and their support and advice has been crucial.

I would also like to thank everyone in the Flow Cytometry and Bioimaging Facilities at Newcastle University and Jonathan Coxhead and Rafiqul Hussain in the Core Genomics Facility. I have sought their guidance many times and they have always been very helpful and insightful. Similarly, in the Core Technician team for the William Leech building, Dane Wilson, Dan Padgett and Michelle Murray have solved probably more than their fair share of problems from me and I have really appreciated their energy in tackling them all.

It would take pages to detail all the contributions made by my colleagues in M3.084 but I can summarise by saying they have all provided immense support, advice and camaraderie and I feel lucky to have worked in such a positive and cohesive environment. Each perfusion was a massive team effort and I am very grateful for all the hours put in by everyone who helped with these. In additional to their surgical support, I have benefited from the general enthusiasm for statistics and all things R of Samuel Tingle and George Kourounis. I would also like to thank Emily Thompson and Sarah Hosgood for all the useful advice they have managed to deliver in short conversations and general encouragement with my work. Again, this is understated for brevity but I have really appreciated Marnie Brown's ability to find solutions to any problem, Chloe Connelly's patience, positivity and experience and Lucy Bates' efforts to keep all the perfusion projects running smoothly. Jeremy Palmer was very generous with the equipment in his lab and a great source of advice.

My friends and family have been a great support and I recognise quite how patient they have been with me over the last year in particular.

Finally, this work would not have been possible without the funding offered by the Wellcome Trust through the 4Ward North PhD scheme and additional support from Northern Counties Kidney Research Fund and Kidneys for Life. Most importantly, I would also like to thank the kidney donors and their families without whom this work would not have been possible. I am humbled by the enormity of their generosity.

Publications

The following manuscript has been submitted for publication from work in this thesis and some passages are quoted verbatim.

AntimiR uptake by human proximal tubule epithelial cells is predominantly macropinocytosis Glover EK, Berlinguer-Palmini R, Thompson ER, Wilson C, Denby L, Reynolds G, Ali S, Lowe M, Lennon R, Sheerin NS [Submitted for publication]

Presentations

Assessing the response to antimiR21 in a human model of kidney ischaemia-reperfusion injury

UK Kidney Week (moderated poster), June 2024, Edinburgh UK

American Transplant Congress (poster), June 2024, Philadelphia USA

Association of Physicians Annual Meeting (oral abstract), June 2024, Newcastle upon Tyne UK

Crick Clinical Research Fellows Meeting (oral abstract), June 2023, London UK

Irish Clinical Academic Training Programme Annual Retreat (oral abstract), December 2022, Dublin, Ireland

Exploring the endocytic uptake mechanism of naked antimiR in human proximal tubule epithelial cells

British Transplant Society Congress 2023 (poster), March 2023, Edinburgh UK

List of abbreviations

4PL	four parameter logistic regression
ADP	adenosine diphosphate
AKI	acute kidney injury
AMP	adenosine monophosphate
antimiR-21	miR-21-5p inhibitor
APAF1	apoptotic protease activating factor 1
AQP1	aquaporin 1
ATP	adenosine triphosphate
BPCA	bayesian principal component method
CA1	carbonic anhydrase 1
CEUS	contrast enhanced ultrasound
CIT	cold ischaemic time
CLIC/GEEC	Clathrin and Dynamin Independent Carriers/GPI-AP enriched early endosomal compartments
DAMPs	damage associated molecular patterns
DBD	donated after brainstem death
DCD	donated after circulatory death
DDA	data dependent acquisition
df	degrees of freedom
DGE	differential gene expression
DGF	delayed graft function
DIA	data independent acquisition
DMSO	dimethyl sulfoxide
DNA	deoxyribonucleic acid
DSAs	donor specific antibodies

DTT	dithiothreitol
EIPA	5-(*N*-ethyl-*N*-isopropyl)amiloride
ELISA	enzyme-linked immunosorbent assay
FAM	fluorescein amidite
FBS	fetal bovine serum
FcR	Fc receptor
FITC	fluorescein isothiocyanate
FSC-A	forward scatter-area
FSC-H	forward scatter-height
GPF	gas-phase fractionation
GPX-4	glutathione peroxidase 4
GSEA	gene set enrichment analysis
H&E	haematoxylin and eosin
HBD	haemoglobin subunit delta
HIF	hypoxia inducible factors
HMGB-1	high-mobility group box-1
HMOX1	heme oxygenase 1
IAM	iodoacetamide
IGF	insulin like growth factor
IGFBP	Insulin like growth factor binding protein
IGBP3	Insulin like growth factor binding protein 3
IPA	ingenuity pathway analysis
IRI	ischaemia-reperfusion injury
K19	cytokeratin-19
KIM-1	kidney injury molecule 1

LCMS	liquid chromatography mass spectrometry
LFC	log_2 fold change
LPS	lipopolysaccharide treatment
MFI	median fluorescent intensity
MHC	major histocompatibility complex
MHC-I	MHC class I
MHC-II	MHC class II
miR	microRNAs
MLKL	mixed lineage kinase domain like pseudokinase
MPTP	mitochondrial permeability transition pores
mRNA	messenger RNA
NGAL	neutrophil gelatinase-associated lipocalin
NES	normalised enrichment score
NMP	normothermic machine perfusion
PBS	phosphate buffered saline
PDCD4	programmed cell death 4
PDGFR	platelet derived growth factor receptors
PECAM-1	platelet/endothelial cell adhesion molecule-1
PFA	paraformaldehyde
PHD	prolylhydroxylase
p-MLKL	phosphorylated MLKL
PTEC	proximal tubule epithelial cells
RAP	receptor-associated protein
RIPK3	receptor-interacting protein kinase 3
RISC	RNA-induced silencing complex

RM-ANOVA	repeated measures analysis of variance
ROS	reactive oxygen species
RRT	renal replacement therapy
rTDT	Terminal Deoxynucleotidyl Transferase Recombinant enzyme
RT-PCR	reverse transcription polymerase chain reaction
SDS	sodium dodecyl sulfate
S1P	sphingosine-1-phosphate
SLC5A2	sodium glucose cotransporter 2
SMA	smooth muscle actin
SSC-A	side scatter-area
STAR	Spliced Transcripts Alignment to a Reference
TBS	tris-buffered saline
TBST	TBS with 0.1% Tween-20
TJP1	tight junction protein 1
TLR	toll like receptors
TUNEL	TdT-mediated dUTP Nick-End Labeling
UTR	untranslated region
UUO	unilateral ureteric obstruction
VEGF	vascular endothelial growth factor
WIT	warm ischaemic time
ZO1	zonula occludens 1

Table of Contents

List of Tables

List of Figures

Chapter 1. Introduction

1.1 The functions of the kidney

The kidneys are important for maintaining physiological homeostasis through their role in water and electrolyte balance, excretion of toxins, maintaining acid-base balance and production or metabolism of hormones involved in blood pressure control, bone metabolism and red blood cell production.[1,2] The healthy kidney filters blood through the semipermeable membrane of the glomerulus so water, electrolytes and smaller proteins, including some albumin, enter the tubule via Bowman's capsule.[2] Larger components of blood, such as red blood cells and immunoglobulins, remain in the capillaries as they are too large to filter through.[2] Once the filtrate enters the proximal tubule, key component are reabsorbed through the epithelium to limit losses particularly of albumin, amino acids, glucose, sodium, bicarbonate and phosphate.[2,3] The proximal tubule is also a key site for gluconeogenesis in the body.[4] Subsequent segments of the nephron work to further reabsorb water and sodium and secrete potassium, with hormonal control facilitating an appropriate response to the body's current requirements.[1,2]

1.2 Kidney transplantation is the optimum renal replacement therapy

Kidney transplantation is the optimum form of renal replacement therapy (RRT) for those with kidney failure, both benefiting the patient and the wider health economy. The long term mortality associated with kidney transplantation is approximately half that of remaining on dialysis,[5,6] with younger recipients likely experiencing the greatest benefit.[6] Transplantation is also recognised to improve quality of life compared to dialysis, the alternative RRT.[7]

Although care in the first year of transplantation is estimated at £28000, subsequent care costs considerably less at £12000 per year.[8] Dialysis is comparatively expensive at around £35000 and £17500 for a year for haemodialysis and peritoneal dialysis respectively.[8,9] Kidney transplant recipients are also considered more likely to work and require less state support than their counterparts on dialysis.

As the demand for donor kidneys exceeds the available organs,[10] it follows that maximising graft longevity would benefit both recipients and those remaining on the waiting list by reducing the demand for re-transplantation. In the UK, 5-year graft

survival for first kidney transplants is 86% and 93% for kidneys from deceased and live donors respectively.[10]

1.3 Ischaemia-reperfusion injury (IRI) affects graft outcomes

One disease process being targeted to improve long term graft outcomes is ischaemia-reperfusion injury. All donor kidneys will endure a period of ischaemia regardless of donor type by nature of the process of transplantation (**Figure 1-1**). However, the duration of this ischaemia will vary and generally be longer for deceased donor kidneys, with an additional first warm ischaemic period for kidneys donated after circulatory (DCD) rather than brainstem (DBD) death.[11]

Delayed graft function (DGF) is considered a clinical reflection of this initial IRI to the kidney transplant.[11] It is defined as a failure of the graft to work immediately leading to the need for dialysis within the first week of transplantation.[11,12]

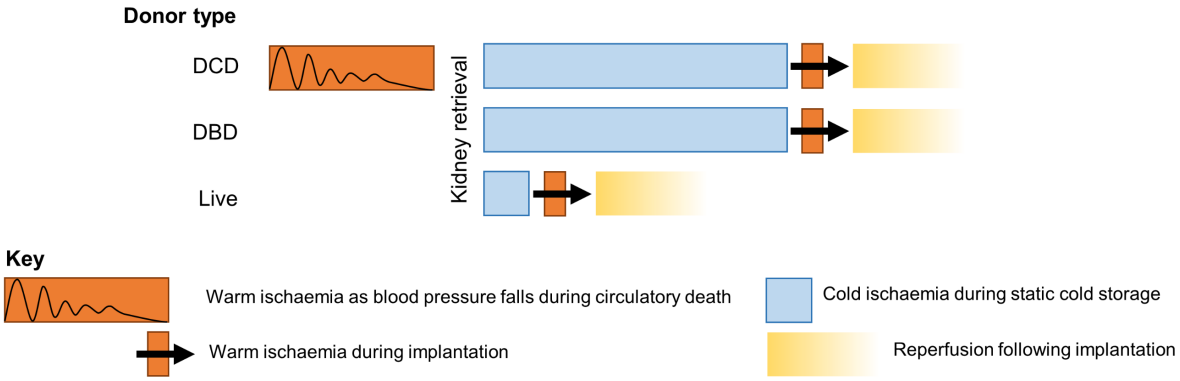

Figure 1-1 Schematic of periods of warm and cold ischaemia that kidneys from different types of donor are exposed to.
Deceased donor are categorised as those donating after circulatory death (DCD) or after brainstem death (DBD). Kidney perfusion is maintained until retrieval for kidneys donated from DBD and live donors. In contrast, blood pressure falls during circulatory death and so kidneys are exposed to warm ischaemia before surgical retrieval. A (usually short) period of warm ischaemia occurs whilst the kidney is placed in the recipient and blood supply is established. Reperfusion follows.

1.3.1 Impact of ischaemia time

The length of ischaemia an organ can tolerate without triggering injury varies with organ type.[13] Data from clinical partial nephrectomies suggest the kidney can tolerate 30-60 minutes of ischaemia without injury.[14] In rodent models, prolonged renal ischaemia caused more severe injury than brief periods[15,16] and with increasing age, kidneys were more susceptible to this injury.[16]

Warm and cold ischaemic times have both been shown to impact on graft outcomes. UK data found that in DCD kidneys a cold ischaemic time (CIT) of ≥24 hours is associated with twice the risk of graft loss by 3 years compared to CIT <12 hours.[17] Interestingly, this relationship was not demonstrated for DBD kidneys[17] suggesting the first warm ischaemic time (WIT) experienced by DCD kidneys likely has an additive effect. In the Netherlands a graft survival benefit at 5 years has been demonstrated from shorter CITs in both DCD and DBD kidneys but the effect was more pronounced in DCD kidneys.[18] In terms of WIT, data from the USA including DCD, DBD and live donor kidneys shows a longer WIT to negatively affect long term outcomes when times less than 20 minutes are compared with those over 30 minutes. A greater effect was seen for deceased donor kidneys compared to live donor kidneys.[19] Overall, these results suggest that all donor kidneys are affected by increased ischaemic times but DCD kidneys appear the most vulnerable.

The ability to tolerate longer ischaemia under cold conditions is explained by reduced metabolic activity at low temperatures. This has been studied in the brain where oxygen consumption, as an indicator of adenosine triphosphate (ATP) production, reduces with cooling.[20]

1.3.2 Impact of age

The finding in rodents that age impacts on the extent of ischaemic renal injury[16,21] may explain the effect of donor age on graft outcomes seen in observational data of clinical kidney transplants in the UK.[17] The risk of graft failure within 3 years of deceased donor transplantation is doubled when the donor is aged ≥60 compared to <40 years old.[17] Similarly, the increased risk of death-censored graft loss was 15% for every additional hour of total ischaemic time for kidneys from DCD donors aged 55 or older compared to less than 2% for younger DCD donors.[22]

1.3.3 Impact of sex

Another factor that may affect response to ischaemia in transplantation is sex, with females generally having more protection against IRI.[23] Willicombe M et al.[24] found recipient female sex to be protective against DGF with an odds ratio of 0.43 and no impact from donor sex. A separate study found that when both kidneys from a donor were transplanted to recipients of opposite sex, the odds ratio of DGF in the male recipient was 1.43 compared to the female recipient.[25] Oestrogen exposure in the recipient may be behind this difference as protection is reduced in post-menopausal

female recipients.[22,25] Interestingly, work from the Netherlands found only donor, rather than recipient, sex to impact on the risk of DGF with male donors having 24% increased risk of DGF.[18]

1.3.4 DGF and graft outcomes

DGF is consistently shown to be more common in kidneys from DCD donors compared to DBD donors.[11,17,18,22,26] In addition to CIT, older age of the donor and recipient have reliably been shown to increase the risk of DGF in DCD kidneys.[27]

In the short term, DGF has a negative impact on the recipient by increasing the length of admission post-transplantation and has been associated with worse kidney function 1 year after transplantation.[28] In China, survival 1 year after deceased donor transplantation was lower in those with (93.6%) vs without (99.7%) DGF.[29]

The significance of DGF on long-term outcomes is more contested. A meta-analysis found studies with shorter follow up times demonstrate a larger effect of DGF on graft loss than those with more than 2 years follow up.[30] A study on DCD kidneys found DGF was associated with poorer graft survival.[28] However, despite the increased rate of DGF in DCD kidneys, data from the UK[27] and The Netherlands[18] shows no difference in graft survival at 5 years between DCD and DBD kidneys. Interestingly, assessment of 10-year graft survival found no impact of DGF in DCD kidneys, but for DBD kidneys DGF was associated with worse graft survival.[26] It may be that the ischaemic injury is greater for a DBD kidney to display DGF and this study showed an association with older age, longer ischaemic time and higher donor serum creatinine that was restricted to the DBD group.[26]

There is also evidence from outside the field of transplantation that short term insults lead to long term damage in the kidney.[31] Data from Canada found hospitalised patients with acute kidney injury (AKI) requiring dialysis to have 3 times the risk of needing chronic dialysis when compared to those without AKI, even though they recovered renal function after the acute episode.[32] Again, age exacerbated these effects.[32]

1.4 Mechanisms of ischaemia-reperfusion injury

The mechanism of injury in ischaemia is multifaceted and exacerbated during the reperfusion phase. Damage at the cell level is largely mediated through accumulation of reactive oxygen species (ROS) and intracellular calcium. More widely, this damage

leads to changes at a transcription level, endothelial cell dysfunction and activation of the immune system.[13,33,34]

1.4.1 Respiration and ATP depletion

In the cytoplasm, glycolysis breaks glucose down into pyruvate and generates a small amount of ATP.[35,36] In the presence of oxygen, pyruvate enters the mitochondrial matrix and is converted to acetyl-CoA.[36,37] This enters the citric acid cycle to generate the electron carriers NADH and $FADH_2$ as substrates for the electron transport chain.[36] Carbon dioxide is also released.[35-37] Fatty acids can also produce acetyl-Co,[38] as can amino acids which also generate pyruvate.[36,39]

The mitochondria are double membrane bound organelles responsible for ATP production in the cell during aerobic respiration through oxidative phosphorylation.[36,37] The inner membrane of the mitochondria contains a series of proteins that together make the electron transport chain.[36] Here, electrons are released from NADH at complex I (NADH dehydrogenase) and at complex II (succinate dehydrogenase, SDH) the production of fumarate from succinate within the citric acid cycle is coupled with creating the electron carrier $FADH_2$.[36,37] Coenzyme Q passes electrons from complexes I and II on to complex III (ubiquinone-cytochrome c reductase) before electrons are transferred to complex IV (cytochrome oxidase).[37,40]

Throughout the electron transport chain, electrons move towards progressively more electronegative electron acceptors ending with oxygen being converted to water at complex IV.[36] The energy released by transferring the electrons to a lower energy state pumps hydrogen ions (at complexes I, III, IV) into the intermembrane space which therefore becomes progressively more positively charged.[36] These hydrogen ions then flow back through the ATP synthase channel towards the relatively negatively charged mitochondrial matrix and the energy from this flow is used to create ATP from adenosine diphosphate (ADP).[36,37]

In the absence of oxygen, as in ischaemia, pyruvate is converted to lactic acid by anaerobic respiration with NAD^+ being released from NADH by lactate dehydrogenase.[35] Only the initial glycolysis stage is therefore contributing to ATP production in anaerobic metabolism, resulting in ATP depletion.[35,41]

The depletion of adenine nucleotides (ADP, ATP) has been demonstrated at the end of ischaemia in mouse, pig and human kidneys.[41] Coupled with ATP depletion in

ischaemia is adenosine monophosphate (AMP) accumulation, resulting in purine breakdown to hypoxanthine which accumulates until oxygenation is restored and onward metabolism to xanthine is permitted.[33,40]

1.4.2 ROS production

Although damage is initiated during ischaemia, the reperfusion phase is key to the production of damaging ROS. The vast majority of these are generated at the mitochondria with a smaller contribution from NADPH oxidase and by xanthine oxidase converting the accumulated hypoxanthine to xanthine.[33,40] It is thought that these processes produce superoxide later in reperfusion and contribute to subsequent inflammation rather than the immediate surge in ROS.[40]

At the mitochondria, it is complex I that is key to production of superoxide at the point of reperfusion, as demonstrated through studies of its selective inhibition.[40,41] During ischaemia, succinate accumulates by reversal of SDH allowing generation from fumarate.[40,41] Much of this fumarate is likely available as a substrate through the breakdown of accumulated AMP.[40] The conditions in the mitochondria during ischaemia result in reversal of the electron transport change so that when perfusion is restored, SDH releases electrons from succinate and these are fed backwards to complex I, resulting in a surge of superoxide formation.[40] Superoxide is directly harmful but also goes on to produce hydrogen peroxide and other ROS to cause oxidative damage.[40]

ROS damage cell proteins, deoxyribonucleic acid (DNA) and membranes through processes including lipid peroxidation and carbonylation of proteins.[42] This damage contributes to cell death through necrosis and apoptosis and release of damage associated molecular patterns (DAMPs) that trigger an immune response.[37,40]

At the mitochondria, part of the effect of ROS is mediated through opening of mitochondrial permeability transition pores (MPTP).[13] The MPTP is kept closed during ischaemia by the low pH, but opens as pH is restored and calcium levels rise, leading to water influx and mitochondrial swelling.[37,43] Transport of hydrogen ions also dissipates the charge gradient across the inner membrane and so prevents ATP synthesis through the electron transport chain.[13]

1.4.3 Electrolyte transport

ATP depletion affects membrane transport of electrolytes during ischaemia, resulting in accumulation of calcium and sodium intracellularly. Reduced activity at the Na^+/K^+-

ATPase leads to accumulation of intracellular sodium which is then passively transported out of the cell using the Na^+/Ca^{2+} exchanger, thereby increasing intracellular calcium.[13,33] Reduced active transport of calcium out of the cell exacerbates this rise.[13,33] Lactic acid from anaerobic metabolism causes intracellular acidosis and the increase in hydrogen ions are transported out of the cell passively, in exchange for sodium ions.[13,33] Thereby adding to intracellular accumulation of sodium, which in turn pulls water intracellularly causing cell swelling.[13,33]

On reperfusion, the hydrogen ions that have accumulated outside the cell are moved on by blood flow being restored.[13,33] This increases the gradient down which the remaining intracellular hydrogen ions leave the cell in exchange for sodium, thereby further increasing intracellular sodium levels.[13,33] Consequently, intracellular calcium is further increased by exchange with sodium.[13,33]

Ultimately, high calcium levels lead to activation of calcium dependent proteases such as calpains.[13,33] During ischaemia, the low pH keeps these enzymes inactive but on normalisation of pH with reperfusion, these enzymes are activated and damage cellular structures.[13,33]

1.4.4 Cell death

Several pathways for cell death have been demonstrated in IRI.[33,44,45] The relative contributions of each vary with the model studied and severity of injury and preventing cell death may not always be beneficial.[33,44-47]

Cell swelling in IRI can lead to cell death by necrosis, generating further inflammation through the release of DAMPs.[33,47] Regulated forms of necrosis are equally inflammatory and include necroptosis, ferroptosis and pyroptosis. [33,44,46,48]

Receptor-interacting protein kinase 3 (RIPK3) is a key molecule in the necroptosis signalling cascade and can be activated downstream of toll like receptors (TLRs), death receptors and interferon signalling, particularly when caspase 8 is inhibited.[44-46,48] Downstream of RIPK3, mixed lineage kinase domain like pseudokinase (MLKL) is activated by phosphorylation, enabling it to translocate to and permeabilise the plasma and mitochondrial membranes.[44-46] Positivity for phosphorylated MLKL (p-MLKL) has been shown in necrotic tubules in biopsies taken from people with acute kidney injury, confirming a contribution of necroptosis in this context.[49] However, as most necrotic tubules were negative for p-MLKL other pathways are also involved.[49]

In ferroptosis, membrane damage is the result of lipid peroxidation occurring in an iron-dependent manner and particularly in cells deplete of antioxidant defences.[47,48] In pyroptosis, membrane pores form downstream of inflammatory signalling.[45,47]

Apoptosis is considered a controlled form of cell death, which triggers little inflammation and may be beneficial in the context of injury by removing damaged cells.[33,45] Signalling cascades leading to apoptosis through caspase activation can be triggered by internal damage or from external signals activating cell surface death receptors.[33,45] Internal signalling to trigger apoptosis includes release of cytochrome c from the mitochondria into the cytoplasm and it is at this point that certain regulators of apoptosis interfere.[50-52] For instance, the inhibitor of apoptosis BCL-2 prevents efflux of cytochrome c from the mitochondria, whereas the pro-apoptotic BAX is essential for this process and BAD achieves its pro-apoptotic effects by blocking BCL-2.[33,45,50-52]

The overlap between these different regulated pathways for cell death is shown in **Figure 1-2**.

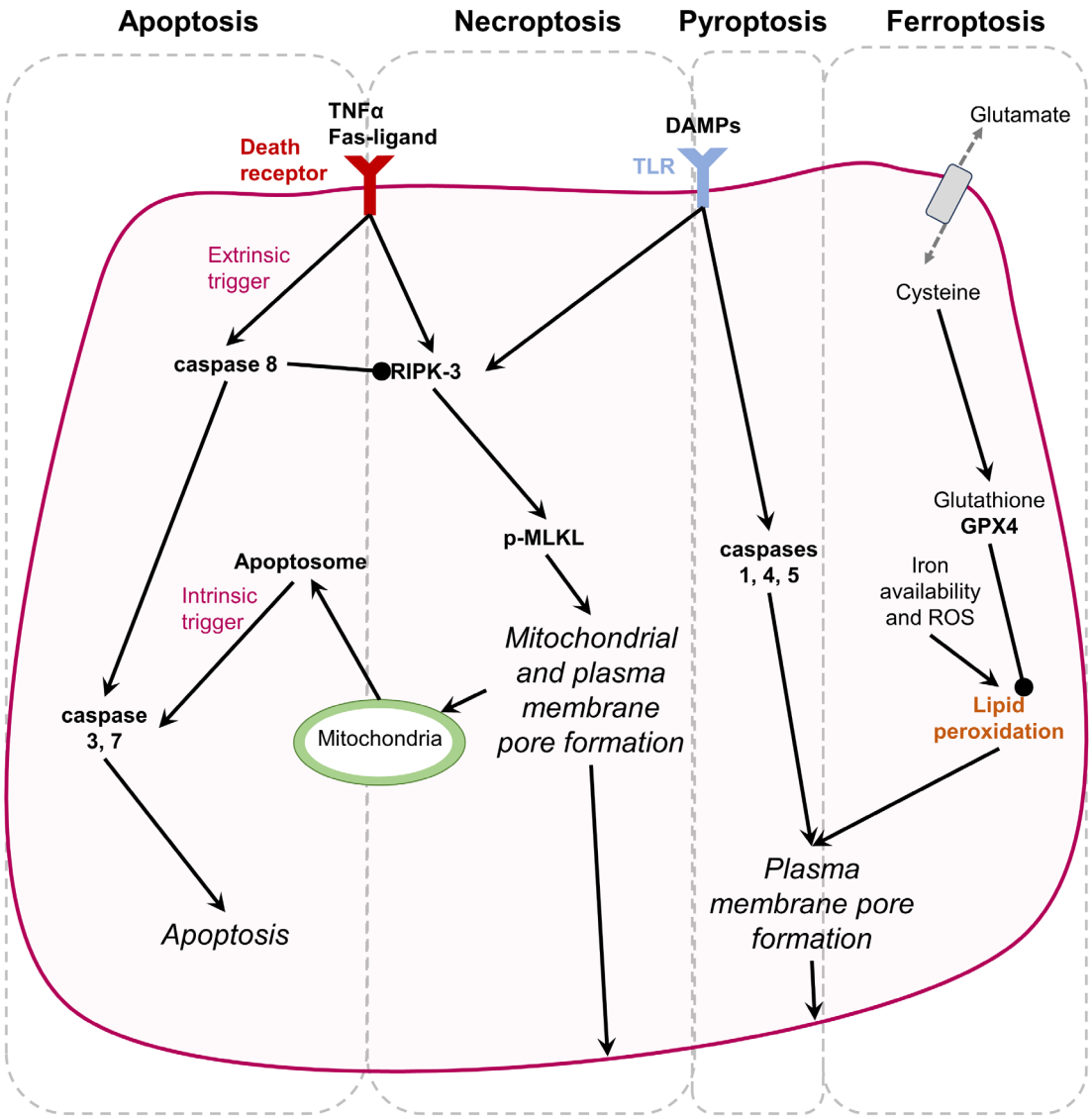

Figure 1-2 Regulated pathways of cell death implicated in renal ischaemia-reperfusion injury.
Apoptosis can be stimulated downstream of extrinsic triggers, such as TNFα and Fas-ligand activating death receptors, or by intrinsic triggers including damage to the mitochondria. Cytochrome c is released from damaged mitochondria and forms a complex called the apoptosome with apoptotic protease activating factor 1 (APAF1), to activate caspase 9. Apoptotic pathways converge on the effector proteases caspase 3 and 7. If caspase 8 is inhibited, death receptors can instead activate receptor-interacting protein kinase 3 (RIPK-3) to phosphorylate mixed lineage kinase domain like pseudokinase (MLKL) to p-MLKL. p-MLKL translocates to and permeabilises the mitochondrial and plasma membranes leading to necrosis through the necroptosis pathway. The binding of damage associated proteins (released during necrosis) to toll like receptors (TLR) can also trigger necroptosis. Alternatively, activation of TLRs can lead to necrosis through the pyroptosis pathway. The third regulated form of necrosis presented here is ferroptosis where lipid peroxidation that occurs in the presence of reactive oxygen species is dependent on iron availability. The cell defence against this process is the antioxidant glutathione peroxidase 4 (GPX-4) which requires glutathione (made from cysteine which is imported into the cell in exchange for glutamate) to prevent lipid peroxidation. A lack of either GPX-4 or glutathione therefore increases the propensity for necrosis through the ferroptosis pathway.[44,45,47,48]

1.4.5 Changes in transcription

The changes in transcription that occur in ischaemia are primarily downstream of the hypoxia inducible factors (HIF) HIF-1 and HIF-2.[33] These are heterodimeric proteins that differ in their α subunits but have a common β subunit.[33] Under normoxic conditions the α subunit is inactivated by the enzyme prolylhydroxylase (PHD).[33] As PHD requires oxygen as a cofactor, HIF-α subunits are stabilised in ischaemia and able to translocate to the nucleus, combine with the β subunit and bind the hypoxia response promoter element.[12,33,53]

Both HIF-1 and HIF-2 are increased with IRI and although they have some common targets their functions appear to differ.[33,53] After renal IRI, HIF-1α accumulates in proximal tubule cells whereas HIF-2α accumulates in endothelial cells.[53] HIF-1 and HIF-2 have vascular endothelial growth factor (VEGF) as a common target to promote angiogenesis but some other targets differ between these transcription factors.[33,53,54] Upregulation of erythropoietin to promote red cell production is predominantly via HIF-2, whereas HIF-1 targets genes involves in glycolysis.[54] TLRs and NF-κB are also considered HIF targets and lead to immune activation.[33]

HIF-1α levels display a second peak during the reperfusion phase, as demonstrated by both *in vitro* work on proximal tubular cells lines (HK-2) and through a rat model of renal IRI.[55] This second peak is thought to be downstream of PI3K/Akt signalling[55] but other factors present in reperfusion such as ROS and cytokines are also thought to stabilise the α subunit.[33]

HIF-1 and HIF-2 appear to offer some protection in IRI.[33] In HIF-2α knockout mice, restored expression only in endothelial cells was sufficient to reduce the injury in response to renal ischaemia-reperfusion.[53] A protective function of HIF-1 has been demonstrated, including in studies relating to renal transplantation.[33,53] However, HIF-1 may also contribute to chronic damage after IRI and has been implicated in epithelial to mesenchymal transition.[53] It may be the peak of HIF-1 during reperfusion that is most important for its protective function.[55]

1.4.6 Immune activation

TLRs are a class of receptors that bind both pathogen associated and endogenous ligands to activate the immune system.[53] Some of the potential endogenous ligands in ischaemia-reperfusion include extracellular matrix components, heat shock proteins and intracellular proteins such as high-mobility group box-1 (HMGB-

1).[33,48,53,56] In renal IRI, it is TLR2 and TLR4 that have been most implicated. These are both found on the cell surface and their expression in tubular epithelial cells is upregulated in ischaemia.[33,34,53,56] Knockout studies in mice have demonstrated their role in mediating injury after IRI through upregulation of cytokines and stimulating apoptosis and leukocyte infiltration.[57,58]

The complement system is also activated in IRI and contributes to inflammation and cell death. Complement upregulates adhesion molecules on endothelial cells and C3 deposition on epithelial cells marks cells for phagocytosis (opsonisation), with terminal pathway activity contributing to both cell lysis and leukocyte recruitment and activation.[33,34]

Sphingosine-1-phosphate (S1P) is released by endothelial cells, platelets and leukocytes and contributes to inflammation by signalling through the G protein coupled receptors $S1P_1R$ and $S1P_2R$ in the proximal tubule epithelium.[53,59] S1P signalling may also be beneficial to epithelial cell survival and protect the endothelium against increased permeability.[59]

In the context of transplantation, lymphocyte recruitment to the kidney is particularly problematic as differentiation of cytotoxic T cells leads to cellular rejection and B-cell activation produces antibodies against the graft (donor specific antibodies, DSAs).[13,33] Some of the pathways leading to this recruitment, differentiation and activation are shown in **Figure 1-3**.

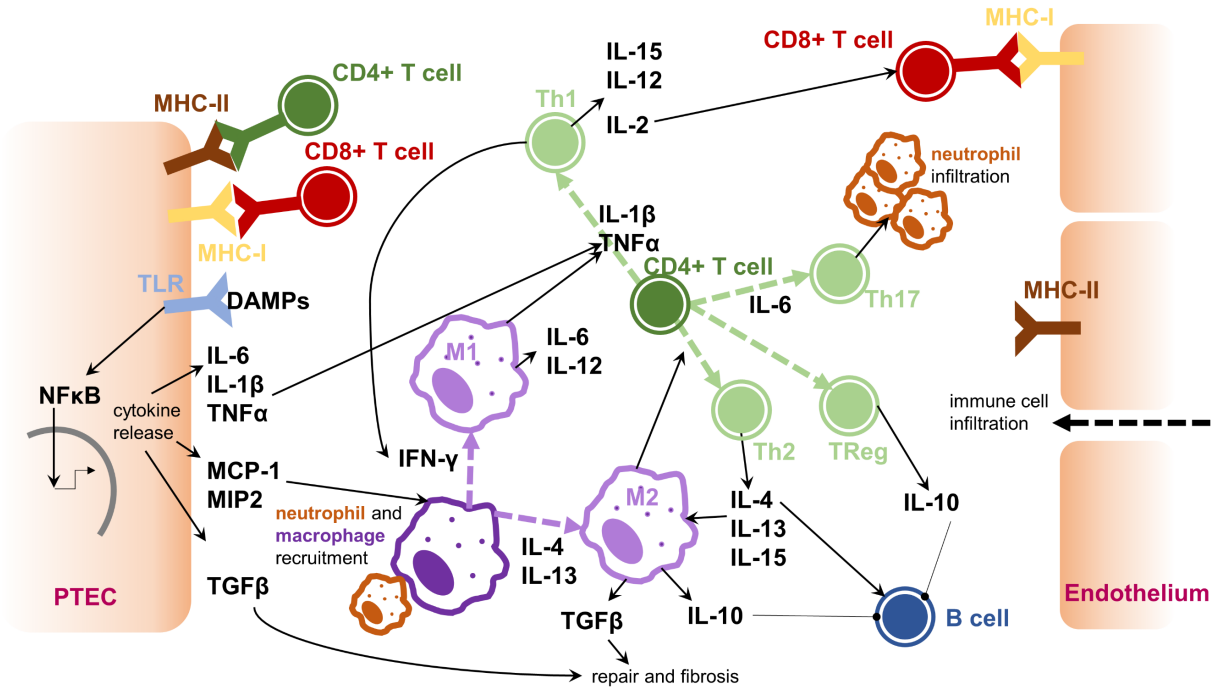

Figure 1-3 Leukocyte recruitment, differentiation and activation in renal ischaemia-reperfusion injury.
Proximal tubule epithelial cells (PTEC) express toll like receptors (TLR) that are activated by damage associated molecular patterns (DAMPs). Through NFκB signalling this results in transcription and release of inflammatory cytokines (e.g. IL-6, IL-1β, TNFα), chemokines (MCP-1, MIP-2) and TGF-β. MCP-1 and MIP-2 lead to recruitment of neutrophils and macrophages. Macrophages differentiate into the pro-inflammatory M1 state under IFN-γ signalling or the repair M2 state through IL-4 and IL-13 signalling. Respectively, these macrophages cause CD4 positive T cells to differentiate into Th1 and Th2 subtypes. The release of proinflammatory cytokines from Th1 cells activates cytotoxic CD8 positive T cells, recruits natural killers cells and promotes differentiation of M1 macrophages. CD4 positive T cells also include Th17 and regulatory (TReg) T cell subtypes which contribute to neutrophil infiltration and anti-inflammatory signalling through IL-10, respectively. Constitutive major histocompatibility complex (MHC) class I (MHC-I) expression in all nucleated cells enables antigen presentation to CD4 T cells. In the injured kidney, MHC class II (MHC-II) is upregulated in endothelial cells and PTEC, allowing these cells to present antigens directly to CD8 T cells, in addition to the professional antigen presenting cells (macrophages, dendritic cells) that usually express MHC-II. Increased permeability of the endothelial barrier also facilitates leukocyte recruitment and migration[33,34,60-64]

1.4.7 Tubular injury

In addition to being key effectors of injury as described above, the proximal tubule epithelium is also particularly vulnerable to damage from ischaemia.[34] Although the kidneys have a relatively high oxygen consumption overall (around 10 mL/min), the oxygen requirement differs between cells of the nephron and this affects their relative sensitivity to ischaemia.[34,65]

The proximal tubule epithelium has a high oxygen requirement linked to its resorptive function and a preference for oxidative phosphorylation through fatty acid oxidation.[4,65-67] The proximal tubule resides in the renal cortex, where the oxygen tension within the kidney is highest, and it has very little capacity for glycolysis instead being a key site of gluconeogenesis within the kidney.[4,36,67] As such, when the oxygen supply is disrupted in ischaemia, these cells are particularly vulnerable to ATP depletion.[47,48,68]

Ischaemic injury in the proximal tubule disrupts the polarity of the epithelium and leads to loss of the brush border.[34] ATP depletion contributes to cell death resulting in increased permeability of the tubule.[34] Kidney injury molecule 1 (KIM-1) and neutrophil gelatinase-associated lipocalin (NGAL) are commonly used injury markers expressed by damaged tubule and whilst KIM-1 has been implicated in neutrophil recruitment, mouse models suggest NGAL may promote repair.[15,34]

In contrast to the cortex, normal conditions in the medulla are relatively hypoxic.[34,69] The tubular segments here have a lower energy requirement and rely on glycolysis, making them less vulnerable to ischaemic injury.[4,34,67,69]

1.4.8 Endothelial dysfunction

Much like tubular epithelial cells, endothelial cells are both damaged by ischaemia-reperfusion and contribute to propagating the injury. Cell adhesion molecules are upregulated on endothelial cells leading to leukocyte infiltration.[33] Loss of cell-cell contacts from damage to the glycocalyx increases vessel permeability, leading to interstitial oedema and permitting the inflammatory infiltrate.[34]

Changes in the vessels from IRI make the tissue more vulnerable to further episodes of ischaemia and create a chronic hypoxia state.[34] There is an increase in vasoconstriction after ischaemia, due to reduced production of vasodilators by damaged endothelial cells and increase in cytokines promoting vasoconstriction.[34] A reduction in the density of capillaries after ischaemia, from the limited ability to regenerate damaged endothelium also generates a state of chronic hypoxia which promotes tubulointerstitial fibrosis.[33,34] The reduction in perfusion is also contributed to by microthrombi forming in small vessels.[34]

1.4.9 Graft loss

The mechanisms by which more severe ischaemia-reperfusion injury leads to poorer long term graft outcomes is presumably multifactorial with vascular changes making

the tissue more vulnerable to further ischaemia insults, incomplete recovery of damaged cells leading to chronic damage and the inflammatory response promoting fibrosis and immune activation which can ultimately lead to rejection (**Figure 1-4**).[70]

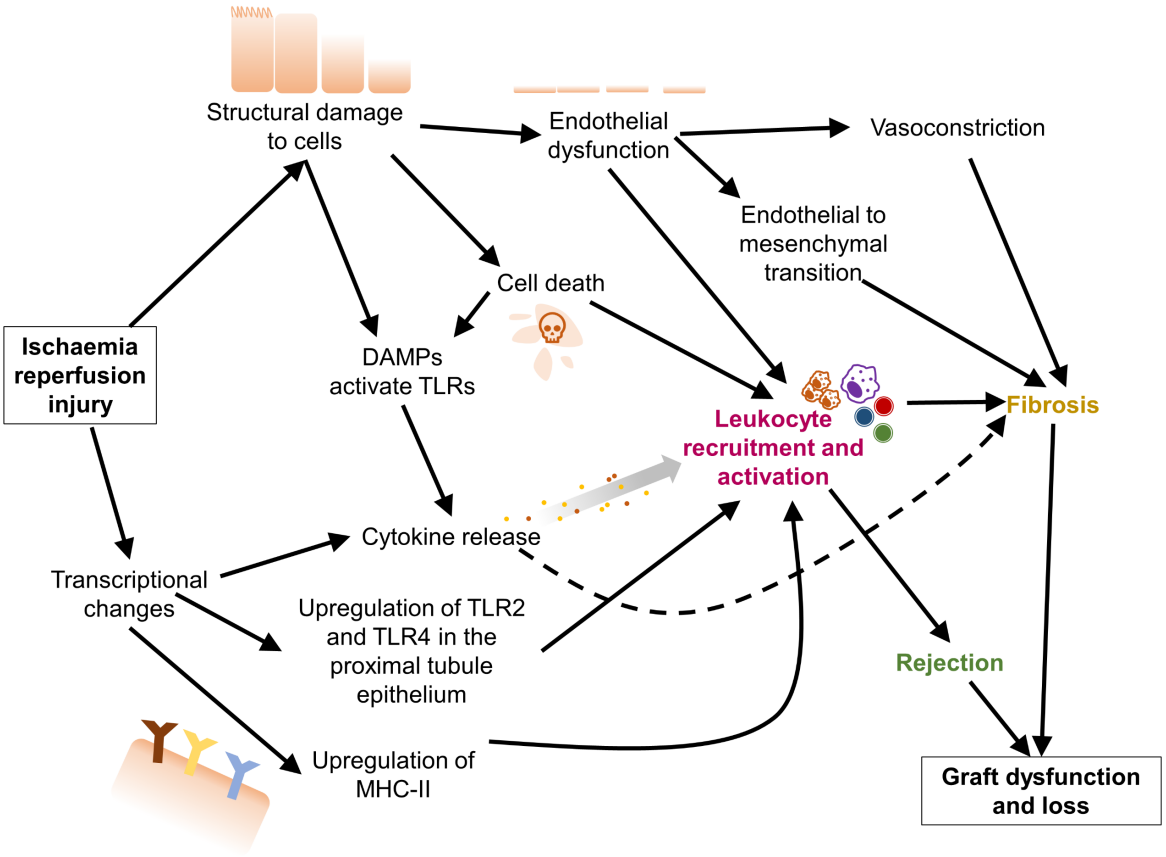

Figure 1-4 Injury pathways leading from the initial ischaemia-reperfusion injury (IRI) in kidney transplantation to chronic graft dysfunction and ultimate graft loss.
The structural damage to cells and transcriptional changes that occur during IRI lead to leukocyte recruitment and activation through increased expression and activity of toll like receptors (TLR) and the associated inflammatory cytokine release. The immune system is further stimulated by upregulation of major histocompatibility complex class II (MHC-II) on endothelial cells and proximal tubule epithelium allowing antigen presentation from these cells directly to cytotoxic T cells, thus contributing to the development of rejection. Structural damage to endothelial cells leads to endothelial dysfunction with increased permeability facilitating immune cell migration. Vasoconstriction contributes to chronic ischaemia and with endothelial to mesenchymal transition leads to fibrosis. DAMPs, damage associated molecular patterns

1.5 microRNAs (miRs) are potential targets to improve IRI

miRs are short non-coding regulator RNA sequences that are initially transcribed as their longer precursors, pri-miR.[71-73] Pri-miR are cleaved in the nucleus to a shorter hairpin structure (pre-miR) by Drosha enzyme before leaving the nucleus through Exportin-5.[71-73] In the cytoplasm, pre-miR are further cleaved into a duplex structure

around 22 nucleotides long by Dicer.[71,72] The strands in this duplex are named by whether in the hairpin structure they represented the 5' (miR-5P) or 3' (miR-3P) end.[74] One will generally be more stable and become the "guide" strand with the complementary strand being degraded.[74] In the case of miR-21, the guide strand is usually miR-21-5P but miR-21-3P may be relevant in some contexts or species.[71,72,75-77]

The gene for pri-miR-21 is located on chromosome 17 within a non-coding region (intron) of the gene *TMEM49*.[73,74] Although located within another gene, pri-miR-21 has its own promoter regions.[73,74] In fact, several promoter regions of different strength have been identified and may be of different importance in different cell types.[73,74] Within miRs, pri-miR-21 is not unique in being located within another gene but the majority of pri-miRs are located in the non-coding regions of DNA found between genes (intergenic) rather than within them.[73,74]

Regulation of miR-21 is complex and can occur at multiple levels. The interaction between miR-21 expression and TGFβ signalling highlights this complexity well and is supported by *in vitro* and rodent studies.[74,78,79] For instance, the TGFβ family member BMP6 negatively regulates miR-21 expression at the transcription level by reducing activity at the promoter for pri-miR-21.[74] Conversely, BMP4 and TGFβ upregulate levels of mature miR-21 at the post-transcriptional level through the downstream Smad proteins.[74,75,80] Certain Smad proteins increase Drosha activity to increase production of pre-miR-21 which can then go on to become mature miR-21.[74,80] In rats, overexpression of the inhibitory Smad7 was found to conversely suppress renal miR-21 expression.[79]

Pri-miR-21 expression can be regulated through the multiple transcription factor binding sites identified in the relevant promoter regions, but also by chromatin structure affecting accessibility to the promoter.[73,80] Regions of DNA called CpG islands have a high frequency of cytosine nucleotides followed by a guanine nucleotide and are important for determining how DNA wraps around histone and other proteins to form chromatin.[81] When cytosines in CpG islands are methylated, the chromatin structure is less open and so promoters are less accessible and expression is silenced.[81] A CpG island has been identified near the promoter region for pri-miR-21 with methylation status able to affect expression.[73,80,81]

To engage with target messenger RNA (mRNA), mature miR must first bind with argonaute proteins to contribute to the formation of the RNA-induced silencing complex.[82,83] mRNA then binds through complementary base-pairing to the miR within the RISC.[82,83] Perfect complementarity of the mRNA with all nucleotides in the miR is not necessary for binding as the miR structure can bulge or loop to accommodate unpaired nucleotides.[82] The most important regions are 6-8 nucleotides long and found at the 5' end of the miR.[82,84] These are called seed regions and binding to only this region can be sufficient to reduce mRNA expression.[82] However, complementarity to other nucleotide sequences in the miR supports this interaction and if strong, can compensate for imperfect complementarity at the seed region.[82] The overall degree of base-pairing between miR and mRNA sequences will determine the affinity of the miR to the target mRNA and the resulting degree of target repression.[82-84]

miRs are thought to silence target expression by multiple mechanisms including both blocking translation of the target mRNA, promoting degradation of the mRNA and perhaps also activating proteases to degrade the target polypeptide.[72,83,84] It has also been suggested that through interaction with nuclear argonaute protein, miR can also affect chromatin structure to silence targets at the transcriptional level.[84] In terms of preventing mRNA translation, this can be achieved by competition of the argonaute complex with initiation factors and through binding target sites in the 5'UTR or coding sequences of the mRNA, in addition to interference with elongation factors leading to incomplete translation.[84] In part, miRs can promote mRNA degradation through recruitment of enzymes to remove the poly(A)tail or cap structures from mRNA and so making the remaining strand vulnerable to enzyme degradation.[85] Additionally, the RISC recruits cytoplasmic units called P or GW bodies, which are involved in mRNA decay.[85]

Although largely considered to be gene silencers, miRs may also cause upregulation. Competition for incorporation into RISC is likely to contribute to this process.[84] In this way, an increase in abundance of one miR could increase expression of another miR's target mRNAs.[84]

For miR-21, it is thought most binding sites are located in the 3'UTR or in coding sequences of target mRNA.[83] Although the sequence of miR-21 is highly conserved between species, the way in which miR-21 interacts with target mRNA has been

shown to vary.[82] Studies in human tissue are therefore most relevant for revealing clinically translatable targets and mechanisms.

A single miR is complementary to multiple mRNA sequences and in this way they are key regulators of cellular processes. Ultimately, the magnitude of change in miR target expression are often small, but a coordinated response across a large number of targets still has the potential to generate a biological effect.[86] Modulating miR action through use of mimics or inhibitors (antimiRs) is therefore attractive as a potential therapeutic.[72] In the case of antimiRs, chemical modifications have improved their resistance to nucleases and improved affinity of binding to target sequences.[3,72,87] In mouse studies, systemic delivery of an antimiR targeting miR-21 (antimiR-21) demonstrates delivery to the kidney cortex[88,89] and persistence after a single dose with a half-life of 4-25 days.[89] In the phase 2 clinical trial (NCT02855268) of an antimiR-21 (lademirsen) in Alport nephropathy, weekly subcutaneous dosing was used.

1.6 miR-21 function in kidney injury

Blockade of miR-21 is of particular interest given its consistent upregulation in IRI,[88,90,91] amongst other models of kidney injury,[92] and negative correlation with transplant outcome.[93-95] miR-21 expression also falls in the recovery phase in a rodent model of IRI.[96] miR-21-5p was shown to be highly expressed in a human kidney model of IRI using ex vivo normothermic machine perfusion (NMP).[97] In ischaemia, miR-21 is upregulated downstream of HIF-1 which binds the miR-21 promoter region.[98,99]

Although miR-21 is expressed in healthy kidney, it has limited function in the unstressed state.[88,100] This is demonstrated by normal development of knockout mice and similar gene expression profiles in kidneys of unstressed knockout animals when compared to wildtype.[88]

1.6.1 Pathways targeted by miR-21

miR-21 contributes to injury processes through regulation of metabolic pathways, particularly inhibiting fatty acid oxidation and promoting ROS generation.[88] It also interacts with fibrotic (TGFβ, ERK/MAPK)[88,101] and inflammatory (NFκB)[101] pathways and these potential effects are summarised in **Figure 1-5**.

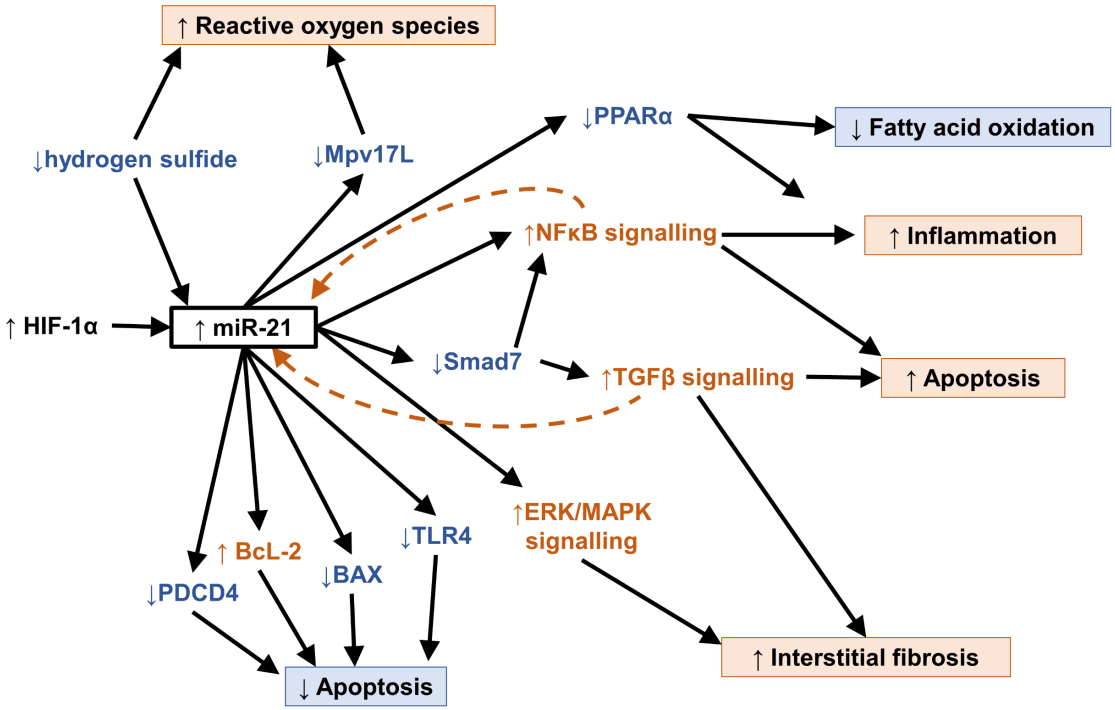

Figure 1-5 Summary of reported targets and pathways through which miR-21 may exert its effect in ischaemia-reperfusion injury.
miR-21 is upregulated downstream of HIF-1α stabilisation in hypoxia and through positive feedback from NFκB and TGFβ signalling. Low levels of the antioxidant hydrogen sulfide can also increase miR-21 expression. Data on the effect of apoptosis is unclear with some studies supporting miR-21 to increase apoptosis whereas others find it to reduce apoptosis. Similarly, it has been reported that NFκB activation is reduced downstream of miR-21, although others report increased activity of this pathway through reduced inhibition from Smad7.[21,78,79,88,99,101-108]

miR-21 has been shown to interact with cellular metabolism in injury through the targets Mpv17L and PPARα.[88,104] Mpv17L is involved in the metabolism of reactive oxygen species whereas PPARα is involved in fatty acid oxidation.[88,104] In mouse models of Alport nephropathy and renal fibrosis, miR-21 knockout or inhibition was associated with increased expression of both PPARα and Mpv17L, relative to miR-21 replete animals and a concurrent reduction in ROS production was observed.[88,104] Interestingly, antimiR-21 treatment exacerbated and miR-21 mimic attenuated the increase in ROS production by HK-2 cells subjected to oxygen and glucose deprivation to mimic ischaemia.[107] There was no reperfusion phase in this model.[107]

There is also a suggestion that oxidative damage can increase miR-21 expression. In a mouse model of IRI, greater miR-21 upregulation with injury in older mice was associated with lower levels of the antioxidant hydrogen sulfide.[21] This upregulation of miR-21 was diminished by supplementing with exogenous hydrogen sulfide.[21]

The interaction between miR-21 and TGFβ signalling is bidirectional with miR-21 both being regulated by and acting through TGFβ signalling. Unilateral ureteric obstruction (UUO) is a common model of renal fibrosis and TGFβ is a key signalling pathway in this injury.[78] Fibrosis in response to UUO is reduced in miR-21 knockout animals compared to wildtype controls and translocation of phosphorylated Smad2/3 to the nucleus, which happens downstream of TGFβ, is prevented.[78] Similarly, Smad7 is a negative regulator of TGFβ signalling and is directly repressed by miR-21 through binding of its 3'UTR.[109] This is in keeping with diminished TGFβ upregulation noted with antimiR-21 treatment in a mouse model of IRI.[21].

The reported effect of miR-21 on NFκB signalling is less consistent. It has been suggested that the suppression of Smad7 by miR-21 disinhibits NFκB signalling, increasing inflammation.[101] In contrast, Song et al.[108] found antimiR-21 to exacerbate the NFκB activation seen with hypoxia-reoxygenation, indicating miR-21 to have an inhibitory effect.

miR-21 regulation of cell apoptosis needs further characterisation in the context of renal IRI. miR-21 has been shown to upregulate the anti-apoptotic factor BcL-2 and suppress tumour suppressor programmed cell death 4 (PDCD4), both of which would predict antimiR-21 to increase apoptosis.[90,106,110,111]

Mouse models of kidney IRI have produced variable results on the effect of antimiR-21 on apoptosis. Song et al.[108] found antimiR-21 to increase apoptosis, assesed by cleaved caspase 3 levels, in addition to increasing PDCD4 expression. However, Xu et al.[99] found antimiR-21 to have no impact on apoptosis in IRI. In contrast, when coupled with ischaemic preconditioning, antimiR-21 treatment increased the amount of apoptosis detected 24 hours after reperfusion.[99]

In *in vitro* and rat models of ischaemic kidney injury, without a reperfusion phase, antimiR-21 treatment was found to increase apoptosis whereas miR-21 mimic improved cell viability.[107] This effect of antimiR-21 was associated with increased expression of pro-apoptotic BAX and reduced expression of the inhibitor BcL-2.[107] In contrast to these findings, Huang et al.[105] found miR-21 inhibition to reduce tubule cell apoptosis when ischaemia-reperfusion was modelled in HK-2 cells.

Results are similarly conflicting in other models of kidney injury. Mouse models of renal fibrosis and Alport nephropathy have shown miR-21 inhibition to reduce levels of cell death.[88,104] In contrast, in a mouse and *in vitro* model of sepsis-induced AKI

stimulated by lipopolysaccharide treatment (LPS), miR-21 improved cell viability by preventing upregulation of TLR4.[102]

The potential to induce apoptosis by targeting miR-21 is appealing in the field of oncology where miR-21 expression is noted to be higher in renal cell carcinoma compared to healthy tissue, and associated with lower PDCD4 expression.[106] In renal cell carcinoma cell lines, antimiR-21 treatment increased PDCD4 expression and outside the kidney, antimiR-21 treatment increased apoptosis in a glioblastoma cell line.[103,106]

Currently, it remains unclear how miR-21 interacts with cell death pathways in different organs and disease states.

1.6.2 The effect of miR-21 inhibition on injury

There are inconsistencies in the reported effect of miR-21 inhibition in different models of kidney injury. At least in IRI, the impact of antimiR-21 treatment on renal injury may in part relate to the length of the reperfusion phase allowed for follow up.

Chau et al.[88] found antimiR-21 treatment given before ischaemia to reduce the degree of renal injury in mice 14 days after the ischaemic insult. Crucially, antimiR-21 also reduced injury when given 5-7 days after reperfusion, demonstrating that inhibition at the time of ischaemia is not essential for benefit.[88] AntimiR-21 pre-treatment also diminished the reduction in renal blood flow and increase in collagen deposition observed 7 days after ischaemic injury in older mice, who were found to express higher levels of miR-21 than their younger counterparts.[21]

However, mouse models of IRI using a shorter follow up of 24 hours of reperfusion have either found no benefit or shown a detrimental effect of antimiR-21 treatment given either before or at the time of ischaemia.[99,108,112] Similarly, in a rat model studying ischaemia without a follow up reperfusion phase, pre-treatment with antimiR-21 increased the level of kidney injury after ischaemia.[107]

miR-21 inhibition has been shown to be protective in the rodent models of other forms of kidney injury including renal fibrosis,[78,113] Alport nephropathy,[104,114] systemic inflammatory response syndrome-related AKI[115] and diabetic kidney injury.[116] Conversely, antimiR-21 treatment increased kidney injury in a mouse model of sepsis-related AKI.[102]

1.7 AntimiR delivery to the kidney

NMP is useful as a method for studying IRI in human organs ex vivo and has the potential to deliver therapeutic agents to organs destined for transplantation, in isolation before they are implanted.[97,117] In the case of antimiRs, a fluorescently labelled antimiR targeting miR-24 has been delivered to human kidneys declined for transplantation using this system.[97] Significant uptake was demonstrated from 4 hours in normothermic conditions but not in hypothermia, supporting a role for active transport in antimiR uptake.[97] Endocytosis as the mechanism of uptake was further supported by colocalisation of the antimiR with endocytosis markers.[97]

In human kidneys, the proximal tubule was a key site of antimiR delivery during NMP.[97] Similarly, antimiR-21 uptake in mouse kidney was most evident in proximal tubule epithelial cells but also demonstrated in endothelium, macrophages, pericytes and myofibroblasts after systemic administration.[88]

Chapter 2. Statement of aims

2.1 Hypothesis

AntimiR-21 protects the kidney against IRI through its effect on metabolic, inflammatory and apoptotic pathways. AntimiR-21 can be effectively delivered to primary human PTEC *in vitro* and with 24 hours ex vivo kidney NMP. Megalin is key in the mechanism for antimiR uptake into PTEC *in vitro*.

2.2 Aims and objectives

The overarching aim of this project is to assess whether antimiR-21 is a useful potential therapeutic in transplant for the initial IRI sustained by kidneys. Specific aims within this are:

- To isolate and characterise pure cultures of PTEC from human kidneys declined for transplant to use as in *in vitro* model for IRI
- To assess if antimiR can be delivered to primary human PTEC *in vitro* without the use of transfection reagents
- To determine the endocytic pathway involved in antimiR uptake into primary human PTEC
- To assess the impact of antimiR-21 on apoptosis in the context of IRI using *in vitro* and ex vivo human models
- To determine the effects of antimiR-21 on gene transcription and translation in human models of kidney IRI using unbiased techniques and to use these results in conjunction with cytokine levels to determine the pathways that have been modulated
- To determine if antimiR-21 is protective against injury following ischaemia-reperfusion in ex vivo kidneys

Chapter 3. Methods

3.1 Culture and maintenance of cell lines

Details of cell lines used are given in the **Table 3-1**. Cell lines were grown at 37ºC with 5% CO_2 in a humidified incubator in media detailed in the **Table 3-1**.

Cell line	Cell type	Complete culture media
HKC-8	human proximal tubular epithelial cells immortalised by an adenovirus vector	DMEM:F12 with L-glutamine and 15 mM HEPES (Lonza #BE12-719F or Scientific Laboratory Supplies 10-092-CV) supplemented per 500 mL of media with 1% Penicillin/ Streptomycin and 10% FBS
HMRC-5	human fibroblasts derived from normal foetal lung tissue	
Caco-2	human epithelial cells derived from colorectal adenocarcinoma	DMEM high glucose with bicarbonate (Sigma Aldrich D5671-500ML) supplemented with 10% FBS, 1% Penicillin/Streptomycin and L-glutamine
HMEC-1	microvascular endothelial cells derived from human foreskins and immortalised by transfection with pSVT vector	MCDB131 without L-glutamine (Gibco 10372-019) and supplemented with 10 ng/mL epidermal growth factor, 1 µg/mL hydrocortisone, 10 nM L-glutamine, 10% FBS by volume and 100 µg/mL of Penicillin/Streptomycin

Table 3-1 Cell lines used and details of relevant complete maintenance media. FBS, foetal bovine serum

Cells were passaged when around 80% confluent. Media, supplements and trypsin were warmed to 37ºC in the water bath. All cell culture techniques were performed using sterile technique in containment level 2 tissue culture hood. Old media was removed and cells washed with sterile phosphate buffered saline (PBS). Trypsin was applied at a volume to cover cells and incubated at 37ºC for around 5 minutes until cells were detached by gentle tapping. An equal volume of complete media was

added to neutralised trypsin and cell suspension was transferred to a 15 mL falcon tube to centrifuged at 300 RCF for 5 minutes. Supernatant was discarded and cells resuspended in 1-2 mL of complete media before seeding into flasks for maintenance (350000 cells in 5 mL of media in T25, 750000 cells in 10 mL of media in T75 flask) or into alternative vessels as required for experimental procedures.

3.1.1 Cell counting

Manual cell count was performed in 1:1 ratio of 0.4% Trypan blue to cell suspension. 10 µL of this mix was applied to each side of bright line haemocytometer and viable cells (excluding blue dye) counted using bright field microscope. The mean count from two regions with a volume of 0.1 µL each were used to calculate the cell count, accounting for the trypan blue dilution factor.

3.2 Isolation and maintenance of primary human PTEC

Human kidneys declined for transplantation and with appropriate consent for research were used for isolation of primary PTEC. Isolation method was adapted from Brown et al.[118] and Bajaj et al.[119] Kidneys from donors under 70 years old and with an expected CIT of less than 30 hours on arrival were used. The exception to this was for the first kidney used where ischaemic time was 32 hours. No kidneys from donors with blood borne viruses were accepted. Where there was concern of possible renal malignancy, only tissue remote to the lesion was collected. No kidneys from donors who required renal replacement therapy in their terminal admission were used.

On receipt of the organ, the inner sterile bag was placed unopened into an autoclaved dish within a containment level 2 tissue culture hood.

3.2.1 Tissue collection and digestion

Capsule was detached using tissue forceps. A scalpel was used to collect thin slices of cortex which were finely diced using single edge razors (VWR, 233-0156). Scalpel blades and single edge razors were changed on blunting. 5-8 g of tissue was placed into a 50 mL falcon tube with 20 mg of reconstituted collagenase (**Table 3-2**) per gram of tissue. The remaining volume of the falcon tube was filled with cold isolation media (**Table 3-2**).

	Base media	Supplements for reconstitution
Isolation media	RPMI (Sigma Aldrich R8758-500ML)	5% (v/v) FBS 2% (v/v) Penicillin/Streptomycin (Sigma Aldrich P0781)
Maintenance media	DMEM/Ham's F-12 1:1 ratio (Sigma Aldrich D8437) with 15 mM HEPES, 2.5 mM L-glutamine and sodium bicarbonate	1.5 mM L-glutamine 1% (v/v) Penicillin/Streptomycin 1 REGM SingleQuot Kit Supplement with growth factors (CC-4127 Lonza/Arxada) containing: 2.5 µg Insulin, 18 ng hydrocortisone, 50 µg GA-100, 0.25 µg adrenaline, 0.5 ml of 5 pM T3, 2.5 µg transferrin, 2.5 mL of 0.5% FBS, 5 ng epithelial growth factor
Collagenase	Worthington Type 2 collagenase from Lorne labs LS004176	reconstituted to 100 mg/mL in calcium-free HBSS from ThermoFisher scientific 14185045 and filtered through 40 µm sterile filter

Table 3-2 PTEC maintenance and isolation media.
Details of media used for primary human proximal tubule epithelial cells and method of collagenase reconstitution. FBS, fetal bovine serum.

Tissue was incubated either for 2-2.5 hours at 37^{o}C or overnight at 4^{o}C followed by 1.5-2 hours at 37^{o}C before proceeding with cell isolation. The falcon tube was gently agitated horizontally during tissue digestion.

3.2.2 Cell isolation

Collagenase digested tissue was passed through a 40 µm nylon cell strainer into clean sterile 50 mL falcon tubes. Filter was changed when clogged and the back of 5 mL syringe was used to encourage material through the strainer.

Filtered cells were centrifuged at 4^{o}C for 10 minutes at 1200 RPM. Supernatant was collected to repeat centrifugation and the initial pellet was resuspended in cold isolation media. The pellet from centrifuging the supernatant was resuspended and

combined with the initial sample. This process was repeated a further time with the second pellet from supernatant centrifugation also being added to the initial sample and made to 25 mL with cold isolation media. This was centrifuged at 4°C for 7 mins at 1200 RPM and supernatant discarded. Pellet was loosened and resuspended in 10 mL of cold isolation media.

Percoll gradients were generated as shown in **Table 3-3**. 7 mL of 1.07 was pipetted into a clean 50 mL falcon tube, 7 mL of 1.04 and then 5 mL of cell suspension were slowly added on top to ensure no mixing. 10 mL cell suspension was therefore distributed between two tubes containing Percoll gradients.

	Stock Percoll	**1.04 density**	**1.07 density**
Composition	10X HBSS 1:9 Percoll	Stock Percoll 5:12 isolation media	Stock Percoll 5: 4 PBS

Table 3-3 Percoll gradient composition.
Method for reconstituting Percoll and generating 1.04 and 1.07 densities from stock dilution

Percoll gradients were centrifuged at 4°C for 25 minutes at 3000 RPM with a break speed of 0. The central layer, consisting of media, and the cells at the lower boundary of this layer, were extracted slowly using a P1000 pipette (**Figure 3-1**). Care was taken to avoid cells from the layer above containing debris, endothelial cells and fibroblasts (**Figure 3-1**).

Extracted cells and media were centrifuged at 1200 RPM for 7 minutes at 4°C, supernatant discarded and cells resuspended in 10 mL of cold isolation media before repeating the centrifugation. The resulting pellet was loosened and resuspended in 2-10 mL of cold isolation media. Manual cell count was performed as described above.

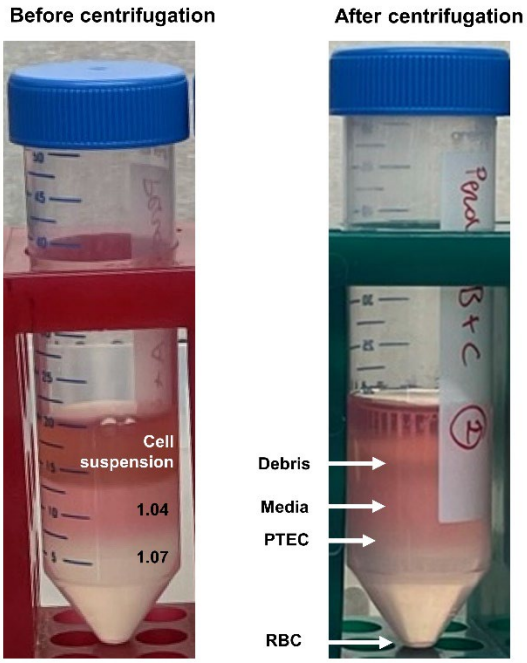

Figure 3-1 Percol gradients for primary human PTEC isolation.
Photograph of 50 mL falcon tubes containing Percoll gradients before (left) and after (right) centrifugation. Cell suspension is added on top of 1.07 and 1.04 density Percoll gradients and after centrifugation, proximal tubule epithelial cells (PTEC) are extracted by removing the media layer and cells and the interphase beneath. Debris layer contains damaged cells, endothelial cells and fibroblasts is above the media layer. Red blood cells (RBC) are most dense so at the base of the tube. Photo acquired with iPhone 12 mini (model MGE23B/A) using the default settings on default camera.

Cells were seeded as required with warmed maintenance media. Optimum seeding density for transwell inserts was 226 666 cells/cm^2 of growing area. Standard media volumes and seeding density for each size of insert are given in **Table 3-4**.

Insert	Growing area (cm^2)	Cells seeded	Media volume in apical compartment	Media volume in basolateral compartment
6-well	4.5	1.06 x 10^6	2 mL	2.5 mL
12-well	1.1	260 000	500 µL	1.5 mL
24-well	0.3	64 000	200 µL	1 mL

Table 3-4 Standard seeding densities for isolated primary human proximal tubule epithelial cells

3.2.3 Maintenance of primary human PTEC

One day after seeding, maintenance media was replaced with fresh warmed maintenance media. Cells from the initial kidney were grown on plastic and passaged when 80% confluent. For subsequent cell isolations, cells were maintained on glass or on transwell inserts (Sarstedt, 0.4 µm pore size, transparent PET membranes with a pore density of 2 x 10^6 pores/cm^2) without passaging and media was changed every 48-72 hours.

3.3 Light microscopy

Light microscopy of cells in culture was performed with Nikon Eclipse TS100 inverted phase contrast microscope. Phase contrast slider was used particularly for cells maintained on transwell inserts to improve clarity. Images of light microscopy were acquired with iPhone 12 mini (model MGE23B/A) using the default settings on default camera.

3.4 Cryopreservation of cells

3.4.1 Cell lines

After cell counting, cells were centrifuged at 300 RCF for 5 minutes and supernatant discarded. Cells were resuspended in 10% dimethyl sulfoxide (DMSO) in fetal bovine serum (FBS) at a concentration of 10^6 cells/mL and aliquoted at 1 mL per cryovial. Cryovials were gradually cooled to -80°C using Corning CoolCell LX Freezing Container or Nalgene™ Mr Frosty® Freezing Container and then transferred to liquid nitrogen stores within 48 hours.

When required, cells were thawed to 37°C, added to complete media, centrifuged at 300 RCF for 5 minutes and supernatant discarded to remove DMSO. Cells were then seeded into flasks as described above. Alternatively, cells were seeded from cryopreservation vials once thawed and media was centrifuged to remove DMSO within 24 hours.

3.4.2 Primary human PTEC

Excess PTEC isolated from human kidneys as described in 3.2 were cryopreserved at the point of isolation by resuspension in either 10% DMSO in FBS or Cryo-SFM (PromoCell C-29910) at 10^6 cells/mL and frozen as described above.

On thawing, a trypan blue cell count was performed and cells were seeded directly onto transwell inserts at the densities given in **Table 3-4**. Media was changed after 24 hours.

3.5 AntimiR treatment

Fluorescein amidite (FAM) labelled scrambled control antimiR (Qiagen YC10202062-FZB) and antimiR-21 (Qiagen 339131 Y104100689-DDB) stock solutions were stored at -20^{o}C after reconstituting with nuclease-free sterile TE buffer (Fisher Scientific 10224683) to concentration of 180 μM and 20 μM respectively. The antimiR-21 used throughout this work specifically targeted miR-21-5P.

To treat PTEC in culture, antimiR was diluted in maintenance media to working concentrations and applied to the apical compartment. At end of treatment period, media was removed and cells washed with PBS and proceeded to analysis by flow cytometry or immunofluorescence.

3.6 Cellular uptake markers

Texas Red-labelled 10 kDa dextran (ThermoFisher D1828) was applied to the apical compartment at a concentration of 1 mg/mL. Human albumin was conjugated with either fluorescein isothiocyanate (FITC; Sigma A9771) or Texas Red (ThermoFisher A23017) and applied to the apical compartment at a final concentration of 0.1 mg/mL.

3.7 Cellular models of hypoxia and free radical stress

3.7.1 Cobalt chloride treatment

Cobalt chloride treatment is routinely used to mimic hypoxia by stabilising HIF. It was used at a concentration of either 100 μM or 200 μM in complete media to treat cells for 24 hours.

3.7.2 Hydrogen peroxide treatment

Hydrogen peroxide treatment is used to mimic oxidative stress.[120] Hydrogen peroxide stock (Sigma H1009-5ML) 30% w/w has a concentration of 9.791 M. Therefore, 10 μL of stock was diluted into 1.22 mL media to generate 80 mM solution which was serially diluted with media to working concentration of 400 μM.

3.7.3 Hypoxic incubator

To mimic ischaemia-reperfusion in cell culture, cells were incubated in 1% oxygen in a humidified incubator that was able to stably maintain this oxygen concentration at

37ºC. Media was changed on return to normoxia (reoxygenation) to mimic reperfusion.

To match media depth of 6-well and 12-well inserts, media volumes used in 24-well inserts was reduced to 900 µL in the basolateral compartment and 135 µL in the apical compartment when maintained in 1% oxygen. Matched normoxic controls were adjusted similarly.

3.8 Immunofluorescence and fluorescent microscopy

3.8.1 Cell seeding

Cells lines were seeded into 8 well chamber slides at 50 000 cells per well in 200 µL of media and incubated in normal conditions for 24-48 hours to adhere.

Primary cells were seeded either into 8-well chamber slides with an increased seeding density of 80 000 cells per well or into 24-well transwell inserts at 68 000 cells/insert.

3.8.2 Fixation and permeabilisation

Media was discarded, cells were washed with cold PBS and fixed either with methanol or 4% at paraformaldehyde (PFA).

Methanol fixation was performed at -20ºC for 15 mins to 1 week and followed by washing twice with PBS-Tween 0.05%.

Fixation with 4% PFA was performed at room temperature for 10-15 minutes. Samples were then washed with PBS and could be stored in PBS at 4ºC for 1 week if required. To permeabilise cells after PFA fixation, cells were incubated in 0.1% Triton-X in PBS for 4 minutes at room temperature then washed three times in PBS for 5 minutes. All subsequent wash steps were performed with PBS.

3.8.3 Blocking and antibody incubations

Cells were blocked with 10% goat serum for 1 hour at room temperature. Blocking buffer was removed and primary antibody applied diluted in PBS (**Table 3-5**). For no primary controls only PBS was applied or alternatively, a comparable concentration of isotype control (**Table 3-5**) was used. Cells were incubated with primary antibody or negative controls overnight at 4ºC.

Cells were washed three times with PBS for 5 minutes then incubated with an appropriate fluorescently conjugated secondary antibody diluted in PBS for 1 hour at

room temperature in the dark. Wash steps were then repeated. Antibodies and concentrations used are shown in (**Table 3-5**).

Target	Host and isotype	Product	Antibody stock (µg/µL)	Dilution	Secon-dary
Primary antibodies					
AQP1	rabbit	Abcam ab168387	0.195	1 in 100	2
E-cadherin	mouse IgG2a	BD transduction 610181	0.25	1 in 100	1
SMA	mouse IgG2a	clone C1A4	0.071	1 in 100	1
TJP1/ZO1	rabbit polyclonal	Sigma Aldrich HPA001636	0.1	1 in 50	2
Cytokeratin -19	mouse IgG2a	ThermoFisher A53-B/A2	0.5	1 in 100	1
RAB7	rabbit	Abcam ab137029/126712	0.011	1 in 200	3
HIF-1α	mouse IgG2b	Novus Biologicals NB100-105	1.0	1 in 50	1
Isotype controls					
-	mouse IgG1	eBiosciences 14-4714-82 clone P3.6.2.8.1	0.5		1
-	mouse IgG2α	R&D MAB0031	0.5		1
-	rabbit polyclonal	R&D rAB-105-C	1.0		2 or 3
Secondary antibodies					
Target	**Host and fluorophore**	**Product**	**Antibody stock (µg/µL)**	**Dilution**	**Number**
Mouse	Goat, Dy650	Immunoreagents GtxMu 003 D650NHSX	1.0	1 in 100	1
Rabbit	Goat, Dy550	Immunoreagents GtxRb 003 D550NHSX	1.0	1 in 100	2
Rabbit	Donkey, AlexFluor594	Biolegend 406418	0.5	1 in 100	3

Table 3-5 Antibodies used for immunofluorescence.
Optimised concentrations are given. The secondary antibodies used have been numbered and use with primary antibodies indicated. Matched isotype controls for primary antibodies were used at equivalent concentrations to demonstrate non-specific secondary antibody binding. AQP1, aquaporin 1; HIF-1α, hypoxia inducible factor 1α; Sigma, Sigma Aldrich; SMA, smooth muscle actin; TJP1/ZO1, tight junction protein 1/zonula occludens 1.

3.8.4 Mounting

For chamber slides, the chamber was removed by loading into the well-separating tool and extra fluid removed by gently tapping. Transwell inserts were cut out using a scalpel and placed cell side up onto glass slides.

Slides were mounted using Vectashield antifade mounting media with DAPI (2B Scientific, H-1200-10). Slides were air dried in the dark and sealed with nail varnish.

3.8.5 Tissue sections

To assess uptake of FAM-labelled antimiR into perfused kidneys, formalin fixed paraffin embedded human kidney sections were deparaffinised with xylene, rehydrated with 100%, 90% and 70% ethanol followed by immersion in deionised water and subsequently mounted with Vectashield antifade mounting media with DAPI (2B Scientific, H-1200-10).

3.8.6 Widefield fluorescent microscopy image acquisition

All widefield fluorescent microscopy images were acquired by ZEISS Axio Imager with X40, X20 or X10 lens. Exposure times were consistent within runs.

Widefield fluorescent microscopy images intended for quantification were acquired using a standardised approach. These images were acquired at random of confluent areas of cells guided by nuclear DAPI signal and blinded to fluorescent signal in the other channels.

Single channel images were converted to .tif using ZEISS Zen Microscopy Software (RRID: SCR_013672) with the same display settings applied to each repeat within a batch. If signal was not to being quantified, single channel images could alternatively be exported as .jpeg.

3.9 TdT-mediated dUTP Nick-End Labeling (TUNEL)

Dead-End™ Fluorometric TUNEL system (Promega G3250) was used on formalin fixed paraffin embedded mounted sections of human kidney tissue as per product literature. Briefly, sections were deparaffinised and rehydrated as described above (**3.8.5**). Sections were then fixed in 4% PFA and incubated in 20 µg/mL Proteinase K for 8-10 minutes at room temperature for antigen retrieval. Slides were washed in PBS and fixed with 4% PFA for 5 minutes at room temperature followed by a further wash before being incubated in equilibration buffer for 5-10 minutes at room temperature. Slides were then incubated for 1 hour at 37°C in a humidified chamber

in the dark with incubation buffer containing Terminal Deoxynucleotidyl Transferase Recombinant enzyme (rTDT) and nucleotide mix to incorporate fluorescein-12-dUTP onto breaks 3´-OH end of fragmented DNA. For each tissue section, a matched negative control was incubated in buffer containing nucleotide mix but no rTDT to provide a negative control for autofluorescence. The reaction was terminated and slides were washed with PBS and mounted with Vectashield antifade mounting media with DAPI (2B Scientific, H-1200-10)**.**

Slides were prepared and imaged by Chloe Connelly.

3.10 Widefield fluorescent microscopy image analysis

3.10.1 Quantifying uptake of fluorescently labelled molecules

Uptake of fluorescently labelled molecules *in vitro* was quantified from single channel .tif files converted to 8-bit format. In Fiji (RRID:SCR_002285), a threshold level was set using the control autofluorescence images to have at least 95% of pixels in the control image below the threshold.

All images were then processed using a macro to count pixels and therefore area of the image above the threshold level in an unbiased manner. This was taken as uptake efficiency.

3.10.2 Automated nuclear count and masking

A mask of nuclei was generated in Fiji (RRID:SCR_002285) from 8-bit format DAPI channel images. The optimum threshold for highlighting nuclear DAPI signal was established subjectively and all subsequent processes were automated with a macro to avoid bias. Mean of optimum thresholds across the batch was applied to all images to convert to a binary mask using the triangle thresholding method.[121]

Masks were processed to fill holes and despeckled. Watershed segmentation was used to separate touching particles.

Particles larger than approximately 2 μm^2 with a circularity 0.3-1.0 were counted as nuclei. Specifically, for images acquired with X10, X20 and X40 objectives on ZEISS Axio Imager, the optimised respective lower limit was set at 8, 20 and 80 pixels (equating to 3.38 μm^2, 2.11 μm^2 and 2.13 μm^2). In images of tissue sections using X10 lens, a size limit 100 times the threshold was used to exclude artefacts from being counted as nuclei.

Masks were manually reviewed for accuracy. Given difficulties in acquiring images of flat areas when cells were on transwell inserts, the threshold used was not optimum for nuclear identification in some areas of certain images. When combined with technical repeats it was considered a reasonable approach to generating an estimated cell count (**Figure 3-2A**).

For HIF1α quantification, the DAPI mask was applied to the Dy650 image to measure nuclear signal intensity. To avoid quantifying areas where nuclei had not been detected discretely, and so areas of cytoplasm assumed to be included, an upper limit for regions of interest was set to 15000 pixels (399 μm^2). An inverse mask of regions with below threshold intensity was generated from the DAPI channel to approximate cytoplasm, given images were acquired from confluent areas of cells (**Figure 3-2B**). Mean nuclear Dy650 intensity could therefore be normalised to mean cytoplasmic intensity per image.

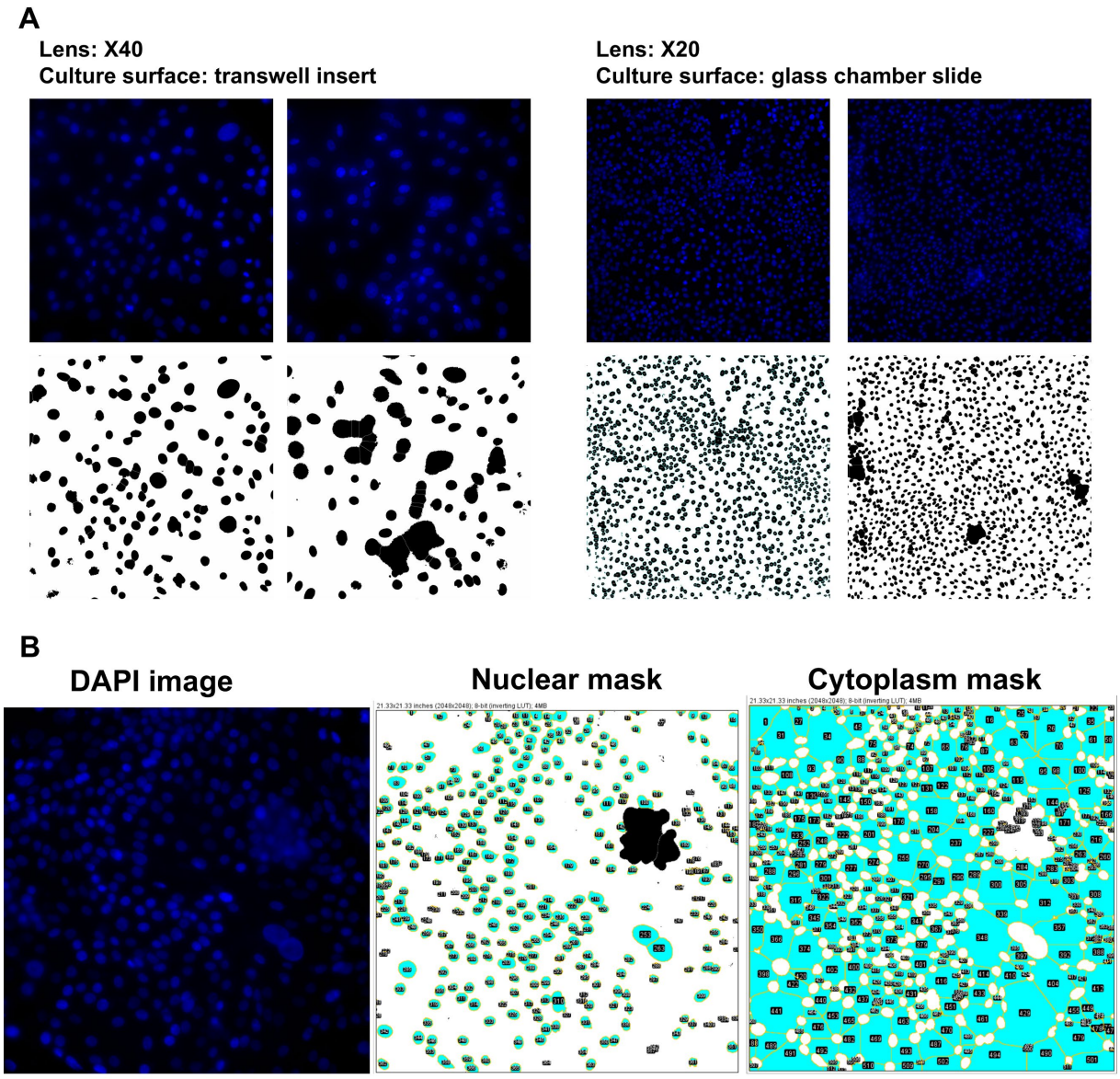

Figure 3-2 Approach to generating masks and automated cell count from DAPI channel images.
A.DAPI channel widefield fluorescent microscopy images and associated automated masks (beneath) of areas positive for DAPI signal, so deemed nuclear. Left panel shows images acquired with X40 objective from primary human proximal tubule epithelial cells (PTEC) maintained on transwell inserts. Panel on right is of PTEC maintained on glass chamber slides and imaged with X20 objective. Right column of both panels shows images in which nuclei were not appropriately segmented by DAPI signal in some areas. **B.** Example DAPI channel image (left) with matched nuclear (DAPI positive) and cytoplasmic (DAPI negative) masks with regions of interest highlighted in cyan. These regions of interest were used to quantifying HIF1α associated signal intensity in the matched Dy650 channel image. Areas not included in the mask are shown in white. Areas of the mask likely to involved both nuclei and cytoplasm were excluded by size from becoming regions of interest for HIF1α signal quantification (black). All images were acquired with ZEISS Axio Imager and masks generated with Fiji.

3.10.3 Automated TUNEL analysis

To estimate the proportion of apoptotic cells, the number of nuclei were counted as described above (**3.10.2**).

A mask of fluorescein signal associated with TUNEL was generated in Fiji (RRID:SCR_002285) from 8-bit format AF488 channel images. The optimum threshold for positive fluorescein signal was established as the mean threshold in negative controls for all tissue to be negative. This threshold was applied to all images to convert to a binary mask using the triangle thresholding method.[121] Masks were processed to fill holes and despeckled. Watershed segmentation was used to separate touching particles.

The minimum particle size was set as a quarter of the threshold for nuclear size (i.e 2 pixels with X10 lens on Axio Imager). A 100-fold upper limit was set to exclude artefacts. Circularity of 0.3-1.0 was required for a particle to be counted. The proportion of apoptotic cells in each image was taken as [TUNEL particle count/DAPI nuclear count]. Automated TUNEL assessment was manually validated by checking 3 images from different kidneys, treatments and time points (**Figure 3-3**).

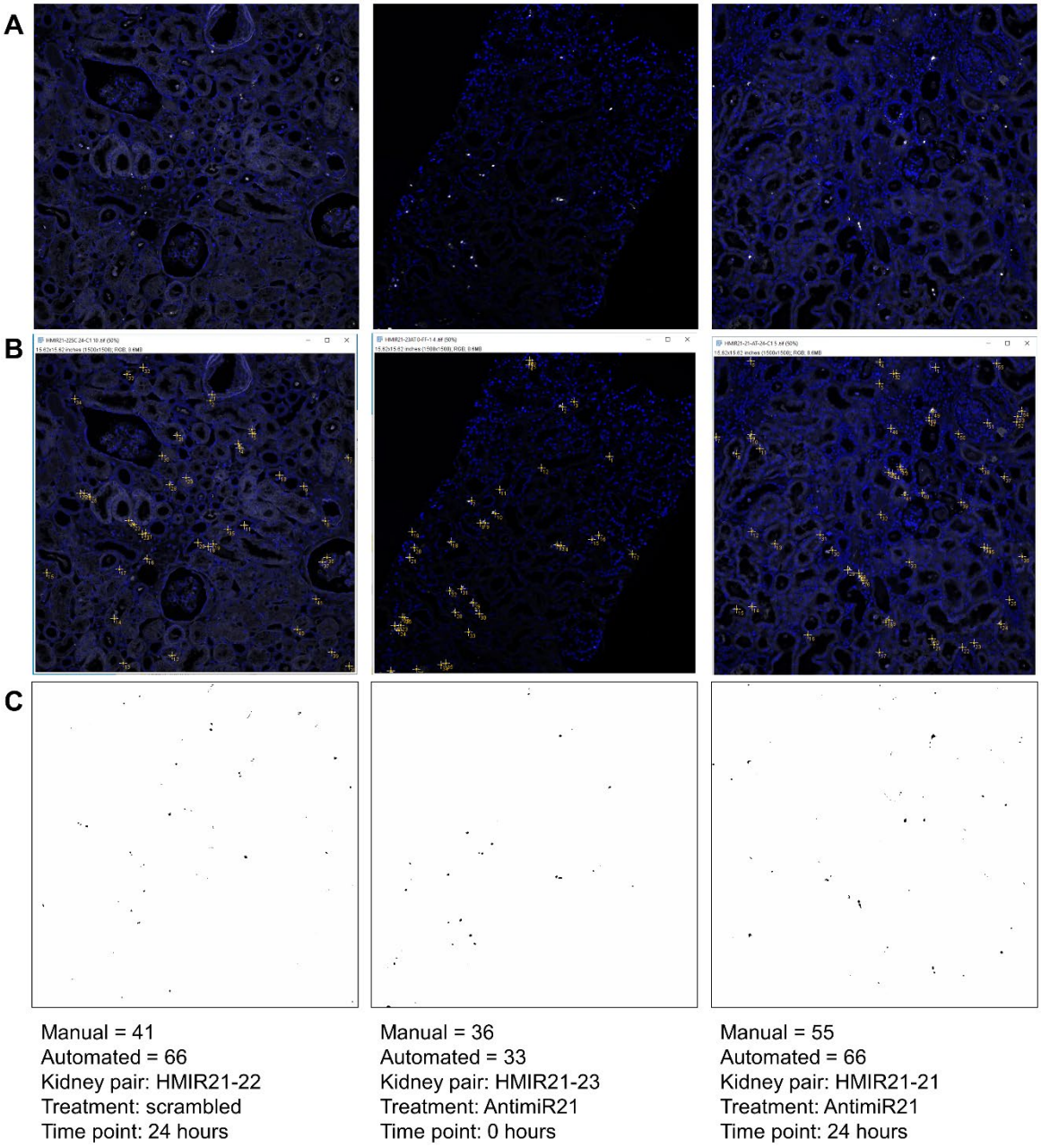

Figure 3-3 Validation of automated TdT-mediated dUTP Nick-End Labeling (TUNEL) analysis.
Validation of method used to quantify apoptosis in human kidney tissue before (0 hours) and after 24 hours of normothermic machine perfusion with either control antimiR (scrambled) or antimiR-21 treatment at 200 nM. **A** shows dual channel images with DAPI nuclear counterstain in blue and AF488 signal in white. Cells deemed positive for fluorescein-dUTP by AF488 signal on manual assessment are indicated by the pointers in **B**. Masks generated in Fiji (RRID:SCR_002285) for automated particle counting are shown in **C** for matched AF488 single channel images. Manual and automated counts are indicated beneath the panel with sample details. Widefield fluorescent microscopy images acquired with X10 lens using ZEISS Axio Imager. Image acquisition was standardised. 5 images were acquired for 0 hour core biopsies and 10 images for 24 hour wedge biopsies.

3.11 Flow cytometry

3.11.1 Cell harvesting

Media was removed from adherent cells, cells washed with PBS and detached by incubation at 37^{o}C with Accutase. Cells were counted either on seeding or on harvesting.

3.11.2 Wash and block

Once in flow tubes, cells were washed by centrifuging at 300 RCF for 5 minutes and supernatant discarded. Cells were resuspended in FACS buffer (2% FBS in PBS) and centrifuged again. Supernatant was discarded and cells incubated with Fc receptor (FcR) block at 1 in 50 dilution in FACS buffer for 15 minutes on ice if antibodies were to be used.

3.11.3 Protocol for detecting cell surface proteins on fixed cells

After FcR block, cells were washed twice with PBS and incubated with Zombie Violet fixable amine-reactive viability dye (Biolegend 423113) diluted 1 in 100 in PBS. Samples were incubated for 15 minutes at room temperature in the dark. Zombie dye was washed off with FACS buffer. Samples were incubated with directly conjugated antibodies or isotype control diluted in FACS buffer for 30 mins on ice (**Table 3-6**). No antibodies were added to one sample as a control for autofluorescence.

Cells were washed twice with FACS buffer to remove excess antibody. Cells were fixed with 4% PFA at room temperature for 15 minutes, washed twice with PBS and resuspended in FACS buffer.

Conjugated target antibodies					
Target - conjugate	**Isotype**	**Product**	**Stock (µg/µL)**	**Stock per 100 µL**	**Isotype control**
CD31-APC	Mouse IgG1κ	ThermoFisher 17-0319-42	0.1	1 µL	3
CD45-FITC	Mouse IgG1κ	Biolegend 304005	0.2	1 µL	Not used
PDGFRβ-PE	Mouse IgG1κ	Biolegend 323605	0.2	1 µL	Not used
PDGFRα-APC	Mouse IgG1κ	Biolegend 323511	0.1	1 µL	3
CD44-PEeFluor610	Rat IgG2b	ThermoFisher 61-0441-82	0.2	1 µL	4
LRP2 – AF647	Mouse IgG1κ	R&D Systems FAB9578	0.2	2 µL	1
CUBN-PE	Mouse IgG1κ	Santa Cruz sc 518059	0.2	2 µL	2
Conjugated isotype controls					
Isotype control		**Product**	**Stock (µg/µL)**	**Stock per 100 µL**	**Number**
Mouse IgG1κ – AlexaFluor 647		R&D Systems IC002R	0.01	2 µL	1
Mouse IgG1κ – PE		Santa Cruz sc-2866	0.2	2 µL	2
Mouse IgG1κ-APC		ThermoFisher 17-4714-42	0.1	1 µL	3
Mouse IgG2b-PEeFluor610		ThermoFisher 61-4031-80	0.2	1 µL	4

Table 3-6 Antibodies for flow cytometry.
Stock concentrations and working dilutions used listed. The isotype control used for target antibodies in the top section of the table are referred to by number in the lower section of the table. CUBN, cubilin; LRP2, megalin.

3.11.4 Protocol for cell surface protein analysis on unfixed cells

When preparing samples without fixation, Zombie dye stage was omitted and instead proceeded from FcR block to antibody incubation. After washes, samples were stored in FACS buffer, in the dark at 4°C and analysed within 4 hours. DAPI was added just prior to running samples at a concentration of 200 ng/mL.

3.11.5 Protocol for cell permeabilisation

To permeabilise cells for intracellular antibody binding, the above protocol for fixed cells was followed but with fixation happening after the incubation with Zombie dye and before the antibody incubation stage. After fixation, cells were incubated with 0.2% Triton-X in PBS for 15 minutes on ice in the dark to permeabilise. Samples were then washed twice with PBS before proceeding to antibody incubation.

3.11.6 Assessing antimiR uptake

As antimiR was FAM conjugated, no antibodies were required for detection. Therefore, if only antimiR uptake was being assessed no FcR block was required.

3.11.7 Apoptosis assay

Apical compartment media was combined with adherent cells harvested from 12-well inserts with Accutase as described above. Apoptosis assay was performed with eBioscience Annexin V Apoptosis Detection Kit APC (88-8007) as per product literature but with 7-AAD (ThermoFisher Scientific 00-6993-50) as the nuclear permeability marker. For both APC-conjugated Annexin V and 7-AAD incubations, cells were incubated with 5 µL of product diluted in 100 µL of binding buffer, whereas unstained controls were incubated in 105 µL of binding buffer alone.

3.11.8 Sample analysis

Prepared samples were stored in the dark at 4ºC and analysed within 4 hours for unfixed cells or 1 week for fixed cells on BD Symphony A5. Up to 10 000 events per sample were recorded.

Results were processed with FlowJo™ Software (BD Life Sciences). Events were first gated to eliminate those with low size (forward scatter area, FSC-A) and low granularity (side scatter area, SSC-A) which were considered debris. The remaining events were considered cells, as demonstrated by the labelled gate on each FSC-A x SSC-A plot in **Figure 3-4**. Next, cells were gated for single cells by eliminating events in which area (FSC-A) had increased more than height (FSC-H), indicating clumped cells (**Figure 3-4**). Single-cells were then gated as live if they had low signal for DAPI or amine-reactive dye (Zombie Violet Biolegend 423113) (**Figure 3-4**). The exception to this was for apoptosis assay data where single cells were gated into 4 quadrants by 7-AAD and APC signal intensity (**Figure 3-5**). A compensation matrix generated from single fluorophore controls was applied to apoptosis assay results before analysis due to spillover between APC and 7-AAD (**Figure 3-5**).

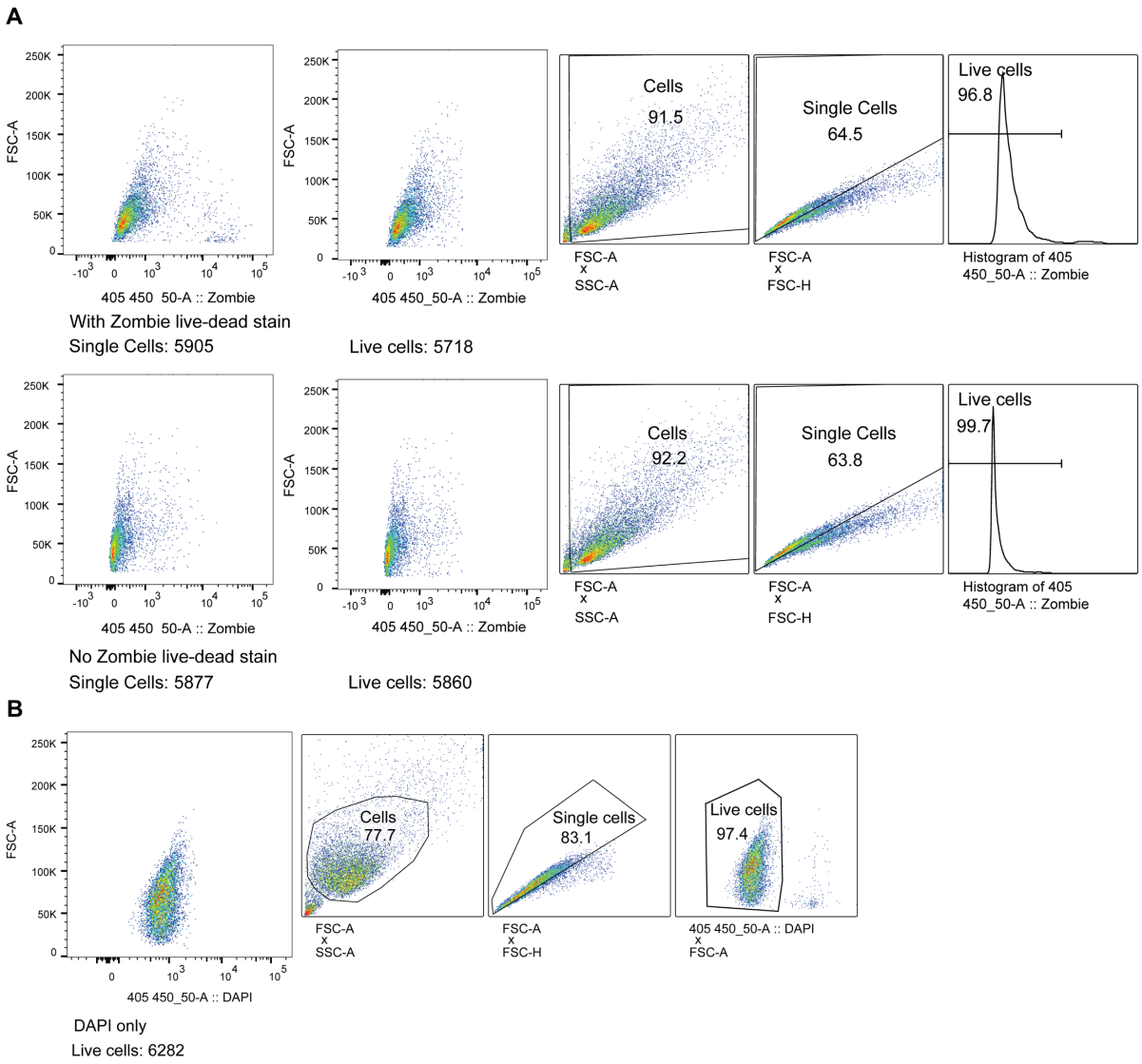

Figure 3-4 Flow cytometry gating strategy.
Successive gating of flow cytometry events as cells, single cells and live cells. Live cells were determined by lower intensity signal in the channel of amine-reactive Zombie Violet viability dye (Biolegend 423113) for paraformaldehyde fixed cells (**A**) or of DAPI for unfixed cells (**B**). The negative (live cell) gate was confirmed by cells not exposed to dye in **A**. In **A**, the left plot shows Zombie signal in all single cells, whereas the neighbouring plot shows only cells gated as being “live” by low Zombie signal. Results displayed are from fixed primary human proximal tubule epithelial cells (**A**) and unfixed HMRC5 (**B**). Cell counts and percent of parent included in each gate are displayed. Analysis and scatter plots performed in FlowJo™ Software (BD Life Sciences)

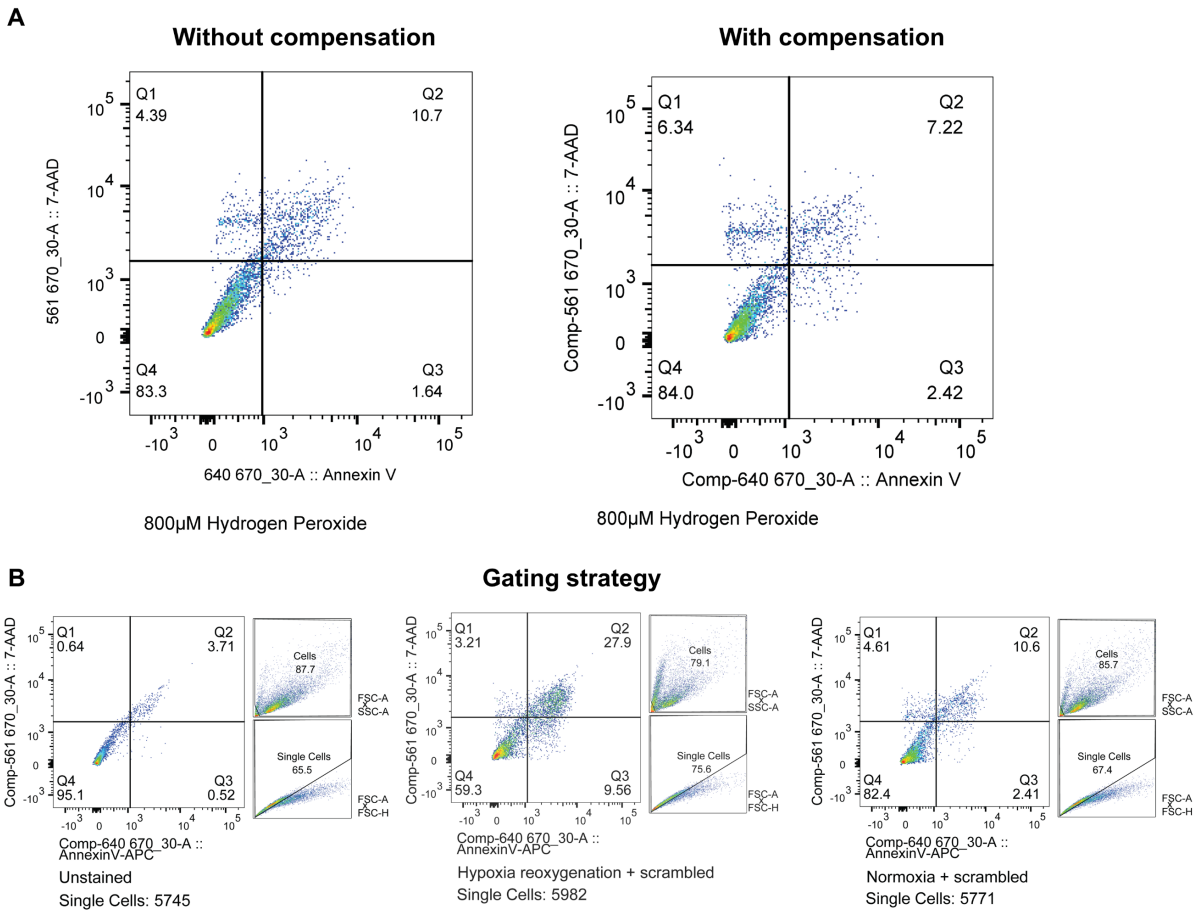

Figure 3-5 Apoptosis assay compensation and gating strategy.
Flow cytometry dot plots of APC and 7-AAD signal in primary human proximal tubule epithelial cells (PTEC). Results are from apoptosis assay using APC conjugated Annexin V and 7-AAD as permeability marker. **A** shows plots with and without compensation for the spillover of APC signal when exciting 7-AAD as APC is also excited by the 561 nm laser. Laser and filter_width wavelengths are indicated on the axes. Data is from PTEC treated with hydrogen peroxide to induce cell death. **B** shows validation of quadrants gating cell state in unstained cells and those exposed to hypoxia-reoxygenation or normoxia in conjunction with control (scrambled) antimiR treatment. Data gated for single cells with ancestry plots shown on the right. Quadrants Q1,2,3 and 4 represent necrosis, late apoptosis, early apoptosis and healthy cells, respectively. Percent of single cells in each quadrant is indicated.

3.11.9 Antibody concentration optimisation

Where antibody concentrations were not already optimised, a range of dilutions was assessed against matched isotype controls and unstained samples. Staining index calculated using cell lines known to express the target protein as shown in **Figure 3-6**. The matched isotype controls for anti-megalin and anti-CD44 antibodies did not result in an increased median fluorescent intensity with increasing concentration, indicating little increase in non-specific binding (**Table 3-6**, **Figure 3-6**). Histograms for all target antibody concentrations were well-separated from the isotype and unstained control peaks. To conserve product, concentrations lower than that giving

the peak staining index were therefore used. Similarly, as isotype control to match anti-megalin antibody did not demonstrate non-specific binding, stock dilution rather than antibody concentration in µg/µL were matched (**Table 3-6**, **Figure 3-6**).

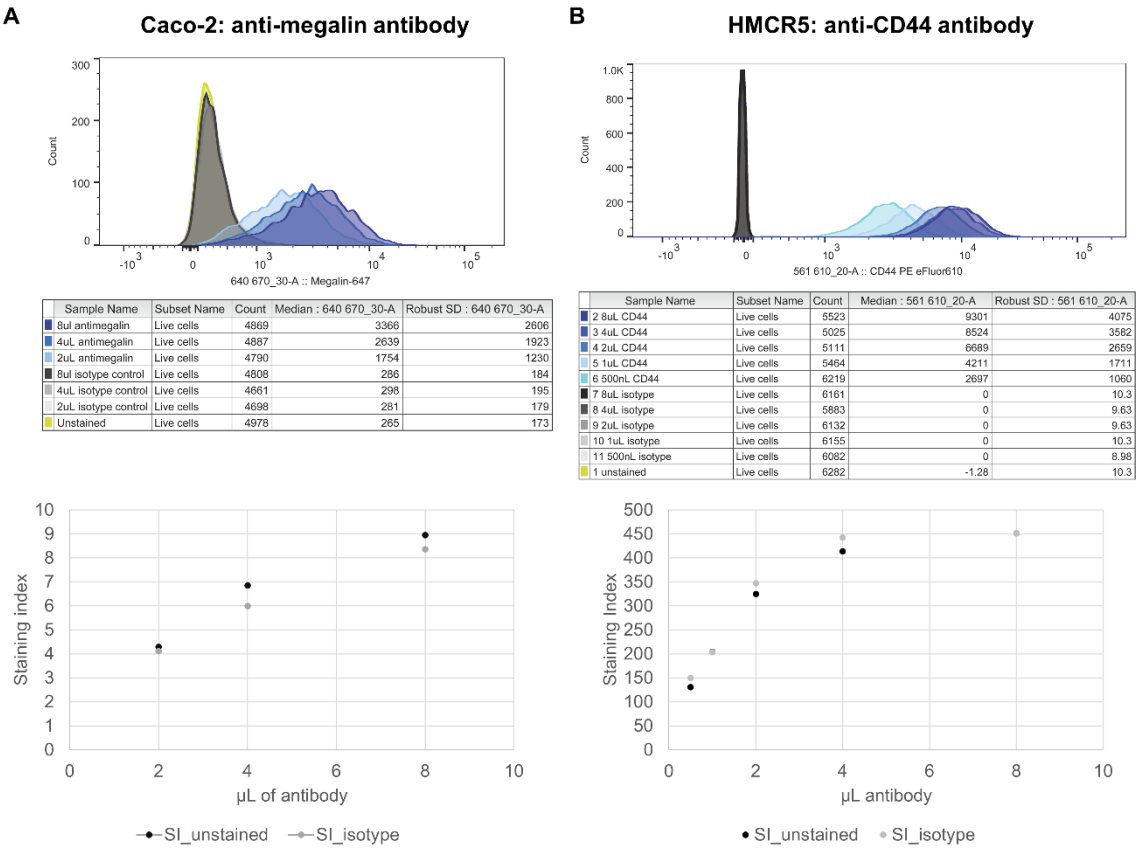

Sample Name	Subset Name	Count	Median : 640 670_30-A	Robust SD : 640 670_30-A
8ul antimegalin	Live cells	4869	3366	2606
4uL antimegalin	Live cells	4887	2639	1923
2uL antimegalin	Live cells	4790	1754	1230
8ul isotype control	Live cells	4808	286	184
4uL isotype control	Live cells	4661	298	195
2uL isotype control	Live cells	4698	281	179
Unstained	Live cells	4978	265	173

Sample Name	Subset Name	Count	Median : 561 610_20-A	Robust SD : 561 610_20-A
2 8uL CD44	Live cells	5523	9301	4075
3 4uL CD44	Live cells	5025	8524	3582
4 2uL CD44	Live cells	5111	6689	2659
5 1uL CD44	Live cells	5464	4211	1711
6 500nL CD44	Live cells	6219	2697	1060
7 8uL isotype	Live cells	6161	0	10.3
8 4uL isotype	Live cells	5883	0	9.63
9 2uL isotype	Live cells	6132	0	9.63
10 1uL isotype	Live cells	6155	0	10.3
11 500nL isotype	Live cells	6082	0	8.98
1 unstained	Live cells	6282	-1.28	10.3

Figure 3-6 Antibody optimisation approach for flow cytometry.
Caco-2 (**A**) and HMRC5 (**B**) cell lines, known to express megalin and CD44 respectively, were used to optimise antibodies for these targets. Events were gated for live single cells. Histograms show event counts by intensity for signal with the laser and filter channel combination appropriate for the fluorophore conjugation of the antibody. Median fluorescent intensity (MFI) and robust standard deviation for different volumes of antibody or isotype control (per total volume of 100 µL) are given in the tables below. Staining index was calculated as $[(MFI_{stained} - MFI_{control})/(2*SD_{control})]$ with control being either unstained (SI_unstained) or matched dilution of isotype control (SI_isotype). These indices are plotted on the graphs below their respective histograms.

3.12 RNA extraction

3.12.1 Cell lysate collection

Adherent cells were washed with cold PBS which was then aspirated completely. The method for cell lysis was dependent on the intended use of extracted RNA. For assessment of mRNA transcripts with either bulk RNA sequencing or Taqman PCR, cells were lysed with 350 µL of buffer RLT supplemented with 10 µL β-

mercaptoethanol per 1 mL. When miR expression would also be assessed, 700 µL of QIAzol was used to lyse cells.

Lysed cells were scraped with a P1000 pipette tip, aspirated into a microcentrifuge tube, vortexed briefly, centrifuged at 4°C to remove bubbles and stored at -80°C.

3.12.2 Tissue homogenisation

Tissue stored in RNA later was thawed and up to 30 mg of tissue added to 700 µL QIAzol in a 2 mL centrifuge tube containing a 5 mm diameter stainless steel bead. Tissue was homogenised in ice-cold conditions using TissueLyser plate at 20 Hz for 2 minutes on each side, repeated as necessary, with frequency increasing to 25 Hz after 8 minutes of homogenisation.

3.12.3 RNA extraction

For cell lysates collected in buffer RLT, RNA was extracted with Qiagen RNeasy Mini Kit (74106). For cell or tissue lysates in QIAzol, RNA was extracted with Qiagen miRNeasy Mini Kit (217004). On-column DNAse digest with RNase-free DNase (Qiagen 79256) was included in the protocol when proceeding to bulk RNA Sequencing or when extracting RNA from tissue.

3.12.4 RNA quality and quantity assessment

RNA was quantified by Nanodrop and, if proceeding to bulk RNA Sequencing, Qubit RNA High Sensitivity Assay Kit (Q32852) on Qubit™ 4 Fluorometer. RNA purity was assessed with A260/280 ratio on Nanodrop. RNA eluates were stored at -80°C if not proceeding immediately to cDNA synthesis.

3.13 Taqman semiquantitative reverse transcription polymerase chain reaction (RT-PCR) for mRNA targets

3.13.1 cDNA preparation

1-2 µg of RNA was used for cDNA synthesis with Tetro cDNA synthesis kit (Bioline BIO-65043) used as per product literature with Oligo $(dT)_{18}$. Thermal cycler settings for reverse transcription were 30 minutes at 45°C. The reaction was stopped with 5 mins at 85°C with the temperature then held at 4°C. cDNA samples were stored at -20°C if not used immediately.

3.13.2 RT-PCR

Taqman gene expression assay was performed as per product literature using 2x TaqMan Gene Expression MasterMix (ThermoFisher 4369016) and up to 100 ng of cDNA per reaction. RNase-free water was used template-free control. Primers used are given in **Table 3-7**. Reaction was performed in a 96 well plate on the Applied Biosystems StepOne Real-Time PCR System using standard ramp speed and quantitative threshold cycle (C_T) approach.

Target	Taqman Probe
CUBN (cubilin)	Hs00153607_m1 FAM-MGB
LRP2 (megalin)	Hs00189742_m1 FAM-MGB
RPLP0 (housekeeper)	Hs00420895_gH FAM-MGB
HRPT1 (housekeeper)	Hs02800695 _m1 FAM-MGB
PDCD4	Hs00377253_m1 FAM-MGB
SLC34A1	Hs01092910_m1 FAM-MGB

Table 3-7 Taqman primers from ThermoFisher

3.13.3 Quantification

Reactions were conducted in triplicate to allow a single repeat C_T to be excluded if required to achieve a standard deviation of <0.25. Mean C_T was normalised to housekeeper protein (ΔC_T). Where control conditions were relevant ΔC_T was normalised to these ($\Delta\Delta C_T$) and $2^{-\Delta\Delta CT}$ calculated to determine fold change.

3.14 TaqMan RT-PCR for miR targets

3.14.1 cDNA synthesis

cDNA from miR target or *RNU48* housekeeper were synthesised individually from total RNA using TaqMan microRNA reverse transcription (RT) kit (4366596) and TaqMan RT assays for miR-21 (4227975-00397) and RNU48 (4227975-001006). 10 ng of total RNA was used for each 15 µL reverse transcription reaction. Reverse transcription was performed with thermal cycler settings of 30 minutes at 16°C followed by 30 minutes at 42°C. The reaction was stopped with 5 minutes at 85°C and then held at 4°C.

3.14.2 RT-PCR for miRNA

TaqMan MicroRNA Assay for miR-21 and RNU48 (4227975-00397; 4227975-001006) were performed using TaqMan Universal Mastermix II with UNG (ThermoFisher, 4440038) as per product literature. RNase-free water and RNA were used as no template controls. Reaction was performed and analysed as for mRNA.

3.14.3 Assay efficiency

Efficiency of Taqman MicroRNA PCR probes for miR-21 and RNU48 were validated and within the accepted range of 90-110% (**Figure 3-7**).[122]

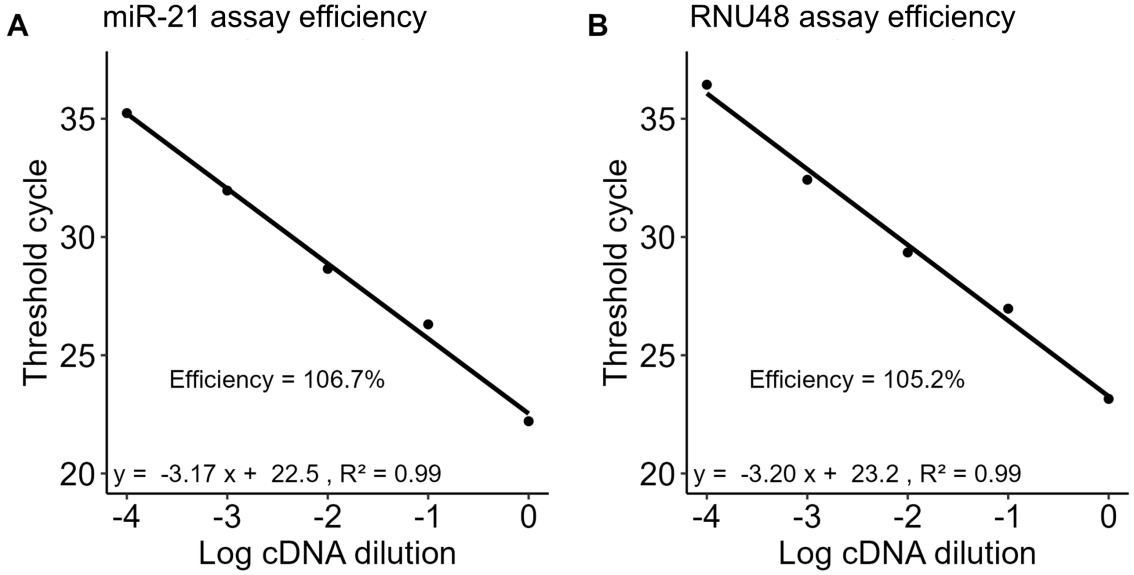

Figure 3-7 Validation of Taqman probes for miR-21 and RNU48.
Performed with diluted cDNA generated from RNA extracted from primary human proximal tubule epithelial cell lysates. Efficiency (%) was calculated as [$10^{-1/slope}$-1]x100.

3.15 Immunoassay

Enzyme-linked immunosorbent assay (ELISA) for VEGF (R&D DY293B) and NGAL (R&D DY1715) were used as per product literature to quantify concentrations in media (VEGF), perfusate (NGAL) and urine (NGAL). A microplate reader measured optical density at 450 nm and 540 nm. Optical density used for analysis was 450 nm reading minus the 540 nm reading. All samples were run in at least duplicate. Sample concentrations were interpolated using a four parameter logistic regression (4PL) standard curve generated from adjusted optical densities of known concentrations of standards (GraphPad Prism version 10.1.2 for Windows, GraphPad Software, Boston, Massachusetts USA, www.graphpad.com).

MSD® cytokine immunoassay was used to measure concentrations of IFN-γ, IL-1β, IL-2, IL-4, IL-6, IL-8, IL-10, IL-12p70, IL-13 and TNFα (V-PLEX® Proinflammatory Panel 1 (human) Kit, K15052D MSD®). Perfusate samples were diluted to 1 in 4 and basolateral media at 1 in 20. All samples were run in duplicate and concentrations were interpolated using a 4PL standard curve using optical densities from known concentrations of standards by Jeremy Palmer and John Butler (DISCOVERY WORKBENCH 4.0 Analysis Software, MSD).

3.16 Modelling IRI with antimiR-21 treatment *in vitro*

3.16.1 Experimental conditions

Isolated PTEC were seeded onto 12-well inserts for collection of lysates for RNA extraction and 6-well inserts for collection of cell lysates for proteomics. Cells were maintained in culture for 5 days (**3.2.3**) at which point media was changed using standard volumes and cells continued to be cultured in normal conditions for a further 24 hours. Samples assigned for hypoxia-reoxygenation were then moved to 1% oxygen incubator for 24 hours. At the end of this period media from both compartments was collected and changed for maintenance media in the basolateral compartment with 40 nM of either control scrambled antimiR or antimiR-21 added to the apical compartment. Cells continued in normal incubation conditions for a further 24 or 48 hours. Media was changed on matched normoxia controls at the same intervals with 40 nM control scrambled antimiR being added to the apical compartment. This experimental process is depicted in **Figure 3-8**.

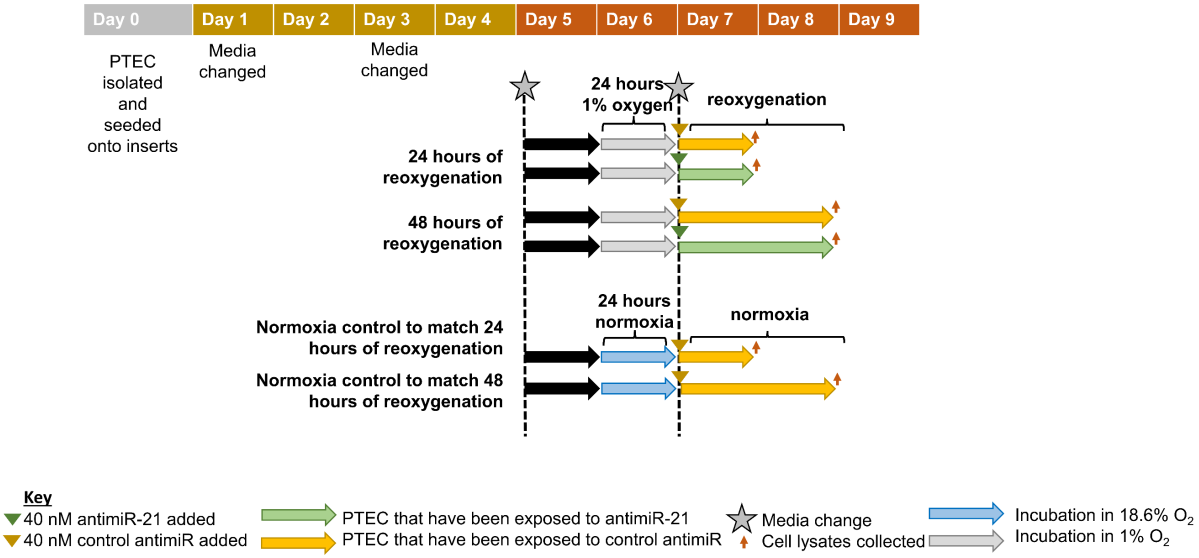

Figure 3-8 Experimental plan to model ischaemia reperfusion with hypoxia-reoxygenation *in vitro* using primary human proximal tubule epithelial cells and assess the effect of antimiR-21 treatment in this context.
Timeline shows initial run-in period as cells are established in culture followed by experimental conditions of either normoxia or hypoxia-reoxygenation (24hr incubation in 1% oxygen followed by return to normal conditions). Apical compartment antimiR treatment is delivered at the point of reoxygenation (or in parallel with this for matched normoxia controls) and cell lysates and media collected after 24 or 48 hours.

3.16.2 Sample collection

Samples were collected at end reoxygenation with matched normoxia controls being collected simultaneously. Apical and basolateral compartment media was removed, centrifuged at 1000 RCF for 20 mins at 4ºC, supernatant collected and stored in aliquots at -80ºC. Cell lysates were collected for bulk RNA Seq using buffer RLT as described in section **3.12** and unfractionated cell lysates for liquid chromatography mass spectrometry-based (LCMS-based) proteomics as described below (**3.18.1**).

3.17 Bulk RNA Sequencing

3.17.1 Cell lysates from 12-well inserts for RNA extraction

2 µg RNA from cell lysates (**3.12**) was provided to the Core Genomics Facility for bulk RNA sequencing. RNA quality was assessed by looking for 18S and 28S peaks to determine RNA sample degradation on Agilent Technologies Tapestation 4200 using RNA screentape sample buffer (Agilent 5067-5577) and screentape (Agilent 5067-5576). Good quality RNA had RINe >7 and this threshold was met for all samples.

1 µg of template proceeded to library generation with Illumina® Stranded mRNA Prep, Ligation (96 samples, Cat No 20040534) paired with IDT® for Illumina® RNA UD Indexes Set A, Ligation (96 Indexes, 96 samples, Cat No 20019654) indexes UDP0049-UPD0072. Libraries were quality checked with Agilent Technologies Tapestation 4200 using D1000 Reagents (Cat No 5067-5583) and Screentape (Cat No 5067-5582). Libraries were assessed for quality and ranged in size from 250-300bp. Concentration was determined using Life Technologies Qubit and a Broad Range dsDNA Qubit Kit (Q32853). Sample molarity was determined from this quality check and sample was diluted to in the region of 2 nM. Indexing was checked on an Illumina MiSeq system using MiSeq reagent Nano Kit version 2 (300 cycles, Cat No: MS-103-1001). Samples were ran on a NovaSeq 6000 system on a Illumina NovaSeq 6000 SP Reagent Kit v 1.5 (100 cycles, Cat No 20028401). RNA sequencing was performed by the Core Genomics Facility, Newcastle University.

3.17.2 Read alignment

RNA sequencing reads were aligned to a reference genome with Spliced Transcripts Alignment to a Reference (STAR) and mapped reads summarised to a count matrix with featureCounts. Alignment was performed by Gary Reynolds.

3.18 Sample preparation for LCMS-based proteomics

Sample preparation was based on the protocol provided by Bio-MS Research Core Facility in at the University of Manchester.

3.18.1 Collection of cell lysate for LCMS-based proteomics

Fractionation of protein lysate from adherent cells

HKC8 maintained in 6-well or 12-well plates were washed once in cold PBS. The plate was then tilted to remove all residual PBS which was discarded. 100 µL of buffer 1 (**Table 3-8**) was added to the well to solubilise cellular proteins. Using a P200 pipette this was scraped into a 1.5 mL microcentrifuge tube and incubated on ice for 30 minutes.

The sample was centrifuged at 14000 RCF for 10 minutes at 4^{o}C. The supernatant was collected as fraction 1 (the more soluble cellular proteins) to combine with an equal volume of 1x S trap lysis buffer.

The pellet was resuspended in 100 µL of buffer 2 for 5 minutes by gentle pipetting to break up the pellet. Centrifugation was performed as above and the supernatant

collected as fraction 2 (less soluble cellular proteins). An equal volume of 2x S trap lysis buffer to the collected sample 2 and topped up to 50 µL with 1x S trap lysis buffer if required (**Table 3-8**). The pellet was resuspended in 50 µL of 1 x S trap lysis buffer and store as the matrix fraction.

Protein content in each fraction was quantified by 96-well plate Pierce BCA Protein Assay Kit (Thermo Fisher 23225) and demonstrated low protein concentrations in the matrix (Fraction 3) component (**Table 3-9**). Therefore, unfractionated cell lysates were ultimately collected for analysis by LCMS-based proteomics.

Buffer1 **(extraction buffer)**	**Buffer2** **(alkaline detergent buffer)**	**2x stock S trap lysis buffer**
10 mM Tris 150 mM NaCl 1% Triton X-100 25 mM EDTA Diluent: LC-MS grade water (Fisher scientific 10763295) Protease inhibitor (Fisher scientific 10085973) added before use	20 mM NH_4OH (Sigma 09859) 0.5% Triton X-100 in PBS made with LC-MS grade water	10% sodium dodecyl sulfate (SDS) 100 mM triethylammonium bicarbonate (TEAB, Sigma 18597) Diluent: LC-MS grade water pH 7.5 Diluted to 1x with an equal volume of LC-MS grade water

Table 3-8 Composition of buffers for cell lysate fractionation

Culture vessel:	**Fraction 1**	**Fraction 2**	**Fraction 3**
6-well plate	106.5 ± 8.40	29.61 ± 2.30	17.25 ± 0.68
12-well plate	55.06 ± 5.16	28.52 ± 1.05	11.04 ± 3.51
Estimated volume of fraction	200 µL	200 µL	50 µL

Table 3-9 Protein concentration (µg/µL) in fractionated HKC8 cell lysates measured by BCA.
Values displayed are mean ± standard deviation of 3 technical repeats. Fraction 1 represents the most soluble (cellular) proteins with fraction 3 being least soluble (extracellular matrix) proteins and fraction 2 being intermediate.

Collection of unfractionated cell lysate

2x S trap lysis buffer (**Table 3-8**) was diluted to 1x S trap lysis buffer with LCMS grade water and protease inhibitor (Fisher scientific 10085973) added. Adherent cells grown on 6-well inserts were washed three times with ice cold PBS in the cold room at 4^{o}C. PBS was aspirated completely and 100 µL of 1X S trap lysis buffer added to lyse cells. The inserts were moved to room temperature to avoid precipitation of sodium dodecyl sulfate (SDS) and cells were scraped into microcentrifuge tube to clear the membrane. Lysate was vortexed and centrifuged at 4^{o}C to remove bubbles before snap freezing and storing at -80^{o}C.

3.18.2 Tissue digest

Snap frozen core biopsies were visually assessed on thawing for presence of glomeruli to confirm the sample included cortex (**Figure 3-9**). As donated kidneys have been flushed, the glomeruli were much paler in the pre-perfusion samples (**Figure 3-9A**). End-perfusion samples appeared generally comparable for the presence of glomeruli on visual inspection (**Figure 3-9B**).

A

B

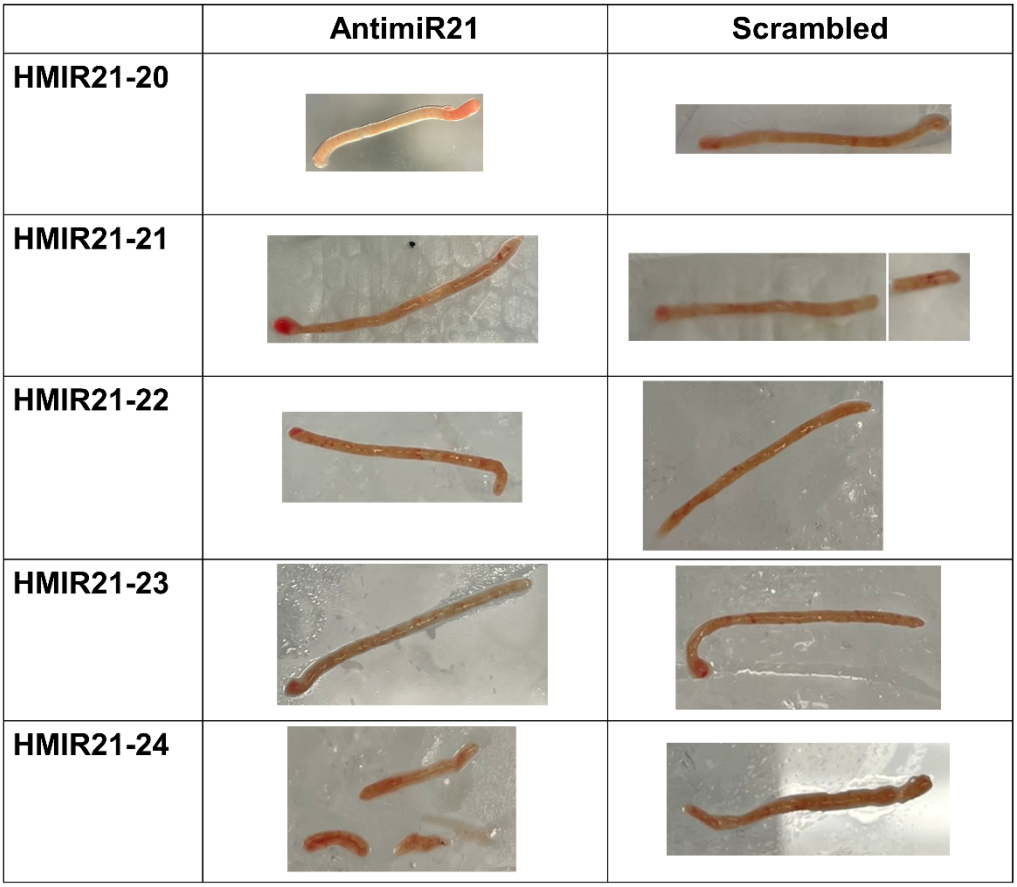

Figure 3-9 Visual appearance of core human kidney biopsies used for protein extraction.
A shows core kidney biopsies from flushed kidneys before (0hr) perfusion are much paler than those taken after 24 hours of perfusion with a blood-based perfusate. Example is taken from a kidney that was perfused with antimiR-21. **B** shows each of the end-perfusion samples used from each kidney donor (HMIR21-20 to 24) and with each treatment (antimiR-21 vs scrambled) given during perfusion. Image in **B** of HMIR21-20 biopsy from the kidney treated with antimiR-21 was taken through Olympus SZ51 microscope (110AL1.5X lens). All other images taken directly with iPhone 12 mini (model MGE23B/A) using default settings on default camera.

Snap frozen tissue was thawed and rinsed with cool PBS without calcium chloride or magnesium chloride (Sigma Aldrich D8537) before mincing with a blade in a petri dish in 1 X S-trap lysis buffer (**Table 3-8**) and transfer to covaris tubes (520185) for sonication. For optimisation work, core and wedge biopsies were homogenised in 500 µL and 1 mL of lysis buffer respectively. For core biopsies from perfusion experiments, 200 µL of lysis buffer was used.

Tissue samples were homogenised with LE220plus500452 and required 2 rounds (30W, 400 seconds, peak power 500, duty factor 40%, cycles/burst 300, average power 200, run time 6m 40 seconds per row, temp 6.9^{o}C) of sonication before transfer to microcentrifuge tubes.

3.18.3 Reduction and alkylation

A known volume of sample was transferred to a microcentrifuge tube and supplemented with 100 mM dithiothreitol (DTT) to achieve a final concentration of 5 mM DTT which was heated to 60^{o}C on a heat block for 10 minutes.

After cooling, the mix was supplemented with 100 mM iodoacetamide (IAM) to achieve a final concentration of 15 mM IAM then briefly vortexed and incubated at room temperature, protected from light, for 30 minutes. The reaction was quenched by adding further DTT (same volume of 100 mM as used to achieve 5 mM concentration) and vortexed. The sample was centrifuged at 14000 RCF for 10 minutes and supernatant (protein lysate) collected into a clean tube.

3.18.1 Protein quantification

Millipore Direct Detect was used to measure protein concentration in cell and tissue lysates. Each card (EMD Millipore Corporation DDAC00010-GR) included a blank sample and 2 µL of sample for analysis for the remaining wells. Each sample was run in single.

3.18.2 S-Trap^{TM} 96-well plate digestion protocol

A known volume of protein lysate was aliquoted and 12% aqueous phosphoric acid added to achieve a final concentration of 1.2% phosphoric acid before vortexing. 75 µg protein in 50 µL was used for cell lysates and 36 µg of protein in 50 µL for tissue.

In the pilot study from PTEC, 50 µL of unquantified cell lysate or 100 µL of media was used on the basis that seeding density and media volumes were standardised. In the pilot study of kidney tissue, 50 µg of protein in 50 µL was used.

350 µL of S-Trap binding buffer (90% aqueous methanol with a final concentration of 100 mM triethylammonium bicarbonate, pH 7.1) was added to the acidified lysate and transferred to the S-Trap plate. The plate was centrifuged at 1000 RCF for 2 minutes and the flow through discarded. This step traps the protein in the protein-trapping matrix of the plate. Captured protein was washed once by adding 200 µL MTBE/Methanol (10/3 v/v) solution to the plate and centrifuging at 1000 RCF for 2 minutes to remove methanol insoluble molecules from the quartz filter. Flow through was discarded. A further 3 washes were performed with 200 µL S-trap binding buffer.

3.18.3 Protein digest

The S-Trap digestion plate was transferred to a clean receiver plate and 2 µg of Trypsin (0.1 µg/µL) added directly to the wells. The plate was covered and incubated overnight (at least 16 hours) at 37^{o}C.

3.18.4 Elute peptides

To elute peptides, the following reagents were added in succession with 2 minute centrifugation at 1000 RCF between each step: 80 µL digest buffer, 80 µL 0.1% aqueous formic acid, 55 µL of 30% aqueous acetonitrile containing 0.1% formic acid. Each flow through contains eluted peptides and so is retained in the collection plate.

3.18.5 R3 desalt and clean up

The 96 well plate was prepared by adding 10 µL of settled beads from prepared POROS R3 to each well to be used. These were washed by adding 200 µL of 50% acetonitrile, centrifuging at 200 RCF for 1 minute and discarding the flow through. The plate was then washed twice with 200 µL of 0.1% formic acid in water.

A maximum of 200 µL of eluted peptides was added to each well and incubated on the plate mixer at 300 RPM for 5 minutes without heating. The plate was centrifuged at 200 RCF for 1 minute to remove the liquid. The sample was washed twice by adding 200 µL of 0.1% formic acid, mixing for 2 minutes at 300 RPM and centrifuging for 1 minute at 200 RCF with flow through discarded.

When eluting the peptides, the collection plate was changed to ensure clean wells. Peptides were eluted by adding 50 µL 0.1% formic acid in 30% acetonitrile mixed for 2 minutes at 300 RPM then centrifuged at 200 RCF and the flow through containing peptides retained. This step was performed twice giving a combined eluate volume of around 100 µL. Eluate was transferred to a sample vial and a pooled sample

produced by combining aliquots of each eluate. Samples were dried to completeness in Heto vacuum centrifuge and stored at 4°C until analysis.

3.19 LCMS-based proteomics data acquisition and generation of protein counts

3.19.1 Data dependent acquisition (DDA)

Prepared samples were run for 60 minutes on Exploris with DDA. Raw data were processed to peptide counts in MaxQuant (Version 2.3.1.0) with human fasta file from UniProt (Taxonomy 9606, SwissProt and TrEMBL, canonical only) and the inbuilt contaminants fasta file.

The output peptide.txt output file from MaxQuant was processed R Studio using msqRob2 after importing as a QFeature. Data was assessed for missingness and log transformed. Peptides were filtered using smallestUniqueGroups to handle peptides mapping to multiple protein groups and decoys (reverse sequences) removed along with potential contaminants. Peptides present in less than 2 samples were removed before normalisation of data and aggregation into protein groups. Packages used were msqRob2,[123-125] limma,[126] QFeatures,[127] MSnbase,[128,129] ExploreModelMatrix.[130]

3.19.2 Data independent acquisition (DIA)

Prepared cell and tissue lysates were run on for 90 minutes on Lumos with DIA. Media samples were run for 60 minutes.

.raw files were imported into DIA-NN[131] 1.8.1 with Thermos MS File Reader add on. Two methods were tested for spectral library creation and the library-free method was ultimately chosen where predicted spectral library was generated from .raw files with library-free search using UniProt human fasta file (UP000005640, taxonomy ID 9606, downloaded 5/2/2024) addended with Cambridge Centre for Proteomics common repository of adventitious proteins (CCP cRAP[132]) fasta file for contaminants (downloaded on 17/10/2023). Deep learning based spectra, RTs and IMs prediction, FASTA digest and match between run options were all enabled.

The alternative method assessed was using a pooled sample from PTEC cell lysates that had undergone gas-phase fractionation (GPF) before analysis. This was used for library preparation with FASTA digest and deep learning enabled. The same fasta file was uploaded as for the library-free method. This library file was then applied to the

.raw files from each sample and protein quantification was performed without FASTA digest, deep learning or match between runs enabled.

DIA-NN output file of normalised protein counts (report.pg_matrix.tsv) was loaded in R Studio and cRAP labelled contaminants extracted and contaminants manually reviewed for exclusion from dataset.

3.19.3 Optimisation of LCMS-based proteomics data acquisition

A pilot study using LCMS-based proteomics was performed to determine the method of data acquisition, minimum treatment time to see an effect from antimiR-21 and sample types to be analysed.

Pilot tissue was from one human kidney (HMIR21-16) with a cold ischaemic time of 16 hours. A wedge biopsy and a core biopsy taken with 23 mm throw of 18G biopsy gun (Argon Medical Devices UK Ltd 360-1080-02) were used to generate tissue lysates.

PTEC from one kidney (HMIR21-09) were seeded into 6-well inserts and used in the below experimental plan (**Figure 3-10**) to collect unfractionated cell lysates at the end of 8, 24 or 48 hours of reoxygenation. AntimiR was added before hypoxia for two of the 24-hour reoxygenation samples in case treating at reoxygenation did not enable sufficient uptake to cause changes in gene expression. Basolateral media was collected at the end of reoxygenation.

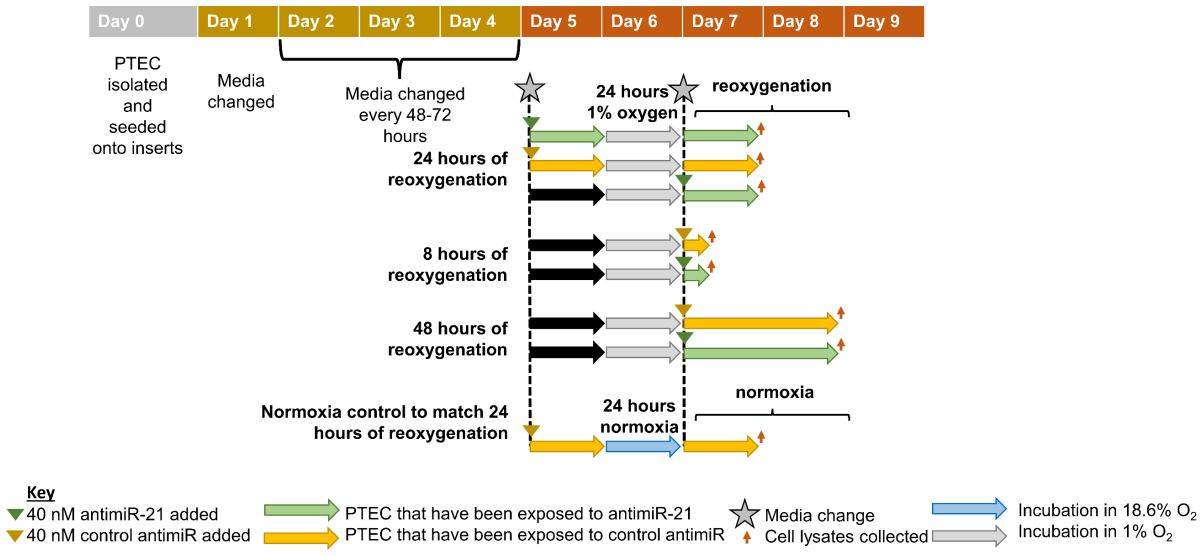

Figure 3-10 Experimental plan to optimise model of hypoxia-reoxygenation in primary human proximal tubule epithelial cells from donor HMIR21-09.
Hypoxic insult was incubation in 1% oxygen incubator for 24 hours whereas normoxia controls were maintained in normal conditions of a 5% carbon dioxide in a humidified incubator for this period. Reoxygenation involved media change and return normal conditions

3.19.4 Comparison of identified proteins by data acquisition method

More proteins were identified with DIA from cell lysates, media and tissue (**Table 3-10**) but the number of proteins identified in media remained low so the decision was made not to proceed with analysis of media by LCMS-based proteomics.

Sample	**PTEC cell lysates**		**Basolateral media**		**Human kidney tissue**	
Method	**DDA**	**DIA**	**DDA**	**DIA**	**DDA**	**DIA**
Proteins identified	4264	6663	345	1028	2387	4278
Non-contaminants	4244	6630	229	988		

Table 3-10 Numbers of proteins identified with proteomics by data acquisition method.
Numbers of proteins identified in cell lysates (8 conditions) from primary human proximal tubule epithelial cells (PTEC) and basolateral media collected at end reoxygenation after a hypoxic insult and from kidney tissue (1 core and 1 wedge biopsy) after cold ischaemic time of 16 hours. Samples analysed with liquid chromatography based proteomics using either data-dependent acquisition (DDA) or data-independent acquisition (DIA).

Presence of PTEC markers, miR-21 targets and injury markers in the proteins identified by DIA and DDA analyses found HIF1A and VEGFA to be identified by DIA

but not DDA (**Table 3-11**). As important genes involved in the response to hypoxia-reoxygenation, DIA was the acquisition method proceeded with.

	DDA	DIA
Cell lysates		
Proximal tubule epithelial cell markers		
AQP1	✓	✓
ZO1	✓	✓
LRP2	×	✓
miR-21 targets		
PDCD4	✓	✓
PPARA	×	×
SMAD7	×	×
Response to hypoxia-reoxygenation		
HIF1A	×	✓
VEGFA	×	✓
Media		
Interleukins	×	×
Heat shock proteins	✓	✓
Collagens	✓	✓
VEGFA	×	✓

Table 3-11 Comparisons of proteins identified in cell lysates by different proteomics methods.
Proteins identified by either data-independent (DIA) or data dependent (DDA) acquisition methods for liquid chromatography mass spectrometry based proteomics on human primary proximal tubule cell lysates and basolateral media

Given the detrimental effect on haemostasis of taking a wedge biopsy of kidney before NMP, it was preferable to use a core biopsy for proteomic analysis to allow start and end comparison. Similar proteins were identified from DIA data for both wedge and core biopsies, with more genes of interest identified than by DDA (**Table 3-12**). There was also an adequate quantity (>50 µg) of protein yielded from a core biopsy.

Cell type	Marker	DIA wedge	DIA core	DDA
Proximal tubule	AQP1	✓	✓	✓
	LRP2	✓	✓	✓
	CUBN	✓	✓	✓
Podocytes	NPHS1	✓	✓	✓
Fibroblast	PDGFRA	×	✓	×
Immune cells	CD45 (PTPRC)	✓	✓	×
Endothelial cells	CD31 (PECAM1)	✓	✓	×
Distal tubule	UMOD	✓	✓	✓
Pathway	**Marker**	**DIA wedge**	**DIA core**	**DDA**
Cell death	PDCD4	✓	✓	×
	BAX	✓	✓	✓
	Caspases (6 and 7)	✓	✓	×
Metabolic	G6PD	✓	✓	✓
	Pyruvate kinase (PKM, PKLR)	✓	✓	✓
Inflammatory	NFKB (1 and 2)	✓	✓	×
Injury	LCN2	✓	✓	×
Ischaemia	VEGFA	✓	✓	×
	HIF1A	×	×	×

Table 3-12 Comparisons of proteins identified in tissue lysates by different proteomics methods.
Proteins identified by either data-independent (DIA) or data dependent (DDA) acquisition methods for liquid chromatography mass spectrometry based proteomics in tissue lysates from either wedge or core human kidney biopsies. DDA results were the same for both biopsy methods. Genes of interest were selected by being markers of cells of interest or involved in pathways of interest in ischaemia-reperfusion

3.19.5 Minimum duration of antimiR treatment

Principal component analysis using proteins with complete data from pilot cell lysates, showed a similar pattern regardless of whether DDA or DIA had been used. Statistics cannot be performed on this pilot data from 1 biological repeat and so caution should be exerted in drawing conclusions from the sparse principal component analysis plots. However, it appears that the 24- and 48-hour

reoxygenation samples treated with antimiR-21 are further from their respective control scrambled antimiR treated samples compared to the 8-hour samples (**Figure 3-11**). Therefore, the shorter time point of 8 hours was eliminated from the final model due to concerns that it may be too short to detect significant protein changes.

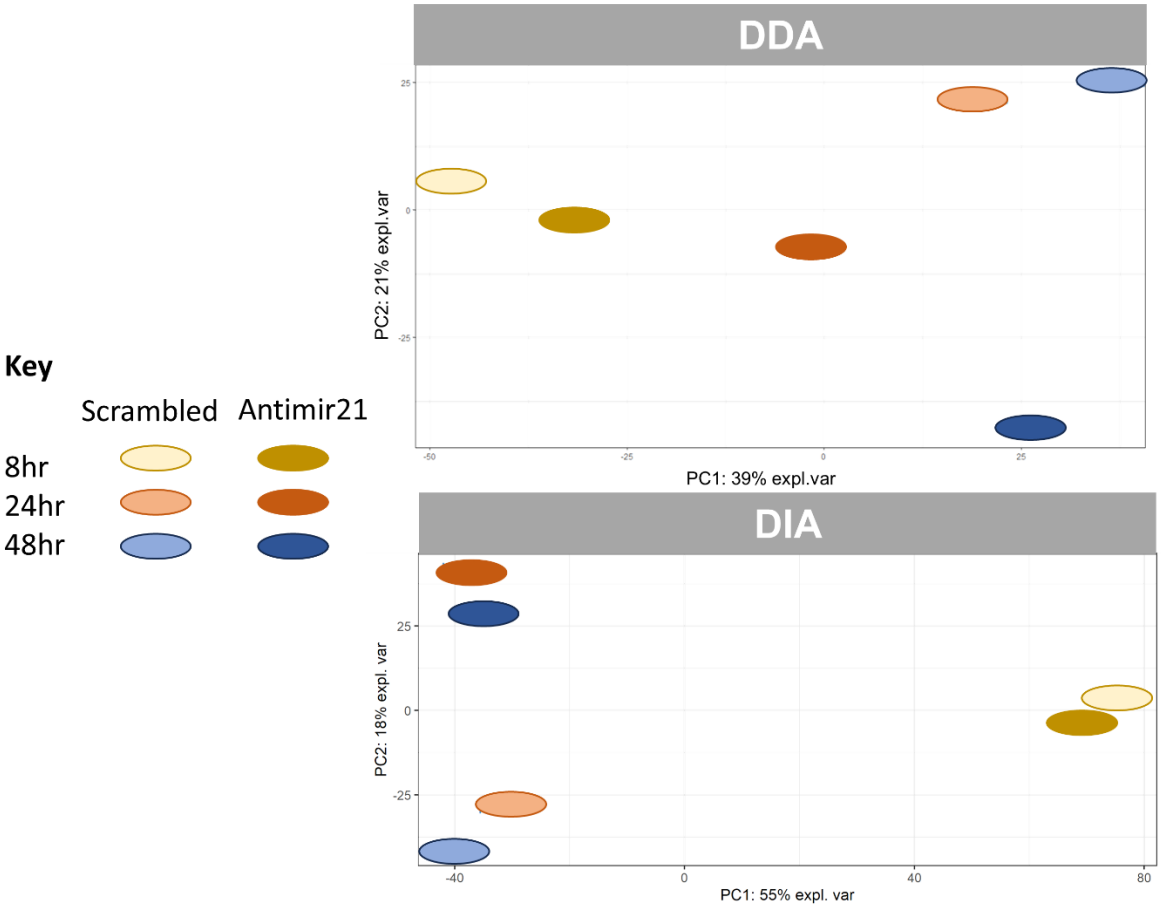

Figure 3-11 Sparse principal component analysis of cell lysate proteomics data.
Plots of proteins with complete data from either data-independent (DIA) or data-dependent (DDA) acquisition of liquid chromatography mass spectrometry proteomics data. Samples are cell lysates from human proximal tubule epithelial cells treated exposed to hypoxia-reoxygenation and treated on reoxygenation with either control scrambled antimiR or antimiR-21. Reoxygenation period was 8, 24 or 48 hours. All samples were treated with antimiR at reoxygenation, other than 24-hour reoxygenation scrambled-treated cells which were treated 24 hours before hypoxia.

3.19.6 Imputation method

For DIA data, where biological repeats were available, missing data was imputed with the web-based tool NAguideR[133] (available at: https://www.omicsolution.com/wukong/NAguideR/) which allows assessment of multiple imputation methods. Proteins were first filtered to remove those were more than 50% of values in a group were missing.

Bayesian principal component analysis[134] was used to impute missing values. However, this method generated some values that were below the limit of detection so the minimum an imputed value could be was set to be the lowest value detected for that protein (**Figure 3-12**).

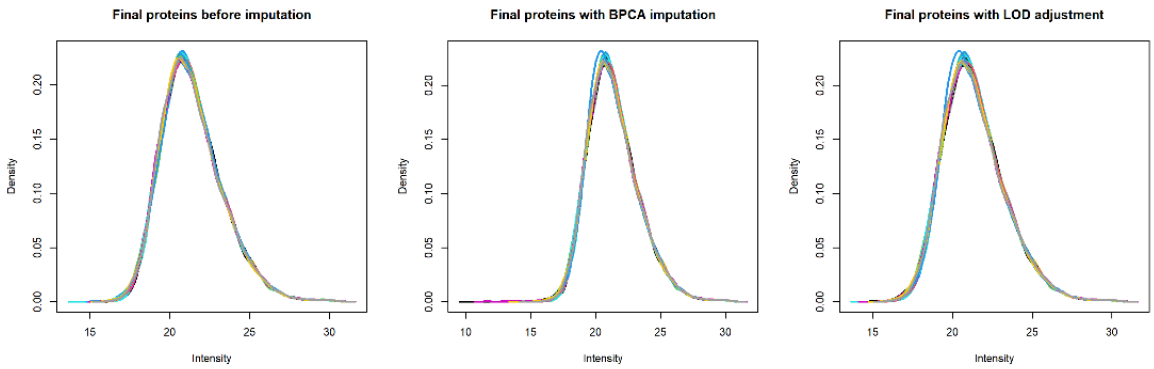

Figure 3-12 Comparison of imputation methods for proteomics data. Log_2 counts of proteins filtered to exclude those with more than 50% of missing values in any group. Each line represents one of 24 samples. Density plot shown before imputation, after imputation with Bayesian principal component method (BPCA) and adjusted for limit of detection (LOD) for each protein. Plots displayed are from liquid chromatography mass spectrometry-based proteomics with data independent acquisition analysed with a library-free method in DIA-NN.[131]

A similar number of proteins remained after filtering for missing values whether library preparation was performed using the gas phase fractionation sample (6717) or with the library-free method (6228). Around 5% of proteins in each dataset were uniquely identified by each method of library preparation.

3.20 Transcriptome and proteome analysis

3.20.1 Sparse principal component analysis

For initial assessment of differences between samples, sparse principal component analysis was performed in R Studio (R Core Team (2023). _R: A Language and Environment for Statistical Computing_. R Foundation for Statistical Computing, Vienna, Austria. https://www.R-project.org/.) using R package mixOmics.[135] As pilot proteomics data did not include biological repeats, missing data could not be imputed and so only proteins with complete data contributed to these plots.

3.20.2 Differential gene expression analysis

The effect of the disease state and the antimiR treatment on differential gene expression was explored in both PTEC data and from perfusion tissue samples using DESeq2. The log_2 fold change of a gene was calculated with DESeq2 and *P* values

from Wald test adjusted for multiple comparisons with Benjamini-Hochberg method as default. The conditions compared and design formulas used are displayed below (**Table 3-13**).

A. ***In vitro PTEC***

Time point	Treatment comparison	Design formula
24 hr reoxygenation	antimiR-21 vs scrambled within hypoxia-reoxygenation	design = ~kidney + oligo
48 hr reoxygenation		
24 hr reoxygenation	Hypoxia-reoxygenation vs normoxia within scrambled	design = ~kidney + oxygen
48 hr reoxygenation		

B. Kidney tissue from normothermic machine perfusions

Time point	Treatment comparison	Design formula
0 hr	antimiR-21 vs scrambled	design = ~kidney + oligo
24 hr	antimiR-21 vs scrambled	design = ~kidney + oligo
AntimiR	**Time comparison**	**Design formula**
Scrambled	0 hr vs 24 hr	design = ~kidney + time
AntimiR-21	0 hr vs 24 hr	design = ~kidney + time

Table 3-13 Design formulas used in DESeq2 to calculate log_2 fold change in gene expression.
The data in **A** is from primary human proximal tubule epithelial cells (PTEC) and the time point refers to the duration of reoxygenation (after 24 hours of incubation at 1% oxygen). The tissue analysed in **B** is from the before and after 24 hours of normothermic machine perfusion. Pairs of kidneys from the same donor were used with one kidney receiving antimiR-21 and the other scrambled control antimiR. Analysis for interaction between antimiR treatment (oligo) and perfusion time was also assessed in **B** with *design = ~kidney + oligo + time + oligo:time*. In both **A** and **B** the factor "kidney" refers to the kidney donor (**A.** n=4 **B** n=5) as data were all paired. "oligo" refers to antimiR treatment.

The DESeq() function includes a normalisation step. As the protein count data output from DIA-NN is already normalised, the normalisation sizeFactor was set to 1 for proteomics data and dispersion check was performed to ensure the data appeared typical (**Figure 3-13**). Volcano plots to visualise differential gene expression were generated with EnhancedVolcano.[136]

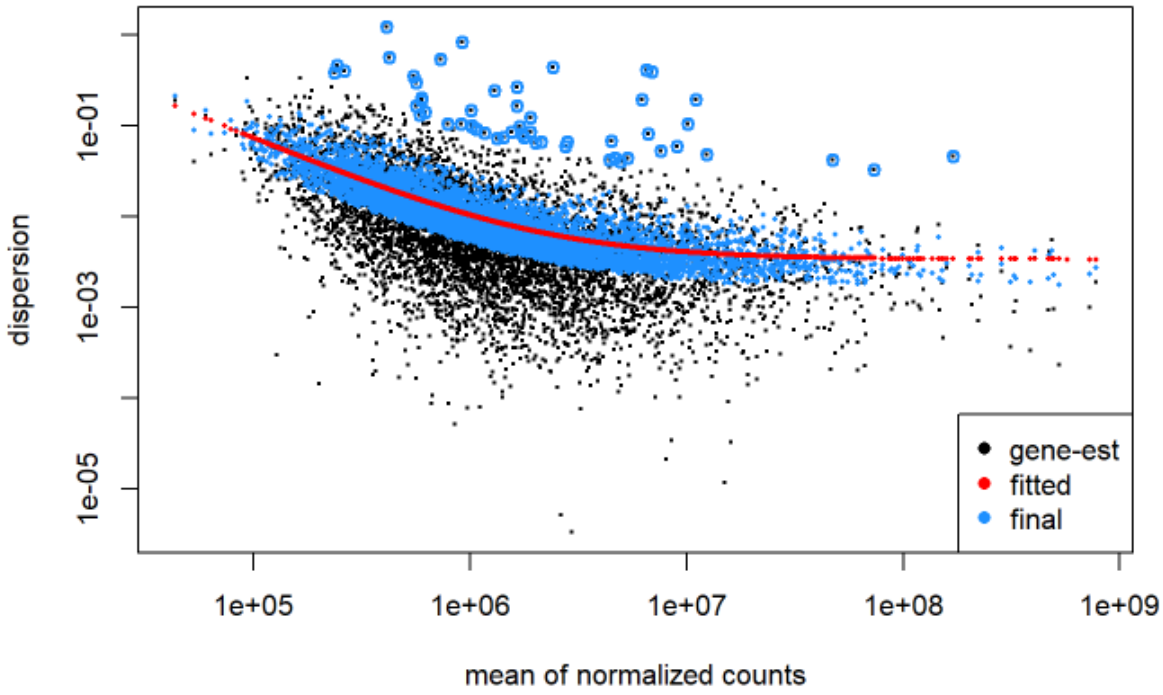

Figure 3-13 Dispersion plot for protein counts from liquid chromatography mass spectrometry-based proteomics.
Data independent acquisition used and protein counts generated in DIA-NN with library-free method. Data shown is from 4 biological repeats of human primary proximal tubule epithelial cells exposed to hypoxia-reoxygenation with a 48 hour period of reoxygenation and either antimiR-21 or scrambled antimiR treatment.

3.20.3 Defining miR-21 targets

A list of miR-21 targets was generated using multiMiR[137] to screen databases for validated and predicted targets of hsa-miR-21-5p on 5/4/2024. Predicted targets were only included if they were present in more than one database. 1819 entries remained after exclusion of duplicates, of which 1569 were validated targets. This equated to 1802 unique entrez_IDs.

3.20.4 Gene set enrichment analysis

Gene set enrichment analysis was performed using fgsea[138] with hallmark[139] and reactome[140] human gene sets accessed from Molecular Signatures Database (MSigDB) with msigdbr.[141] Gene IDs were converted to entrez IDs with biomaRt.[142] Gene sets were filtered by size to exclude those composed of less than 15 or more than 500 genes.

To explore enrichment for miR-21 targets, the MSigDB gene set MIR21_5P[143] within the C3 subcollection of microRNA targets was used. This includes 149 unique genes of which 132 were within the list of miR-21 targets acquired through multiMiR.

A subset of hallmark and reactome gene sets were designated as being enriched with miR-21 targets if more than 15% of their genes were within the miR target list generated from multiMiR. Of the 1077 gene sets that met the size criteria detailed above, 408 were considered enriched for miR-21 targets, as defined by this threshold. Higher thresholds were explored but the threshold of 15% was deemed optimum as the number of pathways included essentially halved for every additional 5% (**Table 3-14**).

Threshold	15%	20%	25%	30%
Enriched gene sets	408	194	96	35

Table 3-14 Optimising threshold for miR-21 target-enrichment of gene sets.
Number of hallmark and reactome human gene sets (composed of between 15 and 500 genes) with the indicated % of included genes being miR-21 targets. The reference list of miR-21 targets was generated using multiMiR and included validated targets in any database and predicted targets if present in more than one database.

3.20.5 Ingenuity pathway analysis

Results of differential gene expression (DGE) analysis were filtered by log fold change and significance to analyse a subset of genes using QIAGEN IPA (QIAGEN Inc., https://digitalinsights.qiagen.com/IPA)[144] to predict activity of diseases and biological processes and to predict activity and identify of upstream regulators.

Diseases and biological processes were filtered to remove cancer pathways using search terms in **Figure 3-14** as deemed less relevant to ischaemia-reperfusion and many processes were repeated without cancer being specified. The p values for the estimated z scores of the remaining pathways were then adjusted for multiple comparisons with Benjamini-Hochberg method.

Predicted upstream regulators were filtered to exclude chemicals and those where results had a strong bias defined with a threshold of ± 0.25.

```
filtered <- pathways %>%
  filter(!grepl("tumor", Diseases.and.Bio.Functions))%>%
  filter(!grepl("oma", Diseases.and.Bio.Functions))%>%
  filter(!grepl("ancer", Diseases.and.Bio.Functions))%>%
  filter(!grepl("Tumor", Diseases.and.Bio.Functions))%>%
  filter(!grepl("neopl", Diseases.and.Bio.Functions))%>%
  filter(!grepl("Neopl", Diseases.and.Bio.Functions))%>%
  filter(!grepl("etastas", Diseases.and.Bio.Functions))
```

Figure 3-14 Filtering out cancer pathways.
Search terms used to filter diseases and biological processes pathways from QIAGEN IPA (QIAGEN Inc., https://digitalinsights.qiagen.com/IPA) to remove cancer-specific pathways.

3.20.6 Correlation analysis between RNA and proteomic results

Pearsons correlation analysis was performed to determine the relationship between differential gene expression assessed by bulk RNA sequencing or LCMS-DIA for genes identified by both methods.

3.21 Statistical Analysis

One-way and two-way repeated measures analysis of variance (RM-ANOVA) were used to compare means of more than two groups within paired data. Paired and unpaired t test compared the mean of 2 groups, as appropriate including as post-hoc analysis when ANOVA revealed a significant effect significant.

Analysis was performed in RStudio Team (2021). RStudio: Integrated Development Environment for R. RStudio, PBC, Boston, MA URL http://www.rstudio.com/. Packages used for data analysis and visualisation included ggplot2[145], rstatix[146] and ggh4x.[147]

3.22 Ethics

The use of donated human kidneys in research was approved by a National Health Service (NHS) Research Ethics Committee (REC) (REC reference 16/NE/0230; IRAS 182637). The NHS Blood & Transplant's Research Innovation and Novel Technologies Advisory Group approved and oversaw allocation of research kidneys to this project. The kidneys involved in this study had been declined for clinical transplantation by all UK transplant centers. Consent for research was obtained from the donor's family by Specialist Nurses in Organ Donation before organ retrieval by the National Organ Retrieval Service. Organs with DNA or commercial restrictions for consent were excluded from this study.

Chapter 4. Establishing an *in vitro* model of ischaemia-reperfusion injury in the proximal tubule epithelium

4.1 Introduction

The proximal tubule is a key site of injury in kidney ischaemia-reperfusion and has been shown to take up antimiR during ex vivo perfusion.[97,148] As such, proximal tubule epithelium is an appropriate *in vitro* model to explore the effects of antimiR-21 treatment in this disease process. Work has been done on the effects of antimiR-21 in human proximal tubule cells lines, such as HK-2 cells, but there are limitations in how well cell lines mimic what happens in the human body.[102,108,110,149,150]

Although originally derived from human tissue, cell lines have been modified and immortalised to allow continual passage.[151] In the case of HK-2 cells, immortalisation is achieved by transfecting with the *E6* and *E7* genes from human papillomavirus-16.[151] Such modifications bring into question the relevance of results obtained from these cells, particularly in relation to effects on cell death.

The difference in functional properties is also highlighted by the requirement for transfection reagents when delivering antimiR to these cells, which is not the case when delivering ex vivo.[97,108] This difference likely relates to poor preservation of endocytic function in most proximal tubule cell lines.[152]

Another limitation of using cell lines is that it does not permit exploration of the impact of biological variability, as cells from a cell line can be considered clones of each other. The ability to use biological repeats is an important benefit of primary cells if aiming to understand the effect of a process in people.

4.1.1 Markers for characterising PTEC

Around half of epithelial cells in the kidney are thought to be from proximal tubule,[153] with single cell analysis confirming proximal tubule epithelium to be an abundant cell type.[154,155] This abundance is useful for cell isolation but must be coupled with comprehensive characterisation and contamination assessment of the resulting isolates. Use of characteristic cell markers proteins is one approach to this assessment.

Cytokeratin-19 (K19)

The cytoskeleton in cells is formed from a network of intermediate filaments and cytokeratins are the predominant intermediate filament in eukaryotic cells.[156] Cytokeratin expression is almost exclusively restricted to epithelial cells, a feature that has made them relevant in the validation of commercially available primary PTEC (ATCC® PCS-400-010, PromoCell® C-12665, Lonza CC-2553). To form a filament a Type I (K9-K28) and Type II (K1-K8;K71-K80) cytokeratin must combine forming a heterodimer.[156] These combinations are expressed in a tissue and cell sub-type specific manner.[156,157]

In the healthy human kidney, it is largely K7, K8, K18 and K19 that are expressed by epithelial cells, with the exact pattern varying with injury.[156-160] Cytokeratin-19 expression cannot reliably be used to differentiate between epithelial cell subtypes within the renal cortex, but will differentiate isolated epithelial cells from contaminating endothelial and mesenchymal cells.

Tight junction protein-1 (TJP1)

Tight junction protein-1 (also called Zonula occludens-1, ZO-1) is involved in tight junctions between cells.[22] Tight junctions are a type of intercellular junction crucial in the formation of barriers by endothelial and epithelial cells and so this protein is widely expressed in these cell types.[161,162] Interestingly, fibroblasts also express TJP1, but in the absence of concurrent claudin-1 expression do not form tight junctions and the expression pattern on immunofluorescence is somewhat different.[162]

Tight junctions are an important epithelial cell characteristic but detection of TJP1 alone will not differentiate isolated epithelial cells from endothelial or mesenchymal cell contamination.

E-cadherin

E-cadherin is a transmembrane protein essential for adherens junctions between epithelial cells.[163] It is expressed in both proximal and distal tubules so again is not a useful marker for confirming the proximal tubule origin of isolated cells but does support the epithelial character.[163]

Aquaporin-1 (AQP1)

The aquaporins are a family of membrane water channels expressed by epithelial and endothelial cells.[164] In the renal tubule, AQP1 is expressed exclusively by the proximal tubule making it an excellent marker to confirm the type of epithelial cell isolated.[165] AQP1 is found on both the apical and basolateral membrane of proximal tubule cells.[166]

Single-cell transcriptome analysis of the human kidney has demonstrated AQP1 expression in the endothelial cells of the glomerulus and descending vasa recta also.[167] However, these cells will not also express the epithelial marker cytokeratin and the vasa recta lies in the medulla so will not be included in the tissue from which cells are initially isolated.[164]

4.1.2 Markers of mesenchymal contamination

In the healthy kidney, resident fibroblasts maintain the extracellular matrix whereas in disease myofibroblasts produce collagen leading to fibrosis.[168,169] These two cell types cannot be differentiated on light microscopy but alpha smooth muscle actin expression is restricted to myofibroblasts.[168] Fate mapping has demonstrated around 35% of myofibroblasts in kidney fibrosis to originate from the bone marrow with the remainder from activation of resident fibroblasts and a smaller proportion from endothelial- and epithelial-mesenchymal transition.[169] Assessment of contaminating non-epithelial cells would ideally be with a cell surface marker so that if contamination levels were high, live cells in the isolate could be sorted. As there is no single cell surface marker commonly used for identifying mesenchymal cells, CD44 and members of the platelet derived growth factor receptor (PDGFR) family were assessed for suitability.

CD44

CD44, also called P-glycoprotein-1, is a cell surface receptor involved in both cell adhesion and cell signalling.[170] Different isoforms are produced from a single gene by alternative splicing, although the standard CD44 is most widely expressed.[170,171] CD44 was first demonstrated on haematopoietic cells but expression has since been identified on mesenchymal cells, endothelial cells and, in some circumstances, epithelial cells as well.[171-174] It is generally reported that CD44 is not expressed in the healthy kidney, other than in passenger leukocytes, peritubular capillaries and resident fibroblasts.[174-178] However, CD44 appears to play a role in epithelial to

mesenchymal transition.[173] Data from human kidney tissue has demonstrated CD44 expression in injured tubular cells, in the context of ischaemia,[178] interstitial fibrosis and tubular atrophy,[177] and transplant rejection.[174]

In vitro, CD44 expression has been demonstrated in the fibroblast cell line HMRC5, human umbilical vein endothelial cells and primary fibroblasts isolated from feline kidneys.[168,177] CD44 has been identified as a useful surface marker to distinguish fibroblasts from undifferentiated cells such as stem cells and partially reprogrammed cells.[179]

Targeting CD44 positive cells in donor kidneys could identify contaminating fibroblasts, myofibroblasts and endothelial cells. However, as cell isolates are generated from ischaemic kidneys, a degree of injury is expected in the proximal tubule which could result in widespread CD44 expression.

PDGFR

PDGFRs are dimers formed by combinations of α and β subunits.[180] Expression of PDGFRα and PDGFRβ both increase in the kidney in disease, including ischaemic tubular injury,[181] are expressed by matrix-producing cells[182,183] and thought to contribute to renal fibrosis.[184]

PDGFRβ expression is increased in fibrotic human kidneys compared to healthy tissue and mouse studies have shown it to play a role in mesenchymal cell proliferation and matrix deposition in the kidney.[184,185] However, its expression is not restricted exclusively to fibroblasts and myofibroblasts, as demonstrated by single-cell RNA sequencing work on human kidney tissue.[186] Although PDGFRβ expression was demonstrated in most matrix producing cells (COL1A1 positive), this population included mesangial cells, immune cells and some epithelial cells.[186] In rats, expression has been demonstrated in the glomerulus, thick ascending loop, distal tubule and collecting duct and injured proximal tubule.[181]

Fibroblasts and myofibroblasts can be differentiated from other PDGFRβ positive cells by co-expression of PDGFRα.[186] The importance of PDGFRα in fibrosis has been demonstrated as knockout animals have less collagen deposition compared to wildtype animals.[187] However, this study found that although PDGFRα colocalised with PDGFRβ, these cells did not express αSMA indicating they were not activated myofibroblasts.[187]

In mouse skin, PDGFRα is exclusively expressed in stromal cells.[188] Only a subset express αSMA as well so they are not exclusively myofibroblasts but they were negative for immune cell markers.[188] In rats there was some PDGFRα expression in S3 segment of proximal tubule cells when proliferating[181] but this segment lies in the medulla so should be excluded from cell populations isolated from renal cortex.

The fibroblasts cell line HMRC5 has high PDGFRα expression, making it a useful positive control.[189]

4.1.3 Markers of endothelial contamination

CD31 is a well-recognised endothelial cell marker, also known as platelet/endothelial cell adhesion molecule-1 (PECAM-1), and an important component of cell-cell junctions.[190] Although expressed by platelets and immune cells as well, both of these cell types would be expected in low numbers in a flushed human kidney donated for transplant. As a cell surface protein, again it could be used for sorting live cells if contamination levels were high.

4.1.4 Modelling ischaemia in vitro

When modelling ischaemia in cell culture it is common to consider ambient oxygen "normoxia" and 1% oxygen "hypoxia".[191,192] However, actual oxygen content of the media and how this relates to physiological conditions is often not considered.[191]

Oxygen content in blood and media

The oxygen content of blood is a combination of the oxygen bound to haemoglobin and the oxygen dissolved in plasma. The dissolved oxygen accounts for a relatively small proportion of total oxygen content.[193,194] Total oxygen content of blood can be calculated with the formula:[193]

$$CaO2 = k1.Hb.SaO2 + k2.PO2$$

CaO_2 = total oxygen content (mL of gaseous oxygen)

k_1 = oxygen carrying capacity of haemoglobin (1.34 – 1.39 mL of gaseous oxygen per gram of haemoglobin)

Hb = haemoglobin concentration (g/L)

SaO_2 = proportion of haemoglobin saturated with oxygen

k_2 = solubility of oxygen in plasma (~0.23 mL of gaseous oxygen per L plasma per kPa or ~9 μM/kPa assuming a temperature of 37°C)

Therefore, for a haemoglobin level of 150 g/L with oxygen saturations of 97% and using partial pressure of oxygen in arterial blood of 13.3 kPa, oxygen content is 198 mL per litre of blood. However, the renal cortex is thought to experience a lower partial pressure of oxygen of 6.0 kPa (~45 mmHg)[65,195] which could be expected to give oxygen saturations of around 80%.[194] These values would give a total oxygen content of 163 mL/L blood.

We can convert this to a molar concentration of oxygen using the ideal gas law:[196]

$$PV = nRT$$

$$n = \frac{PV}{RT}$$

$P =$ ambient pressure (atmospheric pressure at sea level is 101.325 kPa)

$V =$ volume of gas in litres (per litre of blood)

$n =$ moles of gas

$R =$ gas constant $= 8.314$ L.kPa.k^{-1}.mol^{-1}

$T =$ temperature in kelvin $= 310$ kelvin $= 37^{o}$C

This would give oxygen content in arterial blood as 7.8 mM and 6.4 mM for the renal cortex.

For cells cultured *in vitro*, dissolved oxygen will commonly be their only source of oxygen from culture media which does not routinely contain an oxygen carrier such as haemoglobin. Given the low proportion of the oxygen content in blood that is accounted for by dissolved oxygen, it would seem inaccurate to directly compare partial pressure of oxygen in media with blood.

To achieve the same concentration of oxygen in blood by relying solely on dissolved oxygen, a pressure of oxygen exceeding atmospheric pressure would be required (860 kPa for arterial blood and 709 kPa for the renal cortex).

The solubility of oxygen in a liquid is affected in part by the temperature, with lower temperatures increasing solubility, and by the ion composition. The higher ionic strength of cultured media compared to distilled water increases oxygen solubility.[191] Using figures from Al-Ani et al.[191] it can be estimated that oxygen solubility in media is around 9.6 μM/kPa, so only slightly higher than that for plasma. This value is similar to that reported by Place et al.[196]

Pericellular oxygen levels *in vitro*

Other factors in the cell culture set up that affect the oxygen concentration within the media include the depth of the media and the oxygen consumption rate of the cells, both of which can affect the concentration of oxygen directly next to cells. Cells with a high metabolic rate are particularly at risk of having low oxygen levels in their nearest media if they consume it faster than the diffusion coefficient determines it can be delivered.[191,197]

Oxygen consumption of human PTEC in a microfluidic culture plate has been estimated to be 0.3 pmol/hour per cell[198] and this will contribute to the rate that oxygen content of the media falls when it enters hypoxia. Kann et al.[198] demonstrate that to maintain constant oxygen levels, a system with flow was required so that oxygen could be continuously topped up to counteract what was used by the cells. In static media, the partial pressure of oxygen fell by around 5% of its starting value in 1 minute.[198]

The rate at which culture media equilibrates with a new surrounding partial pressure of oxygen is affected by the depth and vessel of the media. Zeitouni et al.[192] found that under normoxic conditions (19.1 kPa oxygen) media in all set ups tested equilibrated to around 18.0 kPa at a similar rate. When transferred to 1% oxygen (1 kPa oxygen), a large drop in oxygen content was observed within the first hour but at different rates depending on the culture vessel used.[192] By 24 hours of exposure to 1% oxygen, the pO_2 in all systems has fallen to less than 1.1 kPa.[192] Adding media that had been equilibrated to 1% oxygen made a relatively small impact of partial pressure of oxygen at 6 hours when applied to confluent cells grown on inserts which is hard to explain.[192] HIF1α was upregulated by 4 hours of exposure to 1% oxygen for cells in inserts and at 1 hour for cells grown in 24 well plates.[192] The depth of media above the cells were similar at 5.5 mm in the plates and 6 mm for the inserts.[192]

Media depth must be kept constant to replicate pericellular conditions between experiments and this is true for normoxic conditions as well.[196] Ficks law can be used to explain the concern of pericellular hypoxia in normoxic conditions when the rate of diffusion of oxygen is exceeded by the cells' oxygen consumption rate.[196]

$$F = \frac{D.\Delta C}{\Delta x}$$

$F =$ diffusion of gas through the media

$D =$ diffusion constant

$\Delta C =$ difference in the concentration of the gas between the air and the pericellular media

$\Delta x =$ distance between these two gas concentrations

Al-Ani et al.[191] developed a calculator which suggests a roughly 50% deficit in oxygen delivery to the pericellular media under normoxic conditions with a 4.5 mm media depth and 226 666 cells/cm^2 seeding density used in my experiments coupled with a 83 amol/cell/second oxygen consumption rate predicted for PTEC[198] and 2.69E-5 diffusion constant for cell culture media.[196] To meet the oxygen consumption rate adequately I would need to seed cells in just under half their current volume of media to achieve a depth of only 2.1 mm which is below what is recommended as the minimum seeding volume for the inserts.[191]

4.1.5 Consistent in vitro modelling

Ultimately, it is challenging to perfectly model normoxia and hypoxia *in* vitro but keeping certain factors constant, such as media depth, seeding density and culture vessel, are essential to ensure reproducibility.

This chapter will characterise and confirm the purity of primary human PTEC isolated from human kidneys declined for transplant, confirm that hypoxia can be induced in these cells and assess them as a useful model for studying the effects of antimiR-21 *in vitro*.

4.2 Methods

4.2.1 Scanning electron microscopy

Primary cell isolates were prepared for scanning electron microscopy by removing media then both washing and fixing with 2% glutaraldehyde in Sorenson's phosphate buffer. Fixation was at 4^{o}C and samples were left in fixative overnight. Samples were then rinsed twice with 0.2 M phosphate buffer before proceeding to dehydration with increasing ethanol concentrations. Samples were stored at 4^{o}C in 100% ethanol until processing by the Electron Microscopy Core Facility.

4.2.2 Characterisation by immunofluorescence

Immunofluorescence for epithelial (K19, TJP1, E-cadherin) and proximal tubule markers (AQP1) was performed for three biological repeats to confirm expression was maintained after extended culture on transwell inserts.

Subsequently, characterisation was limited to confirming widespread K19 positivity on each isolate after a confluent monolayer had formed in culture.

4.2.3 Contamination assessment

Smooth muscle actin positive cells

Immunofluorescence for smooth muscle actin (SMA) was optimised on the fibroblast cell line HMRC-5 (**Figure 4-1**).

Widefield fluorescent microscopy images of isolated cells prepared with immunofluorescence for SMA were acquired at random (4 repeats) of confluent areas with X20 objective. Automated cell count was performed using DAPI channel. Dual-channel images were manually assessed for cells displaying a microtubular pattern of signal consistent with actin to estimate the proportion of isolated cells that were mesenchymal (**Figure 4-1**).

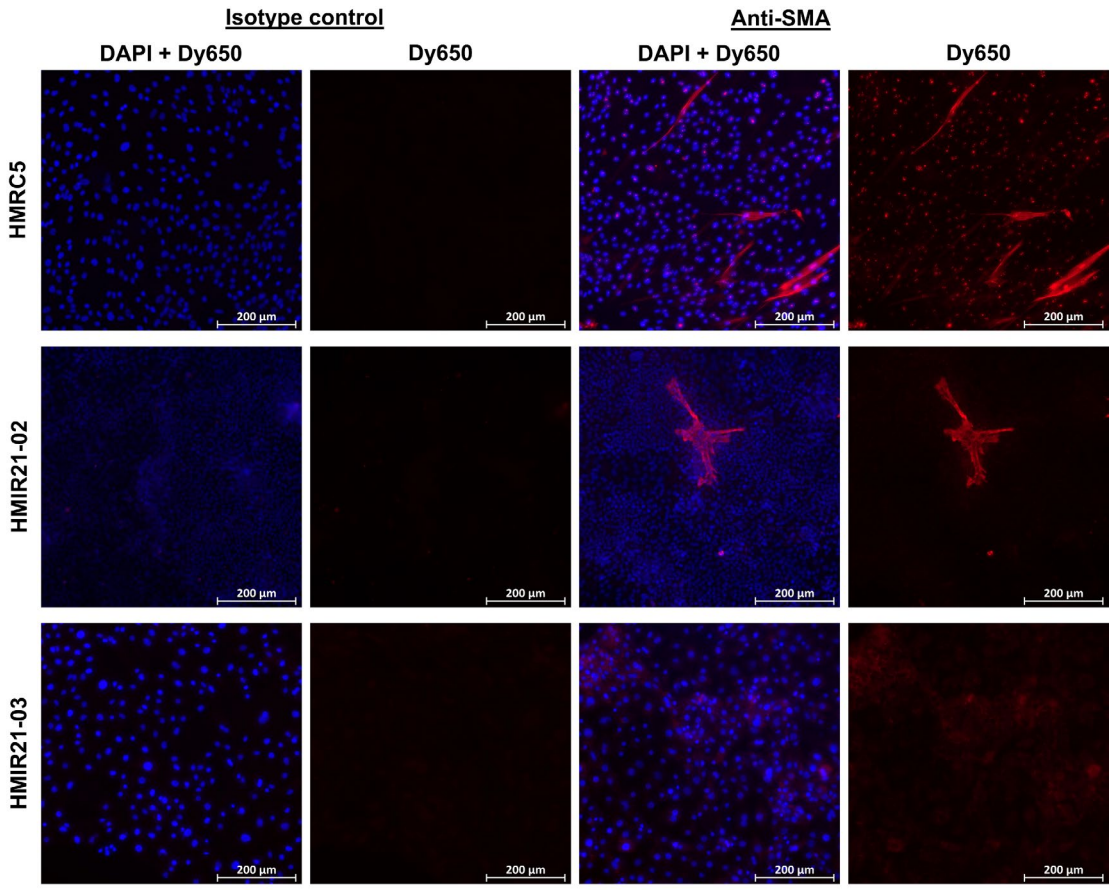

Figure 4-1 Immunofluorescence for smooth muscle actin (SMA) to determine mesenchymal contamination in primary human proximal tubule epithelial cell isolates.
Anti-SMA binding was detected with Dy650 conjugated secondary antibody and nuclei counterstained with DAPI. Images of cells incubated with isotype control shown for non-specific binding. Widefield fluorescent microscopy images acquired with ZEISS Axio Imager using X20 objective. SMA positivity demonstrated in fibroblast cell line (HMRC5). A microtubular pattern of SMA positivity is shown in PTEC isolates from donor HMIR21-02 with 54 cells in this image counted as mesenchymal (5.65%). A less distinct pattern of SMA positivity was demonstrated in PTEC isolates from donor HMR21-03 and no cells in this image were deemed mesenchymal.

Flow cytometry for endothelial and mesenchymal markers

Flow cytometry for endothelial and mesenchymal markers was used on initial cell isolates and on cells harvested after a period in culture to determine optimal approach to determining contamination in PTEC isolates.

CD44 and PDGFRA positivity were explored to assess mesenchymal contamination. Both are expressed by the fibroblast cell line HMRC5 (**Figure 4-2A**). However, high levels of CD44 were also expressed in PTEC isolates (**Figure 4-2B**), particularly after a period in culture, and found to be inconsistent with other approaches of assessing mesenchymal contamination (PDGFRA positivity and SMA positivity, **Table 4-1**).

Therefore, CD44 was not deemed a useful marker for determining mesenchymal contamination in this context.

CD31 was confirmed as an endothelial cell marker (**Figure 4-2A)** and the level of endothelial cell contamination in PTEC isolates was generally found to reduce with time in culture (**Table 4-2**). The exception to this was for cells from HMIR21-05 (**Table 4-2**) where there was a concern that a larger proportion of the debris layer had been collected during the isolation procedure.

The selected approach for determining contamination was CD31 and PDGFRA positivity of cells maintained on transwell inserts and harvested once a confluent monolayer had formed. The difference between the proportion of live single cells in the APC positive gate for isotype control and target antibody treated cells was taken as the degree of contamination (**Figure 4-2**).

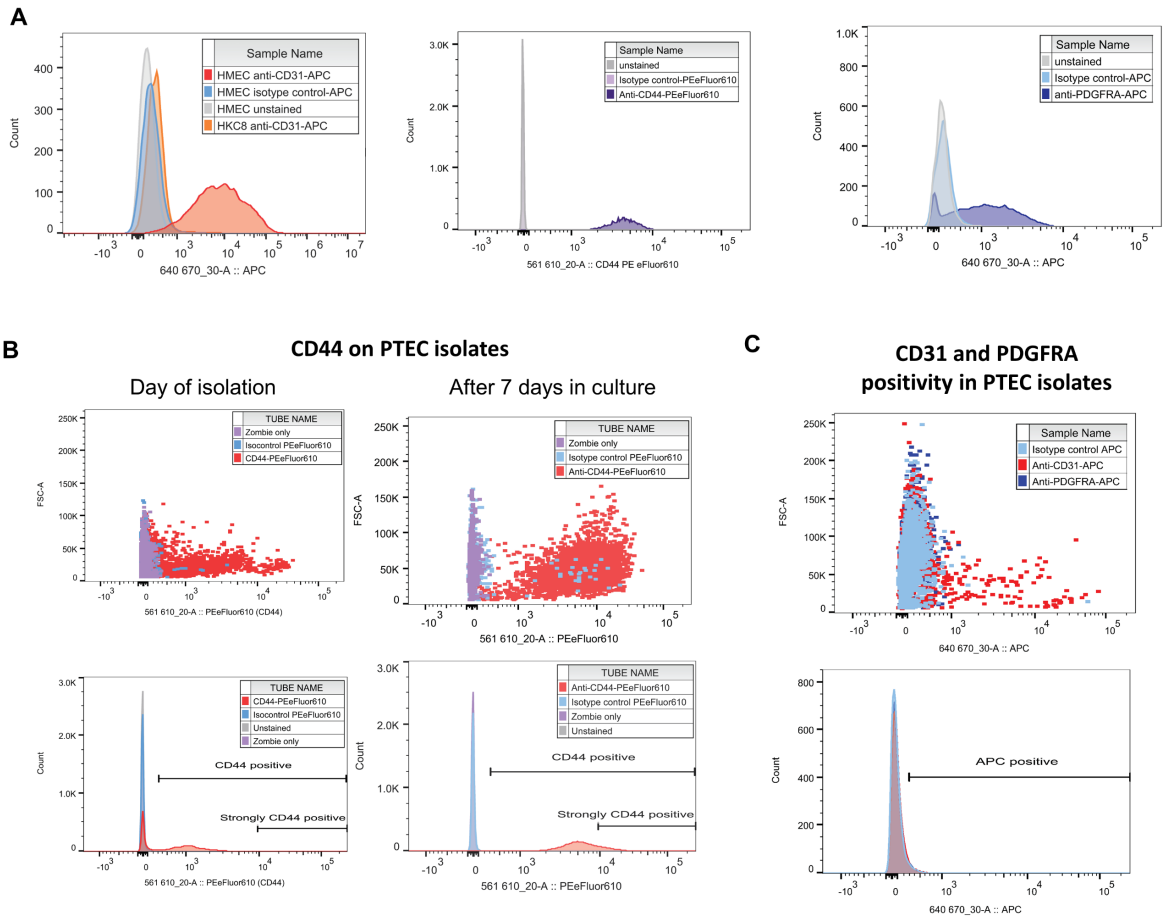

Figure 4-2 Optimisation of contamination assessment by flow cytometry in human primary proximal tubule epithelial cell (PTEC) isolates.

A shows validation of contamination markers in cell lines. Histograms (left to right) display fluorescence associated with anti-CD31 (endothelial marker), anti-CD44 (mesenchymal marker) and anti-PDGFRA (mesenchymal marker) antibodies on cells. Signal from cells incubated without antibodies (unstained) or with isotype control to show background fluorescence. HMEC used as endothelial cell line with CD31 positivity and proximal tubule cell line (HKC8) confirmed absent CD31 signal (left panel). HMRC5 (mesenchymal cell line) displayed positivity for CD44 and PDGFRA (centre and right panel respectively). **B** and **C** shows dot plots, histograms and gating strategy for determining the proportion of cells is PTEC isolate positive for indicated marker. PTEC positivity for CD44 increased with incubation in culture (**B**) and was not deemed a useful mesenchymal cell marker in this context. **C** shows chosen contamination assessment strategy using APC signal associated with CD31, PDGFRA and isotype control in PTEC isolates. All results displayed have been gated for live single cells. Zombie only indicates that cells were incubated with amine-reactive live-dead stain but neither target antibody nor isotype control.

Marker:	**SMA**				**CD44**				**PDGFRA**	
Timepoint:	**After culture**				**At isolation**		**After culture**		**After culture**	
Kidney ID	**Day**	**%**	**Day**	**%**	**Day**	**%**	**Day**	**%**	**Day**	**%**
HMIR21-01	19*	0.00%	21*	0.00%	0	2.53%	5*	91.70%		
HMIR21-02	2#	0.18%	7	2.49%	0	1.00%	7	20.50%		
HMIR21-03	3#	0.15%	7#	1.10%	0	0.14%	11	78.20%		
HMIR21-04	7	0.00%								
HMIR21-05	10	0.00%								
HMIR21-06	5	0.76%							5	0.00%
HMIR21-07	8	0.00%							8	0.43%
HMIR21-08	4	0.00%							4	0.00%
HMIR21-09	6	0.00%							6	0.10%
n	9		3		3		3		4	
Mean ± SD	0.39 ± 0.75%				1.22 ± 1.21%		63.47 ± 37.82%		0.13 ± 0.20%	

Table 4-1 Assessment of mesenchymal contamination in primary human proximal tubule epithelial cell isolates.
Mesenchymal contamination determined by positivity for smooth muscle actin (SMA) on immunofluorescence, or for CD44 or platelet derived growth factor alpha (PDGFRA) on flow cytometry. Whether contamination was assessed on the day of cell isolation (day 0) or after a number of days in culture is indicated. *Cells from HMIR21-01 were passaged and maintained in plastic flasks before seeding into chamber slides or harvesting for flow cytometry. Cells from all other kidneys were maintained without passage and were seeded onto transwell inserts, except for # which were seeded onto chamber slides.

Timepoint	At isolation		After culture: first timepoint		After culture: second timepoint	
Kidney ID	**Day**	**%**	**Day**	**%**	**Day**	**%**
HMIR21-01	0	3.02	5	0.00		
HMIR21-02	0	3.55	7	0.43		
HMIR21-03	0	7.18	11	0.11		
HMIR21-04	0	4.83	6	0.90		
HMIR21-05			4	1.82	9	9.54
n	4		5		1	
Mean ± SD	4.65 ± 1.85 %		0.65 ± 0.74%			

Table 4-2 Assessment of endothelial cell contamination in primary human proximal tubule epithelial cell isolates.
Endothelial contamination determined by positivity for CD31 on flow cytometry. Whether contamination was assessed on the day of cell isolation (day 0) or after a number of days in culture is indicated.

4.2.4 Western blot

Media was removed and adherent cells washed with ice cold PBS. Cold RIPA buffer (150 mM NaCl, 1% Triton X, 0.5% sodium deoxycholate, 0.1% SDS, 50 mM Tris-HCl) with protease and phosphatase inhibitor (Fisher Scientific 10085973) was added at 50-100 µL per 6-well plate well or transwell insert. Cells were scraped with P1000 pipette and lysate collected into microcentifuge tube. Lysates were agitated at 4^{o}C for 20 minutes and then centrifuged at 12000 RCF for 15 minutes at 4^{o}C. Supernatant was collected and stored at -80^{o}C.

Protein in lysates was quantified using the 96-well plate Pierce BCA Protein Assay Kit (Thermo Fisher 23225). A linear standard curve was generated from known concentrations of protein and used to interpolate sample concentrations. If lysate concentration was greater than the most concentrated standard (2 mg/mL), they were diluted 1 in 10 and the assay repeated.

10% resolving gel was prepared with stacking gel on top and details of gel mix are in **Table 4-3**. Gel was placed into gel electrophoresis tank which was then filled with electrophoresis running buffer.

Protein in lysates was quantified as above and 20 µg of sample added to 3 volumes of 4xLaemelli buffer supplemented with 10% β-mercaptoethanol. Samples were heated to 95^{o}C for 10 minutes to denature. 7 µL of protein standard (BioRad 1610374) was loaded into first well with denatured protein lysates samples in subsequent channels.

Gel was run with an initial voltage of 100V before increasing to 140V when the samples had entered the gel.

Component	10% Resolving gel	Stacking gel
d.H_2O	3.96 mL	2.05 mL
30% acrylamide	3.32 mL	0.5 mL
1.5M TrisHCl	2.52 mL	-
0.5M TrisHCl	-	375 µL
10% SDS	100 µL	30 µL
10% ammonium persulfate	100 µL	30 µL
TEMED	5 µL	3 µL

Table 4-3 Constituent components of 10% resolving gel and stacking gel for protein electrophoresis.
Quantities are to produce 1 gel. SDS, sodium dodecyl sulfate; TEMED, tetramethylethylenediamine.

When gel electrophoresis was complete, proteins were transferred onto a 0.2 µm PVDF membrane (BioRad 1704156) using Bio-Rad Trans blot turbo transfer system.

Total protein was quantified using Revert™ 700 Total Protein Stain solution. After protein transfer, the membrane was placed at 37°C for 10 minutes to fully dry, then rehydrated with 100% methanol for 30 seconds and rinsed in tris-buffered saline (TBS) followed by ultrapure water. The protein was stained blue-green by incubation with protein stain solution for 5 minutes at room temperature with gentle agitation, rinsed twice with wash solution and imaged in the 700 nm channel on the LI-COR® Odyssey Fc Imager. The membrane was destained by rinsing with ultrapure water and incubating with destaining solution followed by a further rinse with ultrapure water before proceeding to blocking.

The membrane was blocked with 5% (w/v) non-fat dry milk in TBS with 0.1% Tween-20 (TBST) for 1 hour at room temperature then incubated overnight at 4°C with anti-PDCD4 antibody (CST 9535) diluted 1 in 1000 in 5% (w/v) non-fat dry milk in TBST. After rinsing, the membrane was washed 4 times with TBST and incubated for 1 hour at room temperature with horseradish peroxidase-conjugated anti-rabbit antibody (Sigma A6154) diluted 1 in 10000 with 1% (w/v) non-fat dry milk in TBS. Wash steps were then repeated.

SuperSignal™ West PicoPLUS chemiluminescent substrate (Thermo Scientific 34580) was applied to the membrane for 3 minutes and protein bands visualised using LI-COR ® Odyssey Fc Imager.

Protein bands were quantified using Image Studio Lite (Ver 5.2). Within each sample, the band from the protein of interest was normalised to total protein. Normalised expression was expressed relative to control sample.

4.2.5 AntimiR-21 toxicity assessment

Toxicity from antimiR-21 treatment was assessed using apoptosis assay by flow cytometry. Experimental plan to determine cell death in response to antimiR-21 in combination with hypoxia-reoxygenation when antimiR-21 was given either before or after hypoxic insult is shown in **Figure 4-3**.

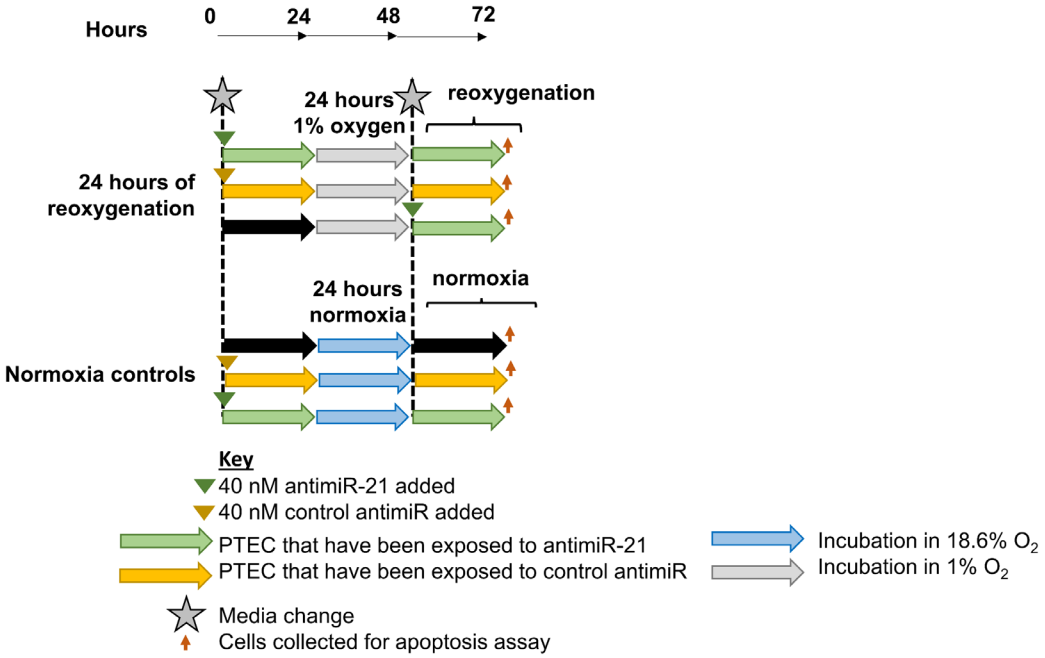

Figure 4-3 Experimental design for apoptosis assay on primary human proximal tubule epithelial cells
After forming a confluent monolayer on transwell inserts, media was changed and where indicated antimiR-21 or scrambled control antimiR treatment was applied to apical compartment. 24 hours later, cells were moved to incubation in 1% oxygen for 24 hours before return to normoxia for reoxygenation. At reoxygenation, media was changed to fresh media without antimiR for those already treated. In the third row, antimiR-21 treatment was applied at reoxygenation. Normoxia controls were treated with or without antimiR-21 or control scrambled antimiR at time 0 with media changes to match hypoxia-reoxygenation samples. Apical media and adherent cells were collected for apoptosis assay at the last timepoint, 24 hours after the last media change.

4.3 Results

4.3.1 Donor and kidney characteristics

Details of the donors and kidneys used for primary proximal tubule cell isolation are provided in **Table 4-4**. The target cold ischaemic time of <30 hours was achieved for all but the first kidney used (HMIR21-01). The amount of tissue collected per kidney donor and the achieved cell yields are detailed in **Table 4-5**. The median (range) cells isolated per g of tissue was 686139 (394118 – 1273581).

Study ID	Side	CIT	Age	Sex	Type	BMI	Weight	HTN	CVD	Diabetes	Admission Cr	Latest Cr	COD	Reason for decline
HMIR21-01	R	32	45	F	DCD	31	80	No	No	T2DM - med	56	37	ICT	Anatomy: cyst and CIT
HMIR21-02	R	13	62	M	DBD	17	48	No	Yes	No	98	120	ICH	Anatomy, perfusion, function
HMIR21-03	L	27	62	F	DCD	28	70	Yes	No	No	32	22	ICH	Recipient unfit
HMIR21-04	R	17.5	50	M	DCD	32	107	No	No	No	59	41	HBD	Anatomy: atherosclerotic disease
HMIR21-05	R	12	55	F	DBD	36	100	Yes	Yes	No	55	48	ICT	Malignancy: areas of haemorrhage on kidney
HMIR21-06	L	18.5	61	F	DCD	32	75	No	No	T2DM - med	96	69	HBD	Anatomy: organ damaged
HMIR21-07	R	13	41	M	DBD	24	73	No	Yes	No	150	155	HBD	Anatomy: multiple haemorrhagic cysts
HMIR21-08	R+L	11	65	M	DCD	38	95	Yes	No	No	75	61	ICH	Malignancy: mass on left kidney
HMIR21-09	R	8.5	58	M	DCD	28	81	Yes	No	No	49	62	TBI	Anatomy: atherosclerosis and adherent fat
HMIR21-10	R	17.5	60	M	DCD	38	123	No	No	No	64	67	ICH	Anatomy: thick firm fat on both kidneys
HMIR21-11	R	14.5	60	M	DBD	25	73	No	No	No	52	45	ICH	Anatomy: severe atherosclerosis
HMIR21-12	R	24	61	M	DCD	25	80	Yes	No	No	58	145	ICH	Anatomical and recipient refused
HMIR21-13	L	18.5	53	F	DCD	25	80	No	No	No	178	40	OD	Anatomy: wedge biopsy of lesion at lower pole
HMIR21-15	R	19	65	F	DCD	34	100	No	No	No	61	50	ICH	Anatomy: poor perfusion and poor quality aortic tissue
HMIR21-16	L	16	59	F	DBD	27	70	No	Yes	No	76	58	ICH	Anatomy: aneurysm extending into kidney
Summary		17± 6	57 ± 7	54% M	67% DCD	29 ± 6	84 ± 18	67% had a comorbidity listed			77 ± 39	68 ± 40	53% ICH	80% Anatomical

Table 4-4 Details of donors and kidneys for proximal tubule epithelial cell isolation.

Donors are listed by Study ID with kidney(s) used indicated as left (L), right (R) or both (R+L). The cold ischaemic time (CIT) at the point of tissue collection is given in hours to the nearest half hour. Age is recorded in years. Kidneys from donors donating after brainstem death (DBD) and circulatory death (DCD) were included. Normothermic regional perfusion was not used. Whether the donor was known to have hypertension (HTN), cardiovascular disease (CVD) or diabetes is indicated. The two with diabetes had type 2 diabetes managed with medication (T2DM - med) which was not insulin. No donors had a history of peripheral vascular disease. Cause of death (COD) was hypoxic brain damage following cardiac arrest (HBD), intracranial haemorrhage (ICH), intracranial thrombosis (ICT), drug overdose (OD) or traumatic brain injury (TBI). The reason the kidney was declined for clinical transplantation is given. Summary shows the mean ± standard deviation (to the nearest integer) for numerical variables or the % in the most frequent categorical variable. Details of donor HMIR21-14 are omitted as no tissue from this kidney could be used for cell isolation given extensive renal lesions. Weight is recorded in kg. BMI, body mass index; Cr, serum creatinine in µmol/L; F, female; M, male

Study ID	Tissue collected (g)	Cell yield	Cells/g
HMIR21-01	6.8	2.68E+06	394118
HMIR21-02	12.4	5.59E+06	450806
HMIR21-03	15	8.87E+06	591333
HMIR21-04	15.6	1.29E+07	825641
HMIR21-05	9.9	1.15E+07	1161616
HMIR21-06	10.1	6.93E+06	686139
HMIR21-07	15.9	9.99E+06	628252
HMIR21-08	19.6	1.20E+07	613265
HMIR21-09	20.2	1.18E+07	584158
HMIR21-10	14.9	1.17E+07	782819
HMIR21-11	10.8	8.89E+06	823603
HMIR21-12	20.7	2.64E+07	1273581
HMIR21-13	19.9	1.02E+07	510955
HMIR21-15	20.5	4.30E+07	2097561
HMIR21-16	20.2	1.64E+07	809426

Table 4-5 Kidney tissue to cell yield.
The amount of human kidney tissue (cortex) collected for primary human proximal tubule cell isolation and the resulting live cell yield. Results are per donor, indicated by study ID.

4.3.2 Characterisation of cells

Isolated cells maintained on transwell inserts formed a monolayer with a cobblestone pattern on light microscopy (**Figure 4-4A**). After an extended period in culture without passage, dome formation was noted which has been attributed to fluid transport across the cells (**Figure 4-4A**).[199] In contrast, cells maintained on glass or passaged and cultured on plastic displayed a more elongated shape suggesting a more

mesenchymal phenotype (**Figure 4-4A**). Absorption of tubular fluid is a key function of PTEC and the presence of microvilli to support this function was confirmed on electron microscopy (**Figure 4-4B)**. The primary cilium, important for signalling,[200] was also identified (**Figure 4-4B**).

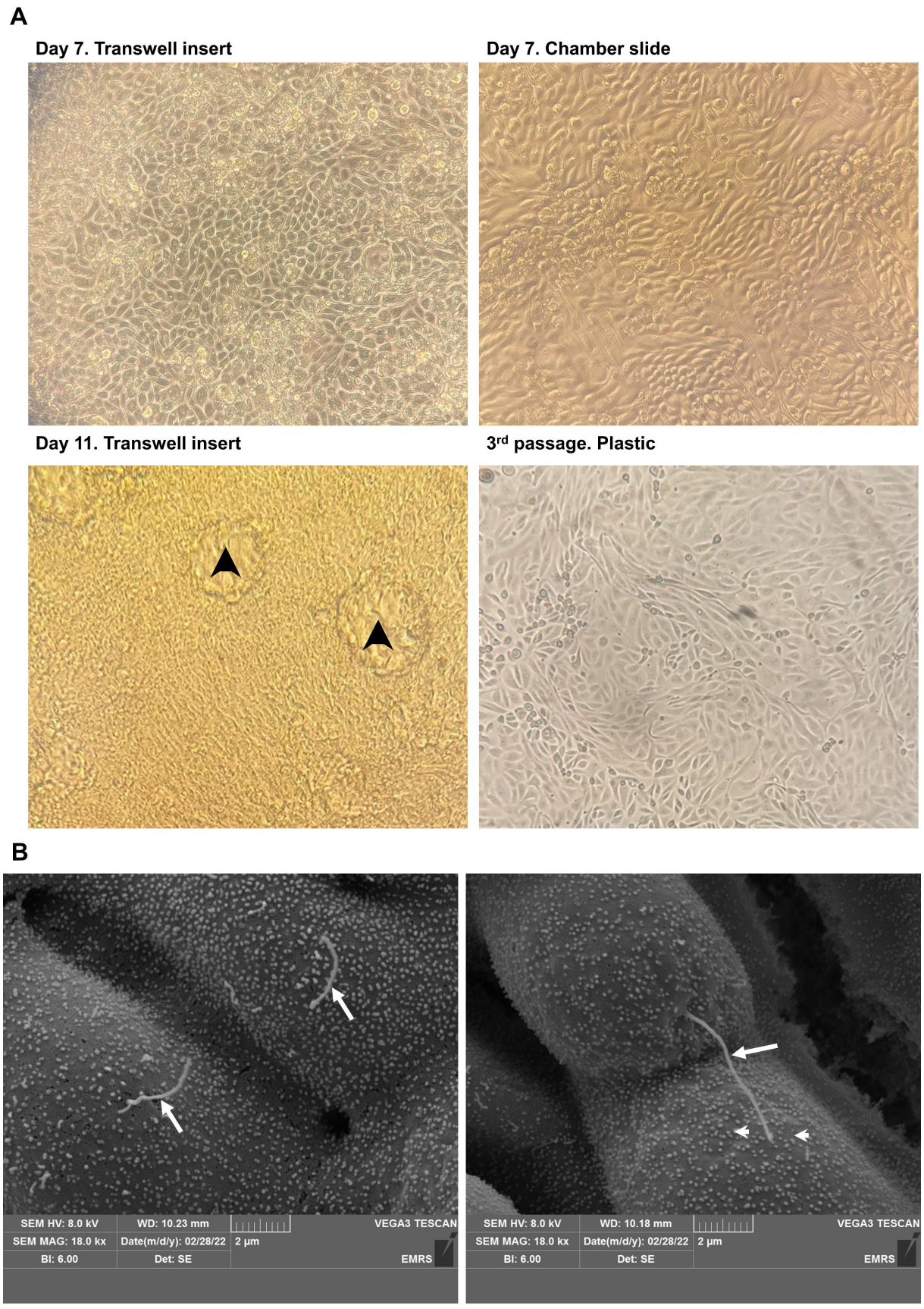

Figure 4-4 Light and electron microscopy characterisation of primary human proximal tubule epithelial cells (PTEC).

PTEC isolated from human kidneys declined for clinical transplantation. **A.** Light microscopy of live PTEC in media. Top row shows PTEC (from donor HMIR21-03) maintained in culture in transwell inserts or on chamber slides for 7 days without passage, imaged with X20 objective using phase contrast. Bottom left shows light microscopy with X10 objective of PTEC (from donor HMIR21-02) maintained without passage for 11 days on transwell inserts and demonstrating dome formation (arrow heads). Bottom right shows 3rd passage of PTEC (isolated from donor HMIR21-01), imaged with X20 objective. **B.** Scanning electron microscopy of isolated PTEC (from donor HMIR21-02) maintained in culture on transwell inserts for 10 days. Primary cilium (large arrow) and microvilli (arrowheads) are demonstrated

A panel of targets were validated on cell lines to characterise isolated PTEC. Although some markers were consistent between primary PTEC and the proximal tubule epithelial cell line HKC8, others had noticeable differences in the pattern of expression highlighting the limitations in using cell lines as an *in vitro* model. Cytokeratin-19 expression was restricted to epithelial cells (**Figure 4-5**,

Figure 4-6B) with expression not demonstrated in the studied fibroblast or endothelial cells (**Figure 4-5**). E-cadherin had a diffuse cytoplasmic pattern of expression in the HKC8 and a similar but less strong pattern of expression in fibroblast and endothelial cell lines (**Figure 4-5**). In contrast, the expected membrane pattern for E-cadherin was more evident in PTEC (

Figure 4-6B). TJP1 was expressed across epithelial, endothelial and fibroblast cells (**Figure 4-5**,

Figure 4-6) but had a distinctive cuboidal pattern only in epithelial cells where signal was strongest at the junction between cells for both primary cells and cell lines (**Figure 4-5**,

Figure 4-6). Signal associated with the water channel and proximal tubule marker aquaporin-1 was not convincing in cell lines (**Figure 4-5**) but was clearly evident in PTEC (
Figure 4-6), highlighting likely differences in the transport function of proximal tubule cell lines compared to primary cells.

Cytokeratin expression is used to validate commercially available PTEC (ATCC® PCS-400-010, PromoCell® C-12665, Lonza CC-2553) and diffuse expression of cytokeratin-19 was confirmed in each batch of isolated PTEC (
Figure 4-7).

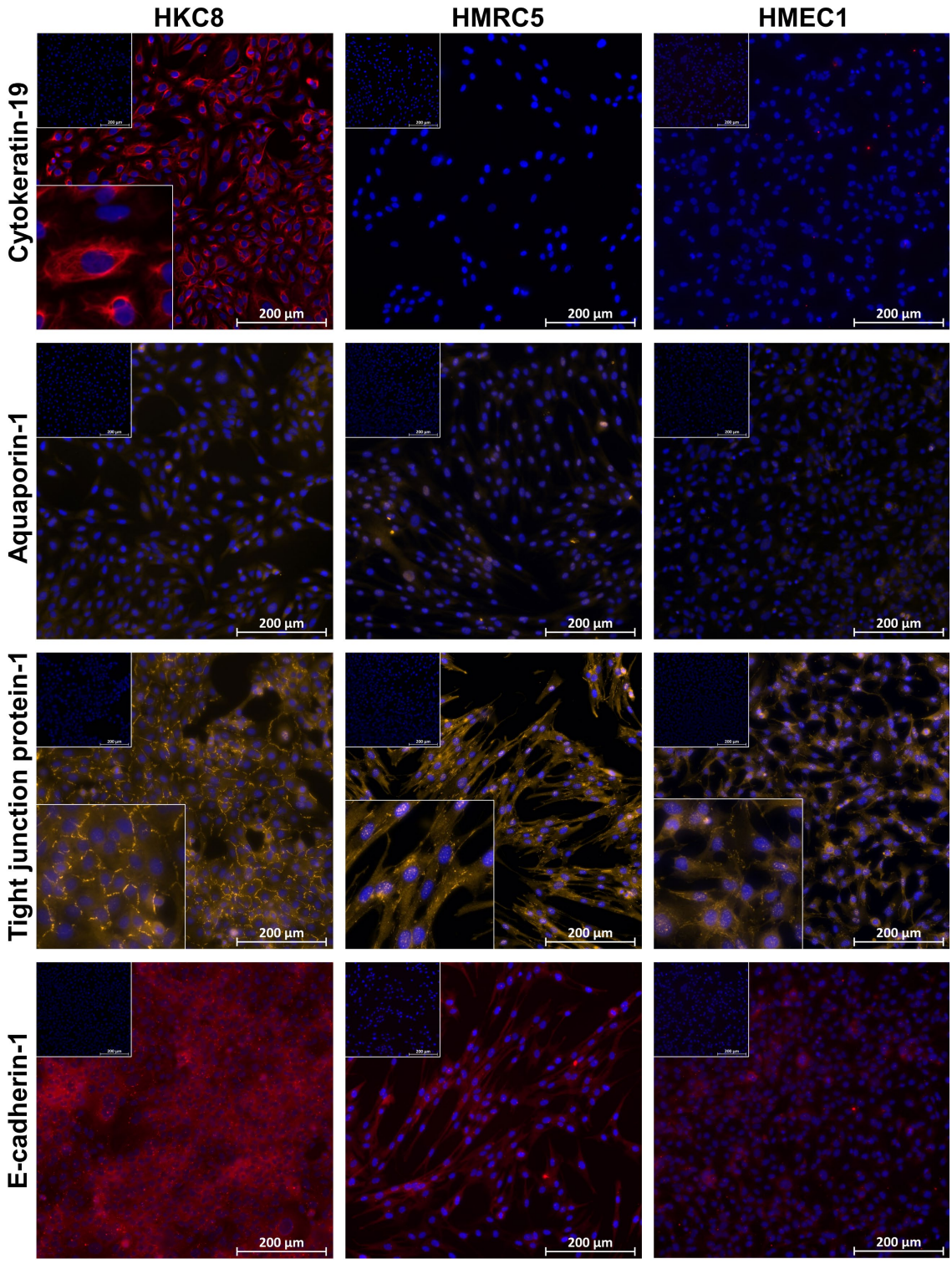

Figure 4-5 Widefield fluorescent microscopy of human proximal tubule (HKC8), fibroblast (HMRC5) and endothelial (HMEC1) cell lines to validate proximal tubule cell marker panel.
Signal associated with the target is shown in either red (Cytokeratin-19, E-cadherin) or yellow (Aquaporin-1, Tight junction protein 1). The no primary antibody image is shown in top left inset and the bottom left inset shows a magnified area of the positive image. Cells were fixed with methanol on chamber slides and nuclei counterstained with DAPI (blue). Images acquired with X20 objective on ZEISS Axio Imager

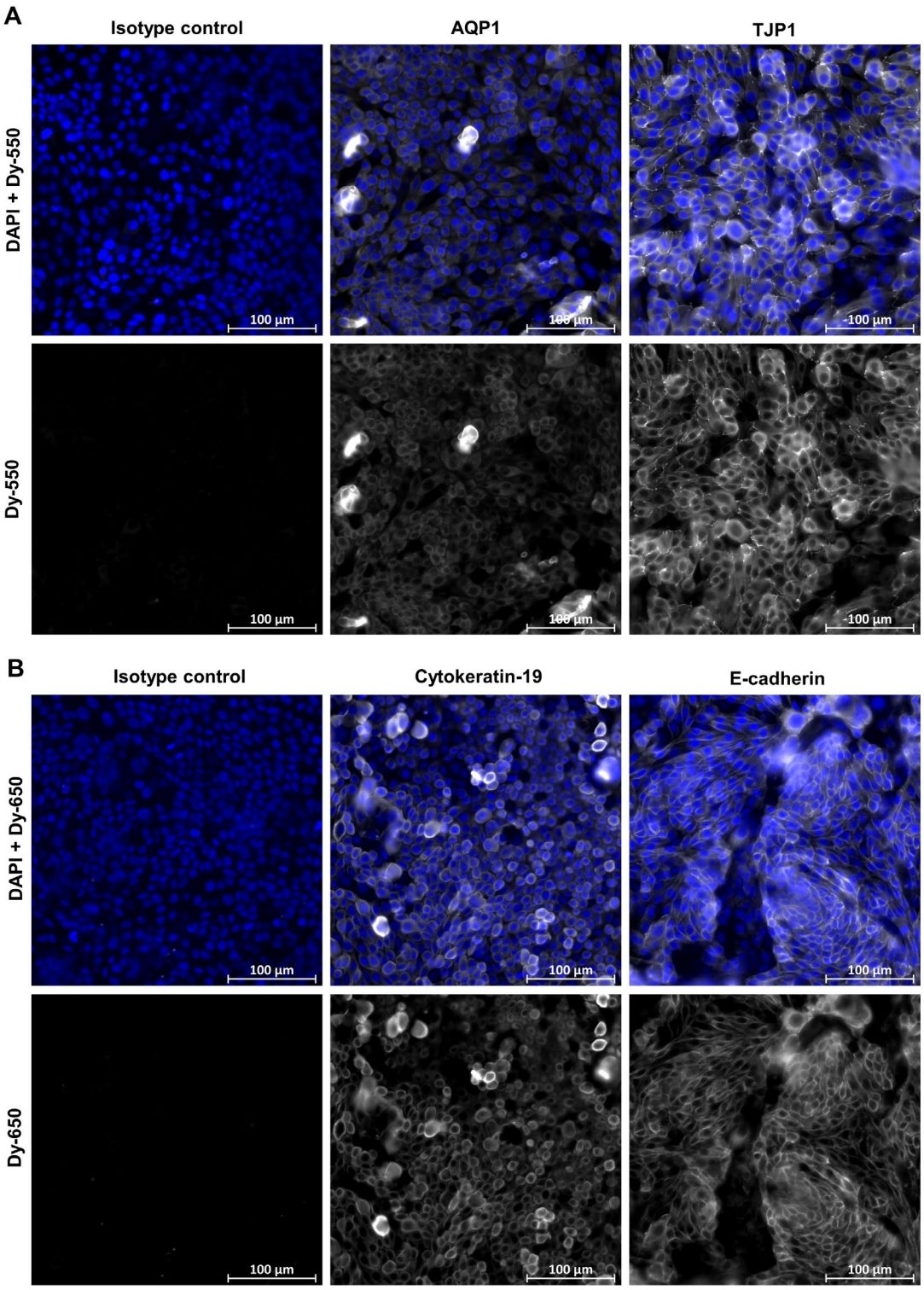

Figure 4-6 Characterisation of isolated primary human proximal tubule epithelial cells by immunofluorescence for epithelial and proximal tubule markers.

Cells maintained on transwell inserts. **A** shows aquaporin-1 (AQP1) and tight junction protein (TJP1) signal detected with dylight-550 (Dy-550; white) conjugated secondary antibody, relative to isotype control. **B** shows cytokeratin-19 and E-cadherin signal detected with dylight-650 (Dy-650; white) conjugated secondary antibody, relative to isotype control. Nuclei counterstained with DAPI (blue). Cells were PFA fixed and permeabilization with Triton-X. Imaged with wide field fluorescent microscopy with X40 objective. Representative images from cells isolated from donor HMIR21-04 (of three biological repeats) are displayed.

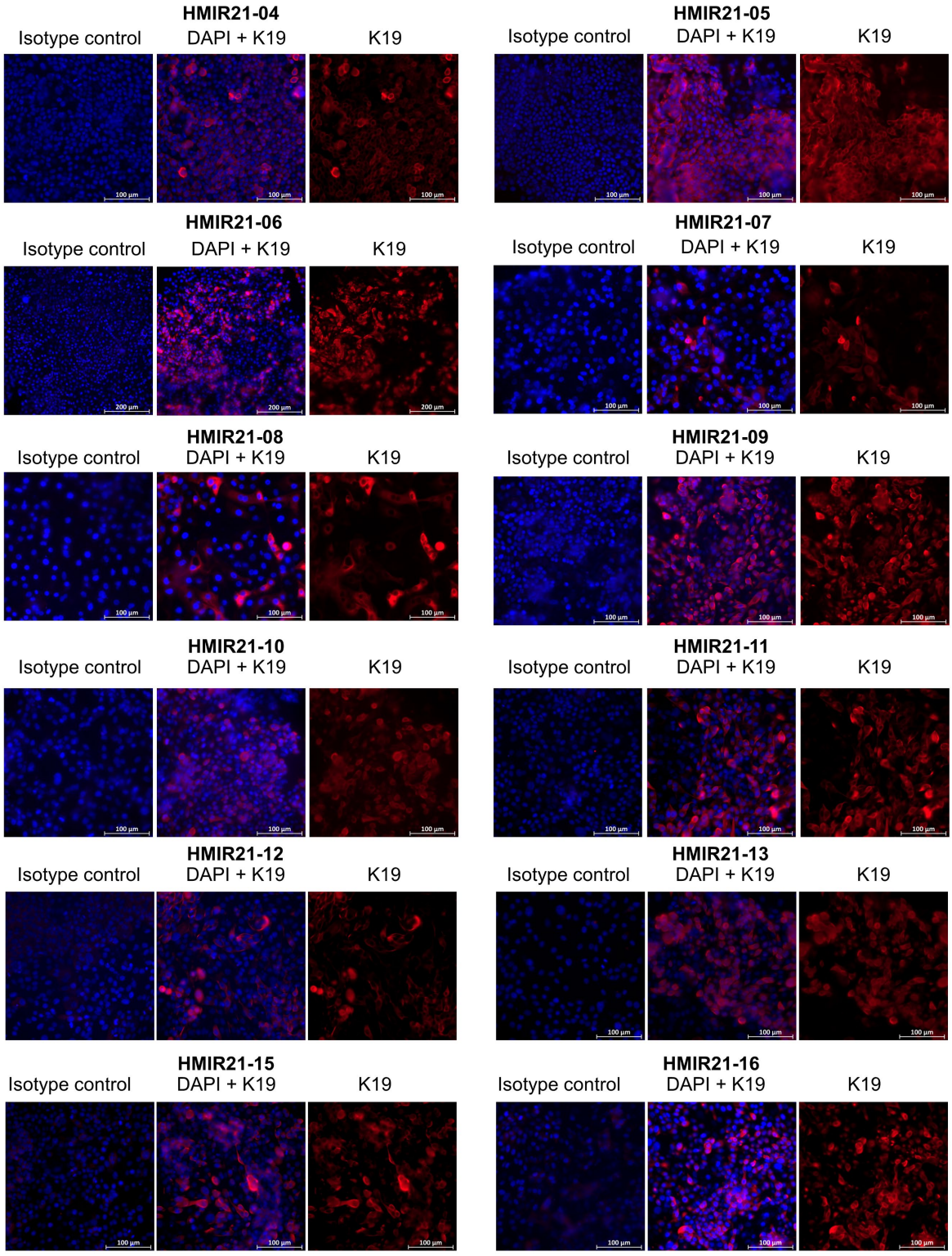

Figure 4-7 Confirmation of dominant epithelial origin of cell isolates generated from human kidney cortex.

Each batch of cells is indicated by the donor ID (HMIR21-) and each panel shows dual channel images for cells incubated with isotype control (left) and anti-cytokeratin-19 antibody (DAPI + K19). Cytokeratin-19 binding was detected with Dy650 conjugated secondary antibody (red) and this single channel image is shown for each “DAPI + K19” image. Nuclei countertained with DAPI (blue). Cells maintained on transwell inserts, PFA fixed and permeabilised with Triton-X. Widefield fluorescent microscopy images acquired with X40 objective on ZEISS Axio Imager other than for HMIR21-06 where X20 objective used

4.3.3 Contamination levels

Contamination of PTEC with endothelial and mesenchymal cells was confirmed to be low, at less than a combined 5% of isolated cells maintained in culture. This purity was achieved by only collecting cortex and separating cells by density with Percoll gradients.

Study ID	Day	CD31	PDGFRA	Total contamination
HMIR21-06	5	1.18%	0.00%	1.18%
HMIR21-07	8	2.17%	0.43%	2.60%
HMIR21-08	4	3.97%	0.00%	3.97%
HMIR21-09	6	1.10%	0.10%	1.20%
HMIR21-10	6	0.08%	0.00%	0.08%
HMIR21-11	6	0.38%	0.00%	0.38%
HMIR21-12	6	1.53%	0.00%	1.53%
HMIR21-13	6	0.77%	0.73%	1.50%
HMIR21-15	6	0.99%	0.00%	0.99%
HMIR21-16	6	0.21%	0.00%	0.21%
Mean ± SD		**1.24 ± 1.15%**	**0.13 ± 0.25%**	**1.36 ± 1.18%**

Table 4-6 Level of endothelial and mesenchymal cell contamination in primary human proximal tubule cell isolates generated from kidney cortex.
Contamination level determined by flow cytometry as the % of live single cells positive for endothelial (CD31) or mesenchymal (PDGFRA) cell marker. Cells were seeded on the day of isolation and maintained on transwell inserts. The number of days after isolation that cells were harvested for flow cytometry is indicated for each batch.

4.3.4 Inducing hypoxia

VEGF is secreted by PTEC in response to hypoxia[201] so to confirm that incubation in 1% oxygen for 24 hours was adequate to induce hypoxia in isolated PTEC secreted VEGF was measured in basolateral media. VEGF was secreted by cells maintained in normoxia and there was no clear increase demonstrated after incubation in 1% oxygen for 24 hours (**Figure 4-8**).

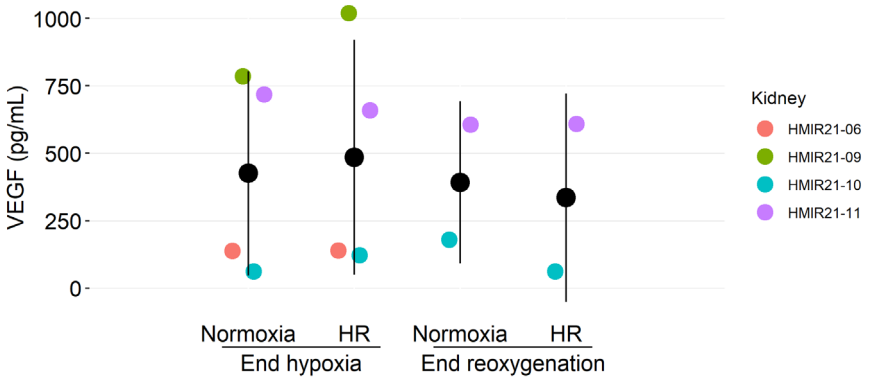

Figure 4-8 Basolateral vascular endothelial cell growth factor (VEGF) secretion.

VEGF concentration in the media of the basolateral compartment of primary human proximal tubule cells (PTEC) maintained on 12-well transwell inserts. PTEC were incubated in 1% oxygen to induce hypoxia on day 4 (HMIR21-10), 5 (HMIR21-06) or 7 (HMIR21-9 and 11) after isolation and seeding. Media was collected and changed at the end of hypoxia when cells were reoxygenated for 24 hours before further media collection. The timings for media changes and collection in normoxia samples matched those for cells exposed to hypoxia-reoxygenation (HR). All cells received 40 nM scrambled control antimiR treatment from 24 hours before hypoxia or matched timepoint. There was no difference in VEGF concentrations between normoxia and HR treated cells at either time point (paired t test: end hypoxia *P*=.417, end reoxygenation *P*=.519)

Another method used to confirm hypoxia was immunofluorescence to assess for HIF1α stabilisation leading to nuclear translocation. In normoxia, nuclear HIF1α signal was lower than that in the cytoplasm. After 4 hours incubation in 1% oxygen nuclear signal was higher than cytoplasmic indicating nuclear translocation of HIF1α and so confirming that the cells were in a hypoxic state (**Figure 4-9**). Quantification of nuclear HIF1α signal relative to cytoplasmic signal confirmed an effect from time in hypoxic conditions (**Figure 4-9A**).

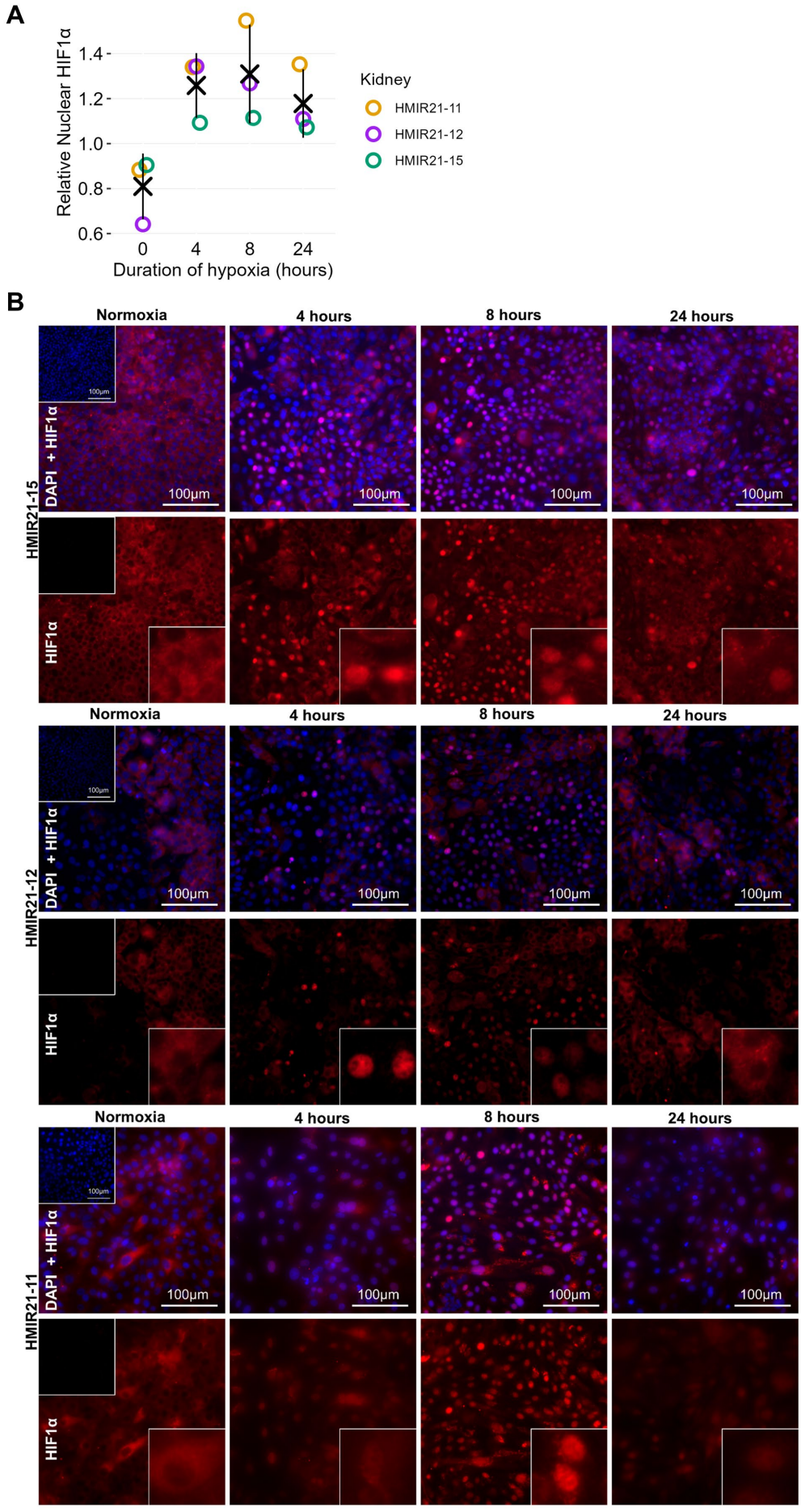

Figure 4-9 Confirmation of HIF1α stabilisation.

Immunofluorescence to show HIF1α stabilisation leading to nuclear translocation in primary human proximal tubule epithelial cells maintained on transwell inserts and incubated in 1% oxygen for up to 24 hours or maintained in normal conditions (normoxia, 0 hr). Intensity of fluorescent signal associated with nuclear (DAPI positive) HIF1α is shown in **A** relative to the cytoplasmic (DAPI negative) signal. Coloured circles give the mean of 6 images from each biological repeat with mean and standard deviation of three biological repeats overlaid in black. Time in hypoxia had a significant effect on nuclear HIF1α signal (repeated measured analysis of variance *P*=.012). Representative images from each biological repeat (HMIR21-11, HMIR21-12, HMIR21-15) are shown for each time point in **B** with the no primary inset top left within normoxia. Dual channel images (DAPI + HIF1α) show both nuclear counterstaining with DAPI (blue) and HIF1α associated signal (red). Bottom row in each panel shows single channel image for HIF1α associated fluorescence with bottom right inset giving magnified area. Cells were PFA fixed and permeabilised with Triton X. Widefield fluorescent microscopy image acquisition was standardised and blinded to HIF1α associated signal. Images were acquired with X40 objective on ZEISS Axio Imager

4.3.5 miR-21 expression

miR-21 is expressed in the human proximal tubule[100] and high baseline levels of expression were confirmed in isolated PTEC with mean ± standard deviation (n=4) C_T values for miR-21 of 23.75 ± 1.97. This was similar to housekeeper expression with C_T values for RNU48 of 25.78 ± 0.20. AntimiR-21 treatment did not significantly affect miR-21 expression levels, nor did hypoxia-reoxygenation or treatment with the hypoxia mimic cobalt chloride (

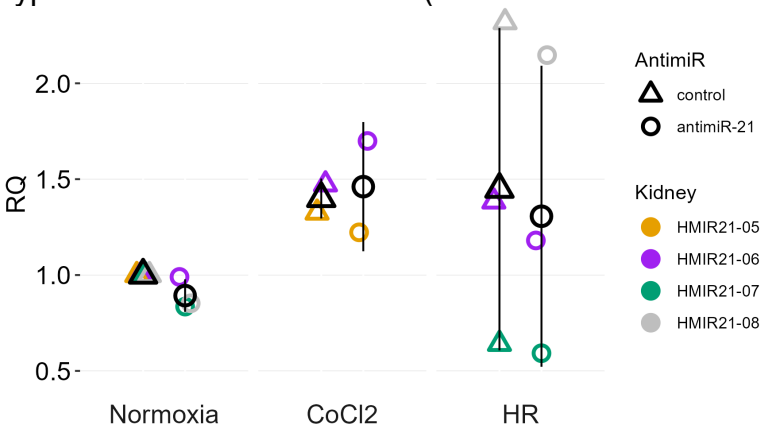

Figure 4-10).

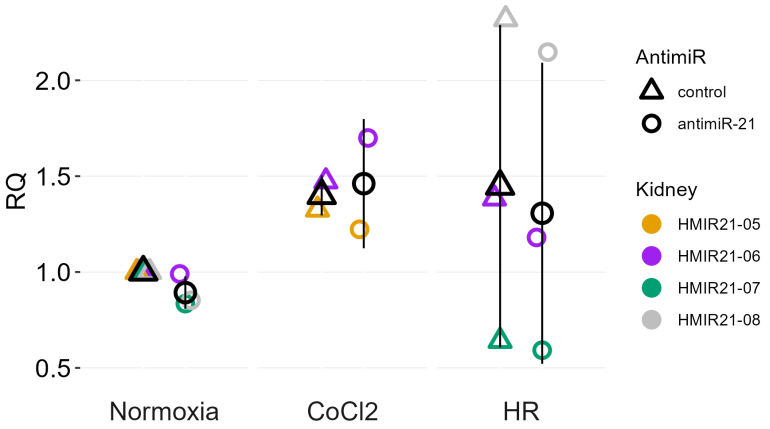

Figure 4-10 miR-21 expression in primary human proximal tubule epithelial cells (PTEC).
Expression measured with reverse transcription polymerase chain reaction and normalised to RNU48. Cells maintained in normoxia and treated with control (scrambled) antimiR were used as the reference for relative quantification (RQ) within each repeat. Mean ± standard deviation RQ values are displayed in black with biological repeats indicated by colours. Cobalt chloride (CoCl2) treatment combines the results of one repeat exposed to 100 μM $CoCl_2$ and a second exposed to 200 μM $CoCl_2$, both pretreated with 18 hours of control antimiR treatment. PTEC exposed to 24 hours of hypoxia (1% oxygen) followed by 24 hours of reoxygenation (HR) received antimiR treatment (control or antimiR-21) at the point of reoxygenation. There was no difference in miR-21 expression by conditions or by antimiR when assessed by repeated measures analysis of variance (*P*>.05)

4.3.6 antimiR-21 toxicity assessment

An apoptosis assay was performed to examine the impact of antimiR-21 treatment on cell death. It was noted that the baseline level of late apoptosis in cells maintained in normoxic conditions was affected by the number of days that PTEC had been maintained for in culture (**Figure 4-11A**). In PTEC harvested for apoptosis assay 6 days after isolation there was more late apoptosis than in those harvested 8-9 days after isolation (**Figure 4-11A**; adjusted *P*=.015, t test with Benjamini-Hochberg adjustment for multiple comparison). A similar trend was seen for cells exposed to hypoxia-reoxygenation which this was not statistically significant (**Figure 4-11A**).

AntimiR-21 treatment at either 10 nM or 40 nM did not affect the viability of cells maintained in normoxia, regardless of the day of harvest (**Figure 4-11B, Table 4-7A**).

When cells were incubated in hypoxia on day 7 or 8 after isolation, hypoxia-reoxygenation did not reduce cell viability compared to cells maintained in normoxia (**Table 4-7B**, **Figure 4-11C**) with 92-93% of cells classified as healthy in both conditions with scrambled control antimiR treatment. There was also no significant effect from antimiR-21 treatment on cell viability in hypoxia-reoxygenation at this timepoint with >86% classified as healthy (**Table 4-7B, Figure 4-11C**).

For cells that were incubated in hypoxia 4 days after isolation, the mean (n=3) percent of healthy cells was 65% with control antimiR treatment, compared to 80% for normoxic controls (*P*=.076, paired t test; **Figure 4-11**C, **Table 4-7**B). AntimiR-21 treatment before hypoxia significantly reduced the proportion of healthy cells after hypoxia-reoxygenation at this early timepoint when compared to control antimiR treatment (*P*=.014, t test with Benjamini-Hochberg adjustment for multiple comparison). This effect was not seen when antimiR-21 treatment was given at reoxygenation (**Table 4-7B**, **Figure 4-11C**). RM-ANOVA also revealed a significant effect of treatment on the proportion of cells classified as late apoptotic, however there was no significant difference between antimiR-21 and control antimiR treatments during hypoxia-reoxygenation by paired t test.

The trend for more cell death in both normoxia and hypoxia-reoxygenation for cells harvested earlier after isolation was confirmed within batches of cells, suggesting this was an effect from the cell state rather than a coincidence associated with biological variability (**Figure 4-11D**).

A. Impact of timing after cell isolation

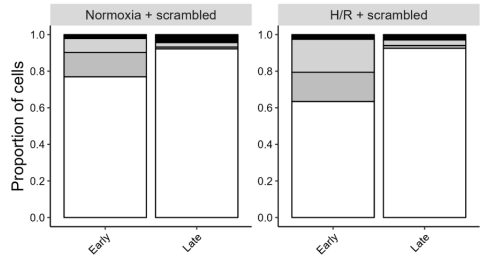

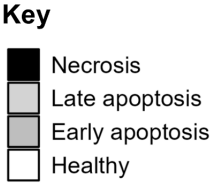

B. AntimiR-21 in normoxia

Early: antimiR treatment on day 3

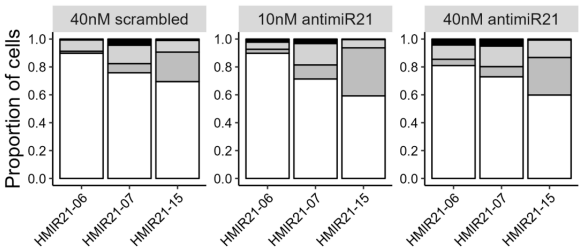

Late: antimiR treatment on day 8

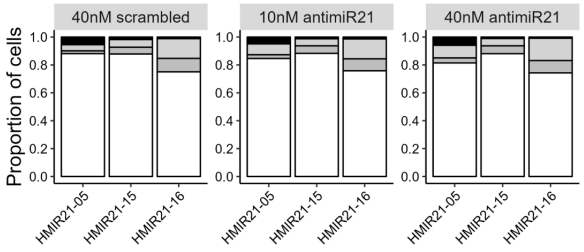

C. AntimiR-21 in hypoxia reoxygenation

Early: hypoxia on day 4

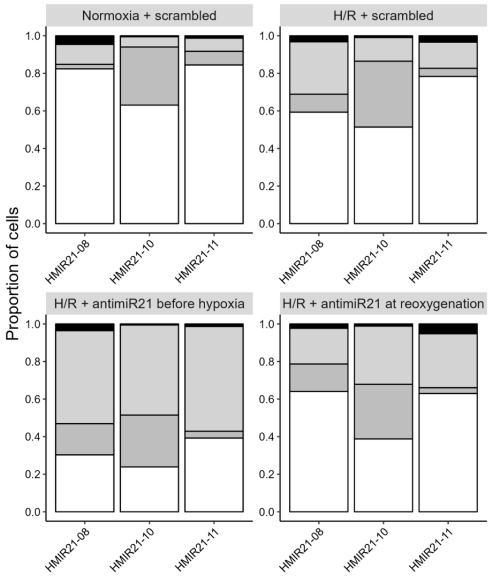

Late: hypoxia on day 7 or day 8

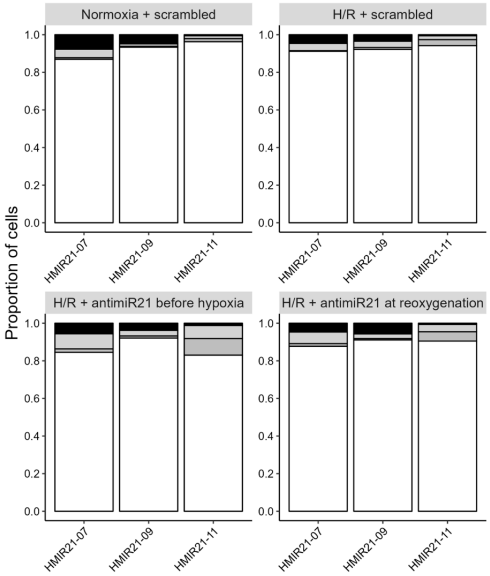

D. Impact of timing on antimiR response within biological repeat

Normoxia (HMIR21-15)

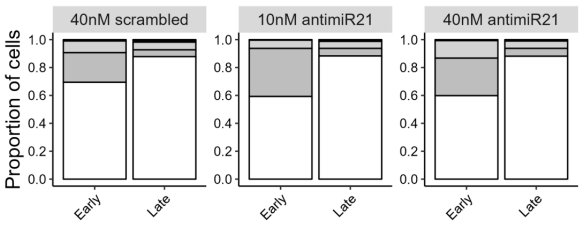

Hypoxia reoxygenation (HMIR21-11)

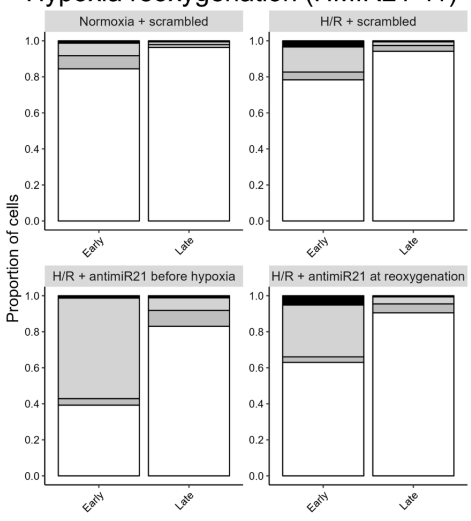

Figure 4-11 Cell death in response to hypoxia-reoxygenation and antimiR treatment.
Apoptosis assay results from human primary proximal tubule epithelial cells maintained in culture on transwell inserts and exposed to hypoxia-reoxygenation (H/R) or normoxia and treated with either antimiR-21 or scrambled (control) antimiR. Adherent and detached cells in the apical compartment were included for analysis with the graphs showing the proportion of single cells in each cell state, as detailed in the key. Cells in normoxia experiments had 24 hours of antimiR treatment before harvesting. Cells exposed to H/R were incubated in 1% oxygen for 24 hours with scrambled antimiR treatment given 24 hours before hypoxia whereas antimiR-21 treatment was given either before hypoxia or at the point of reoxygenation. Reoxygenation continued for 24 hours before harvesting cells and media was changed at reoxygenation regardless of antimiR treatment. The normoxia samples within these experiments had media changes and antimiR treatments at timepoints to match H/R with scrambled antimiR. **A** shows the mean (n=3) proportion of cells in each cell state after maintenance in normoxia or exposure to H/R by whether the cells were harvested early (day 6) or late (day 9 or 10) in the period after cell isolation. Within the cells maintained in normoxia the early timepoint was associated with more late apoptosis (*Padj*=.015, t test). The data for each repeat is shown individually in **C**. **B** shows the effect of antimiR-21 treatment on cell death in normoxia, by whether cells were treated early or late in the period after cell isolation. Each bar indicates a biological repeat labelled by the donor study ID. There was no difference by treatment for either timepoint (repeated measures analysis of variance, RM-ANOVA). **C** shows the effect of antimiR-21 treatment on cell death in cells exposed to H/R, by whether cells were treated early or late in the period after cell isolation. Each bar indicates a biological repeat. At the early timepoint, treatment affected the proportion of cells that were healthy and undergoing late apoptosis (*Padj*=.001 and *Padj*=.006 respectively, RM-ANOVA). **D** shows the impact that timing in the period after cell isolation (early vs late) has on cell death in cells from the same biological repeat either exposed to normoxia or H/R and antimiR treatments. This data also features in **B** and **C** where the days of treatment are detailed. *P* values were adjusted for multiple comparisons with Benjamini-Hochberg method (*Padj*)

A. Effect of antimiR-21 on cell death in normoxia

Timing: AntimiR treatment early after cell isolation (day 3)					
AntimiR:	**40 nM Scrambled**	**10 nM AntimiR-21**	**40 nM AntimiR-21**	**RM-ANOVA**	
Cell state	**Mean ± SD**	**Mean ± SD**	**Mean ± SD**	***P***	***P.adj***
Necrosis	2.06 ± 2.09%	1.99 ± 1.43%	3.39 ± 2.32%	.316	.316
Late apoptosis	9.87 ± 2.88%	8.76 ± 5.68%	12.47 ± 2.25%	.183	.261
Early apoptosis	9.71 ± 10.27%	15.79 ± 16.52%	12.91 ± 12.20%	.196	.261
Healthy	78.33 ± 10.43%	73.43 ± 15.41%	71.23 ± 10.70%	.143	.261
Timing: AntimiR treatment late after cell isolation (day 8)					
AntimiR:	**40 nM Scrambled**	**10 nM AntimiR-21**	**40 nM AntimiR-21**	**RM-ANOVA**	
Cell state	**Mean ± SD**	**Mean ± SD**	**Mean ± SD**	***P***	***P.adj***
Necrosis	2.91 ± 2.29%	2.61 ± 2.03%	2.70 ± 2.83%	.744	.744
Late apoptosis	8.76 ± 6.64%	9.88 ± 6.15%	11.09 ± 7.11%	.229	.744
Early apoptosis	6.01 ± 4.72%	6.06 ± 3.75%	6.58 ± 3.54%	.552	.744
Healthy	87.60 ± 0.62%	87.33 ± 2.40%	85.97 ± 3.96%	.667	.744

B. Effect of antimiR-21 on cell death in hypoxia-reoxygenation

Timing: hypoxia early after cell isolation (day 4)						
Condition:	**Normoxia**	**Hypoxia-reoxygenation**			**RM-ANOVA**	
AntimiR:	**Scrambled**	**Scrambled**	**AntimiR-21 before hypoxia**	**AntimiR-21 at reoxygenation**		
Cell state	**Mean ± SD**	**Mean ± SD**	**Mean ± SD**	**Mean ± SD**	***P***	***P.adj***
Necrosis	2.20 ± 2.13%	2.62 ± 1.46%	1.97 ± 1.53%	3.06 ± 2.37%	.803	.908
Late apoptosis	7.93 ± 2.58%	18.50 ± 8.23%	56.30 ± 13.10%	27.13 ± 7.05%	.003	**.006**
Early apoptosis	13.79 ± 15.08%	16.45 ± 16.33%	16.28 ± 11.48%	15.69 ± 12.90%	.908	.908
Healthy	79.70 ± 15.43%	65.07 ± 17.29%	34.80 ± 13.72%*	57.20 ± 16.11%	<.001	**.001**
Timing: hypoxia late after cell isolation (day 7 or 8)						
Condition:	**Normoxia**	**Hypoxia-reoxygenation**			**RM-ANOVA**	
AntimiR:	**Scrambled**	**Scrambled**	**AntimiR-21 before hypoxia**	**AntimiR-21 at reoxygenation**		
Cell state	**Mean ± SD**	**Mean ± SD**	**Mean ± SD**	**Mean ± SD**	***P***	***P.adj***
Necrosis	4.40 ± 3.59%	2.90 ± 2.07%	3.56 ± 2.23%	3.70 ± 2.66%	.426	.426
Late apoptosis	2.43 ± 1.79%	3.11 ± 0.97%	5.98 ± 2.66%	4.17 ± 1.87%	.052	.208
Early apoptosis	0.99 ± 0.59%	1.48 ± 1.52%	3.93 ± 4.25%	2.37 ± 2.27%	.222	.296
Healthy	92.17 ± 4.80%	92.53 ± 1.53%	86.53 ± 4.88%	89.77 ± 1.81%	.175	.296

Table 4-7 Cell death in response to hypoxia-reoxygenation and antimiR treatment.

Apoptosis assay results from primary human proximal tubule epithelial cells to explore the effect of antimiR-21 treatment in normoxia and hypoxia-reoxygenation (HR) at different timepoints after cell isolation. Adherent and detached cells in the apical compartment were included for analysis. **A**. Cells maintained in normoxia with 24 hours of antimiR treatment before harvesting. **B.** Cells exposed to HR were incubated in 1% oxygen for 24 hours with 40 nM scrambled control antimiR treatment given 24 hours before hypoxia whereas 40 nM antimiR-21 treatment was given either before hypoxia or at the point of reoxygenation. Reoxygenation continued for 24 hours before harvesting cells and media was changed at reoxygenation regardless of antimiR treatment. The normoxia controls in **B** had media changed and antimiR treatment at timepoints to match HR samples treated with scrambled control antimiR. n=3 for both A and B. In **A** and **B,** cell states are defined as necrosis (7AAD positive, Annexin V negative), late apoptosis (double positive), early apoptosis (Annexin V positive, 7AAD negative) and healthy (double negative) and the mean ± standard deviation (SD) for the percentage of cells within each state is given. The effect of treatment on the % in each state was assessed by repeated measures analysis of variance (RM-ANOVA). For cell states with adjusted *P* values (*P.adj)*<.05 (bold) within **B**, paired t test compared treatments to the reference of HR with control antimiR, * *P.adj* <.05. Benjamini-Hochberg method adjusted RM-ANOVA and t test results for multiple comparisons.

4.3.7 Selected miR-21 targets are not consistently modulated by antimiR-21

miR-21 targets that have been modulated in the context of ischaemia-reperfusion include *PDCD4*, *PPARA*, *RECK* and *SMAD7*.[79,88,90,99,108-110,112,149] The ability of antimiR-21 treatment to increase expression of these targets in normoxia and in the context of hypoxia-reoxygenation or cobalt chloride treatment was explored in isolated PTEC. There were no consistent change in these targets at the RNA (*PDCD4*, *PPARA*, *RECK*, **Figure 4-12C**) or protein (*PDCD4* and *SMAD7*, **Figure 4-12A-B, D**)) level with these treatments.

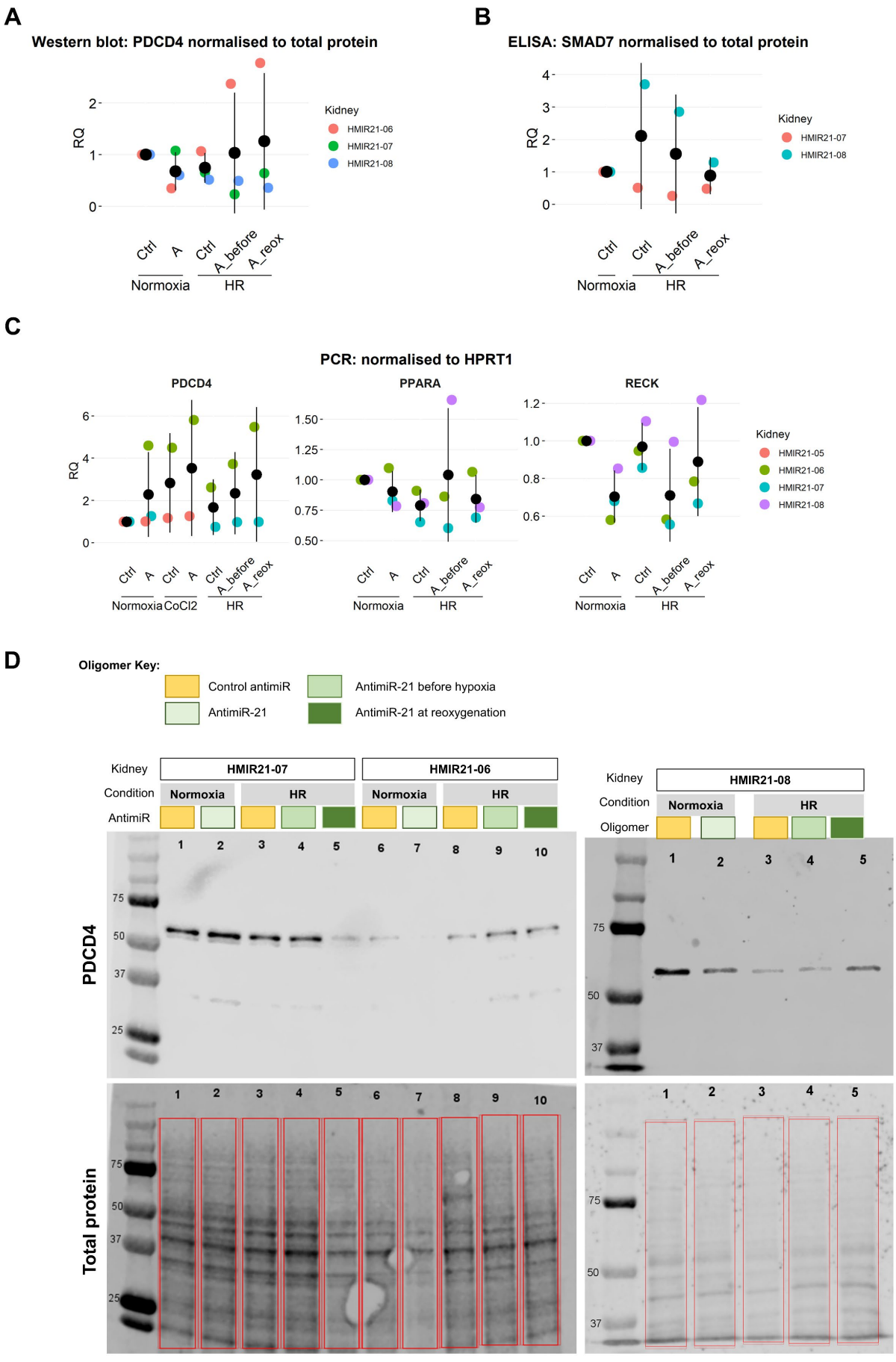

Figure 4-12 Assessment of miR-21 target modulation by antimiR-21.

Modulation of known miR-21 target (PDCD4, RECK, PPARA, SMAD7) expression by 40 nM antimiR-21 treatment was assessed in primary human proximal tubule epithelial cells using western blot (**A, D**), ELISA (**B**) or reverse transcription polymerase chain reaction (RT-PCR; **C**). PTEC were maintained in normoxia or exposed to the hypoxia mimic cobalt chloride (CoCl2) or hypoxia-reoxygenation (HR). PTEC exposed to HR were incubated in 1% oxygen for 24 hours followed by media change and return to normal conditions for 24 hours of reoxygenation. AntimiR treatment was added 24 hours before hypoxia for scrambled (Ctrl) antimiR and selected antimiR-21 treated cells (A_before). Alternatively, cells received antimiR-21 treatment with the media change at reoxygenation (A_reox). Cells maintained in normoxia had 48 hours of antimiR treatment to end in-line with the end-hypoxia timepoint of cells exposed to H/R. Cobalt chloride treatment (100 μM for HMIR21-05 and 200 μM for HMIR21-06) was started 24 hours into antimiR treatment with cells collected 24 hours later. Target protein expression was normalised to total protein for western blot (**A**, **D**) and ELISA (**B**) results using total protein stain and BCA assay respectively. Target mRNA expression was normalised to HPRT1 (**C**). Cells maintained in normoxia and treated with control (scrambled) antimiR were used as the reference for relative quantification (RQ) within each repeat. Coloured dots give the RQ values for each biological repeat (PTEC isolated from different kidney donors) with mean ± standard deviation of these overlaid in black. **D** shows western blot membrane with band for PDCD4 at 60 kDa and the areas quantified on total protein stain for normalisation below

4.4 Discussion

Cell lines are recognised to have limitations for modelling human disease and processes *in vitro*. Of particular concern when studying the effects of antimiRs, are the reduced transport function of cell lines compared to primary human PTEC.[152] In this chapter I have demonstrated the ability to isolate primary human PTEC from human kidneys declined for transplant, and their relevance as an *in vitro* model to study the effect of antimiR-21 in IRI.

The ability to maintain the epithelial cell phenotype in primary PTEC was confirmed by light and electron microscopy, with persisting cuboidal pattern and presence of microvilli (**Figure 4-4**). The cuboidal pattern was dependent on culture surface and passage, being lost when cells were passaged or if cells were maintained on a surface that did not encourage polarisation, such as a glass (**Figure 4-4**). The use of freshly isolated PTEC therefore appears to be advantageous over commercially available alternatives, which are commonly sold at second passage (ATCC® PCS-400-010, PromoCell® C-12665) and so may have lost some of their proximal tubule epithelium phenotype.

Polarisation of PTEC and the barrier function of confluent monolayers that developed was not directly assessed. However, E-cadherin expression appeared to be restricted to the periphery of the cells on immunofluorescence, in keeping with its involvement in barrier function (

Figure 4-6). This was in contrast to the homogenous pattern in the HKC-8 cell line (**Figure 4-5**). Lower E-cadherin expression in the HK-2 cell line is thought to contribute to the differing barrier function, as assessed by transepithelial electrical resistance, between HK-2 and primary cells.[163]

AQP1 expression was more convincing in the primary cells than HKC-8 (**Figure 4-5**, **Figure 4-6**). As a key marker of the proximal tubule, this difference again highlights the limitations of using cell lines.[165] This finding is in keeping with less striking AQP1 expression previously noted in HK-2 cells when compared to primary cells.[202]

Isolating epithelium from the proximal tubule involved a combined approach of firstly only using cortex tissue, to limit the presence of other epithelia and secondly separating cells based on density. Coupled with the general abundance of proximal tubule epithelium, this was successful in isolated proximal tubule epithelial cells as confirmed by immunofluorescence characterisation (
Figure 4-6,
Figure 4-7). Importantly, contamination with other cell types was kept low with less than 5% of cells being either mesenchymal or endothelial in origin (**Table 4-6**). Given the isolation technique, some epithelial cells may have originated from the distal convoluted tubule.[165] Contamination with these cells was not directly assessed but is expected to be low given the lower abundance of these cells and the widespread AQP1 positivity of isolates (
Figure 4-6).[155,165]

Next, I have confirmed that incubation in 1% oxygen can stabilise HIF1α to mimic the hypoxia of ischaemia-reperfusion (**Figure 4-9**). There is a concern that conditions considered “normoxic” *in vitro* are likely to be lower than physiological due to the reliance on dissolved oxygen and relative rates at which oxygen is consumed and able to diffuse through the media.[191,193] Despite these concerns, HIF1α was largely cytoplasmic in normoxic conditions indicating adequate PHD activity to prevent translocation to the nucleus.[33] These finding demonstrate a clear difference in the oxygenation of cells incubated in 1% oxygen compared to 18.6% oxygen, thereby validating the experimental model.

Although VEGF is also considered a downstream marker of hypoxia, the response observed in primary PTEC was inconsistent with no clear change in VEGF secretion after hypoxia (**Figure 4-8**).[33,54,203,204] This differs from other studies of primary human PTEC, in which an approximately 4-fold increase in VEGF secretion has been demonstrated after incubation in 3% oxygen for 72 hours or 1% oxygen for 24 hours.[205,206] It is difficult to compare directly with these studies, but key culture conditions may have contributed to differences in results. Depth of media and

seeding density would influence the rate and extent of oxygen deprivation with volume affecting the concentration. Perhaps more importantly, the source tissue and passage number of cells used could affect their response to hypoxia. Of note, the PTEC used in my work were isolated from human kidneys declined for transplant, with a minimum CIT of 8.5 hours and cells were only used at first passage. The ischaemic period of nephrectomy kidneys used by El Awad et al.[205] was likely considerably shorter and both El Awad et al.[205] and Nakamura et al.[206] used primary cells after at least one passage which, as already discussed, could alter their phenotype (**Figure 4-4**).

Ultimately, HIF1α nuclear translocation is a more useful method to confirm rapid induction of hypoxia as, unlike VEGF secretion, it does not rely on changes at a transcriptional level. This is in keeping with the increased nuclear translocation of HIF1α from 4 hours of incubation in 1% oxygen detected in my work (**Figure 4-9**). In contrast, El Awad et al.[206] found a rise in VEGF secretion was not detected until cells had been incubated in 1% oxygen for at least 24 hours.

To be a suitable model to explore the effects of antimiR-21 treatment, PTEC must express miR-21. miR-21 expression was confirmed at high levels in isolated PTEC, with threshold cycle values similar to that for the housekeeper. The literature supports an increase in miR-21 levels in kidney ischaemia,[90,91] but I did not find a significant upregulation with either hypoxia-reoxygenation or cobalt chloride treatment in PTEC. The fold-change in miR-21 expression with hypoxia or mimics *in vitro* is generally low with a less than 2-fold increase, and in some cases no change in expression is detected.[88,90,99] If indeed present, the difficulty detecting an increase in expression may relate in part to high baseline levels requiring a large amount of miR to be produced to double expression.

AntimiRs can prevent the action of miRs without targeting them for degradation, by preventing binding to target mRNA sequences.[72] Therefore, a change in miR-21 expression levels is not a requirement for downstream effects to be seen. Indeed, although there was no difference in miR-21 expression with antimiR-21 treatment, results from apoptosis assay indicate an adequate dose was given to have a biological effect.

I could not demonstrate consistent modulation of selected miR-21 targets *PDCD4*, *PPARA*, *RECK* and *SMAD7*, identified from work in rodent models and cell

lines.[79,88,90,99,108-110,112,149] Modulation of miR targets has been shown to be cell-type specific and it is feasible that targets will also vary between species.[207] It is therefore essential that *in vitro* models are as relevant to the disease process as possible. My findings also support the importance of incorporating biological variability into models to determine consistent antimiR effects, as well as the role that global transcriptomic and proteomic approaches could play in identifying these.

Time in culture after isolation was found to be an important factor in the level of cell death detected in primary PTEC by apoptosis assay, with higher levels of cell death earlier after isolation (**Figure 4-11**, **Table 4-7**). Time after isolation appears to influence the response to both antimiR-21 treatment and the stress from hypoxia-reoxygenation and may relate to a more proliferative state of cells at an earlier stage. The contact between confluent cells is thought to reduce proliferation,[208] which has been associated with lower expression of miR-21 in tubular epithelial cells.[90,149] The response to other biological stimuli, such as TGFβ, varies with cell confluency *in vitro*, so this factor may also be key in the response to hypoxia-reoxygenation and antimiR-21 treatment.[208] Variation of miR-21 expression with cell confluency is not something that I assessed.

In keeping with mouse work showing no change in gene expression in the healthy kidneys lacking miR-21,[88] antimiR-21 treatment had no impact on cell death in PTEC maintained in normoxia (**Figure 4-11B**, **Table 4-7A**). The reduction in healthy cells observed with antimiR-21 treatment in hypoxia-reoxygenation was restricted to the early timepoint and only reached significance when antimiR-21 treatment was started before hypoxia (**Figure 4-11C**, **Table 4-7B**). Given the variable effect of antimiR-21 on cell death noted in the literature and in my work, there is likely a complex interaction between the injury state, proliferative activity and antimiR treatment. For this model, it seems important to allow the PTEC to stabilise and become confluent before exposure to hypoxia-reoxygenation. Arguably, this will be more akin to the single period of ischaemia before transplantation than two periods of hypoxia only a few days apart would be.

The work in this chapter has revealed important parameters when using isolated human PTEC to model ischaemia-reperfusion and demonstrated a low dose of 40 nM antimiR-21 is adequate to produce a biological response in cells. Further assessment of the mechanism of antimiR uptake into these cells and the downstream gene expression changes will be explored in subsequent chapters.

Chapter 5. AntimiR uptake by human proximal tubule epithelium is predominantly by macropinocytosis

5.1 Introduction

One of the challenges in using antimiR therapies is ensuring effective delivery to the intended target cells.[209,210] Fortunately, the kidney, along with the liver, is one of the easiest organs to target with systemic administration of oligonucleotides.[210] There are several studies in mice in which naked antimiR has been delivered to the kidney by systemic administration, without the need for a particular carrier molecule.[104,211] Chemical modifications have improved resistance of antimiRs to nucleases and the affinity of binding to target sequences.[72,87,209] Additionally, the phosphorothioate backbone of the antimiR is thought to enable naked uptake, referred to as "gymnosis".[212-214]

As oligonucleotides are smaller than 6 nm, they are freely filtered from the blood in the glomerulus and pass through to the tubular lumen.[210,211] The proximal tubule epithelium is responsible for reabsorbing much of the glomerular filtrate so unsurprisingly is the main site of antimiR uptake in the kidney.[88,97,104,215-217] The proximal tubule has been shown to be the main site of antimiR uptake in human kidneys using an ex vivo perfusion model, with uptake occurring to a lesser extent in the cells of the glomerulus and blood vessel walls.[97] The cells within the kidney that take up antimiR may vary with the disease state. Gomez et al.[104] showed that in mice with an early Alport nephropathy phenotype there was antimiR-21 uptake in podocytes and mesangial cells, which was not seen in healthy controls.[88]

AntimiR uptake into the proximal tubule epithelium is an active endocytic process as it is does not occur at 4^{o}C and fluorescently labelled antimiR colocalises with markers of the early and late endosome.[97] The importance of active transport is consistent with data from HeLa cells where both cooling and energy depletion prevented nucleic acid uptake.[218] However, endocytic transport encompasses a variety of mechanisms for cellular uptake and the mechanism of oligonucleotide uptake by PTEC is unknown.[219-221]

5.1.1 Endocytic pathways

Endocytic transport can be divided into those that depend on the GTPase dynamin for vesicle formation and those that do not.[219-221] Dynamin dependent mechanisms are those that are receptor-mediated.[220] This includes clathrin-mediated endocytosis

and fast endophilin-mediated endocytosis, which is clathrin-independent.[220] Caveolin mediated endocytosis is another dynamin dependent mechanism but less relevant to the proximal tubule where caveolin expression is minimal.[219,222,223]

The dynamin independent processes are macropinocytosis and CLIC/GEEC (Clathrin and Dynamin Independent Carriers/GPI-AP enriched early endosomal compartments).[219,220] Macropinocytosis generates much larger vesicles than the other mechanisms of endocytosis, through cell protrusions indiscriminately encapsulating large volumes of extracellular fluid.[219,220] The CLIC/GEEC pathway is likely less relevant for antimiR uptake, being mainly involved in the uptake of surface proteins.[224,225]

AntimiR uptake may involve binding of cell surface receptors in a competitive manner, as it can be inhibited by high concentrations of control oligonucleotide.[212,213] Megalin and cubilin are key endocytic receptors in the proximal tubule. They are large proteins expressed on the apical surface of proximal tubular epithelial cells and bind a wide range of ligands to facilitate their clathrin-mediated endocytosis from the tubular lumen.[215,226]

Megalin is a member of the low density lipoprotein receptor family and composed of an extracellular domain and a transmembrane domain with a cytoplasmic tail.[226] The cytoplasmic tail includes NPXY motifs that bind adaptor proteins such as Dab2 and AP-2 to allow connections with clathrin-coated pits.[226-228] Cubilin consists only of an extracellular domain and so must complex with other proteins for endocytosis, namely megalin or amnionless.[226-228]

5.1.2 Intracellular trafficking of antagomir

Once delivered to the target cell, the antimiR must access the appropriate intracellular compartment in order to bind its target miR and so have a biological effect.[210,229] Although it is generally thought that mature miRs are located in the cytosol, there is evidence they are found in the nuclear compartment also.[230] Specifically, mature miR-21 was identified in both the cytoplasmic and nuclear compartments of HeLa cells.[231]

After endosomal uptake, antimiRs must leave the endosomal pathway to engage with their targets.[229] In human ex vivo kidneys target sequence antimiR was shown to exit the endosome by its colocalisation with the RISC complex.[97] Oligonucleotides are able to move between the nucleus and cytoplasm and the mechanism by which this

is achieved differs depending on the chemical structure of the oligonucleotide.[232] For those with a phosphorothioate backbone, transport is active with little role for diffusion.[232] The binding of antisense oligonucleotides to proteins after they have left the endosome may be key in determining the subcellular destinations of these molecules.[229]

5.1.3 Inhibition of endocytic pathways

To investigate the relative contributions of different endocytic pathways, targeted inhibitors can be used.

Specific siRNA knockdown of megalin and cubilin have been used *in vitro* to assess their role in endocytic uptake of certain ligands.[233] Inhibition has also been achieved with competitive inhibitors and antibodies.[234-236] One such inhibitor for megalin is receptor-associated protein (RAP).[226,235,237] RAP is involved in the normal processing of megalin after endocytosis and is predominantly located in the endoplasmic reticulum.[237] However, administration of soluble RAP will block the ligand binding domain of megalin and so prevent further ligand endocytosis.[237,238] This has been shown with both mouse models and *in vitro* studies.[234,235,237,239]

Inhibitors have also been used to target clathrin as a common mediator of receptor-mediated endocytosis.[225]Chlorpromazine prevents clathrin-coating of pits required for clathrin-mediated endocytosis.[240-243] However, toxicity makes chlorpromazine challenging to use with tolerated concentrations being cell-type specific.[240-244]

Macropinocytosis can be visualised using a fluid-phase marker such as a fluorescently labelled dextran.[245-247] Macropinocytosis can be reduced by inhibiting the Na-H exchanger on the plasma membrane.[225,248,249] This ion channel is essential for the cytoplasmic alkalinisation needed for macropinosome formation as key GTPases involved (Cdc42 and Rac1) are pH sensitive.[248] Although acidification can also prevent clathrin-mediated endocytosis, this only occurs at much lower pH levels.[248]

EIPA (5-(*N*-ethyl-*N*-isopropyl)amiloride) is more effective at blocking the Na-H exchanger than amiloride and HOE694, as demonstrated by effectively reducing albumin uptake in OK cells and alkalinisation of the endosome at lower concentrations.[250] Much like chlorpromazine, toxicity is a concern with EIPA and must be thoroughly assessed to identify the tolerated concentration for the cells being used.[243,251,252]

5.1.4 Relevance of uptake mechanisms to in vitro models

The study of antimiR action in the kidney *in vitro* has largely relied on the use of cell lines with antimiR delivery by transfection reagents, despite naked delivery being achieved with *in vivo* and ex vivo models.[88,90,97,102,104,108,110,149,150,211,253,254] The type of endocytic pathway used for entry may determine whether oligonucleotides reach a compartment that allows biological activity.[229] Therefore, it is important that *in vitro* models are as translatable as possible. In this chapter I will assess the ability to delivery antimiR to primary human PTEC *in vitro* without the use of transfection reagents, and investigate the likely entry mechanisms involved.

5.2 Methods

5.2.1 Uptake in cold conditions

To assess the effect of temperature on antimiR uptake media was cooled to 4ºC before application and cells maintained at this temperature for the duration of treatment.

5.2.2 LRP2 knockdown

Primary human PTEC and Caco-2 were transfected with siRNA to knockdown *LRP2* (megalin) using Lipofectamine RNAimax transfection reagent (ThermoFisher 13778). Caco-2 were used as megalin and cubilin are also expressed in the intestinal epithelium.[226] PTEC were transfected at least 48 hours after seeding. Control (SCBT sc-37007) and *LRP2* siRNA (SCBT sc-40103) were reconstituted to 10 µM as per product literature and stored at -20ºC in sterile aliquots. Lipofectamine mix consisted of OPTI-MEM® and Lipofectamine in a 50:3 ratio. siRNA mix was prepared as per **Table 5-1** depending on target concentration and scaled up as required.

Transection mix was produced by mixing equal volumes of lipofectamine mix with siRNA mix and incubating at room temperature for 5 minutes.

Final transfection concentration (nM)	Volume of 10 µM siRNA (µL)	Volume of OPTI-MEM® (µL)
400	12	3
200	6	9
100	3	12
50	1.5	10.5
10	0.3	15

Table 5-1 siRNA mix for *LRP2* knockdown

Transfection was performed on cells seeded into 12-well inserts. 30 µL of transfection mix was added to 170 µL of complete media in apical compartment of inserts. After 4 hours, media in apical compartment was topped up to total volume of 300 µL. 24 hours after transfection, transwell inserts were moved to a new plate and media in both compartments was changed.

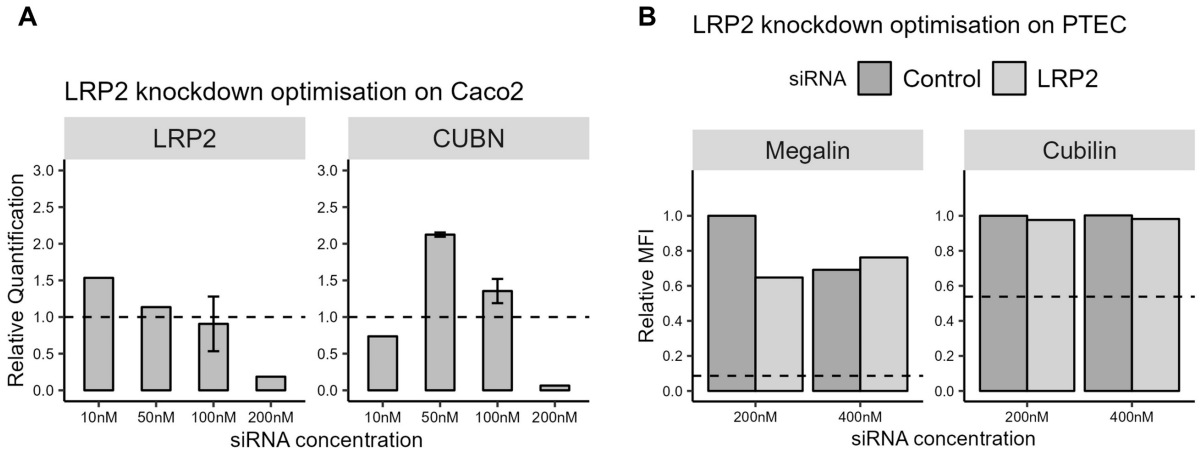

Figure 5-1 *LRP2* knockdown optimisation.
A. Megalin (*LRP2*) and cubilin (*CUBN*) mRNA expression in Caco-2 assessed by RT-PCR, 72 hours after transfection with siRNA targeting *LRP2* at concentration ranges given. Quantification at each concentration is relative to cells treated with the same concentration of control siRNA. n=1 other than for 50 nM and 100 nM where n=2 and mean ± standard deviation are presented. **B**. Megalin and cubilin protein expression assessed by flow cytometry of fixed permeabilised human primary proximal tubule epithelial cells (PTEC, 1 biological repeat) 120 hours after transfection with 200 nM or 400 nM of control or LRP2 siRNA. Median fluorescent intensity (MFI) of fluorophore conjugated to antibody targeting megalin or cubilin is given relative to cells treated with 200 nM control siRNA. Values for cells incubated with isotype control antibody is shown as dashed line.

The 200 nM siRNA concentration was effective for achieving *LRP2* mRNA knockdown in Caco-2 (**Figure 5-1A**) and this concentration was used in PTEC as it was noted that control siRNA impaired *LRP2* protein expression in these cells when used at higher concentrations (**Figure 5-1B**). Albumin or antimiR were added to apical compartment 96 hours after transfection with 200 nM LRP2 siRNA or control, to determine the impact of knockdown on uptake.

5.2.3 Confocal microscopy image acquisition and colocalisation

Images for co-occurrence analysis between antimiR, albumin, dextran and RAB7 were acquired by Leica SP8-STED Confocal microscope using X63/1.4NA oil lens. A z-stack was acquired using optimal voxel size (X,Y≤44 nm, Z=130 nm) as calculated using Nyquist calculator. Z-stacks of albumin and dextran uptake consisted of 20

slices and those for RAB7 immunofluorescence were 13 slices. Areas demonstrating marker uptake were targeted for image capture in the treated cells. Image acquisition was standardized and within each biological repeat images were captured with identical setting for control and treated cells to allow comparison.

Deconvolution and colocalisation analysis were performed in Huygens Software (www.SVI.nl - RRID:SCR_014237). Firstly, images were deconvolved with identical settings used for all images within each biological repeat. Deconvolution settings were optimised against untreated cells. Pixels to include in colocalisation analysis of images of treated cells were all above the threshold values set by the highest control image (excluding outliers). Images with excessive artefact or minimal signal above control thresholds were excluded to leave a minimum of 5 stacks included per biological repeat. Colocalisation was assessed by Manders' overlap coefficient.

5.2.4 Pathway inhibition

EIPA was reconstituted to a stock solution in DMSO (Santa Cruz Biotechnology sc-202458). The toxicity of concentrations of EIPA was first explored in Caco-2 cells to guide optimisation in PTEC (**Figure 5-2**). For controls, matched concentrations of DMSO were used e.g 100 µM EIPA equated to 0.1% DMSO. Nuclear fragmentation, as shown by DAPI pattern, was observed in Caco-2 exposed to EIPA concentrations of ≥50 µM on widefield fluorescent microscopy (**Figure 5-2A**) and with the lower concentration of 20 µM on confocal microscopy (**Figure 5-2B**). Reduced dextran uptake was achieved with 2 µM EIPA in Caco-2 (**Figure 5-2**).

The concentration of EIPA tolerated by primary human PTEC without signs of toxicity was established by assessing response of PTEC to incubation with 0.25-100 µM EIPA for 24 hours. An amine-reactive fixable live/dead stain was used to determine viability by flow cytometry as described in main methods. Fluorescent microscopy assessed nuclear appearance, after 4% PFA fixation and counterstaining with DAPI, by both wide field fluorescent microscopy and confocal microscopy.

RAP with a polyhistidine tag was made in house in the Lowe lab, University of Manchester. [255] RAP and EIPA were diluted to working concentrations with maintenance media. EIPA was added to both apical and basolateral compartments whereas RAP was only added to apical compartment. Pretreatment was for 1 hour before addition of antimiR, albumin or dextran to the apical compartment with continued inhibitor exposure.

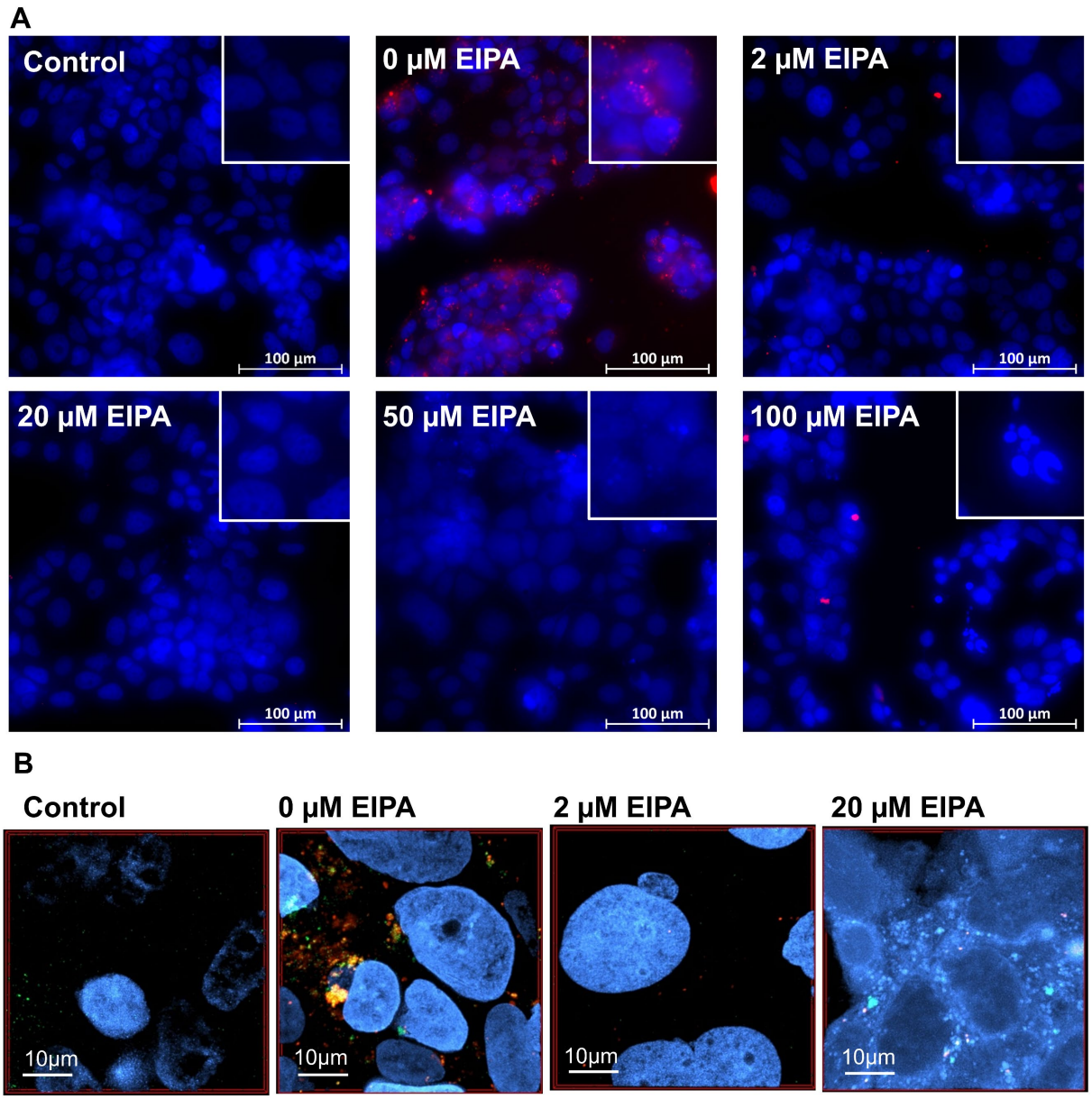

Figure 5-2 Assessing optimal concentration of 5-(N-ethyl-N-isopropyl)-amiloride (EIPA) in Caco-2.
Caco-2 cells were treated with 1 mg/mL Texas Red-labelled dextran (red) and in **B** also with 40 nM FAM-labelled antimiR (green) for 6 hours, after a 40-minute pre-treatment with EIPA. Control cells were not treated with dextran, antimiR or EIPA. **A** shows widefield fluorescence microscopy with insets (top right) showing magnified area. **B** shows confocal fluorescent microscopy. In both panels, cells treated with 0 µM EIPA were exposed to a DMSO concentrations to match those in the highest concentration of the run (0.1% (**A**) and 0.02% (**B**)). Nuclei counterstained with DAPI (blue). Widefield fluorescent microscopy images acquired with ZEISS Axio Imager using X40 objective. Confocal microscopy images acquired with Leica SP8-gSTED 3X using X63/1.4NA oil lens

5.2.5 Chlorpromazine treatment

Chlorpromazine hydrochloride powder was reconstituted in dH_2O to produce a stock solution. Stock solution was diluted to working concentrations with complete maintenance media. Cells were treated with diluted chlorpromazine as described for EIPA. There was no reduction with albumin uptake on fluorescent microscopy with 5 µg/mL chlorpromazine treatment (**Figure 5-3A**) and toxicity was detected at the lower concentration of 500 ng/mL (**Figure 5-3B**). A non-toxic concentration of chlorpromazine that was able to prevent receptor-mediated endocytosis, marked by albumin uptake, was not established so this approach was not used further.

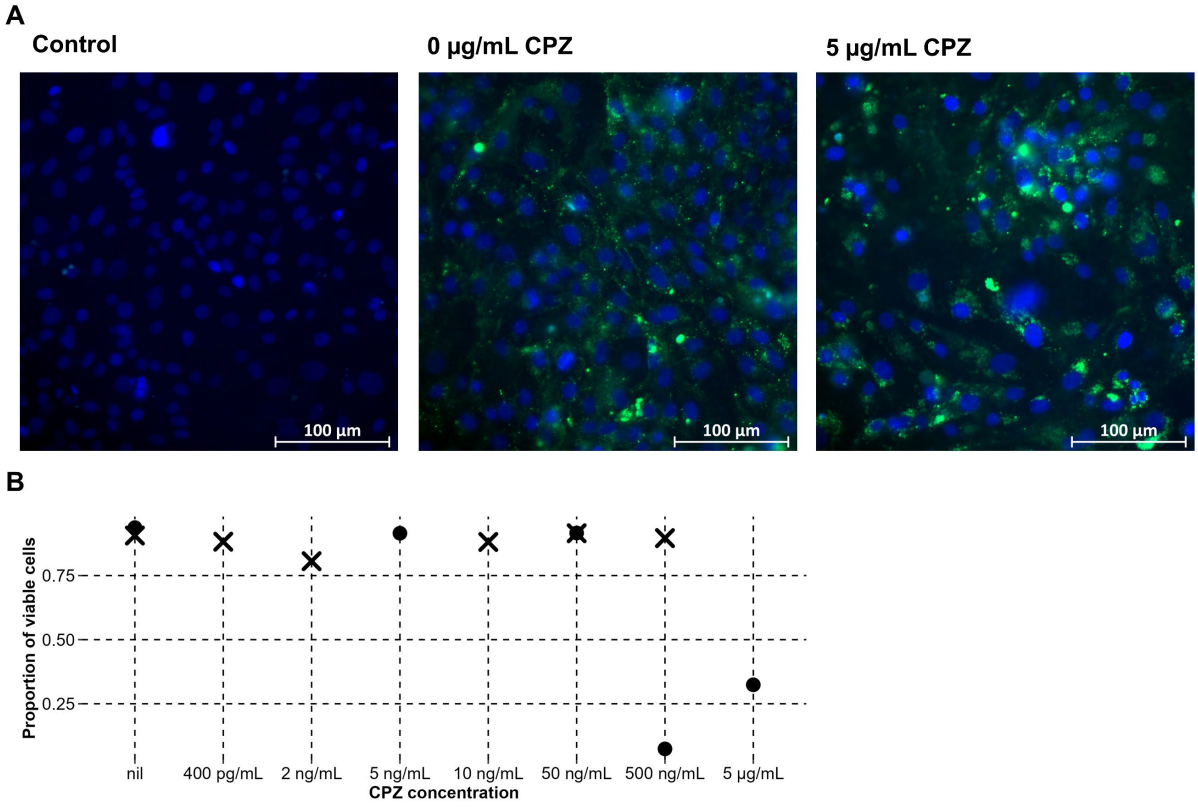

Figure 5-3 Assessment of optimum chlorpromazine concentration.
Viability of primary human proximal tubule epithelial cells (PTEC) after 24 hours of exposure to clathrin mediated endocytosis inhibitor chlorpromazine (CPZ) assessed by nuclear appearance on widefield fluorescent microscopy in cells counterstained with DAPI (**A**) and by viability on flow cytometry based on exclusion of amine-reactive dye (**B**). Exposure to 20 µg/mL CPZ detached almost all cells (image not shown). Shapes in **B** representing two technical repeats. In **A** PTEC were treated with FITC-labelled albumin (green) at 0.1 mg/mL 1 hour into 24 hours of CPZ treatment with control cells not treated with albumin or CPZ. Images acquired with ZEISS Axio Imager with X40 objective.

5.3 Results

5.3.1 AntimiR uptake by PTEC is temperature dependent

To confirm if the mechanism for antimiR uptake into primary human PTEC is an active process, the effect of temperature was explored by treating cells with FAM-labelled antimiR in warm and cold conditions (
Figure 5-4). In PTECs incubated for 8 hours with 160 nM antimiR at 4°C, a median (interquartile range) of 2.24% (2.94%) of pixels were above the threshold set as positive for FAM signal. For PTECs treated with antimiR at 37°C, more uptake was indicated by an increase in FAM positive area to 8.58% (5.57%). In cells not incubated with antimiR, FAM signal was lower, as expected, at 1.34% (0.89%) at 37°C and 0.52% (0.29%) at 4°C, which reflects a degree of autofluorescence. These results confirmed uptake was temperature dependent, in keeping with an active process.

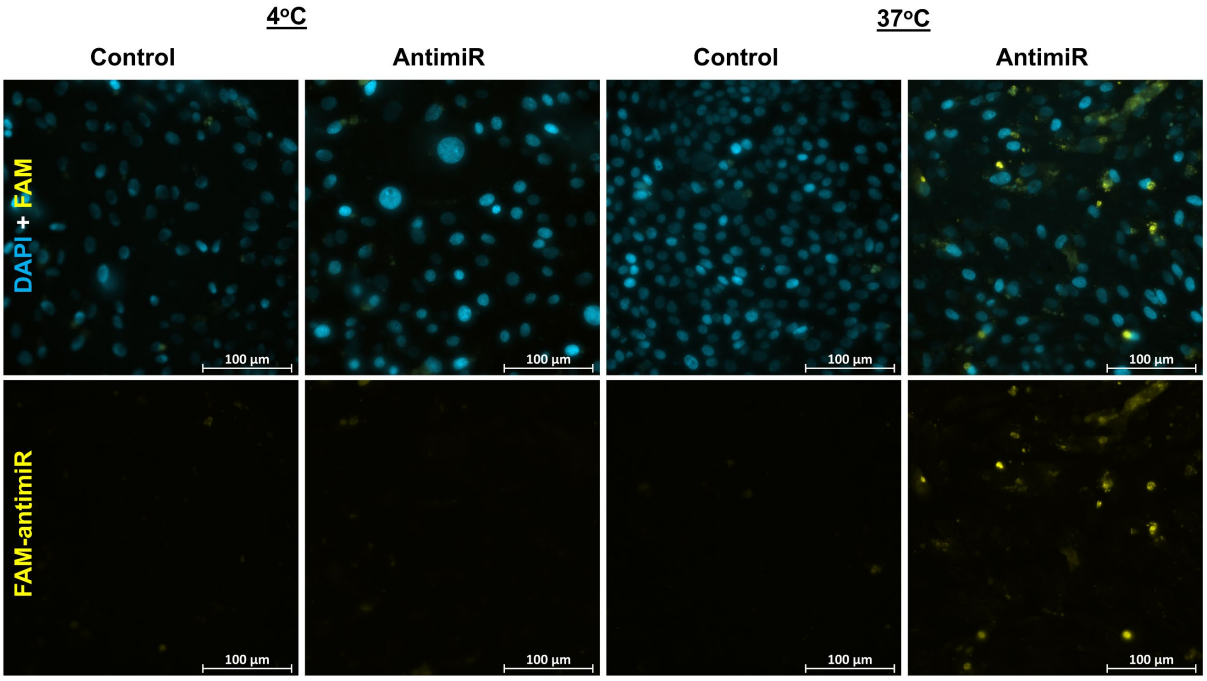

Figure 5-4 Effect of temperature on antimiR uptake.
Fluorescent microscopy of naked FAM-labelled antimiR (yellow) uptake into primary human proximal tubule epithelial cells (PTEC) after 8 hours of exposure to antimiR at 4°C or 37°C. PTEC were maintained on transwell inserts and 160 nM antimiR was added to apical compartment. Nuclei are counterstained with DAPI (cyan) and control cells, not exposed to antimiR, are shown for each temperature. Images shown are representative of the 6 images acquired at random for each condition. Images acquired with ZEISS Axio Imager using X40 objective.

5.3.2 AntimiR uptake is concentration and time dependent

Reports suggest that uptake of naked antimiR requires 10-100 fold higher concentrations compared to when transfection reagents are used.[256] However, the use of higher concentrations may lead to toxicity.[256] To assess if lower concentrations could achieve effective uptake in primary human PTEC, I treated cells with a range of concentrations.

Twenty-four hour incubation with 10 nM FAM-labelled antimiR was not sufficient to reliably detect uptake into PTEC as there was no significant increase in FAM-positive areas above that of untreated controls (**Figure 5-5**). In contrast, both 40 nM and 160 nM treatments were sufficient to detect an increase in FAM positive areas above the autofluorescence control with a mean of 49% and 87% (n=4) of confluent areas designated positive, respectively (**Figure 5-5**). A vesicular pattern of FAM signal was detectable with the 40 nM concentration, in keeping with an endocytic process (**Figure 5-5**).

In terms of the speed of uptake, flow cytometry data found the FAM signal from PTEC treated with 40 nM antimiR to increase steadily from 1 hour to 24 hours of treatment (**Figure 5-5**). I therefore demonstrate that in these PTEC, unassisted uptake could be achieved with similar concentrations and speed to when transfection reagents are used.

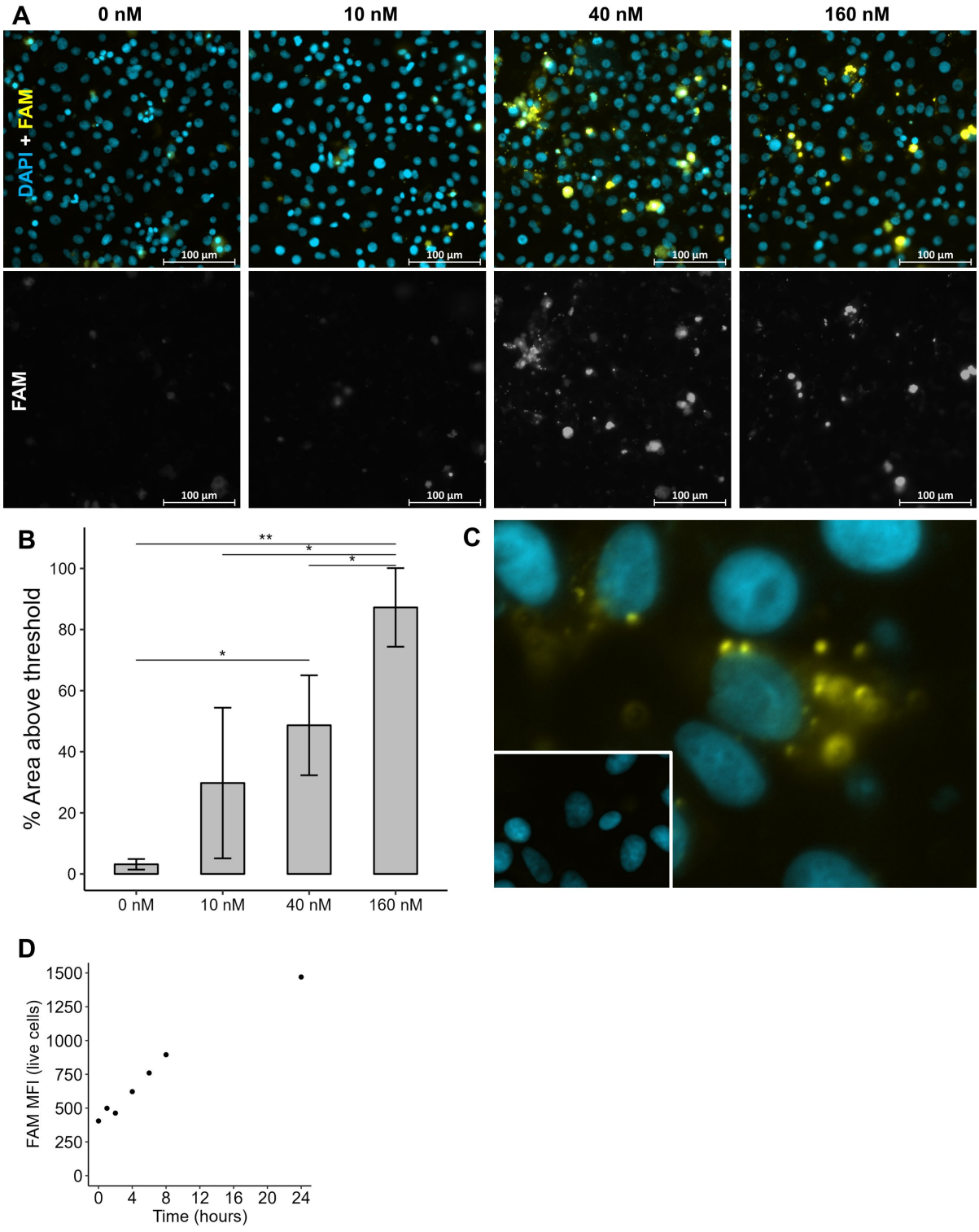

Figure 5-5 Naked antimiR uptake into primary human PTEC.

Fluorescent microscopy of naked FAM-labelled antimiR (yellow) uptake into primary human proximal tubule epithelial cells (PTEC) after 24 hours of exposure to antimiR in culture media. PTEC were maintained on transwell inserts. AntimiR was used at a concentration of 10 nM, 40 nM or 160 nM. **A** shows representative images with magnified area of 40 nM treatment in **C** demonstrating vesicular pattern (untreated in insert). **B** shows mean ± standard deviation area of FAM channel image that is above the threshold (set by control images) for 3 (10 nM) or 4 (40 nM, 160 nM) biological repeats. Image acquisition was standardized with the same number of images (5 for n=1, 6 for n=3) per condition within each biological repeat. Repeated measures analysis of variance $P = .004$. Statistically significant difference by paired t-test with Benjamini & Hochberg correction for multiple comparisons indicated with $*P<.05$, $**P<.01$. Images acquired with ZEISS Axio Imager with X40 objective. **D** shows median fluorescent intensity (MFI) in FAM channel assessed by flow cytometry for PTEC treated for up to 24 hours with 40 nM FAM-labelled antimiR (n=1). Results displayed are for live cells (negative for amine-reactive live/dead stain). Increasing MFI indicates increasing cell uptake of antimiR.

5.3.3 AntimiR colocalizes with endocytosis markers

After a 24-hour incubation, a high proportion of antimiR-associated FAM signal was found to overlap with dextran- and albumin-associated fluorescence, in keeping with uptake being via an endocytic process (**Table 5-2**, **Figure 5-6**). Co-occurrence of antimiR with the late endosome marker RAB7 was also demonstrated after 8 hours of antimiR treatment but at a lower level (**Table 5-2**, **Figure 5-6**).

Marker	Mean ± SD	n	Images per repeat
Dextran	0.854 ± 0.042	3	5
Albumin	0.943 ± 0.080	2	6
RAB7	0.308 ± 0.167	3	6

Table 5-2 Proportion of antimiR co-occurring with markers of endocytosis. Manders coefficients for proportion of fluorescent signal associated with antimiR (FAM) co-occurring with positive signal for dextran, albumin (both Texas Red labelled) or RAB7 (detected with AF594-conjugated secondary antibody). The number of biological repeats (n) and images sampled from each of these is indicated. Only pixels brighter than control images were included in co-occurrence analysis. SD, standard deviation.

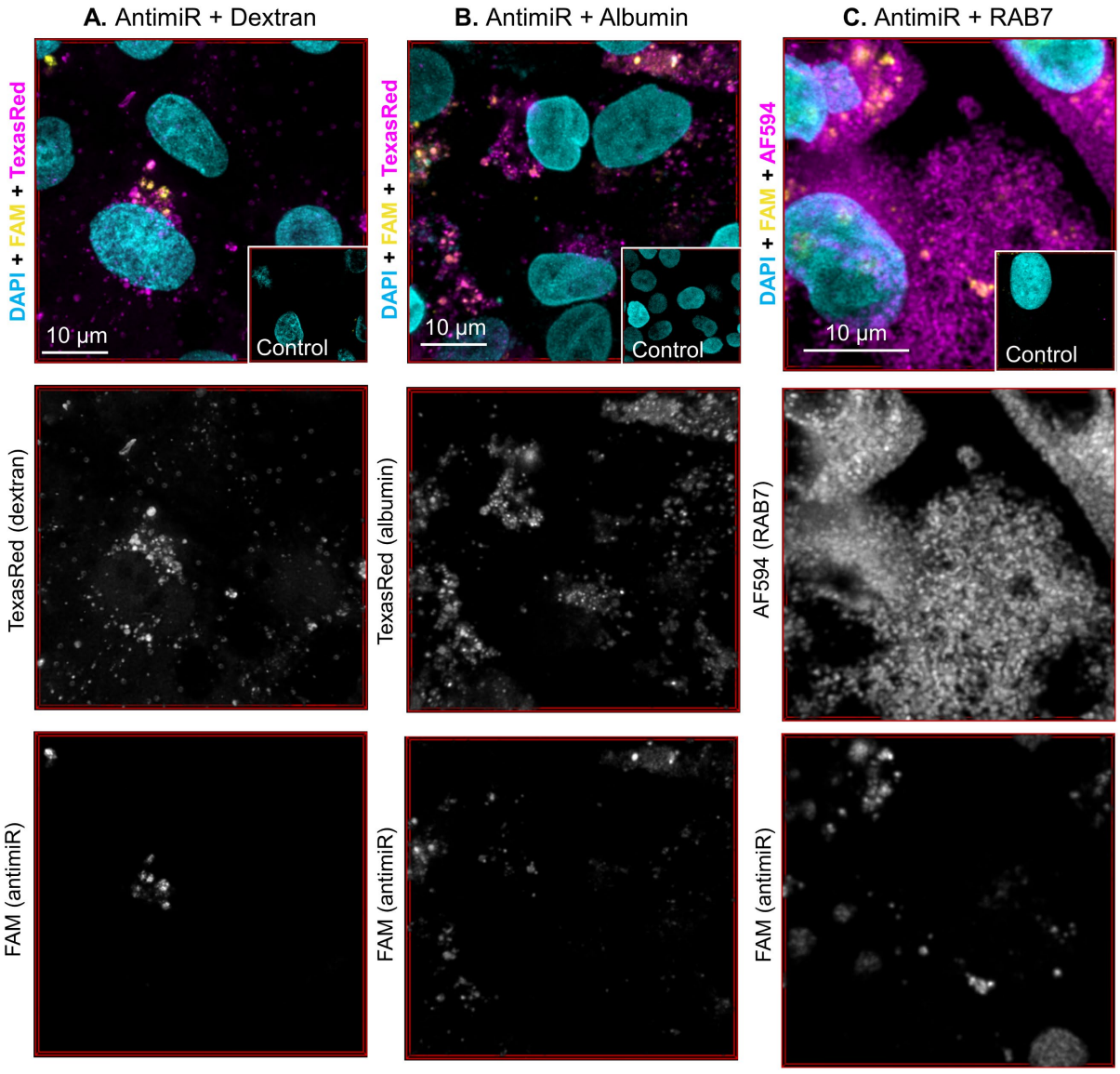

Figure 5-6 Co-occurrence of antimiR with endocytosis markers.
Confocal microscopy of primary human proximal tubule epithelial cells (PTEC) treated for 24 hours with 40 nM FAM-labelled antimiR (yellow) and either **A** 1 mg/mL Texas Red-labelled dextran (magenta), **B** 0.1 mg/mL Texas Red-labelled albumin (magenta). **C** shows PTEC treated for 8 hours with 40 nM FAM-labelled antimiR with subsequent immunofluorescence for RAB7 using AF594 conjugated secondary antibody (magenta). Co-occurrence of FAM signal with marker in magenta is shown in orange. Nuclei counterstained with DAPI (cyan). Representative multichannel image shown with control in inset. All control images are of PTEC not treated with albumin, dextran or antimiR and in **C**, an isotype control for anti-RAB7 antibody was used. Associated single channel images are shown in greyscale below. All images presented are max projections of deconvolved z-stacks acquired with Leica SP8-gSTED 3X using X63/1.4NA oil lens

5.3.4 Blocking macropinocytosis reduces antimiR uptake

EIPA is recognized to be cytotoxic at high concentrations[243,251,252] so first an appropriate non-toxic concentration for PTEC was ascertained. Toxicity in response to EIPA was assessed by light microscopy, by flow cytometry using both amine-reactive fixable live/dead stain and apoptosis assay and by fluorescent microscopy of nuclei counterstained with DAPI (**Figure 5-7**). Nuclear appearance on fluorescent microscopy was found to be most sensitive at detecting toxicity with abnormal nuclear appearance demonstrated with EIPA concentrations of 2 μM and above. There was no evidence of toxicity on exposure to 500 nM EIPA (**Figure 5-7**) so this concentration was used to assess the effect of macropinocytosis inhibition on antimiR uptake.

Incubation of PTEC with 500 nM EIPA reduced uptake of the macropinocytosis marker dextran and of antimiR (**Figure 5-8 A and C**) to around 28% and 56% of control conditions, respectively. The reduction in antimiR uptake with EIPA treatment indicates macropinocytosis to be one mechanism of antimiR uptake into PTEC. There was also a trend for a reduction in albumin uptake but this was not statistically significant (**Figure 5-8 B and D**) and as macropinocytosis is a non-selective process, this is not an unexpected finding.

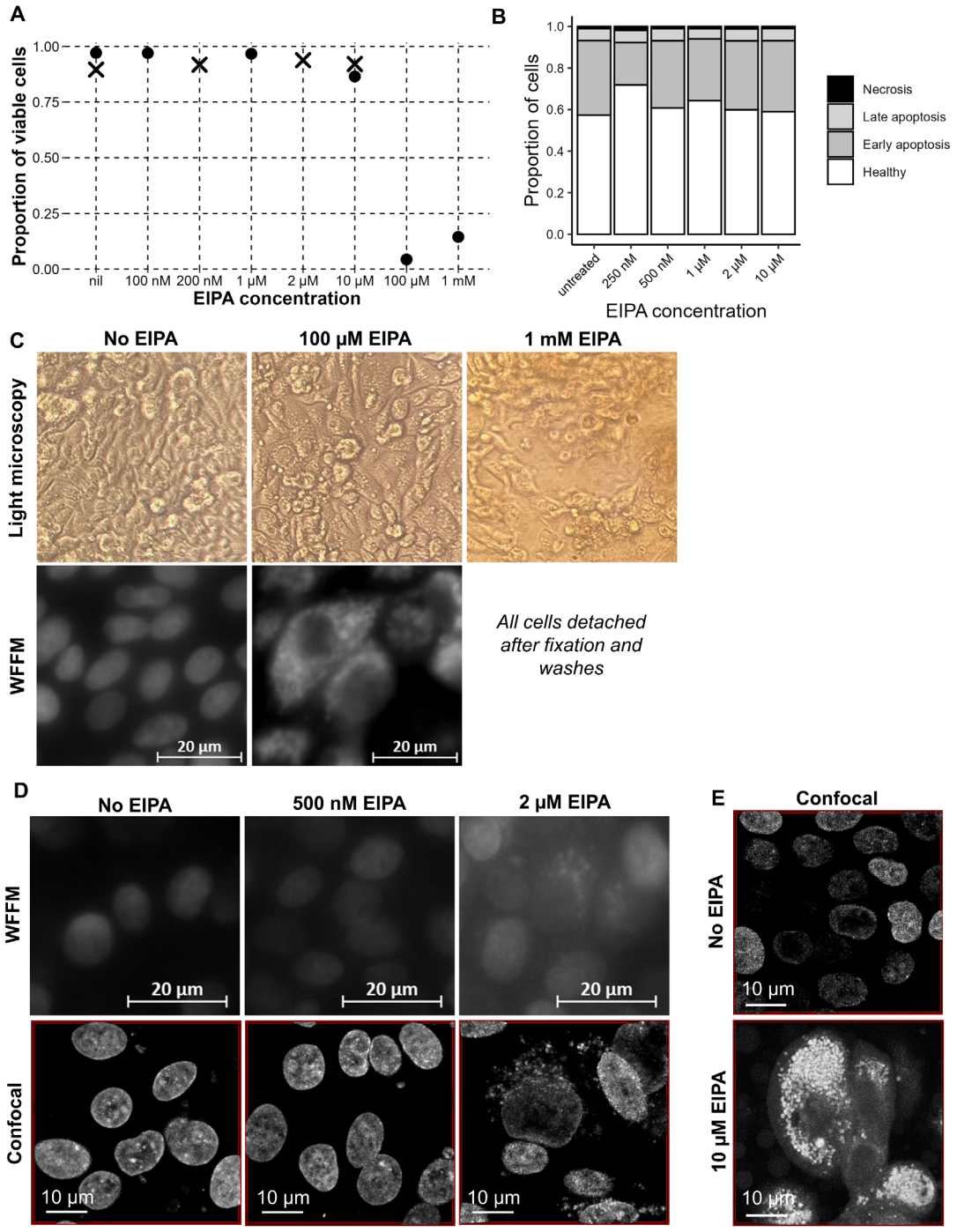

Figure 5-7 Assessing tolerated EIPA concentration in PTEC.
Viability of primary human proximal tubule epithelial cells (PTEC) maintained in culture on transwell inserts and exposed to 24 hours of treatment with the macropinocytosis inhibitor 5-(N-ethyl-N-isopropyl)-amiloride (EIPA) at a range of concentrations. Viability assessed by amine-reactive live/dead stain on flow cytometry (**A**) with shapes grouping results by biological repeat. Flow cytometry apoptosis assay results are shown in **B** (n=1). Phase contrast light microscopy is shown in **C** with nuclear appearance when stained with DAPI and imaged by wide field fluorescence microscopy (WFFM) using ZEISS Axio Imager with X40 lens. **D** shows nuclear appearance on fluorescence microscopy when stained with DAPI and acquired with either WFFM or confocal microscopy. Confocal images presented are max-projections of deconvolved z-stacks acquired with Leica SP8-gSTED 3X using X63/1.4NA oil lens. 4% PFA fixation was used before DAPI staining.

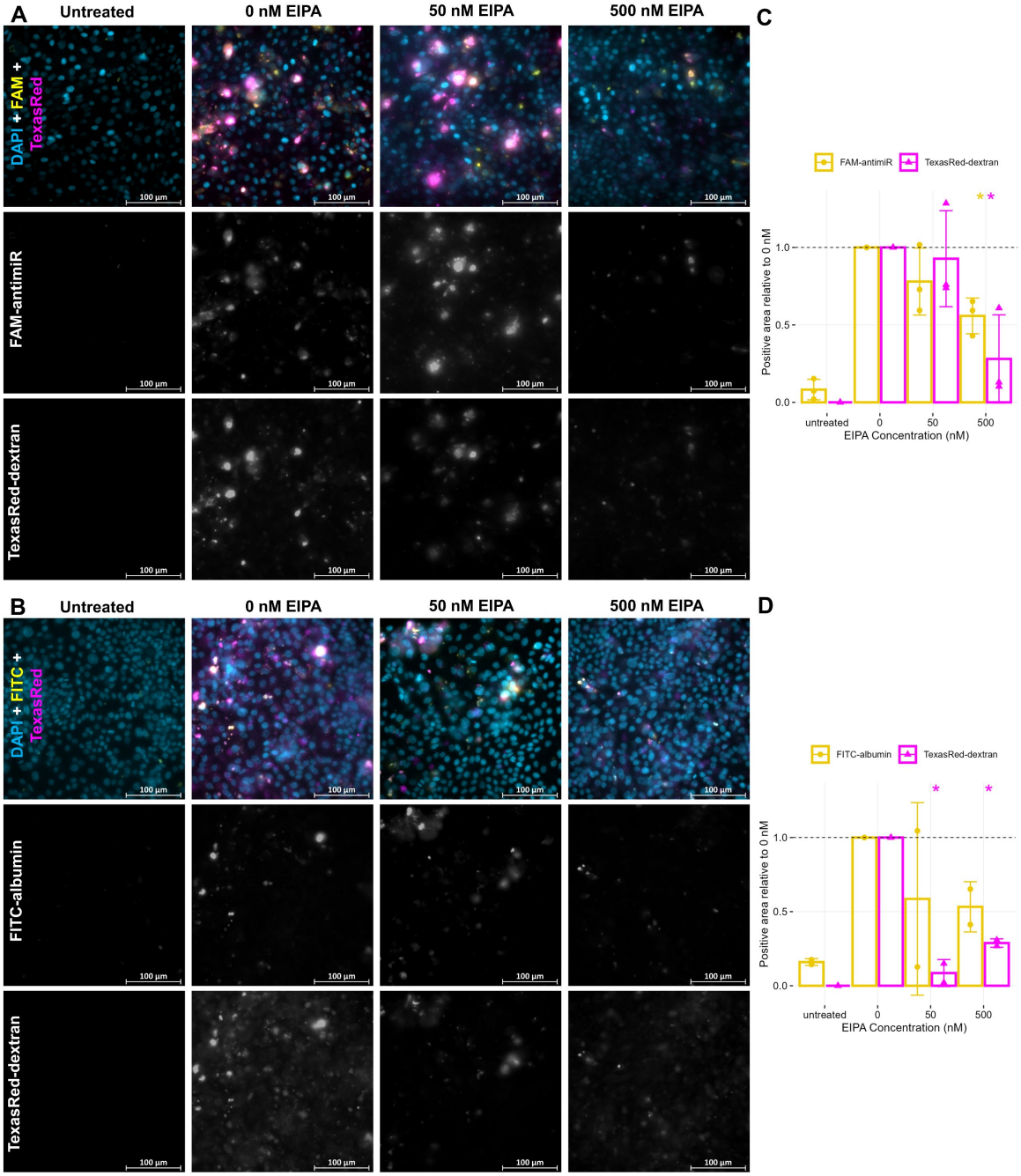

Figure 5-8 Effect of EIPA on antimiR uptake in PTEC.
Fluorescent microscopy of primary human proximal tubule epithelial cells (PTEC) maintained on transwell inserts and treated with 1 mg/mL Texas Red-labelled dextran and either 40 nM FAM-labelled antimiR (**A**) or 0.1 mg/mL FITC-labelled albumin (**B**) for 24 hours after 1 hour pre-treatment with given concentration of the macropinocytosis inhibitor 5-(N-ethyl-N-isopropyl)-amiloride (EIPA) or equivalent dimethyl sulfoxide control media (0 nM EIPA). Images shown are representative of 6 images acquired at random from each condition for each biological repeat. Untreated PTEC in left column were not treated with EIPA, antimiR or dextran, as autofluorescence control. Effect of EIPA on uptake of labelled reagents used in **A** and **B** are quantified in **C** and **D** respectively as areas of FITC, FAM or Texas Red channel above threshold set by untreated controls and reported relative to 0 nM EIPA treatment. Mean ± standard deviation of (**A:** n=3, **B:** n=2) biological repeats are presented as bars with individual results as shapes. Statistically significant difference in EIPA treatments from 0 nM was assessed by paired t-test *P<.05. Images acquired with ZEISS Axio Imager with X40 objective.

5.3.5 Megalin knockdown or inhibition does not reduce antimiR uptake

Given the key role played by megalin for reabsorption of much of the filtrate[228] in the proximal tubule, I next explored the effect of blocking this pathway on antimiR uptake. An approximately 35% reduction in megalin protein expression was achieved 120 hours after *LRP2* siRNA knockdown, as detected by flow cytometry on permeabilised cells (**Figure 5-9**). This was not associated with a reduction in FAM signal, indicating no effect on antimiR uptake (**Figure 5-9**). This level of knockdown also did not affect albumin uptake (**Figure 5-9**), suggesting that the levels of megalin expression were still sufficient to meet the requirements of this receptor-mediated endocytic pathway.

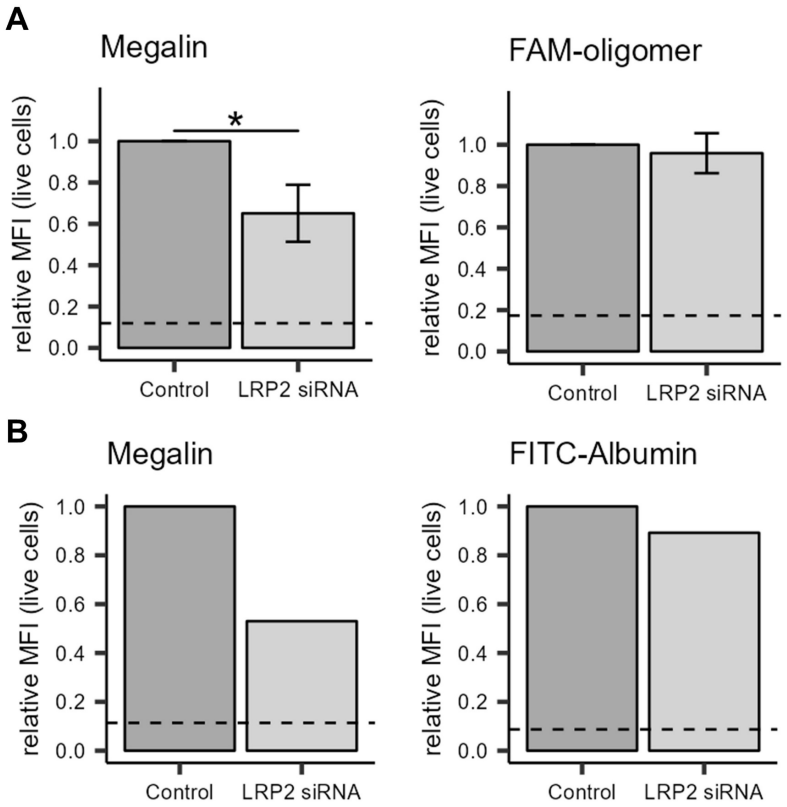

Figure 5-9 Impact of *LRP2* knockdown on antimiR and albumin uptake. Protein expression of megalin (LRP2) in primary human proximal tubule epithelial cells (PTEC) 120 hours after transfection with 200 nM *LRP2* siRNA (light grey) is shown as median fluorescent intensity (MFI) relative to corresponding control siRNA transfected cells (dark grey). FAM (**A)** and FITC (**B**) signal indicates uptake after a 24-hour incubation with 40 nM antimiR (oligomer) or 0.1 mg/ml albumin, respectively, starting 96 hours after transfection of these cells. Results are presented relative to control transfection. Dotted line represents values for isotype controls for anti-LRP2 antibody or autofluorescence in untreated cells in the case of FAM-antimiR (**A**) and FITC-albumin (**B**). Results displayed are of live single cells that have been PFA fixed and permeabilised to allow detection of total LRP2 expression. Mean ± standard deviation of n=3 biological repeats are presented in **A** with difference between groups determined by paired t-test. **P*<.05. No statistics were performed in **B** as n=1

As *LRP2* knockdown was not adequate to reduce megalin-mediated uptake of albumin, competitive inhibition was used instead. Receptor-mediated endocytosis mediated by megalin was blocked by RAP treatment, as demonstrated by reduced albumin uptake (**Figure 5-10**). Conversely, RAP treatment did not reduce antimiR uptake (**Figure 5-10**), thereby confirming that megalin-mediated uptake is not a key contributor to antimiR entry into PTEC. An increase in antimiR uptake was noted with RAP treatment in one repeat but given variability in results is difficult to interpret further.

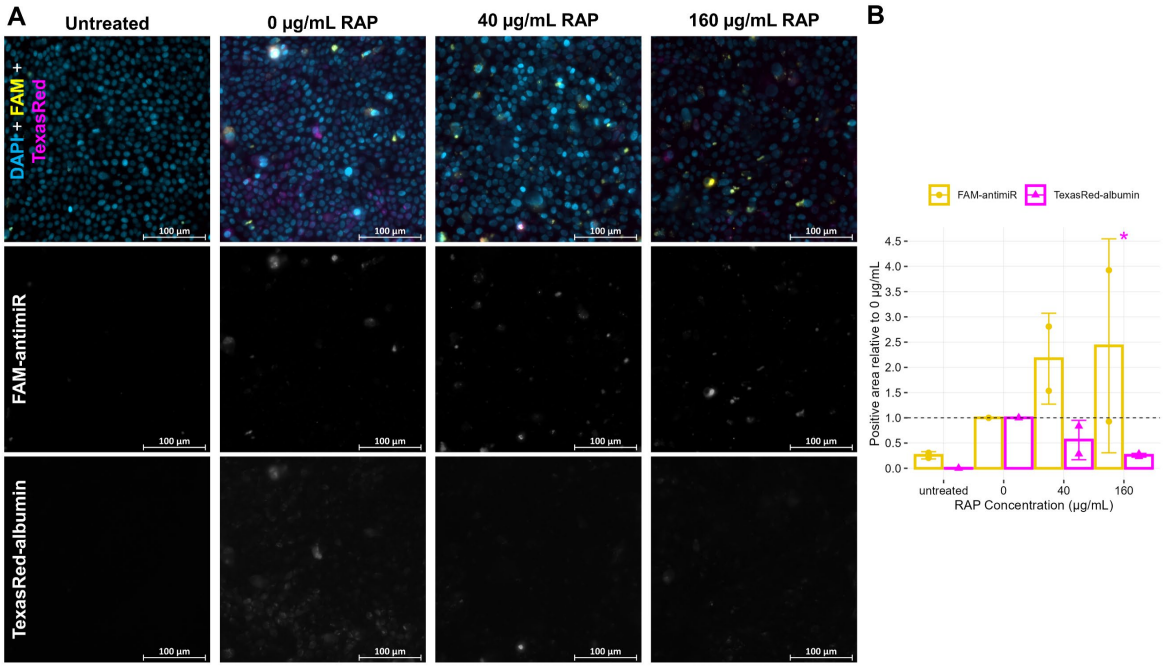

Figure 5-10 Effect of megalin inhibition on antimiR uptake.
Fluorescent microscopy of primary human proximal tubule epithelial cells maintained on transwell inserts and treated with 160 nM FAM-labelled antimiR and 0.1 mg/ml Texas Red-labelled albumin for 24 hours, after 1 hour pre-treatment with given concentration of receptor-associated protein (RAP) or control media. Images shown in **A** are representative of the 6 images acquired at random from each condition for each biological repeat (n=2). Control PTEC in left column were not treated with RAP, antimiR or albumin and so show autofluorescence only in the FAM and Texas Red channels. Effect of RAP treatment on antimiR and albumin uptake are quantified in **B** as area of image in FAM and Texas Red channel above threshold set by untreated controls and reported relative to 0 µg/mL RAP treatment. Mean ± standard deviation of (n=2) biological repeats are presented as larger shapes with individual results as smaller shapes. Difference of 40 and 160 µg/mL RAP treatments from 0 µg/mL RAP was assessed by paired t-test. **P*<.05. Images acquired with ZEISS Axio Imager with X40 objective.

5.4 Discussion

The uptake and effects of antimiRs has largely been explored through animal models and the use of cells lines.[108,110,149,211,253,254] The study of antimiRs in proximal tubule cell lines has required the use of transfection reagents.[108,110,149,253] In contrast, the work in this chapter demonstrates primary human PTECs can take up antimiR without the use of transfection reagents and that this is predominantly through macropinocytosis.

High levels of co-occurrence of antimiR with albumin and dextran, both endocytic markers, and co-occurrence with late endosome marker RAB7 were shown (**Figure 5-6**).[257] These findings are in keeping with existing data that endocytosis is a key uptake mechanism for antimiRs.[97,221] In terms of which endocytic pathways are involved, macropinocytosis was found to be important in PTEC as the inhibitor EIPA reduced antimiR uptake (**Figure 5-8**).

Dextran was used as a fluid phase marker and it has been suggested that 10 kDa dextran can enter by pathways aside from macropinocytosis.[246] However, these additional pathways are not thought to be clathrin-mediated.[246] Furthermore, the substantial blockade of dextran uptake by EIPA treatment shown here supports macropinocytosis as being the dominant entry mechanism for this molecule (**Figure 5-2**, **Figure 5-8**).

The use of EIPA as a macropinocytosis inhibitor requires careful optimisation and assessment. I found nuclear appearance to be the most sensitive measure of toxicity (**Figure 5-7**). The abnormal nuclear pattern noted with higher concentrations may relate to DNA damage caused by amiloride.[252] Perhaps unsurprisingly, primary PTEC were more sensitive to toxicity from EIPA than the intestinal cell line Caco-2. However, even Caco-2 tolerated much lower concentrations than are commonly used to block macropinocytosis in this and other epithelial cell lines, highlighting the importance of transparent toxicity assessment to validate results.[250,258]

Interestingly, macropinocytosis has also been discussed as a possible mechanism by which therapeutics could be delivered to cells in the context of malignancy.[259] Although macropinocytosis occurs in most cells, the activity of the pathway varies greatly by cell type and condition.[220,260] Epithelial cells are recognized to be macropinocytically active and this activity can be enhanced by epithelial derived

growth factor receptor stimulation.[260,261] The potential for other cell types to take up naked antimiR *in vitro* may therefore differ.

Involvement in antimiR uptake of receptor-mediated endocytosis through megalin is not supported by this work as partial knockdown and competitive inhibition with RAP had no effect (**Figure 5-9**). However, given the difficulties with chlorpromazine optimisation, clathrin-mediated endocytosis was not effectively targeted and so the role of cubilin- and amnionless- mediated endocytosis remain unexplored.[227] Much like RAP inhibits megalin-mediated endocytosis, intrinsic factor-B_{12} is a high affinity ligand of cubilin and could be an alternative approach to block uptake at this receptor.[234]

There is variable data on the interaction between megalin and cubilin expression and this was also observed in my data. For instance, in OK cells, knockout of megalin or cubilin did not affect mRNA expression of the other gene.[262] In contrast, in HK-2 cells megalin siRNA knockdown reduced both megalin and cubilin mRNA expression whereas cubilin siRNA only knocked down its target.[233] I found megalin knockdown to also reduce cubilin expression at the mRNA level in Caco-2 cells (**Figure 5-9Figure 5-1A**) but not at the protein level in PTEC (**Figure 5-9B**). With this limited data it is difficult to know if this difference relates to the cell type or assessment at the mRNA vs protein level. Transcriptional changes suggests a potential transcription factor or signalling role for megalin, perhaps through proteolytic cleavage of the cytoplasmic domain during regulated intramembrane proteolysis.[227,233,262] However, it is unclear if these functions exist *in vivo*.[227]

Another receptor of interest for oligonucleotide uptake is *SIDT2*.[263] This is a transmembrane protein able to transport single stranded RNA into lysosomes and expressed by many cell types.[263] In HeLa cells, confocal microscopy was used to show uptake of fluorescently labelled antimiR-16 at concentrations of 500 nM and 1 µM.[263] siRNA knockdown of *SIDT2* 72 hours prior to antimiR administration significantly reduced fluorescent uptake but did not prevent it completely.[263] Uptake by this pathway was shown to be biologically active as naked administration of 20 nM antimiR-16 downregulated miR-16 expression and *SIDT2* knockdown at least partially preserved miR-16 levels.[263]

Given that EIPA only partially suppressed antimiR uptake, I suspect it is not the only pathway of antimiR uptake in these cells. It would not be unique for molecules to

enter PTEC by multiple endocytic pathways, as has been shown to be the case for albumin where both receptor-mediated endocytosis and macropinocytosis are involved.[3,264] As discussed, the role of receptor-mediated endocytosis has not been fully explored in this work. A combination of receptor-mediated endocytosis and macropinocytosis is also thought to be how siRNA within a lipid nanoparticle carrier enters HeLa cells, with no role for caveolin or CLIC/GEEC pathways.[265] There may be some overlap between cell entry mechanisms used by naked antimiRs and other oligonucleotides such as siRNAs, although transport between compartments of the cell is thought to be different.[212]

I have demonstrated that antimiR can consistently be delivered to primary human PTEC at concentrations similar to those commonly used alongside transfection reagents, as opposed to the micromolar concentrations reportedly required for gymnosis.[213,214,221,266] It has been suggested that the uptake mechanism of oligonucleotides can affect biological activity, so it is important that *in vitro* models are as relevant as possible.[229,267] Furthermore, avoiding high concentrations of antimiR is likely advantageous to limit toxicity from these agents.[256] Primary human PTEC therefore provide an excellent model in which to study the effects of antimiR *in vitro* and the downstream effects of delivering antimiR-21 in this way will be assessed in subsequent chapters.

Chapter 6. The downstream effects of antimiR-21 in a human *in vitro* model of kidney IRI

6.1 Introduction

The downstream effect of miR-21 inhibition in the kidney has largely been explored in animal models and in cell lines.[78,79,99,104,106,108,112,150,254] As already discussed, there are limitations in using cell lines to model biological processes *in vitro.* Crucially, transfection reagents are required to deliver antimiRs to proximal tubule cell lines, whereas I have shown primary human PTEC take up antimiR without transfection reagents, in keeping with findings *in vivo* and ex vivo.[34,88,97]

The proximal tubule is a key site of ischaemia-reperfusion injury, miR-21 expression and antimiR uptake, making primary human PTEC an important *in vitro* model in which to study the effects of antimiR-21 in hypoxia-reoxygenation.[34,88,97,100] miRs have a large number of targets and so unbiased global techniques are useful to understand the extent of changes downstream of antimiR treatment.[72] As miRs can impact on protein expression by simply blocking target mRNA, in addition to triggering degradation, looking at gene expression at both the RNA and protein level gives a fuller understanding of the effects of antimiR-21.[72]

In this chapter, I use bulk RNA sequencing and LCMS-based proteomics to explore the effects on gene expression of antimiR-21 treatment in a human model of kidney IRI. Understanding the downstream impact of antimiR-21 in human cells will allow insights into its role as a potential therapeutic in kidney IRI.

6.2 Methods

The 4 biological repeats of primary human PTEC used for this work are from HMIR21-12, HMIR21-13, HMIR21-15 and HMIR21-16.

6.2.1 Selection of library preparation method for proteomics

Initial analysis of differential gene expression was performed with two methods of library preparation to determine whether to proceed with the library-free method or by using the gas-phase fractionated sample to generate the library for peptide identification. There was a different number of differentially expressed proteins with antimiR-21 treatment vs control antimiR and with hypoxia-reoxygenation compared to normoxia depending on which library-preparation method had been used (**Table 6-1**).

	GPF only	In both	Library-free only
AntimiR-21 vs Control			
24 hr	1	1	6
48 hr	36	22	24
Normoxia vs hypoxia reoxygenation			
24 hr	164	512	211
48 hr	56	98	69

Table 6-1 Differentially expressed proteins by library preparation method. Number of significantly differentially expressed proteins identified on liquid chromatography mass spectrometry-based proteomics analysis by library preparation method used. Where a differentially expressed gene was identified by both methods of library preparation, it is listed under “In both”. 24 and 48 hours (hr) are the length of reoxygenation that followed the 24-hour period of hypoxia. The two methods of library preparation used were the library-free method and library preparation from a pooled gas-phase fractionated (GPF) sample.

	GPF	Library-free	Bulk RNA Seq
Upregulated with antimiR-21			
24 hr		**IGFBP3**	AHNAK ASPM PPFIA4 THBS1
48 hr	YAP1 NUCB1 SEPTIN10 PGRMC1 S100A10 ERBB2	**IGBFP3** NUCB1 SNRPD1 IDI1	VEGFA LDHA ARRDC3 GAPDH VIM TXNIP THBS1 PGK1 PPFIA4 SLC2A3 **IGFPB3** FGB
Downregulated with antimiR-21			
24 hr	GRPEL1 RNF17	GRPEL1 WW2	SCD
48 hr	RPLP1	DHX30	HIF1A PFKFB2 ATP5MC3 TFRC CMBL

Table 6-2 Differentially expressed miR-21 targets by analysis technique.

miR-21 targets that are differentially expressed with antimiR-21 treatment compared to control (scrambled) antimiR treatment of primary human proximal tubule epithelial cells exposed to hypoxia-reoxygenation. Reoxygenation was for either 24 or 48 hours (hr) following a 24-hour period of hypoxia. Gene expression was analysed with liquid chromatography mass spectrometry-based proteomics with data independent acquisition or bulk RNA sequencing (Seq). For proteomics data, library preparation for protein identification was in DIA-NN and used either gas-phase fractionated (GPF) samples to generate the library or library-free method. IGFBP3 is highlighted in red as this gene was one of the top upregulated miR-21 targets in RNA data but differential expression was only identified at a protein level with library-free method.

Insulin like growth factor binding protein 3 (*IGFBP3*) was one of the top differentially expressed miR-21 targets with antimiR-21 treatment identified by bulk RNA sequencing, but at the protein level differential gene expression was only identified with the library-free method (**Table 6-2**). Given that both library preparation methods were otherwise comparable in terms of number of genes identified and number of differentially expressed genes, the dataset produced from library-free method was proceeded with for further analysis.

6.2.2 Selection of thresholds for pathway analysis

As the number of significantly differentially expressed genes with antimiR-21 treatment was small and it is generally advised to have at least 100 genes available for pathway analysis with QIAGEN IPA (QIAGEN Inc., https://digitalinsights.qiagen.com/IPA), different thresholds for significance were explored for this analysis. A “Strict” set of thresholds used only adjusted *P* values whereas “Relaxed” criteria allowed a lower threshold for significance by using unadjusted *P* values for datasets of DGE with antimiR-21 vs control to ensure at least 100 genes proceeded to pathway analysis (**Table 6-3**). Conversely, hypoxia-reoxygenation resulted in a large number of significantly differentially expressed genes compared to normoxia at the RNA level so the significance threshold was more stringent for these datasets (**Table 6-3**).

Comparison	Dataset	Time	Strict			Relaxed		
			LFC	Significance	Genes	LFC	Significance	Genes
antimiR-21 vs control	DIA	24 hr	0.2	Padj<.15	22	0.2	P<.05	217
		48 hr	0.2	Padj<.15	163	0.2	P<.05	449
HR vs normoxia		24 hr	0.2	Padj<.15	989	0.2	Padj<.15	989
		48 hr	0.2	Padj<.15	311	0.2	Padj<.15	311
antimiR-21 vs control	RNA	24 hr	0.2	Padj<.15	24	0.2	P<0.5	114
		48 hr	0.2	Padj<.15	107	0.2	P<0.5	239
HR vs normoxia		24 hr	0.2	Padj<.001	2263	0.2	Padj< .001	2263
		48 hr	0.2	Padj<.001	1510	0.2	Padj< .001	1510

Table 6-3 Thresholds of log_2 fold change (LFC) and significance for differential gene expression results to be included in pathway analysis.
Pathway analysis performed with QIAGEN IPA (QIAGEN Inc., https://digitalinsights.qiagen.com/IPA). Differential gene expression data was from 4 biological repeats of primary human proximal tubule epithelial cells exposed to hypoxia-reoxygenation (HR) where a 24-hour period of hypoxia was followed by either 24 or 48 hours (hr) of reoxygenation and compared to normoxia (HR vs normoxia), or comparison was made within hypoxia-reoxygenation by antimiR treatment with either antimiR-21 or control (scrambled) antimiR delivered at reoxygenation (antimiR-21 vs control). “Strict” criteria used only adjusted *P* values (Padj) whereas the “Relaxed” criteria allowed unadjusted *P* value (P) threshold for the comparison of antimiR-21 vs control. The number of genes meeting these thresholds for liquid chromatography mass spectrometry-based proteomics with data independent acquisition (DIA) and bulk RNA sequencing (RNA) are detailed.

6.3 Results

6.3.1 Biological repeat contributed the greatest variability between samples

Sparse principal component analysis demonstrated the samples to cluster primarily by biological repeat, rather than treatment conditions (**Figure 6-1**). This was the case regardless of whether it was the effect of hypoxia-reoxygenation or antimiR treatment being explored. However, there was some consistency in the spatial relationship on the plot between treatment pairs, suggesting an effect from both hypoxia-reoxygenation and from antimiR-21 treatment (**Figure 6-1**).

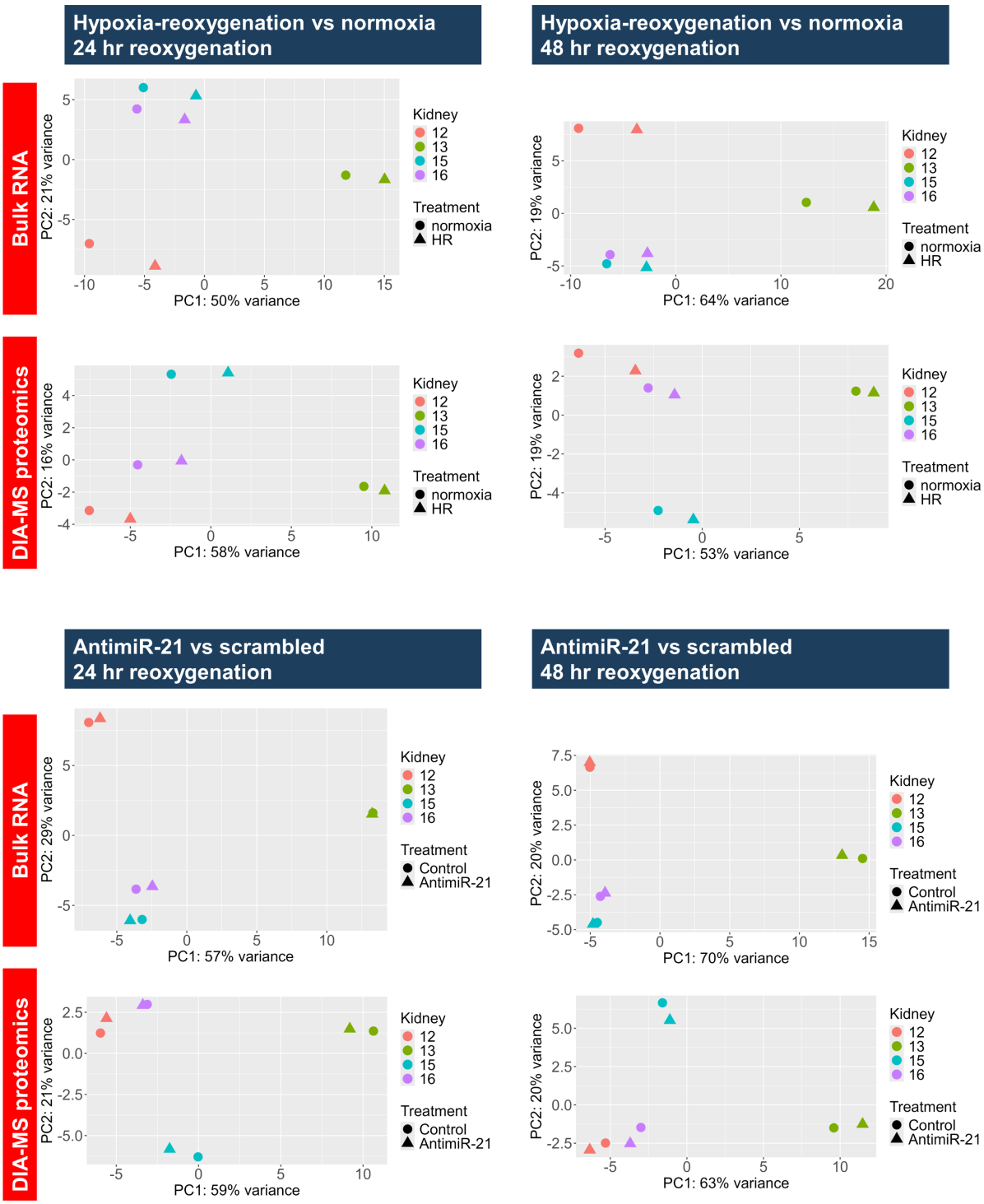

Figure 6-1 Sparse principal component analysis plots (SPCA).
SPCA for gene expression in primary proximal tubule epithelial cells (PTEC) isolated from 4 human kidneys (colours), assessed by bulk RNA sequencing and liquid chromatography mass spectrometry-based proteomics with data independent acquisition (DIA-MS). In the top panel, PTEC were exposed to 24 hours (hr) of hypoxia (incubation in 1% oxygen) followed by 24 or 48 hours of reoxygenation and treatment with 40 nM scrambled (control) antimiR compared to matched PTEC from the same donor maintained in normoxia throughout and with the same duration of scrambled antimiR treatment. In the lower panel, all PTEC were exposed to hypoxia-reoxygenation with either 40 nM of antimiR-21 or control antimiR treatment from reoxygenation.

6.3.2 miR-21 targets are upregulated with antimiR-21 treatment

Hypoxia-reoxygenation was associated with a much larger number of significantly differentially expressed genes than the effect of antimiR-21 treatment within this stressed state as shown in volcano plots in **Figure 6-2**. Over both timepoints and modalities of analysis, there were a total of 26 miR-21 targets that were differentially expressed with antimiR-21 treatment and these are detailed in **Table 6-4**. In keeping with miR targets being disinhibited by antimiR treatment, these targets were more likely to be upregulated by antimiR-21 treatment and downregulated in response to hypoxia-reoxygenation (**Table 6-4**). Interestingly, differentially expressed genes were commonly modulated in opposite direction by antimiR-21 treatment and hypoxia-reoxygenation, even when they were not known miR-21 targets (**Table 6-5**).

Within PTEC exposed to hypoxia-reoxygenation, the miR-21 target most differentially expressed between antimiR-21 and control treatment was *IGFBP3* (**Table 6-4**). *IGFBP3* was downregulated by hypoxia-reoxygenation when compared to normoxia (**Figure 6-2A, Table 6-4**). As shown by protein and RNA counts, *IGFBP3* expression was preserved in cells that underwent hypoxia-reoxygenation with antimiR-21 treatment, particularly after 48 hours of reoxygenation (**Figure 6-2C**). As shown in volcano plots in **Figure 6-2B**, this preservation of expression translates to a relative upregulation of *IGFBP3* with antimiR-21 treatment compared to control antimiR treatment during hypoxia-reoxygenation.

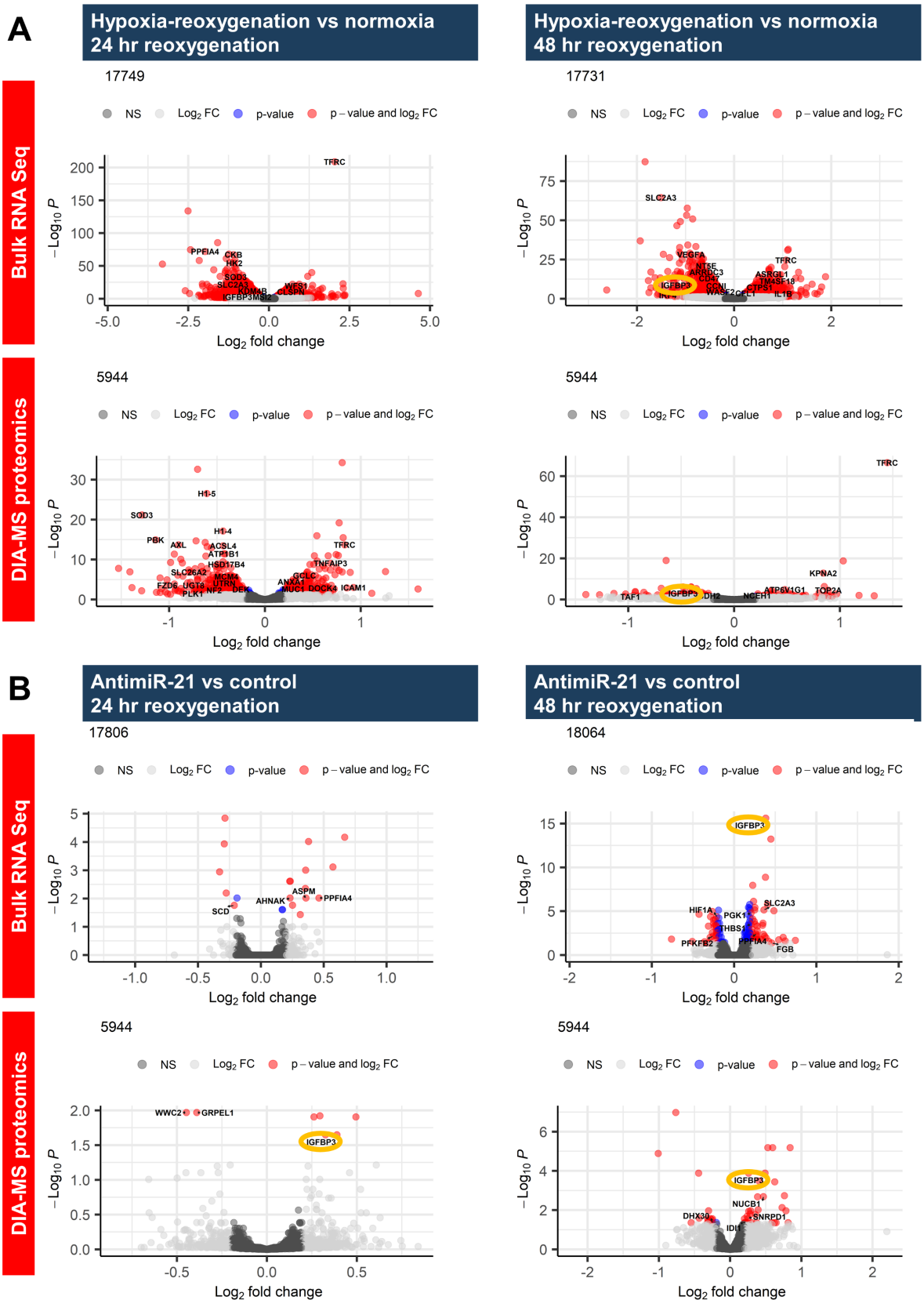
A
Hypoxia-reoxygenation vs normoxia
24 hr reoxygenation
Hypoxia-reoxygenation vs normoxia
48 hr reoxygenation
Bulk RNA Seq
DIA-MS proteomics
17749
17731
5944
5944
NS
Log2 FC
p-value
p – value and log2 FC
−Log10 P
Log2 fold change
TFRC
PPFIA4
CKB
HK2
SOD3
SLC2A3
RDMB
IGFBP3
MCM4
CLSPN
SLC2A3
VEGFA
NT5E
ARRDC3
CD47
IGFBP3
CCNL
IL1B
H1-5
SOD3
H1-4
PBK
AXL
ACSL4
ATP1B1
HSD17B4
TFRC
TNFAIP3
SLC26A2
MCM4
GCLC
ANXA1
ICAM1
FZD6
UGT8
PLK1
NF2
DEK
MUC1
DOCK4
KPNA2
TAF1
IGFBP3
DH2
NCEH1
ATP6V1G1
TOP2A
B
AntimiR-21 vs control
24 hr reoxygenation
AntimiR-21 vs control
48 hr reoxygenation
Bulk RNA Seq
DIA-MS proteomics
17806
18064
5944
5944
ASPM
AHNAK
PPFIA4
SCD
IGFBP3
HIF1A
SLC2A3
PGK1
THBS1
PFKFB2
PPIA4
FGB
WWC2
GRPEL1
IGFBP3
IGFBP3
NUCB1
DHX30
SNRPD1
IDI1

C

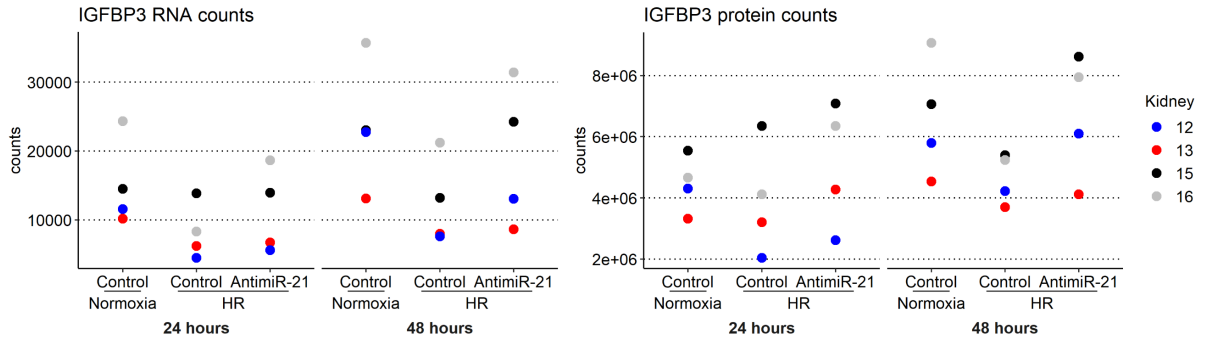

Figure 6-2 Differential gene expression (DGE) analysis in primary human proximal tubule epithelial cells (PTEC) treated with hypoxia-reoxygenation and antimiR-21 treatment.
DGE in PTEC exposed to 24 hours of hypoxia (incubation in 1% oxygen) followed by 24 or 48 hours of reoxygenation and treatment with 40 nM scrambled (control) antimiR compared to matched PTEC maintained in normoxia throughout and with the same duration of control antimiR treatment is shown in **A**. **B** shows DGE in PTEC exposed to hypoxia-reoxygenation (HR) as described above with 40 nM antimiR-21 treatment from reoxygenation compared to PTEC treated with control antimiR. Gene expression was explored with bulk RNA sequencing (Seq) or liquid chromatography mass spectrometry-based proteomics using data-independent acquisition (DIA-MS proteomics). DGE was analysed with DESeq2 and results are from 4 biological repeats with *P* value of Wald's test statistic adjusted for multiple comparisons with Benjamini-Hochberg method (p-value). Log_2 Fold change (Log_2 FC) threshold of 0.2 and p-value threshold of 0.05. NS indicates when neither Log_2 FC nor p-value threshold met. Selected miR-21 targets are labelled in **A** and all miR-21 targets meeting thresholds are labelled in **B**. The miR-21 target *IGFBP3* is highlighted to demonstrate downregulation with hypoxia-reoxygenation compared to normoxia (**A**) and upregulation with antimiR-21 treatment during hypoxia-reoxygenation (**B**). Number of genes included in each plot is indicated next to legend. **C** shows raw RNA and protein counts for *IGFBP3* in PTEC under the conditions detailed above with paired samples indicated by colour.

miR-21 target	AntimiR-21 vs control								Hypoxia-reoxygenation vs normoxia							
	24 hr				48 hr				24 hr				48 hr			
	RNA		DIA-MS		RNA		DIA-MS		RNA		DIA-MS		RNA		DIA-MS	
	logFC	padj	logFC	padj	logFC	padj	logFC	padj	logFC	padj	logFC	padj	logFC	padj	logFC	padj
AHNAK	0.232	0.010							-0.878	<0.001			-0.432	0.035		
ARRDC3					0.169	0.028							-0.569	<0.001		
ASPM	0.358	0.010							-0.564	0.036			0.441	<0.001		
ATP5MC3					-0.157	0.009			-0.163	0.033			0.206	0.008		
CMBL					-0.160	0.044										
DHX30							-0.250	0.043	0.253	0.001			0.185	0.038		
FGB					0.457	0.043										
GAPDH					0.174	<0.001			-0.360	<0.001			-0.521	<0.001		
GRPEL1			-0.390	0.011							0.471	0.008				
HIF1A					-0.212	<0.001			0.377	<0.001						
IDI1							0.228	0.043								
IGFBP3			0.389	0.022	0.384	<0.001	0.491	<0.001	-0.973	0.002			-1.198	<0.001	-0.482	0.001
LDHA					0.140	0.003			-0.419	<0.001			-0.194	0.001		
NUCB1							0.466	0.002					-0.246	0.001		
PFKFB2					-0.256	0.007							0.257	0.028		
PGK1					0.205	<0.001							-0.542	<0.001		
PPFIA4	0.462	0.010			0.268	0.004			-1.981	<0.001			-0.716	<0.001		
SCD	-0.212	0.017							-0.372	<0.001			-0.633	<0.001		
SLC2A3					0.363	<0.001			-1.118	<0.001			-1.505	<0.001		
SNRPD1							0.253	0.027					0.222	0.032		
TFRC					-0.141	0.039			2.040	<0.001	0.834	<0.001	1.069	<0.001	1.447	<0.001
THBS1	0.173	0.025			0.204	<0.001										
TXNIP					0.190	<0.001							-0.476	<0.001		
VEGFA					0.132	0.016			-0.989	<0.001	-0.615	0.003	-0.885	<0.001		
VIM					0.189	<0.001			-0.501	<0.001			-0.568	<0.001		
WWC2			-0.448	0.011												

Table 6-4 miR-21 targets that were significantly differentially expressed in primary human proximal tubule epithelial cells with antimiR-21 treatment. Expression after antimiR-21 treatment compared to control antimiR administered for 24 or 48 hours from reoxygenation, following a 24-hour period of hypoxia. 26 miR-21 target genes were significantly differentially expressed with antimiR-21 treatment and the differential gene expression of these targets with hypoxia-reoxygenation compared to normoxia is also displayed for comparison. Cell lysates were analysed by liquid chromatography mass spectrometry based proteomics using data-independent acquisition (DIA-MS) and bulk RNA sequencing (RNA). Log_2 fold change (logFC) and *P* values adjusted for multiple comparisons with Benjamini-Hochberg method (padj) are shown. Mean ± standard deviation of collated logFC values for antimiR-21 vs control are 0.123 ± 0.272 (n=30) and -0.280 ± 0.781 (n=39) for HR vs normoxia (*P*=.004; t test). More values indicate upregulation of miR-21 targets in the antimiR-21 vs control data (70%) than the HR vs normoxia (30.8%; *P*=.003; Chi Squared test X^2 = 8.945, df=1).

Gene	AntimiR-21 vs control								Hypoxia-reoxygenation vs normoxia							
	24 hr				48 hr				24 hr				48 hr			
	RNA		DIA-MS		RNA		DIA-MS		RNA		DIA-MS		RNA		DIA-MS	
	logFC	*P*	logFC	*P*	logFC	*P*	logFC	*P*	logFC	*P*	logFC	*P*	logFC	*P*	logFC	*P*
ADAMTS1	0.168	.025			0.186	<.001							-0.389	<.001		
ANGPTL4					0.322	.016	0.597	<.001	-1.590	<.001			-0.964	<.001		
CA9					0.381	<.001	0.407	<.001	-1.345	<.001			-0.686	<.001	-0.351	.017
CAV1	0.251	.017			0.193	.004			-0.817	<.001			-0.493	<.001		
FBXO16	0.354	.004			0.176	.006			-1.286	<.001			-0.470	<.001		
HILPDA	0.573	<.001			0.281	.002			-1.711	<.001			-0.658	<.001		
RAPGEF3	-0.285	<.001			-0.186	<.001										
RNASET2					0.176	<.001	0.301	.043	-0.342	<.001	0.661	<.001	-0.670	<.001		
RPAP3-DT	-0.276	.006			-0.182	.044										
SLC48A1	-0.292	<.001			-0.251	<.001			0.265	.003			0.311	<.001		
STC1	0.379	<.001			0.236	<.001			-1.135	<.001			-0.450	<.001		
ZNF395					0.174	<.001	0.645	.043	-1.293	<.001	-1.529	<.001	-0.499	<.001		

Table 6-5 Differential expression of genes that are not miR-21 targets. Differential gene expression for genes that are significantly differentially expressed with antimiR-21 treatment compared to control antimiR treatment administered for 24 or 48 hours from reoxygenation, following a 24-hour period of hypoxia. Expression was analysed by bulk RNA sequencing (RNA) and liquid chromatography mass spectrometry proteomics using data-independent acquisition (DIA-MS). Only genes differentially expressed across both time points or both modalities are shown. Only genes not classified as miR-21 targets are displayed. Differential expression of these genes with control antimiR treatment during hypoxia-reoxygenation relative to maintenance in normoxic conditions is shown for comparison. Genes that are upregulated in red and downregulated in blue. Only values with adjusted *P* values (*P*) <.05 are displayed. Benjamini-Hochberg method was used to adjust for multiple comparisons. logFC, $\log_2$ fold change.

Another way explored to demonstrate antimiR-21 target engagement was to broadly compare the direction of change in expression of miR-21 targets and genes that were not miR-21 targets within each dataset. AntimiR-21 treatment could be expected to upregulate miR-21 targets whereas the indirect action on genes that are not miR-21 targets could go in either direction. A greater proportion of miR-21 targets had a predicted positive fold change with antimiR-21 treatment compared to genes that were not miR-21 targets, in keeping with this expectation. However, this did not equate to a significant difference in mean fold change between the groups (**Table 6-6A**). When analysis was restricted to include only differentially expressed genes (adjusted *P*<.05), there was no difference in the proportion of genes upregulated by miR-21 target status (**Table 6-6B**). Although the difference in mean fold change between targets and not targets reached significance (*P*<.05) for some timepoints or analysis modalities, it should be noted that mean fold changes did not indicate a large difference between genes grouped in this way (**Table 6-6**). Ultimately, assigning genes to these large groups did not provide robust evidence for antimiR-21 and miR-21 target engagement.

A. All fold change in expression

AntimiR-21 vs control

Hours	Sample	Genes (n)			Genes upregulated (%)		Chi square test			Mean ± SD LFC		t test
		Total	Targets	Not targets	Targets	Not targets	X^2	*P*	df	Targets	Not targets	*P*
24	DIA-MS	5944	919	5025	63.3	58.8	6.30	.012	1	0.025 ± 0.123	0.018 ± 0.130	.135
48	DIA-MS	5944	919	5025	58.4	54.3	5.22	.022	1	0.022 ± 0.134	0.016 ± 0.160	.264
24	RNA	17806	1676	16130	50.1	48.7	1.10	.294	1	0.008 ± 0.096	0.006 ± 0.153	.495
48	RNA	18064	1675	16389	54.7	50.5	10.35	.001	1	0.007 ± 0.091	0.008 ± 0.156	.850

Hypoxia-reoxygenation vs normoxia

Hours	Sample	Genes (n)			Genes upregulated (%)		Chi-square test			Mean ± SD LFC		t test
		Total	Targets	Not targets	Targets	Not targets	X^2	*P*	df	Targets	Not targets	*P*
24	DIA-MS	5944	919	5025	46.2	44.8	0.57	.451	1	-0.030 ± 0.229	-0.026 ± 0.230	.605
48	DIA-MS	5944	919	5025	57.3	52.2	8.05	.005	1	0.016 ± 0.213	-0.003 ± 0.230	.023
24	RNA	17749	1672	16077	54.2	47.1	30.89	2.729 E-08	1	0.026 ± 0.281	-0.040 ± 0.371	2.980 E-12
48	RNA	17731	1666	16065	50.4	48.7	1.64	.200	1	0.009 ± 0.239	-0.007 ± 0.316	.04

B. Differential gene expression

AntimiR-21 vs control

Hours	Sample	Genes (n)			Genes upregulated (%)		Fisher exact test	Mean ± SD LFC		t test
		Total	Targets	Not targets	Targets	Not targets	*P*	Targets	Not targets	*P*
24	DIA-MS	7	3	4	33.3%	100.0%	.143	-0.150 ± 0.468	0.344 ± 0.104	.089
48	DIA-MS	46	5	41	80.0%	65.9%	1	0.238 ± 0.298	0.158 ± 0.465	.710
24	RNA	20	5	15	80.0%	66.7%	1	0.202 ± 0.258	0.144 ± 0.332	.723
48	RNA	153	17	136	70.6%	65.4%	.790	0.115 ± 0.219	0.073 ± 0.253	.514

Hypoxia-reoxygenation vs normoxia

Hours	Sample	Genes (n)			Genes upregulated (%)		Chi-square test			Mean ± SD LFC		t test
		Total	Targets	Not targets	Targets	Not targets	X^2	*P*	df	Targets	Not targets	*P*
24	DIA-MS	723	114	609	36.0%	37.4%	0.037	0.847	1	-0.165 ± 0.449	-0.120 ± 0.458	.334
48	DIA-MS	167	20	147	45.0%	38.1%	0.122	0.727	1	0.036 ± 0.630	-0.123 ± 0.586	.262
24	RNA	5049	571	4478	55.9%	43.5%	30.572	<.001	1	0.030 ± 0.408	-0.100 ± 0.551	<.001
48	RNA	3710	437	3273	48.7%	43.7%	3.736	0.053	1	0.000 ± 0.390	-0.050 ± 0.484	.036

Table 6-6 Impact of miR-21 target status on direction of regulation.

Assessment of how miR-21 target status affects whether a gene is upregulated or downregulated in primary human proximal tubule epithelial cells treated with antimiR-21 (compared to control antimiR) for 24 or 48 hours at the point of reoxygenation after a 24-hour period of hypoxia. Control-treated hypoxia-reoxygenation samples were additionally compared to normoxia controls. Cell lysates were analysed by liquid chromatography mass spectrometry based proteomics using data-independent acquisition (DIA-MS) or bulk RNA Sequencing (RNA). **A.** presents the results from all genes analysed whereas **B** gives only differentially expressed genes (adjusted *P*<.05). Results are split into the two comparisons made of antimiR-21 vs control antimiR and hypoxia-reoxygenation vs normoxia. Number of genes included with each approach is given per technique and within this the number of miR-21 targets (Targets) and other genes (Not targets). Chi-square test or fisher-exact tests were used to assess for an interaction between gene target status and direction of change in expression depending on observed counts. Mean ± standard deviation (SD) of log_2 fold change (LFC) of genes is presented with any difference between Targets and Not targets assessed by a t test. Statistical significance was determined as *P* <.05 and values meeting this threshold are in bold. df, degrees of freedom.

A number of gene sets were significantly enriched by hypoxia-reoxygenation or antimiR-21 treatment and are detailed in **Figure 6-3** and **Figure 6-4** respectively. A gene set that was enriched in multiple datasets was HALLMARK_HYPOXIA. Interestingly, this gene set of 215 genes included 37 (17.2%) miR-21 targets and was negatively enriched with hypoxia-reoxygenation in RNA data (**Figure 6-3**, **Figure 6-5A**) and positively enriched with antimiR-21 treatment on both proteomics and RNA data (**Figure 6-4**, **Figure 6-5A**). This finding is in keeping with the involved miR-21 targets being generally downregulated by hypoxia-reoxygenation and relatively upregulated by antimiR-21 treatment. Other gene sets considered enriched for miR-21 targets are also highlighted in **Figure 6-3** and **Figure 6-4** and appear generally to be more positively enriched, as opposed to negatively enriched, with antimiR-21 treatment (**Figure 6-4**).

Hypoxia-reoxygenation vs normoxia 24 hr reoxygenation

Hypoxia-reoxygenation vs normoxia 48 hr reoxygenation

Bulk RNA Sequencing

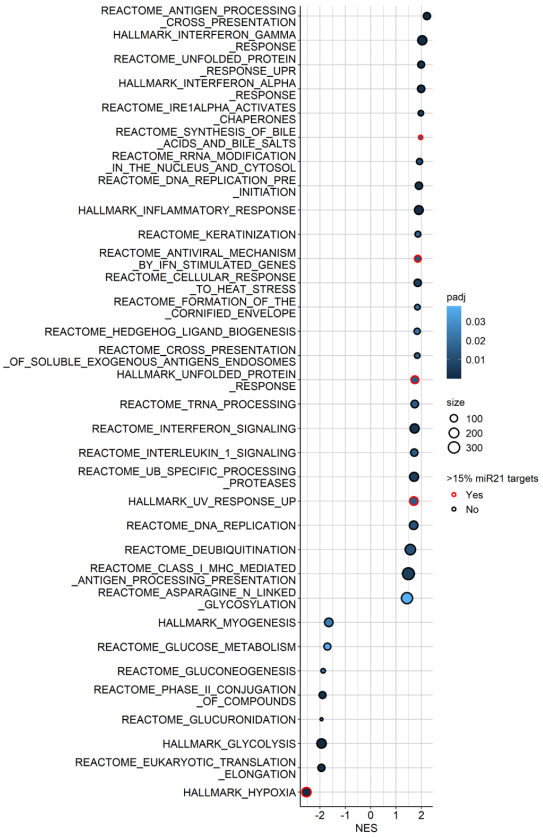

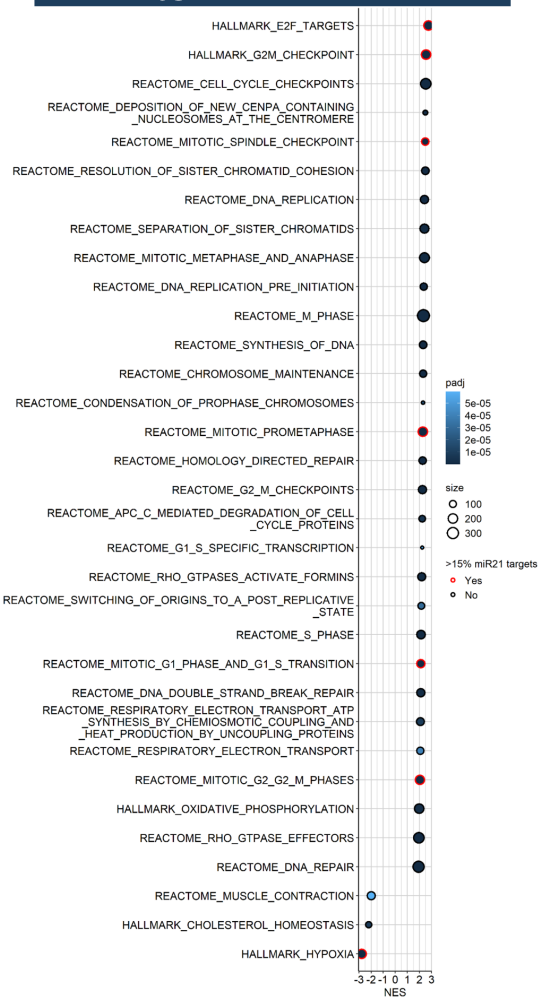

DIA-MS proteomics

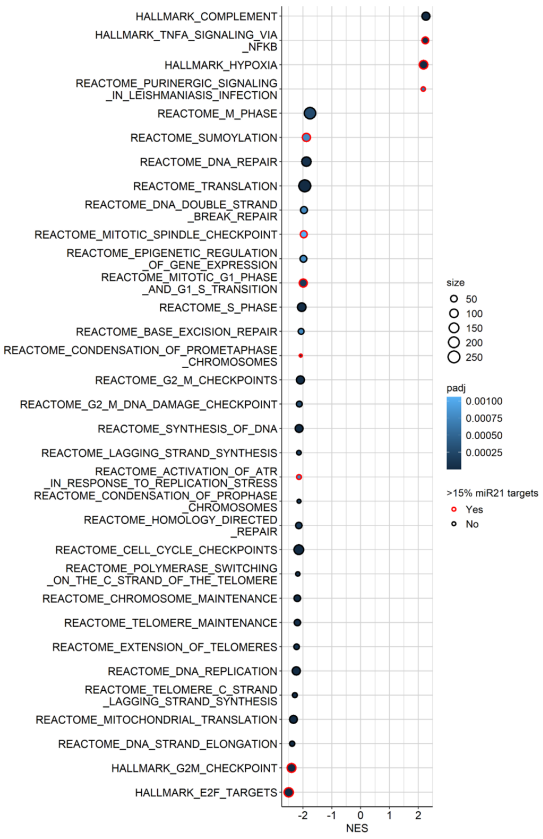

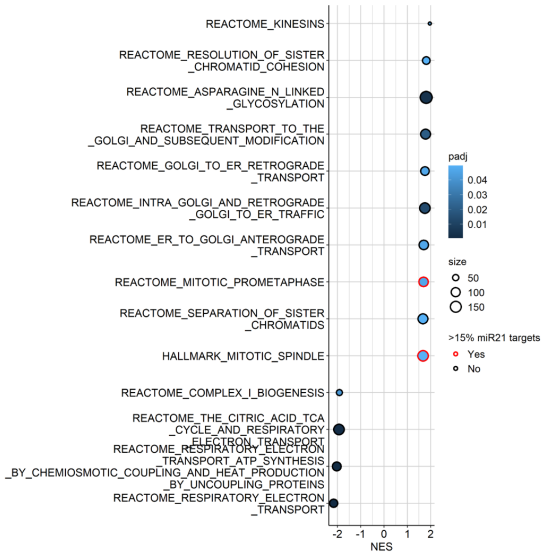

Figure 6-3 Gene set enrichment analysis (GSEA) for hypoxia-reoxygenation vs normoxia.
GSEA on datasets of differential gene expression (DGE) in primary human proximal tubule epithelial cells (PTEC) exposed to hypoxia-reoxygenation vs normoxia. PTEC exposed to 24 hours of hypoxia (incubation in 1% oxygen) followed by 24 or 48 hours of reoxygenation and treatment with control (scrambled) antimiR compared to matched normoxia controls. Gene expression was explored with bulk RNA Sequencing or liquid chromatography mass spectrometry-based proteomics using data-independent acquisition (DIA-MS). Normalised enrichment score (NES) for the gene set is plotted with the number of genes identified from gene set in datasets is indicated by size. P values are adjusted by Benjamini Hochberg method and gene sets in which more than 15% of genes are miR-21 targets are highlighted in red as enriched. 33 most significantly enriched gene sets are displayed.

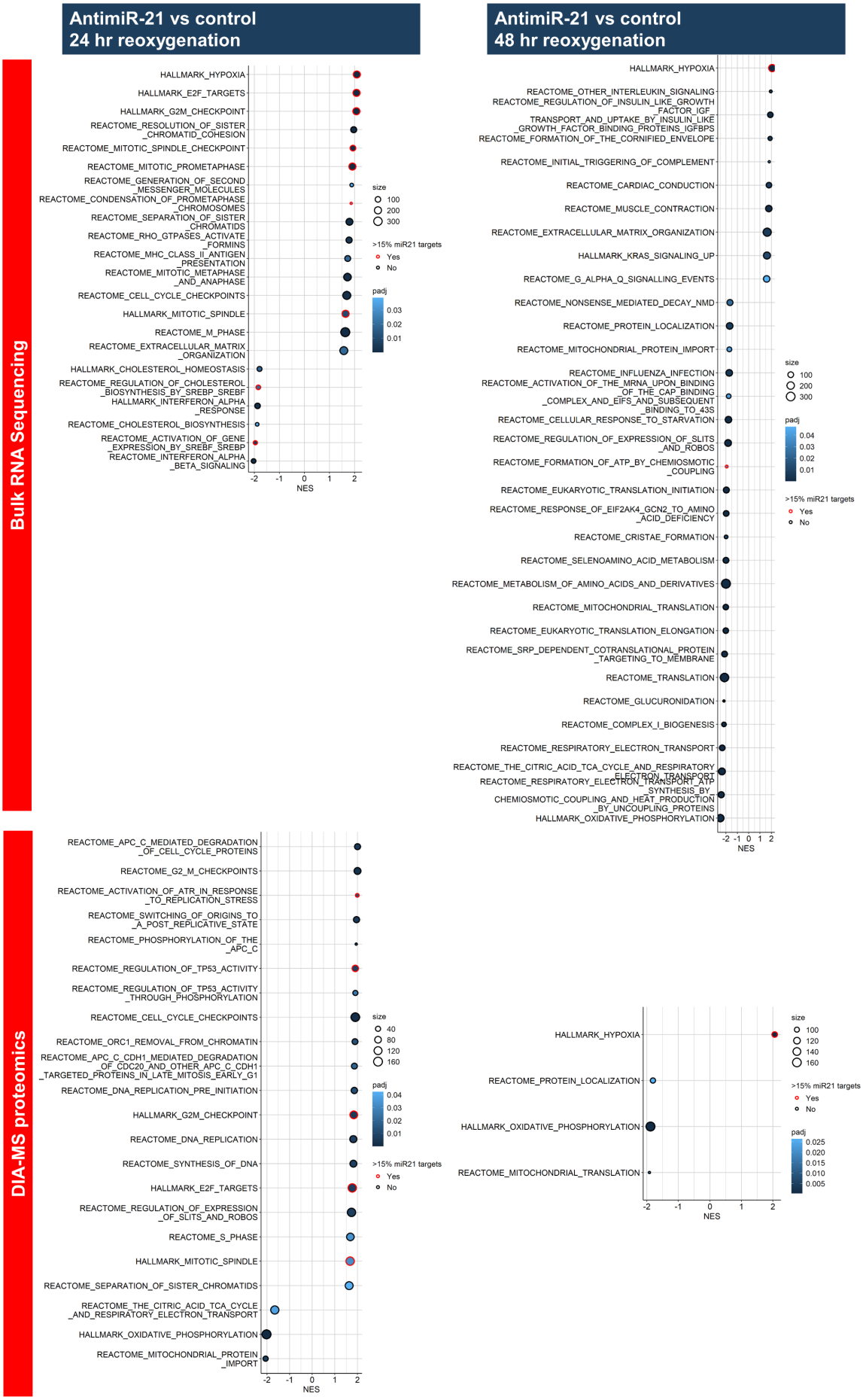

Figure 6-4 Gene set enrichment analysis (GSEA) for antimiR-21 treatment vs control.

GSEA on datasets of differential gene expression (DGE) in primary human proximal tubule epithelial cells (PTEC) with hypoxia-reoxygenation and antimiR-21 treatment. PTEC exposed to 24 hours of hypoxia (incubation in 1% oxygen) followed by 24 or 48 hours of reoxygenation and treatment with 40 nM antimiR-21 or control (scrambled) antimiR. Gene expression was explored with bulk RNA sequencing or liquid chromatography mass spectrometry-based proteomics using data-independent acquisition (DIA-MS proteomics). Normalised enrichment score (NES) for the gene set is plotted with the number of genes identified from gene set in datasets indicated by size. *P* values are adjusted by Benjamini Hochberg method and gene sets in which more than 15% of genes are miR-21 targets are highlighted in red as enriched.

In **Figure 6-5A** the top differentially expressed gene sets across the different timepoints, modalities and comparisons are summarised, with those gene sets enriched for miR-21 targets highlighted. At this level, opposite effects of hypoxia-reoxygenation and antimiR-21 treatment are less apparent and some differences between timepoints and modalities are demonstrated.

When miR-21 targets within genes contributing to the enrichment of the HALLMARK_HYPOXIA gene set are extracted for further analysis, many are shown to be significantly downregulated by hypoxia-reoxygenation whereas antimiR-21 treatment resulted in relative upregulation (**Figure 6-5B**). Such an opposing pattern of regulation was less apparent in HALLMARK_G2M_CHECKPOINT, another gene set enriched for miR-21 targets with 49 of the 204 genes (24.0%) being miR-21 targets (**Figure 6-5B**). Although there was significant downregulation of miR-21 targets with hypoxia-reoxygenation on the proteomics data, the converse pattern was seen with RNA analysis (**Figure 6-5B**). There was still a trend for upregulation of these targets with antimiR-21 treatment, as expected, but none reached significance (**Figure 6-5B**).

A final approach used to provide evidence of target engagement by antimiR-21 was enrichment analysis with a gene set of 149 miR-21 targets (MIR21_5P). In proteomics data, this gene set was positively enriched by antimiR-21 treatment and negatively enriched by hypoxia-reoxygenation, with the normalised enrichment score reaching significance for one timepoint in each comparison (**Figure 6-5C**).

Overall, across the multiple methods used there is some evidence of broad miR-21 target upregulation with antimiR-21 treatment, suggesting antimiR-21 has bound miR-21.

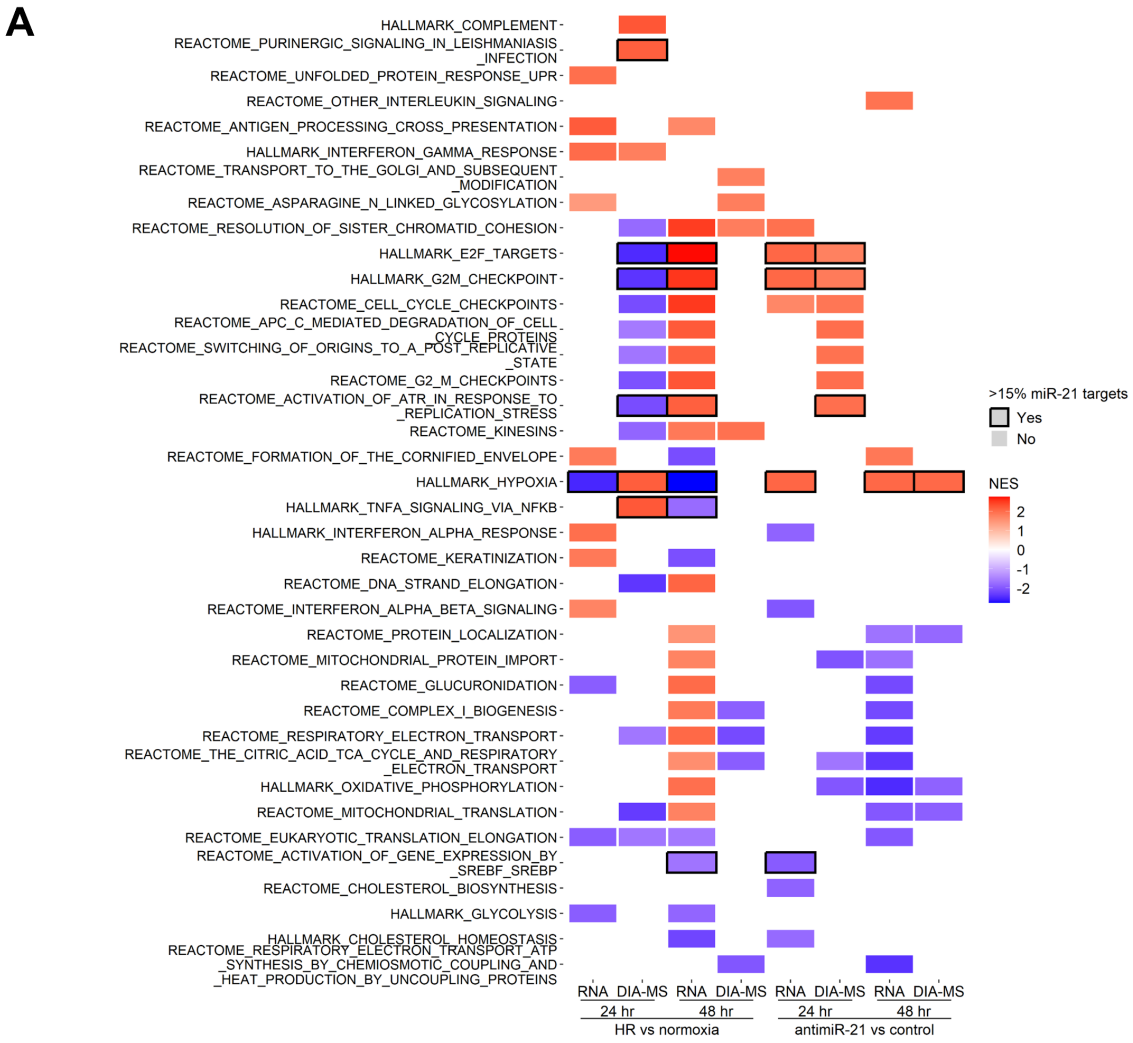
A
HALLMARK_COMPLEMENT
REACTOME_PURINERGIC_SIGNALING_IN_LEISHMANIASIS_INFECTION
REACTOME_UNFOLDED_PROTEIN_RESPONSE_UPR
REACTOME_OTHER_INTERLEUKIN_SIGNALING
REACTOME_ANTIGEN_PROCESSING_CROSS_PRESENTATION
HALLMARK_INTERFERON_GAMMA_RESPONSE
REACTOME_TRANSPORT_TO_THE_GOLGI_AND_SUBSEQUENT_MODIFICATION
REACTOME_ASPARAGINE_N_LINKED_GLYCOSYLATION
REACTOME_RESOLUTION_OF_SISTER_CHROMATID_COHESION
HALLMARK_E2F_TARGETS
HALLMARK_G2M_CHECKPOINT
REACTOME_CELL_CYCLE_CHECKPOINTS
REACTOME_APC_C_MEDIATED_DEGRADATION_OF_CELL_CYCLE_PROTEINS
REACTOME_SWITCHING_OF_ORIGINS_TO_A_POST_REPLICATIVE_STATE
REACTOME_G2_M_CHECKPOINTS
REACTOME_ACTIVATION_OF_ATR_IN_RESPONSE_TO_REPLICATION_STRESS
REACTOME_KINESINS
REACTOME_FORMATION_OF_THE_CORNIFIED_ENVELOPE
HALLMARK_HYPOXIA
HALLMARK_TNFA_SIGNALING_VIA_NFKB
HALLMARK_INTERFERON_ALPHA_RESPONSE
REACTOME_KERATINIZATION
REACTOME_DNA_STRAND_ELONGATION
REACTOME_INTERFERON_ALPHA_BETA_SIGNALING
REACTOME_PROTEIN_LOCALIZATION
REACTOME_MITOCHONDRIAL_PROTEIN_IMPORT
REACTOME_GLUCURONIDATION
REACTOME_COMPLEX_I_BIOGENESIS
REACTOME_RESPIRATORY_ELECTRON_TRANSPORT
REACTOME_THE_CITRIC_ACID_TCA_CYCLE_AND_RESPIRATORY_ELECTRON_TRANSPORT
HALLMARK_OXIDATIVE_PHOSPHORYLATION
REACTOME_MITOCHONDRIAL_TRANSLATION
REACTOME_EUKARYOTIC_TRANSLATION_ELONGATION
REACTOME_ACTIVATION_OF_GENE_EXPRESSION_BY_SREBF_SREBP
REACTOME_CHOLESTEROL_BIOSYNTHESIS
HALLMARK_GLYCOLYSIS
HALLMARK_CHOLESTEROL_HOMEOSTASIS
REACTOME_RESPIRATORY_ELECTRON_TRANSPORT_ATP_SYNTHESIS_BY_CHEMIOSMOTIC_COUPLING_AND_HEAT_PRODUCTION_BY_UNCOUPLING_PROTEINS
RNA DIA-MS RNA DIA-MS RNA DIA-MS RNA DIA-MS
24 hr 48 hr 24 hr 48 hr
HR vs normoxia
antimiR-21 vs control
>15% miR-21 targets
Yes
No
NES
2
1
0
-1
-2
B
HALLMARK_HYPOXIA
miR-21 targets
ZNF292
WSB1
VLDLR
VHL
VEGFA
TNFAIP3
TGFBI
SLC2A3
RBPJ
PPFIA4
PGM1
PGK1
NOCT
MYH9
MAP3K1
LDHA
KLHL24
KLF7
KLF6
IL6
IGFBP3
HSPA5
HK2
GAPDH
FOXO3
EGFR
CDKN1A
CCNG2
BCL2
ALDOA
log2FoldChange
0.5
0.0
-0.5
-1.0
-1.5
p.adj<0.05
Yes
No
RNA DIA-MS RNA RNA RNA DIA-MS
24 hr 48 hr 24 hr 48 hr
HR vs normoxia
antimiR-21 vs control
HALLMARK_G2M_CHECKPOINT
miR-21 targets
TPX2
TOP2A
TMPO
TGFB1
TENT4A
STMN1
SRSF2
SNRPD1
SMC4
SMC1A
RAD21
PURA
PRC1
PLK1
PBK
NUSAP1
NSD2
MYC
MEIS1
MCM6
MCM3
LMNB1
KPNA2
KNL1
HNRNPU
HMGB3
GSPT1
E2F2
E2F1
DMD
DDX39A
CDC25A
BUB1
BIRC5
ATRX
p.adj<0.05
Yes
No
log2FoldChange
0.5
0.0
-0.5
-1.0
DIA-MS RNA RNA DIA-MS
24 hr 48 hr 24 hr
HR vs normoxia
antimiR-21 vs control
C
MIR21_5P gene set (DIA-MS)
antimiR-21 vs control
hypoxia-reoxygenation vs normoxia
24hr
48hr
24hr
48hr
padj
0.04
0.08
0.12
-1
0
1
NES

Figure 6-5 Top enriched gene sets and modulation of miR-21 targets.
Gene set enrichment analysis on differential gene expression datasets from cell lysates analysed by bulk RNA sequencing (RNA) or liquid chromatography mass spectrometry-based proteomics using data-independent acquisition (DIA-MS). Primary human proximal tubule epithelial cells exposed to 24 hours of 1% oxygen (hypoxia) followed by reoxygenation and administration of 40 nM antimiR-21 or scrambled antimiR for 24 or 48 hours (antimiR-21 vs control). Control antimiR-treated hypoxia-reoxygenation samples compared to matched normoxia controls (HR vs normoxia). **A.** Shows normalised enrichment scores (NES) for list of gene sets that includes 4 most positively enriched and 4 most negatively enriched gene sets per dataset. Gene sets enriched for miR-21 targets are outlined. *P* values of NES were adjusted for multiple comparisons with Benjamini-Hochberg method and only NES with adjusted *P*<.05 are displayed. **B.** Shows differential gene expression of miR-21 targets within leading edge genes contributing to significant enrichment of selected gene sets, for those datasets in which these gene sets were significantly enriched. Genes that are significantly differentially expressed are outlined in black. **C**. Gene set enrichment analysis on DIA-MS datasets for the MIR21_5P gene set of miR-21 targets from msigdbr, of which 44 genes were present in the data. Adjusted *P* values (padj) of NES provided by Benjamini-Hochberg method.

6.3.3 Ingenuity pathway analysis

Pathway analysis was performed to predict the downstream effects of antimiR-21 treatment in the context of hypoxia-reoxygenation (

Figure 6-6A). Pathways relating to blood vessel formation, cell survival and migration were predicted to be modulated in a consistent direction regardless of whether the strict or relaxed thresholds were used for inclusion of genes in the analysis. These groups of pathways are displayed in
Figure 6-6B and show predicted activation by antimiR-21 treatment and inhibition with hypoxia-reoxygenation, thereby suggesting antimiR-21 treatment may counteract some of the response to hypoxia-reoxygenation.

RNA data predicted pathway modulation downstream of antimiR-21 treatment more commonly than proteomics data. Regardless, proteomics data was largely concordant with results from RNA data. For instance, proteomics data also predicted activation of vasculogenesis downstream of antimiR-21 treatment at both 24 and 48 hours of reoxygenation (Z scores 1.48 and 2.01 respectively) and with adjusted *P* values approaching significance at 0.081 and 0.056, respectively.

A

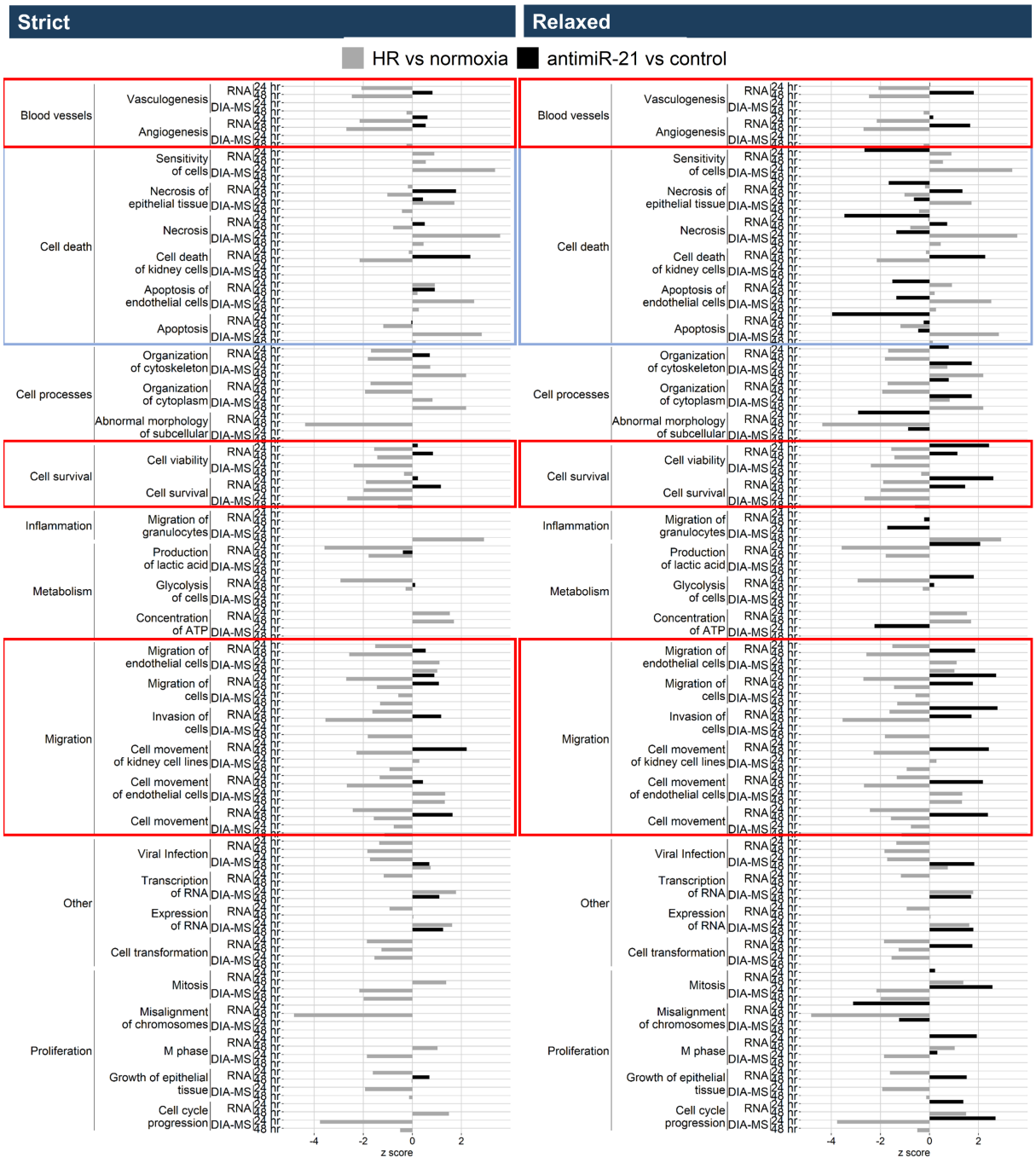
Strict
Relaxed
HR vs normoxia
antimiR-21 vs control
Blood vessels
Vasculogenesis
Angiogenesis
Cell death
Sensitivity of cells
Necrosis of epithelial tissue
Necrosis
Cell death of kidney cells
Apoptosis of endothelial cells
Apoptosis
Cell processes
Organization of cytoskeleton
Organization of cytoplasm
Abnormal morphology of subcellular
Cell survival
Cell viability
Cell survival
Inflammation
Migration of granulocytes
Metabolism
Production of lactic acid
Glycolysis of cells
Concentration of ATP
Migration
Migration of endothelial cells
Migration of cells
Invasion of cells
Cell movement of kidney cell lines
Cell movement of endothelial cells
Cell movement
Other
Viral Infection
Transcription of RNA
Expression of RNA
Cell transformation
Proliferation
Mitosis
Misalignment of chromosomes
M phase
Growth of epithelial tissue
Cell cycle progression
RNA 24 hr
RNA 48 hr
DIA-MS 24 hr
DIA-MS 48 hr
-4
-2
0
2
z score

B

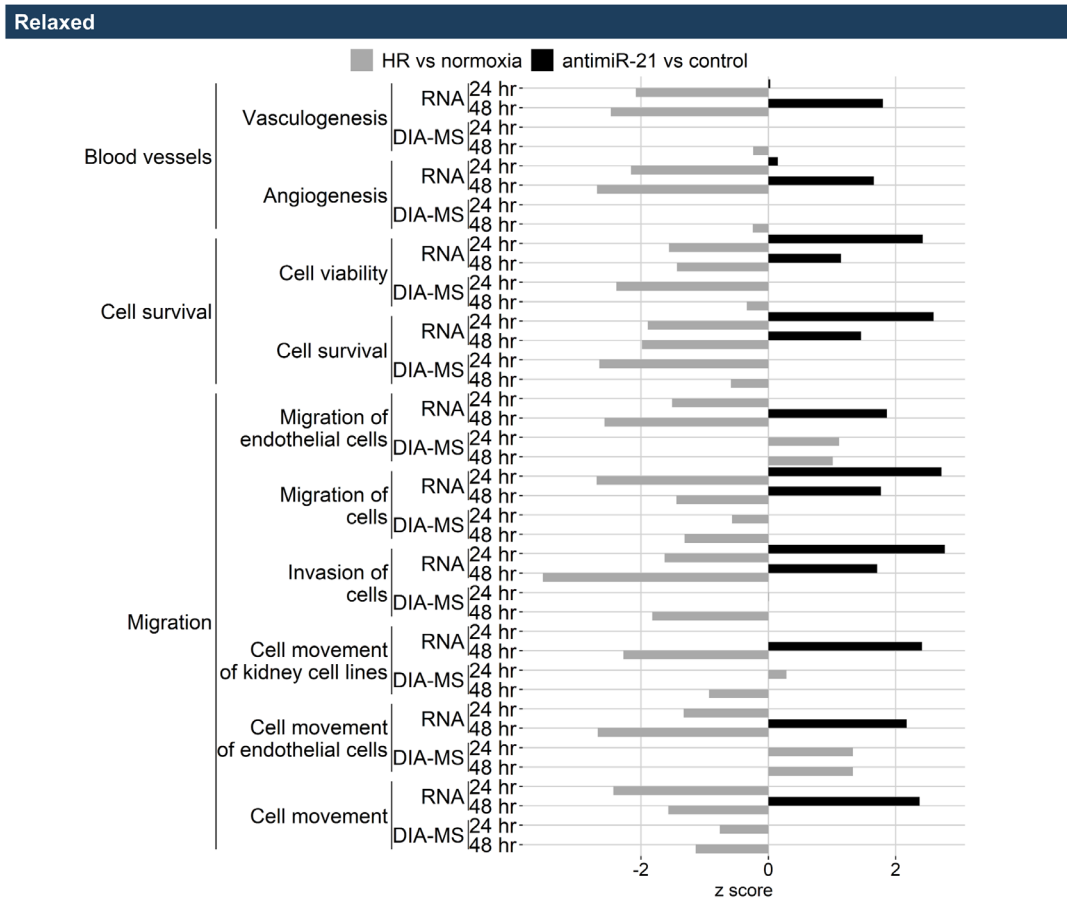

Figure 6-6 Ingenuity pathway analysis (IPA).
IPA using differential gene expression datasets from cell lysates analysed by bulk RNA sequencing (RNA) or liquid chromatography mass spectrometry-based proteomics using data-independent acquisition (DIA-MS). Primary human proximal tubule epithelial cells exposed to 24 hours of 1% oxygen (hypoxia) followed by reoxygenation and administration of 40 nM antimiR-21 or control antimiR for 24 or 48 hours with matched normoxia controls treated with control antimiR. Grey bars show predicted effect of hypoxia-reoxygenation compared to normoxia (HR vs normoxia). Black bars show predicted effect of antimiR-21 treatment at reoxygenation compared to control antimiR treatment. Log_2 fold change threshold of 0.2. All analysis of HR vs normoxia used a false discovery rate (FDR) after Benjamini-Hochberg correction of p values of 15% on DIA-MS datasets and 0.1% on RNA datasets. **A** Two sets of significance thresholds were used for inclusion of genes from antimiR-21 vs control datasets to enable at least 100 genes to be included with “Relaxed” thresholds. FDR 15% was used as “Strict” threshold for antimiR-21 vs control comparison and unadjusted *P* <.05 for “Relaxed” threshold. Positive z scores indicate predicted pathway activation and negative z scores indicate predicted inhibition. Only z scores with *P*<.05 after Benjamini-Hochberg adjustment for multiple comparison are displayed. Displayed pathways meet a z score threshold of 1.5 for both comparisons when analysis is performed with relaxed criteria. Red boxes outline groups of pathways that show concordance between strict and relaxed gene inclusion thresholds. Blue box highlights pathway groups that are inconsistent between inclusion thresholds in terms of predicted antimiR-21 effect. **B** shows selected groups of pathways of interest from relaxed analysis.

The effect of antimiR-21 and hypoxia-reoxygenation on the activity of upstream regulators was predicted and those regulators with confident predictions are detailed in

Figure 6-7A. Five regulators of interest for blood vessel formation (HIF1A, EPAS1, VEGF) and cell survival (STAT3, FOXA1) are highlighted in

Figure 6-7B. Again, there was a trend for antimiR-21 and hypoxia-reoxygenation to have opposite effects on the predicted activity of these regulators. AntimiR-21 treatment was predicted to increase the activity of HIF1A, EPAS1, VEGF and STAT3 but inhibit FOXA1, with the converse predicted for hypoxia-reoxygenation. This pattern was consistent across results from both the strict and relaxed gene inclusion criteria.

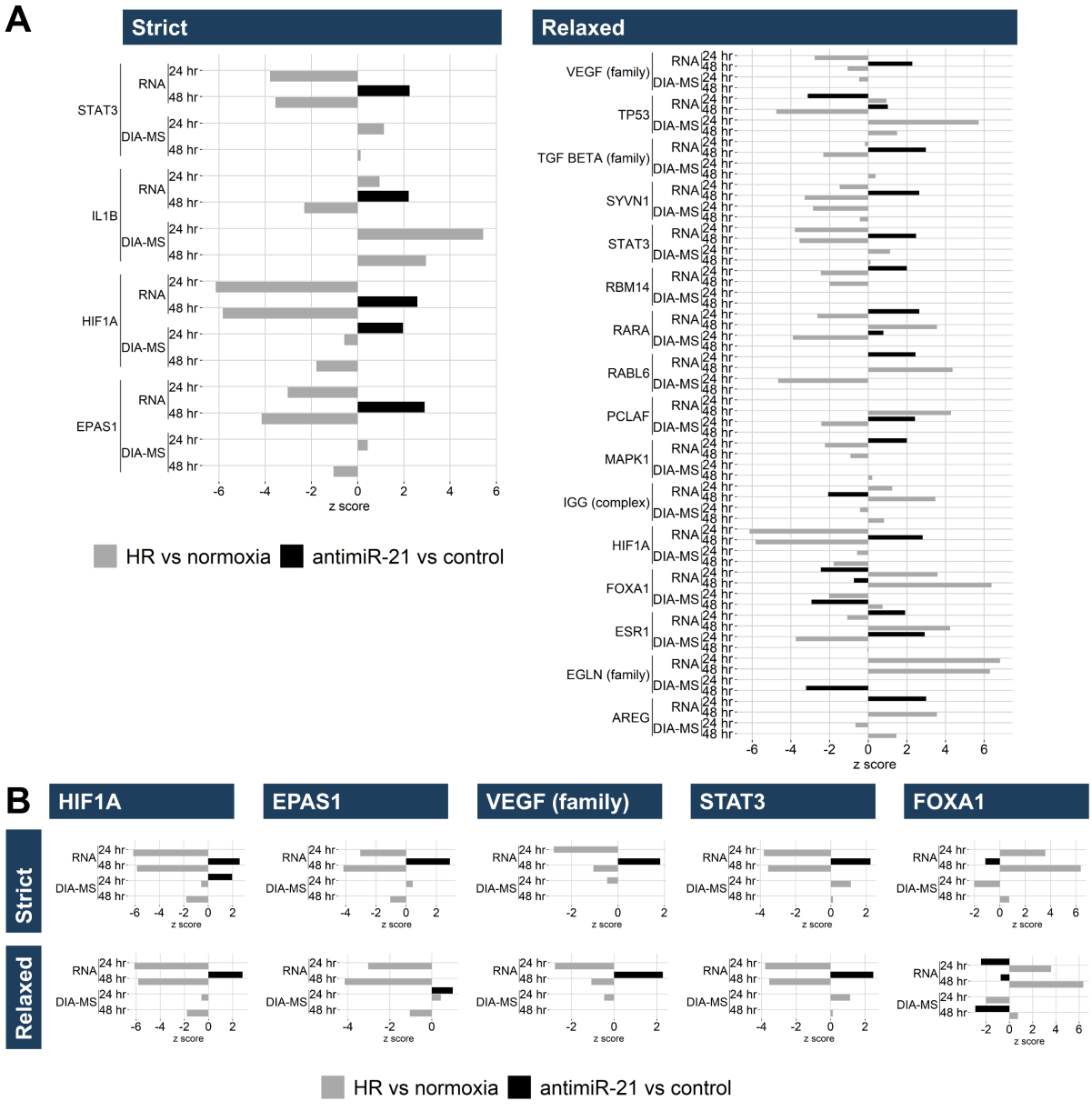

Figure 6-7 Predicted activity of upstream regulators.

Predicted activity of regulators determined by QIAGEN IPA (QIAGEN Inc., https://digitalinsights.qiagen.com/IPA) using differential gene expression datasets from cell lysates analysed by bulk RNA sequencing (RNA) or liquid chromatography mass spectrometry-based proteomics using data-independent acquisition (DIA-MS). Primary human proximal tubule epithelial cells exposed to 24 hours of 1% oxygen (hypoxia) followed by reoxygenation and administration of 40 nM antimiR-21 or control antimiR for 24 or 48 hours with matched normoxia controls treated with control antimiR. Grey bars show predicted effect of hypoxia-reoxygenation compared to normoxia (HR vs normoxia). Black bars show predicted effect of antimiR-21 treatment at reoxygenation compared to scrambled control antimiR treatment. Log_2 fold change threshold of 0.2. All analysis of HR vs normoxia used a false discovery rate (FDR) after Benjamini-Hochberg correction of *P* values of 15% for DIA-MS datasets and 0.1% for RNA datasets. Two sets of significance thresholds were used for inclusion of genes from antimiR-21 vs control datasets to enable at least 100 genes to be included with "Relaxed" thresholds. FDR 15% was used as "Strict" threshold for antimiR-21 vs scrambled comparison and unadjusted *P* value <.05 for "Relaxed" threshold. Positive z scores indicate predicted activation of upstream regulator with negative z scores indicating predicted inhibition. Only z scores with *P*<.05 after Benjamini-Hochberg adjustment for multiple comparison are displayed. **A** shows upstream regulators meeting a z score threshold of +/-2 for both comparisons as this indicates a more confident prediction. **B** shows predicted effect with both threshold methods for 5 selected upstream regulators of relevance to blood vessel formation and cell survival.

6.3.4 Correlation between RNA and proteomic results

As miRs can reduce the expression of their targets at a protein level without necessarily causing degradation of the bound mRNA, the correlation between RNA sequencing and proteomics results were explored.[72] In the datasets comparing gene expression in hypoxia-reoxygenation vs normoxia, RNA and proteomics data were largely positively correlated (**Figure 6-8A**). A positive correlation between RNA and proteomics data was also found for the datasets of antimiR-21 treatment vs control antimiR (**Figure 6-8B**). There was no correlation between proteomics data on the effect of antimiR-21 at the two timepoints of 24 and 48 hours of reoxygenation (**Figure 6-8B**).

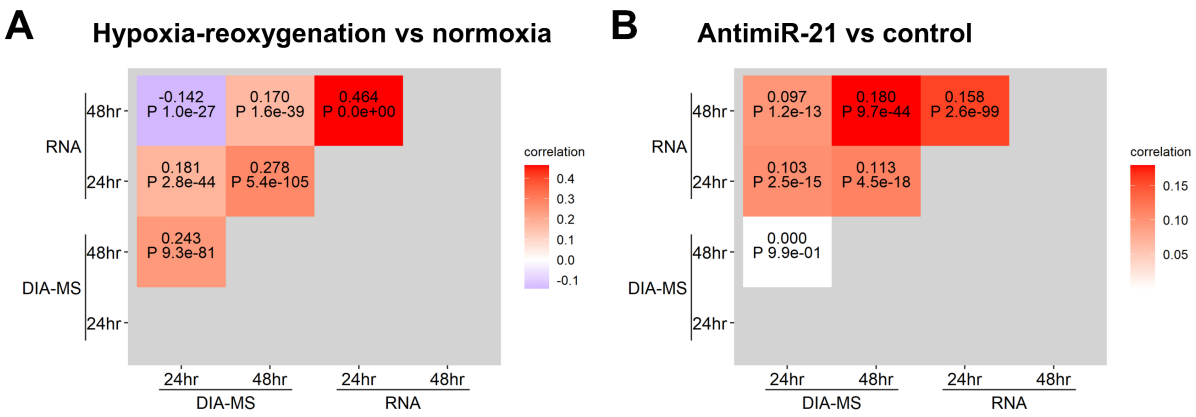

Figure 6-8 Correlation between RNA and proteomics data.
Heatmaps of pearson correlation coefficient between datasets of differential gene expression (DGE) assessed by bulk RNA Sequencing (RNA) or liquid chromatography mass spectrometry-based proteomics using data-independent acquisition (DIA-MS). **A** DGE in primary human proximal tubule epithelial cells (PTEC) exposed to hypoxia followed by either 24 or 48 hours of reoxygenation with 40 nM control antimiR treatment compared to matched normoxia controls. In **B**, DGE in PTEC exposed to hypoxia-reoxygenation with 40 nM antimiR-21 treatment compared to control scrambled antimiR treatment. Plots are annotated with correlation coefficient and *P* value.

6.3.5 Cytokine response

Cytokine levels secreted into the basolateral compartment were measured to assess the inflammatory response to hypoxia-reoxygenation and the impact of antimiR-21 treatment on this. There was a trend for increased IL-2, IL-6, IL-8 and TNFα secretion during hypoxia (**Figure 6-9A**). During reoxgenation IL-10, IL-2 and IL-8 levels significantly increased above normoxic levels (**Figure 6-9B**). AntimiR-21 treatment diminished this increase during reoxygenation for IL-10 and IL-2 (**Figure 6-9B**).

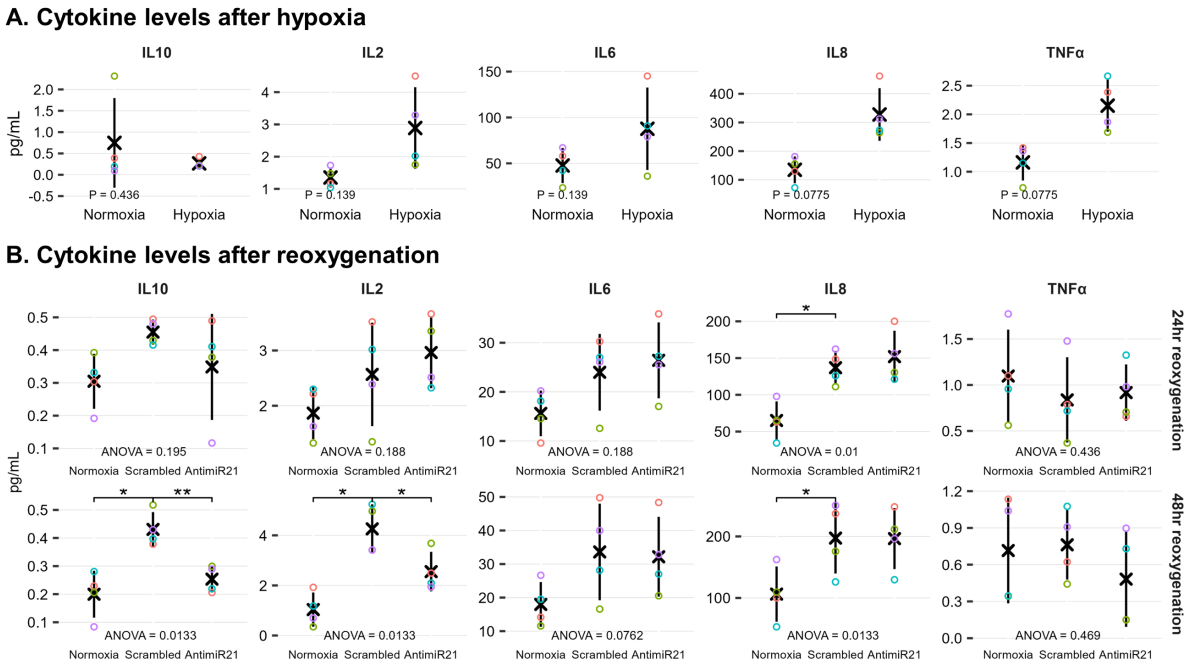

Figure 6-9 Cytokine levels measured in basolateral media of primary human proximal tubule epithelial cells (PTEC).
PTEC were maintained on transwell inserts. In **A** media collected after 48 hours of incubation either all in normal conditions (Normoxia) or with the final 24 hours in 1% oxygen (Hypoxia). Media was changed at the end of hypoxia to 40 nM of scrambled control antimiR or antimiR-21 in fresh maintenance media as the PTEC returned to normal conditions for the reoxygenation phase. Matched normoxia controls were treated with 40 nM scrambled control antimiR. PTEC were maintained for 24 or 48 hours of reoxygenation before collection of media in **B**. Media from matched normoxia controls was collected at the same time point. Mean ± standard deviation concentrations of 4 biological repeats are shown in black with results of individual repeats as coloured circles. Paired t test was used to assess for statistically significant difference between normoxia and hypoxia in **A.** *P* values adjusted by Benjamini Hochberg method are displayed for each cytokine. Repeated measures analysis of variance (RM-ANOVA) was performed for each panel in **B** and adjusted P values are displayed beneath each plot. Where a significant difference between groups was identified by RM-ANOVA, comparison against Scrambled was conducted with a paired t-test. Adjusted P values that reached significance are indicated by * *P*<.05, ** *P*<.01, *** *P*<.001

6.3.6 PTEC composition

To assess for evidence of epithelial cells from other nephron segments, the RNA counts of different markers were assessed in the 24-hour normoxia control samples of each primary human PTEC isolate (**Figure 6-10**). Counts generally clustered by gene but the counts detected for each proximal tubule cell marker was variable with *AQP1*, *LRP2* and *SLC5A2* (sodium glucose cotransporter 2) being the most highly expressed. The expression of markers from other nephron segments was generally lower, with the exception of the distal convoluted tubule marker *SLC12A3* which encodes the thiazide-sensitive sodium-chloride cotransporter.

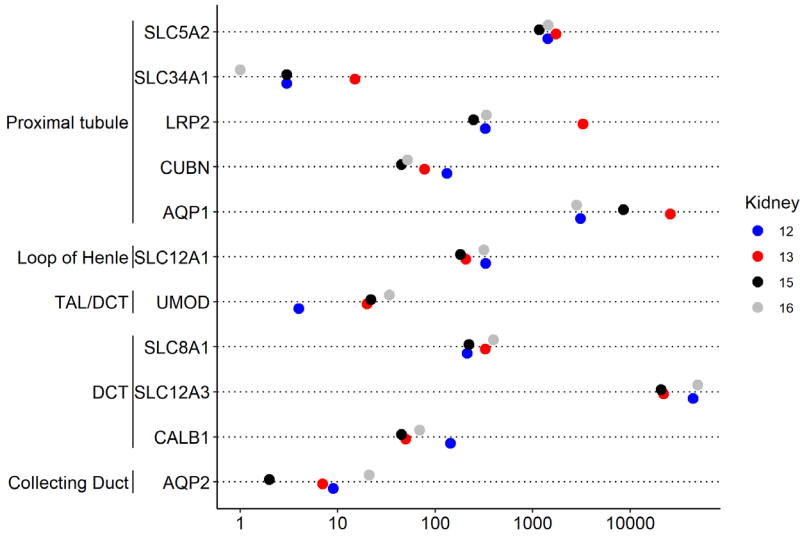

Figure 6-10 Sample composition assessment.
RNA counts of genes used as markers of different nephron segments in primary human proximal tubule epithelial cell isolates maintained in normoxia. Colours indicate the donor from which cells were isolated.

6.4 Discussion

In this chapter I have shown that antimiR-21 can modulate miR-21 targets in human primary PTEC exposed to a model of IRI. The use of primary human PTEC, which do not require transfection reagents to take up antimiR, adds important data to improve understanding on the downstream effects of antimiR-21 in this disease process.

A key finding in this chapter is the high biological variability between PTEC batches. Samples clustered predominantly by kidney donor rather than treatment type, whether that be hypoxia-reoxygenation vs normoxia or antimiR-21 vs control (**Figure 6-1**). By using paired samples, I was able to reveal the difference in gene expression likely attributable to experimental conditions, rather than donor. Unlike cell lines or animal models, using multiple isolates of primary cells allows identification of consistent downstream effects across biological repeats.

Although cell isolates are likely to include some epithelial cells originating from nephron segments other than the proximal tubule, marker counts appear broadly similar between repeats, suggesting a similar level of contamination in each batch. It is not possible to predict the level of contamination with this data but given the diffuse AQP1 positivity displayed on preliminary immunofluorescence data (**Figure 4-6**), it would seem low.

AntimiRs can block the action of their target miR without necessarily degrading it, and indeed, there was no reduction in miR-21 levels noted with antimiR-21 treatment in preliminary work (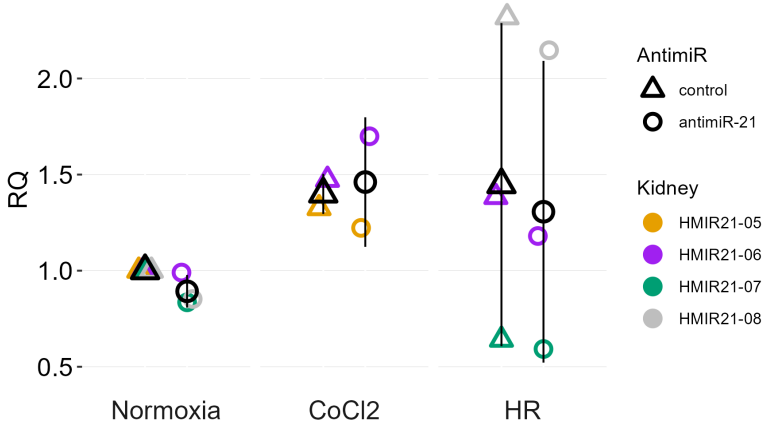

Figure 4-10).[72] Therefore, alternative approaches were taken to demonstrate antimiR-21 had engaged with its target miR-21. AntimiR-21 is predicted to disinhibit and so increase the expression of miR-21 targets. In keeping with this prediction, differentially expressed miR-21 targets were more likely to be upregulated than downregulated by antimiR-21 treatment at reoxygenation (**Table 6-4**). Similarly, a trend for increased expression with antimiR-21 treatment was noted in miR-21 targets within the leading edge genes contributing to enrichment of particular gene sets **Figure 6-5B**).

A gene set of miR-21 targets was also shown to be positively enriched with antimiR-21 treatment, at least within proteomics data at 24 hours of reoxygenation (**Figure 6-5C**). This enrichment was not observed in RNA data and may relate to how miR-21 targets were defined for this analysis. A gene can be designated a miR-21 target based on experimental or *il silico* data. I considered a gene a miR-21 target if there was experimental evidence to support this or it was predicted to be a target in at least 2 databases. miRDB includes within the MIR21_5P gene set, genes with a prediction score of at least 80 (within a range of 0 to 100) for being a miR-21 target.[143] As such, this is more restrictive and only 44 of these 149 genes were identified in either the RNA or proteomics analysis, despite over 900 miR-21 targets being identified in each dataset by the broader definition (**Table 6-6A**). Furthermore, none of the miR-21 targets that were differentially expressed with antimiR-21 treatment featured in the MIR21_5P gene set.[143] Similarly, of genes with existing data to support being important miR-21 targets in kidney IRI, only *SMAD7*, *PDCD4* and *RECK* met the required prediction score so *BAX*, *TLR4*, *MPV17L* and *PPARA* were not included.[21,78,79,88,99,101-108,143] Expression of all 7 of these genes was identified by RNA sequencing, whereas protein expression only detected *PDCD4* and *BAX*. It is

standard to limit gene sets to less than 500 genes to improve accuracy of normalised enrichment scores, as such, some restrictions on the miR-21 targets included will be required.[268,269] However, selecting the genes most relevant to the tissue and process being studied is challenging.

miR-21 expression has been shown to increase in ischaemia-reperfusion and in this model antimiR-21 was delivered at the point of reoxygenation, to mimic the reperfusion phase.[88,90,91] It is encouraging to note that even when delivered after the initial insult, miR-21 targets could be modulated by antimiR-21 and seemingly with opposite action to the effect of hypoxia-reoxygenation. There were 26 miR-21 targets differentially expressed downstream of antimiR-21 treatment in the context of hypoxia-reoxygenation and these genes were largely upregulated by antimiR-21. Downregulation of miR-21 targets by hypoxia-reoxygenation relative to expression in normoxia is in keeping with the expected increase in miR-21 activity with ischaemia-reperfusion.[88,90,91]

Key miR-21 targets identified as being upregulated by antimiR-21 in mouse and cell line models of kidney IRI, were not differentially expressed in this *in vitro* human model using primary PTEC. Some of these targets, such as *PDCD4*, are also thought to be upregulated by the stress of ischaemia-reperfusion alone and so unpicking the effect of this insult vs antimiR-21 could be challenging.[108] miR-21 targets are thought to vary by cell type and biological variability likely contributes to the differing results from my work.[207,270,271] Preliminary data did in fact show the expected *PDCD4* upregulation with hypoxia to be enhanced by antimiR-21 treatment, but only in PTEC from one donor (**Figure 4-12**).

Cell survival, cell migration, cell proliferation and blood vessel formation are all important processes for kidney repair after IRI.[33,34,272,273] Hypoxia-reoxygenation, was predicted to reduce the activity of these pathways (
Figure 6-6). AntimiR-21 was found to counter some of this effect particularly in the case of cell survival, cell migration and blood vessel formation (
Figure 6-6).

Conducting meaningful predictions of which biological pathways were likely to have been activated or repressed by antimiR-21 was challenging given the small number of differentially expressed genes. By comparison, many more genes were differentially expressed with hypoxia-reoxygenation alone and with greater fold changes. Confidence in the predictions was provided by concordance between results generated using either the relaxed or strict significance thresholds for gene

inclusion criteria, either timepoint and either type of input data (RNA vs proteomics) as well as the concordance between pathways relating to similar biological processes.

The predicted increased in blood vessel formation pathways downstream of antimiR-21 treatment is particularly interesting given the link between IRI, capillary rarefaction and the subsequent chronic hypoxia and detrimental impact on kidney function.[33,34]HIF-1α, HIF-2α (encoded for by *EPAS1*) and the VEGF family have a role in promoting blood vessel formation and were accordingly predicted to be regulators with increased activity downstream of antimiR-21 treatment.[33,53,54] Although expression levels do not directly relate to activity levels, it was interesting to note *VEGFA* expression was upregulated by antimiR-21 treatment and is listed as a miR-21 target (**Table 6-2**). The observed downregulation of *HIF1A* RNA expression by antimiR-21 treatment does not necessarily contradict this predicted increased in HIF-1α activity given this is more dependent on stability of the protein.[33]

Angiopoietin-like 4 *(*ANGPTL4*)* expression may also contribute to the predicted increase in blood vessel formation as it was found to be downregulated by hypoxia-reoxygenation with antimiR-21 preserving some of this expression (**Table 6-5**). Hypoxia is generally reported to upregulate ANGPTL4 downstream of HIF-1α and the contrasting finding in my data may relate to assessing expression during the reoxygenation phase.[274,275] One interpretation of the effect of antimiR-21 is therefore that it better preserves ANGPTL4 expression into the reperfusion phase.

ANGPTL4 is an important regulator of lipid metabolism but data on its role in kidney disease has produced mixed results.[274-280] It is likely that the action of ANGPTL4 is tissue and disease specific and may vary with sialylation state.[275,281] ANGPTL4 was pro-angiogenic in a mouse model of diabetes and a chicken chorioallantoic model and is thought to act both through and independent of VEGF to have this effect.[274,275]

The absence of a detrimental signal in cell survival pathways from antimiR-21 treatment is reassuring and in keeping with apoptosis assay results (**Figure 4-11**) which found no increase in cell death with these experimental conditions. The two regulators likely contributing to this improved cell survival are FOXA1 and STAT3. FOXA1 expression has been found to increase in models of sepsis- and radiation-associated kidney injury and be proapoptotic in these settings.[282,283] FOXA1 activity

was predicted to increase with hypoxia-reoxygenation but be reduced by antimiR-21 treatment.

STAT3 activation is generally associated with increased injury and apoptosis in models of kidney injury, including a mouse model of ischaemia-reperfusion.[284-287] However, Xu et al.[288] found enhancing the increase in activated STAT3 expression with IRI to be anti-apoptotic and anti-inflammatory in their mouse model of IRI. Interestingly, in my work STAT3 activity was predicted to be reduced by hypoxia-reoxygenation which is in contrast to these existing works, regardless of their findings on the downstream effects of STAT3. As my proteomics approach did not assess phosphorylation status, it is not possible to directly assess the accuracy of this particular prediction directly.

The miR-21 target most consistently upregulated in primary human PTEC by antimiR-21 treatment was IGFBP3. This gene was found to be downregulated by hypoxia-reoxygenation and antimiR-21 treatment appeared to preserve expression (**Figure 6-2C**). There is limited existing data on the role of IGFBP3 in IRI in the kidney but this upregulation may well contribute to the predicted increase in activity of cell survival pathways with antimiR-21.

Modulation of IGFBP3 expression by hypoxia appears to be cell-type specific. In a neuronal cell line used to model brain infarction, IGFBP3 was downregulated by hypoxia in keeping with the response I observed in PTEC.[289] In contrast, IGFBP3 levels were increased in patients experiencing acute myocardial infarction and also in a cardiomyoblast cell line exposed to hypoxia.[290,291] Similarly, in both *in vitro* and mouse models of ischaemic liver injury IGFBP3 levels increased with injury.[292]

There are 6 insulin like growth factor binding proteins and IGFBP3 is the most abundant.[293] IGFBPs have multiple mechanisms through which to enact their downstream effects.[293] In part, these proteins are important regulators of insulin like growth factors (IGFs) which have been implicated in modulation of cell proliferation and cell death.[293] The half-life of free IGF is a matter of minutes and so binding to IGFBPs is essential to stabilises them and increase delivery to the receptor IGF1R expressed on most cells.[293] Conversely, binding by IGFBPs can also inhibit the action of IGFs through sequestration.[293,294] IGFBPs also have IGF-independent action with IGFBP3 able to enter the nucleus by virtue of its nuclear localisation sequence.[293]

IGFBP3 is generally considered to suppress cell proliferation but the effect in human proximal tubule epithelial cells remains unclear. Data from glioblastoma models, mouse cardiac cells, primary human mesangial cells and a metastatic renal cell carcinoma cell line support IGFBP3 to suppress cell proliferation and this is thought to be an IGF dependent action.[294-297] However, in primary human PTEC derived either from normal or affected tissue of nephrectomies for renal cell carcinoma blocking IGFBP3 had no impact on proliferation.[297] These PTEC did express IGFBP3 and IGF-I but with relatively low levels.[297] There is likely to be some redundancy between IGFBPs, given mice and zebrafish develop normally when IGFBP3 is knocked out, and this could compensate for blocking *IGFBP3* particularly when baseline expression is low.[297]

The effect of IGFBP3 on cell death is less consistent and again may vary by cell-type. IGFBP3 was found to be pro-apoptotic in models of acute myocardial infarction and ischaemic liver injury as well as in mouse podocytes *in vitro*. [290,292,298] Conversely, it was protective against cell death in neuronal cell line used to model ischaemia-reperfusion.[289]

The trend for increased cytokine secretion observed at the end of hypoxia further validates the model in that the hypoxic insult was adequate to produce an inflammatory response.[33,34] Similarly, secretion of IL-10, IL-2 and IL-8 were increased by 48 hours of reoxygenation above baseline of cells maintained in normoxia, with a similar trend seen for IL-6.[33,34] AntimiR-21 was able to reduce IL-2 and IL-10 levels after 48 hours of reoxygenation. It is unclear what the net effect of such changes in cytokine secretion would be. Whilst a reduction in IL-2 secretion could be expected to have an anti-inflammatory effect in part through reduced activation of cytotoxic T cells, IL-10 is an anti-inflammatory cytokine and so a reduction in levels may well be detrimental.[33,34] Ultimately it would be interesting to understand how these cytokine secretion levels changed over a longer period.

There was positive correlation between differential gene expression analysis for RNA and proteomics-derived data, with correlation coefficients similar to what has been previously reported, particularly in data looking at the effect of hypoxia-reoxygenation.[299] The strength of correlation was moderate at best and lower correlation coefficients were generally observed in the data on antimiR-21 effect. The strength of correlation is likely reduced by the relative rates at which antimiRs are able to modulate RNA and protein levels, particularly for proteins with longer half-

lives. It may be that for this model, 24 hours is near the limit at which protein changes can be detected in response to antimiR treatment.

Using software to provide predictions on biological pathway activity can glean useful results but is ultimately limited by the relevance of input data to the cell type and disease process being studied. Through the combination of differential gene expression analysis, subsequent pathway analysis and immunoassay results for cytokine secretion, a schematic is proposed in **Figure 6-11** for the downstream effects of antimiR-21 treatment in human PTEC exposed to hypoxia-reoxygenation. Despite the limitations of a generic pathway analysis approach, it is reassuring to note that the above existing literature from kidney, IRI or hypoxia models supports the differentially expressed genes as largely modulating the identified pathways in the predicted manner or at least not have a consistent opposing effect to what has been predicted.

The data in this chapter finds primary human PTEC to be a feasible model in which to study gene expression changes downstream of antimiR treatment in kidney IRI. Gene expression changes downstream of antimiR-21 identified from work in IRI using small animal and cell line models were not found to be modulated in this human *in vitro* model, thereby highlighting the importance in using the most relevant models possible to identifying findings that might translate to people. It is promising to note that gene expression can be modulated even when antimiR-21 is delivered at reoxygenation and that the predicted downstream response is largely one that would encourage repair. Clearly, this *in vitro* model still has its limitations, particularly in that the response in cells other than the proximal tubule could not be directly assessed.

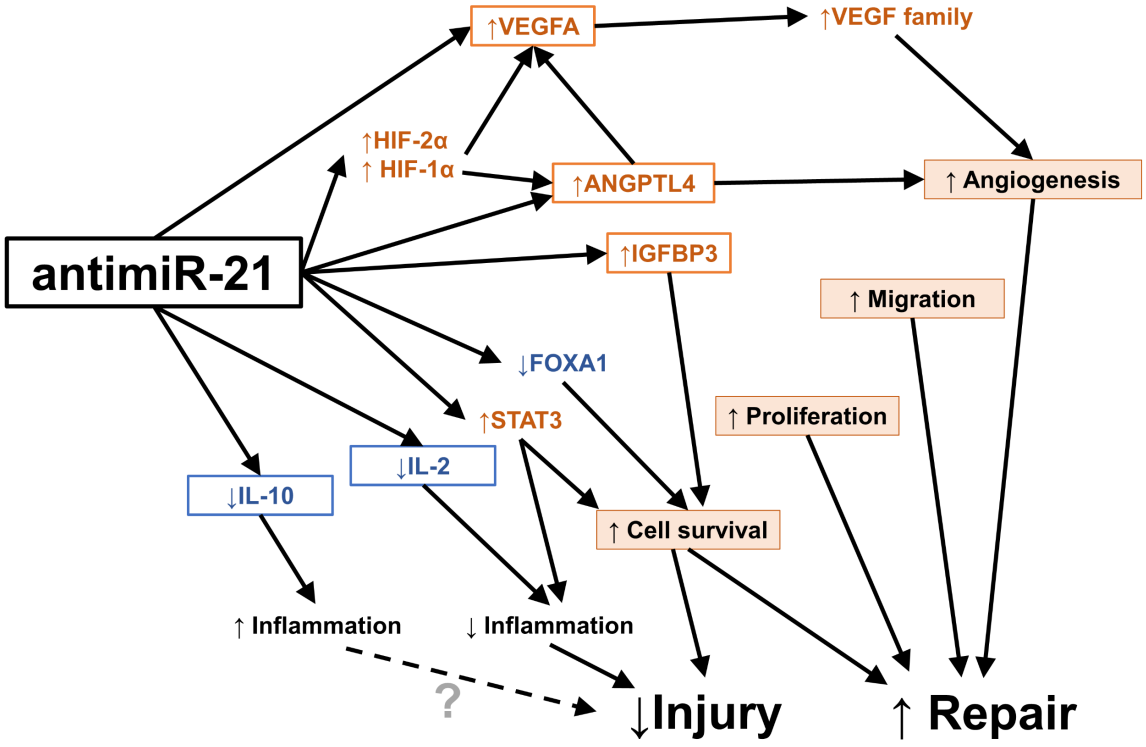

Figure 6-11 Proposed mechanism by which antimiR-21 treatment of primary human proximal tubule epithelial cells could increase repair and reduce injury following hypoxia-reoxygenation.
Proposed mechanism is based on results from bulk RNA sequencing and liquid chromatography mass spectrometry-based proteomics. AntimiR-21 was found to increase VEGFA, ANGPTL4 and IGFBP3 expression (outlined in orange). Secretion of IL-10 was reduced and IL-2 increased, as measured in media by immunoassay. Ingenuity pathway analysis predicted increased activity of the regulators HIF-1α, HIF-2α and the VEGF family of proteins which interact with ANGPTL4 and independently promote angiogenesis also. Activation of STAT3 and inhibition of FOXA1 could be expected to increase cell survival and, in the case of STAT3 also reduce inflammation. Biological pathways predicted to be activated by Qiagen IPA Software are shown in orange boxes. The effect on inflammation and injury remains less clear given the change in cytokine secretion observed.[33,34,272-275,282,283,288,289]

Chapter 7. AntimiR-21 delivery in normothermic machine perfusion

I lead on the perfusion experiments reported in this chapter but they were a team effort with contributions to set up, monitoring, sampling and clear up from Samuel Tingle, George Kourounis, Chloe Connelly, Beth Gibson, Sam Lee, Madi Cooper, Rhys Pook, Marnie Brown, and Lucy Bates.

7.1 Introduction

NMP can be used to model ischaemia-reperfusion in human kidneys from deceased donors and provides an opportunity to assess organ quality, assess potential therapeutics and recondition organs before implantation.[300-302] Although hypothermic and subnormothermic perfusion strategies are also used, normothermia has the advantage of preserving metabolic activity and so allowing active drug uptake.[97,303-306] Uptake of antimiR into human kidneys with this method is indeed temperature dependent.[97]

As the kidneys produce urine during NMP, crystalloid has generally been infused throughout to balance these losses.[97,307,308] However, recirculating the urine provides better stability to enable extended perfusions of 24 and 48 hours, expanding the utility of this model to explore the downstream effects of potential therapies.[307-309] In terms of drug deliver, recirculation also comes with the advantage of preventing urinary drug loss from the system.

The composition of perfusate for kidney perfusions is highly variable, particularly relating to nutrient and oxygen delivery.[310,311] Most will use a blood-based perfusate to ensure adequate oxygen delivery in normothermia, particularly for extended perfusions.[311] However, acellular methods which rely only on dissolved oxygen are appealing for preserving resources and there is also interest in synthetic oxygen carriers to replace the requirement for haemoglobin.[304,311,312] It is common to use 95% oxygen in kidney perfusions but providing a more physiological level of oxygenation in a red cell-based perfusate has not been shown to increase injury and instead perhaps provides a more relevant model of IRI at implantation.[307,311,313]

In terms of nutrients, it is common to provide some amino acids and glucose either with or without insulin.[97,307,310,311] Different segments of the nephron have different requirements for glucose and amino acids as substrates for metabolism so it seems sensible to provide both.[4,69] On the basis that humans need 50-100 g of glucose per day (in the form of carbohydrate) and kidneys are expected to consume 10% of this,

it seems appropriate to deliver 5 g of glucose per kidney for a 24 hour period.[69] Indeed this is similar to that provided by different published protocols.[97,307] Based on clinical protocols using insulin and glucose infusion to manage hyperkalaemia with the intent of being glycaemically neutral, it would be expected that only 2 units of insulin would be required for delivery of 5 g of glucose.[314] It is interesting to note that perfusions with either no insulin or 100 units of insulin have both maintained metabolic activity.[97,307]

Despite all these considerations, blood based NMP with urine recirculation remains an imperfect model of renal IRI but offers the best opportunity in which to assess potential therapeutics without the risk of harm to people. In addition to the concerns of waste and cytokine accumulation from recirculation, leukocytes are an important omission from the model in that they are key mediators of injury.[13,33,315]

In this chapter I have optimised 24-hour NMP for antimiR-21 delivery to human kidneys declined for transplantation by adapting the existing systems used at Newcastle University. I have demonstrated this to be a viable model in which to study the downstream effects of antimiR-21 treatment. As with *in vitro* work, the use of paired data has allowed better understanding of biological variability and generated a large human dataset on gene expression changes in renal IRI which can be further explored for alternative therapeutic targets.

7.2 Methods

Human kidneys declined for transplant and with appropriate consent for research were perfused using NMP for 24 hours. Three single kidneys were perfused to optimise the perfusion protocol. Five pairs of kidneys were used in the final experiment to determine the effect of antimiR-21 treatment.

7.2.1 Criteria for kidneys

Kidneys were not accepted for this study if the donor was known to have a blood borne virus, a CIT >30 hours was anticipated by the start of perfusion or renal malignancy was suspected in a kidney to be perfused. Pairs were only accepted if deemed likely well matched in size. All kidney offers were discussed with a surgical colleague before accepting to confirm anatomical suitability for perfusion. Kidneys were not accepted from donors requiring renal replacement therapy or with worsening AKI.

7.2.2 Perfusion protocol

Kidneys were prepared by surgical colleagues (Mr Samuel Tingle and Mr George Kourounis). The renal artery was cannulated with 12 Fr straight tip arterial cannula (Medtronic 77012) and the ureter cannulated with a 6-10 Fr feeding tube, depending on size (Vygon 311.06/08/10). For kidney pairs, the same size feeding tube was used to cannulate both ureters. In single optimisation kidneys HMIR21-17 and HMIR21-18, the vein was also cannulated (Medtronic 76024). All subsequent perfusions, including all pairs of kidneys, had free drainage of the vein into the reservoir. Kidneys were weighed before perfusion.

The perfusion set up is shown in **Figure 7-1**. Before connecting the kidney, the circuit was primed with perfusate components (**Table 7-1**), warmed to 37^{o}C and oxygenated with Medical Air (BOC) at 100 mL/min/kidney and Medical Oxygen (BOC) at 10 mL/min/kidney. Research grade packed red cells compatible with the donor blood group were the final component to be added.

Flow and pressures were zeroed and pH and gas analysis conducted on perfusate before connecting the kidney. The kidney was flushed with cool 0.9% sodium chloride and perfusion started by connecting the arterial cannula to the arterial limb of the circuit. Infusions commenced (**Table 7-1**) as clamps were released. For pairs of kidneys, the left kidney was always started first with the right kidney starting 5-10 minutes later. For pairs of kidneys, the left kidney was not connected until a minimum of 12 hours CIT had been achieved.

After the first single kidney perfusion, evaporation from the circuit was minimised by sealing the bowl as able with a single-use shower cap and rubber bungs for unused ports.

Figure 7-1 Perfusion set up for normothermic machine perfusion of pairs of human kidneys using urine recirculation.
Human kidney is sat on perforated plastic tray within covered glass bowel (**A**) and perfusate drains freely into the venous limb (**B**) of the perfusion circuit (Medtronic M449802B) to return to the reservoir (**C)** through a 30 µm filter. A centrifugal pump (**D**) pumps perfusate from the reservoir and on to the oxygenator (**E**, Affinity Pixie™ oxygenation system) to which tubing (**M**) delivers a mix of medical air (**L)** and medical oxygen (**K**). When required, the temperature of the perfusate is measured by connecting a thermometer (Digi-Sense® Thermistor Meter 2025-93) to a specific port in the oxygenator. The perfusate circuit next passes through a flow probe (**F**, Medtronic TX50P flow transducer). Pressure in the circuit is measured by a pressure probe (**G**) sat at the level of the kidney and connected to the arterial limb of the circuit (**H**) via a three-way tap (**G**). The arterial limb (**H**) carrying oxygenated perfusate connects to the kidney via the cannulated renal artery. The pump is controlled by Medtronic Bio-console 560 (**J** on the base of the trolley) which allows flow and pressure readings to be displayed on the screen (**I**). The circuit is warmed by warm water from the heat exchanger (**O**, Hico Hico-variotherm 550) flowing through the oxygenator (**E**) via the blue tubing shown. Infusions are controlled by 3 syringe drivers (**N**, Graseby 3100 and Alaris GH CareFusion) per kidney and are delivered into the reservoir (**C**) through central ports. The ureter of the kidney is cannulated with a feeding tube (**P**) allowing urine to be recirculated into the perfusate via the reservoir. When urine measurements and samples are required, this feeding tube is diverted to a 15 mL falcon tube on the side of the reservoir (**Q**). The perfusion circuit for the paired kidney is shown on the right of the image.

Kidney:	HMIR21-17	HMIR21-18	HMIR21-19	Pairs (per kidney)
Components added to reservoir				
Red blood cells	1 unit	1 unit	1 unit	1 unit
Albumin	250 mL of 5%	100 mL of 20%	100 mL of 20%	100 mL of 20%
Cefuroxime*	750 mg	750 mg	750 mg	750 mg
Ringers acetate	None	170 mL	170 mL	170 mL
Calcium gluconate 10%	10 mL	10 mL	10 mL	10 mL
Mannitol 10%	10 mL	20 mL	20 mL	20 mL
Sodium bicarbonate 8.4%	10 mL	25 mL (diluted with 75 mL of water)	15 mL (diluted in 42 mL of water)	15 mL (diluted in 42 mL of water)
Heparin	8000 units	5000 units (5 mL of 1000 units/mL) 2nd bolus given at 12 hours of 5000 units	5000 units (5 mL of 1000 units/mL) 2nd bolus given at 12 hours of 5000 units	5000 units (5 mL of 1000 units/mL) 2nd bolus given at 12 hours of 5000 units
Initial volume (without blood)	**306 mL**	**411 mL**	**368 mL**	**368 mL**
Infusions				
Actrapid® (insulin) 2 units in 24 hours	0.208 units/mL at 0.4 mL/hr	0.0208 units/mL at 4 mL/hr	0.0208 units/mL at 4 mL/hr	0.0208 units/mL insulin and 5% glucose mixed 50:50, infused at 8 mL/hr
Glucose 4.8g in 24 hours	50% at 0.4 mL/hr	5% at 4mL/hr	5% at 4mL/hr	
Epoprostenol sodium	5 µg/mL at 0.8 mL/hr	1 µg/mL at 4mL/hr	1 µg/mL at 4 mL/hr	1 µg/mL at 4 mL/hr
Synthamin with Cernevit	1.0 mL/hr	4.0 mL/hr	1.0 mL/hr	1.0 mL/hr
Total infusion rate	**2.6 mL/hr**	**16 mL/hr**	**13 mL/hr**	**13 mL/hr**

Table 7-1 Perfusate composition.
Components of starting perfusate and infusions for 24-hour normothermic machine perfusion of human kidneys. Composition for sequential single optimisation kidney perfusions (HMIR21-17/18/19) are given and the resulting composition for paired kidney perfusions where both kidneys from one donor are perfused simultaneously on separate circuits. All quantities and rates are per circuit. Each kidney in a pair received the same volume of red blood cells by mixing two units of red blood cells and adding half of the total volume to each circuit. For paired perfusions the volume of red blood cells added per circuit was 275-320 mL (median 280 mL) giving a total starting volume of 643-688 mL. Cefuroxime was diluted in 6 mL water. Amino acids were provided as synthamin 17 without electrolytes (Baxter Healthcare Ltd) containing 16.5 g/L nitrogen equivalent to 103 g/L protein. Synthamin was supplemented with 0.5 mL reconstituted multivitamin (Cernevit, Baxter Healthcare Ltd) per 50 mL Synthamin. Actrapid® Novo Nordisk 100 units/mL was diluted to working concentration with 0.9% sodium chloride. 20% albumin was Alburex® 20, CSL Behring UK Limited. The prostacyclin epoprostenol sodium was supplied as Flolan 0.5 mg Powder with Solvent for Solution from GlaxoSmithKline UK and diluted from 10 µg/mL to working concentration with 0.9% sodium chloride. Red blood cells were provided via NHS Blood and Transplant in a saline based solution containing adenine, glucose and mannitol (SAG-M solution). Ringers acetate Aquapharm no.9.

7.2.3 Perfusion parameter monitoring

The perfusion parameters of pump speed, pressure and flow were available continuously on the console and recorded every 30 minutes for 1 hour, hourly until 4 hours and 2-hourly until the end of perfusion, along with reservoir volume. Pump speed was adjusted to target pressure of 75 mmHg but with pressures of 85 mmHg tolerated if required to achieve a minimum flow of 100 mL/min/100 g kidney.

7.2.4 Urine output measurements and fluid sampling

Urine output was measured into a 15 mL centrifuge tube with volumes less than 2 mL being confirmed with a P1000 pipette. Urine recirculation into the reservoir was started after a period of stabilisation, specifically once the first 30 minutes or 10 mL of urine (whichever came first) was collected. This first urine was sampled with any excess being discarded. For all subsequent urine output assessments (at 1 hour, 2 hours and every 2 hours subsequently) time to 10 mL or volume in 20 minutes was recorded and any excess urine not required for sampling was returned to the reservoir to minimise losses. A 6 mL urine sample was collected if available 2 hourly for the first 4 hours and 4-hourly subsequently.

Blood gas analysis (using RAPIDpoint 500e Blood Gas System (Siemens)) was performed on approximately 200 µL of perfusate, collected after 1 mL was aspirated from tubing and returned to reservoir to remove the static volume. Blood gas analysis measured pH, haemoglobin oxygen saturation, pO_2, pCO_2 as well as haemoglobin, sodium, potassium, glucose, bicarbonate, lactate and calcium concentrations. Arterial limb samples were taken at each of the perfusion parameter time points. Additionally, venous limb samples were collected at 2 hours, 4 hours and every 4 hours subsequently to allow calculation of oxygen consumption by the following formula.

$$Oxygen\ consumption\ \left(\frac{mL\ of\ oxygen}{100\ mL\ of\ perfusate}\right) =$$

$$\left[1.39.Hb_{\frac{g}{dL}}.\left(\frac{FO_2Hb}{100}\right)_{arterial} + 0.023.pO_{2_{arterial}}\right] -$$

$$\left[1.39.Hb_{g/dL}.\left(\frac{FO_2Hb}{100}\right)_{venous} + 0.023.pO_{2_{venous}}\right]$$

$$Oxygen\ consumption\ (mL/min/kg) = \frac{Oxygen\ consumption_{mL/100mL}.Flow\ rate_{dL/min}}{weight\ of\ kidney_{kg}}$$

Notes: FO_2Hb is percentage of haemoglobin that is saturated with oxygen.

Perfusate samples (6 mL) were collected from the arterial limb of the circuit at the same time as urine samples, with the addition of a baseline sample taken before the kidney was connected.

Perfusate and urine samples were stored on ice for no longer than 8 hours before batches were centrifuged at 2000 RCF at 4^{o}C for 10 minutes and the supernatant aliquoted for storing at -80^{o}C.

7.2.5 Adjustments during perfusion

Target pO_2 was 10-26 kPa and target pCO_2 less than 6.0 kPa. The target range for sodium concentration was 130-160 mmol/L.

For kidney pairs, each circuit was adjusted individually based on measured parameters. Acidosis was balanced with 8.4% sodium bicarbonate at a volume of 5 or 10 mL if the pH was less than 7.20 or 7.10 respectively. If the sodium concentration was ≥145 mmol/L before supplementing, the sodium bicarbonate would first be diluted with 5 volumes of ultrapure water. A degree of acidosis was tolerated to avoid excessive addition of sodium.

The circuit was supplemented with 600 mg of glucose if concentrations were <4.0 mmol/L. The concentration of glucose used was determined by the sodium level in the perfusate with 5% and 50% glucose solution used for a sodium of ≥145 mmol/L of <145 mmol/L respectively. A higher dose of 1.2 g of glucose was added for glucose levels <1.5 mmol/L.

7.2.6 AntimiR treatment

To optimise the dose of antimiR required to ensure tubular uptake, single kidneys were treated with either 40 nM or 200 nM FAM-labelled scrambled control antimiR (Qiagen YC10202062-FZB) 2 hours into perfusion. The volume of 180 μM stock required to achieve this concentration was calculated based on the volume of perfusate components at the start of perfusion. Core biopsies were taken before perfusion, immediately before antimiR treatment and at 12 and 24 hours of perfusion.

Fluorescence (as a surrogate for antimiR concentration) in perfusate and urine samples was measured by diluting the sample 1 in 4 with Ringers acetate. Fluorescence in the FAM channel (excitation λ 485 nM, emission λ 530 nm) in 100 μL of diluted sample was measured by Teican Spark 20 M plate reader. Black-walled 96-well plates were used (Greiner 655087).

For paired perfusions, 100 μM stock of unlabelled scrambled control antimiR (Qiagen Custom Inhibitor invivo large scale 339204 ASO10MG-I-has-miR-21-5p YCI0202524) or antimiR-21 (Qiagen Custom Inhibitor invivo large scale 339204 ASO10MG-I-has-miR-21-5p YCI0199330) targeting miR-21-5P was added to the arterial limb of the circuit, once urine recirculation had started, to achieve a treatment concentration of 200 nM. After the kidneys had been surgically assessed as perfusable on arrival, randomisation (Simple Randomisation Service from www.sealedenvelope.com) was performed to determine whether the left or right kidney received antimiR-21, with the contralateral kidney receiving the control scrambled antimiR.

7.2.7 Biochemical analysis

A bolus of creatinine (10 mg in 0.5 mL, Sigma) was added to the perfusate once urine recirculation had started to allow calculations of creatinine clearance. Urinary and perfusate creatinine concentrations and urinary sodium concentrations were measured by the laboratory at Newcastle Upon Tyne NHS Foundation Trust. For selected optimisation work, perfusate osmolality was also reported. Perfusate sodium levels were taken from blood gas analysis.

Calculations used for creatinine clearance and fractional excretion of sodium are given below. Creatinine and sodium concentrations were in mmol/L.

$$Creatinine\ clearance\ \left(\frac{mL}{\min}\right) = \frac{Creatinine_{Urine}}{Creatinine_{Perfusate}}.UrineFlow_{mL/min}$$

$$Fractional\ excretion\ of\ sodium\ (\%) = \ 100\left[\frac{Sodium_{Urine}.Creatinine_{Perfusate}}{Sodium_{Perfusate}.Creatinine_{Urine}}\right]$$

7.2.8 Contrast enhanced ultrasound

Contrast enhanced ultrasound (CEUS) was performed on kidney pairs to assess microvascular perfusion 2 and 23.5 hours into machine perfusion. A view including both cortex and medullary pyramids was identified on ultrasound (Philips EPIQ7 ultrasound machine with QLab 8.1 Software, Philips) in the longitudinal plane using the eL18-4 probe covered with a sterile cover and placed onto the lateral edge of the kidney.

1 mL of sulphur hexafluoride microbubbles (SonoVue®, Bracco UK Ltd) reconstituted to 8 μL/mL was diluted further with 4 mL of perfusate in a 5 mL syringe and injected as a rapid bolus into the arterial limb of the circuit via a three-way tap. A cineloop was captured of at least 60 seconds from contrast administration. Contrast images were

acquired with 60% gain. The MFI overlay image was acquired with the same gain settings for all images from one pair of kidneys. Raw DICOM files were imported to QLAB Advanced Quantification Software (Release 15.5 Philips) and regions of interest (artery and a 25 mm^2 homogenous square of cortex) identified for analysis using ROI QApp. Signal intensity (dB) of each region was exported against time, with time zero taken as the first frame showing noticeable signal change from the administered contrast.

Data was cropped to 30 seconds and plotted as a curve with a loess span of 0.06 to smooth the data. Peak intensity and time to 90% of peak intensity in the cortex relative to the artery were outputted. Area under the curve (AUC) was calculated with the trapezoidal method for the first 10 seconds. Analysis was performed using a shiny app developed by Samuel Tingle (stingle.shinyapps.io/Time_intensity_analysis/) in R (R Foundation for Statistical Computing, Vienna, Austria).

7.2.9 Tissue sampling

Core biopsies were taken using the 23 mm throw of an 18 G BioPince™ Ultra full core biopsy instrument (Argon Medical 360-1580-02), expected to yield a core of tissue around 19 mm long. Biopsies were taken at a shallow angle to sample cortex before and at the end of perfusion for kidney pairs. Core biopsies were also taken at two timepoints during perfusion for single kidney optimisation perfusions.

Wedge biopsies were collected only at the end of perfusion and by cutting down the long axis from the lateral edge of the kidney to sample medulla and cortex as required.

Tissue stored in RNA later was no larger than 5 mm in any direction and stored in approximately 5 volumes of RNA later. Samples were kept at 4°C for 16-48 hours to allow the solution to permeate the tissue before long term storage at -80°C.

Tissue for formalin fixation was stored in 10% neutral buffered formalin for at least 24 hours before changing to PBS and ongoing storage at 4°C until paraffin embedding and sectioning and mounting of 3 µm sections.

To snap freeze, tissue was wrapped in foil and snap frozen on dry ice or in liquid nitrogen before ongoing storage at -80°C.

Tissue stored for later single-cell RNA sequencing was washed in PBS and stored in pre-cooled CryoStor® cell cryopreservation media CS10 (Sigma Aldrich C2874-100ML) in a Nalgene™ Mr Frosty® Freezing Container that had been pre-cooled to 4 degrees, for about 10 minutes, before transfer to -80ºC for at least 20 hours. Long term storage was in liquid nitrogen with all samples being transferred within 1 week.

7.2.10 Histology

Haematoxylin and eosin (H&E) staining

Formalin fixed paraffin embedded tissue sections were dewaxed and rehydrated with xylene and reducing ethanol dilutions (100%, 90%, 70%) followed by 3 minutes in running deionised water. Sections were stained with Mayers' modified haematoxylin (Sigma Aldrich 51275) for 15 mins, this was washed with alkaline tap water and then incubated with 1% acid alcohol for 90 seconds. After a further wash, sections were stained with eosin Y (Sigma Aldrich HT110316) and then washed and dehydrated with increasing ethanol dilutions followed by xylene (Honeywell 534056). Slides were mounted with DPX mountant (Sigma Aldrich 6522-500ML).

Periodic Acid Schiff (PAS) staining

Formalin fixed paraffin embedded tissue sections were dewaxed and rehydrated as above. Slides were immersed in periodic acid (Sigma Aldrich 395132) at room temperature for 5 mins, briefly rinse in deionised water and transferred to Schiff Reagent (VWR 351204L) for 15 minutes. The stain was developed by running in warm water until dark pink, approximately 3 minutes. Nuclei were counterstained for 90 seconds in Haemalum Mayer (TCS Biosciences HS315). Slides were rinsed in deionised water then rehydrated and mounted with DPX mountant.

Imaging

Bright field microscopy images of stained and mounted tissue sections were acquired with the CMOC colour camera SC50 and Cellsens Standard software using X20 objective.

7.2.11 Single-cell suspension

The process for generating a single cell suspension was optimised on kidney tissue after extended cold ischaemia, after perfusion and after cryopreservation.

Cryopreserved tissue was thawed in a 37ºC waterbath until just able to extract from cryopreservation media. Biopsy was washed by placing in cooled complete media in

a 12-well plate and briefly rocking by hand before transfer to a fresh well to repeat the process. Freshly collected tissue was rinsed with cool PBS.

Washed tissue was cut into 1 mm chunks using scissors. Minced tissue was added to 5 mL of digest solution (0.13 units/mL Liberase TM (Roche) and 40 units/mL DNase (Qiagen 79254) in RPMI-1640 (R8758 Sigma) supplemented with 2% Streptomycin/Penicillin) to incubating at 37^{o}C with gentle agitation (100 RPM) in a 50 mL falcon supported at around 40^{o}. Incubation time was 30 minutes for freshly collected tissue and 10-30 minutes for cryopreserved tissue.

The reaction was terminated with an equal volume of complete media (RPMI-1640 supplemented with 2% Streptomycin/Penicillin and 5% FBS) and disaggregated through a 70 µm cell strainer (Greiner 542070) using the butt of a 2 mL syringe. Disaggregated cells were washed by centrifugation at 300 RCF at 4^{o}C for 5 minutes and resulting supernatant stored on ice. The pellet was resuspended in no more than 100 µL of complete media with total volume including pellet recorded to calculate cell yield. Cell count was performed with trypan blue before diluting sample with a further 1-2 mL of complete media and repeating the wash step and cell count.

7.3 Results

7.3.1 Donor and kidney characteristics

Three single kidneys were used to optimise the protocol for 24-hour NMP with tissue from a further single-kidney (BRNMP05) used to generate a single cell suspension from cryopreserved tissue. Five pairs of kidneys were used for 24-hour NMP experiments to assess the effect of antimiR-21 treatment. The details of the donors and kidneys are given in **Table 7-2**. Kidneys within each pair were well matched in size (**Table 7-3**). The donor for kidney pair HMIR21-20 was graded as D2 on the UK donor risk index category whereas all other kidney pair donors were in the highest risk category, D4.[316]

A. Kidneys for optimisation work

Study ID	Side	CIT	Age	Sex	Type	BMI	Weight	HTN	PVD	CVD	Diabetes	Admission Cr	Latest Cr	COD	Reason for decline
HMIR21-17	L	22	48	M	DCD	33	117	Yes	No	No	T2DM	64	53	HBD	Malignancy: solid suspicious mass on right kidney
HMIR21-18	R	10	76	M	DCD	23	70	No	No	No	No	125	76	HBD	Age and history
HMIR21-19	R	21	64	F	DBD	24	60	Yes	No	No	No	45	44	ICH	Anatomy: damage to vein and artery at retrieval
BRNMP05	L	18	72	M	DCD	30	77	Yes	No	No	T2DM - med	54	55	ICH	All centres declined after fast track

B. Kidney pairs

Study ID	CIT	Age	Sex	Type	BMI	Weight	HTN	PVD	CVD	Diabetes	Admission Cr	Latest Cr	COD	Reason for decline
HMIR21-20	15.5	42	F	DBD	23	62	No	No	No	No	98	166*	HBD	Malignancy: suspicious necrotic mass on pancreas
HMIR21-21	18	72	F	DCD	24	63	Yes	Yes	Yes	T2DM - insulin	68	50	HBD	Malignancy: pelvic mass without available histology service
HMIR21-22	29	73	M	DBD	25	74	No	No	No	T2DM - diet	83	77	HBD	Glomerulosclerosis on punch biopsy of right kidney and CIT
HMIR21-23	29.5	73	M	DBD	22	75	Yes	No	Yes	No	80	76	ICH	Malignancy: insufficient biopsy of spleen to conduct all required tests
HMIR21-24	13	79	F	DCD	23	64	No	No	No	No	48	55	ICH	Anatomy: calcified aortic patch
Summary	21 ± 8	68 ± 15	60% F	60% DBD	23 ± 1	68 ±6	60% had a comorbidity listed				75 ± 19	65 ± 14	60% HBD	60% malignancy

Table 7-2 Donor and kidney characteristics for normothermic machine perfusion.

Details of donors (by Study ID) and kidneys used for optimisation (**A**) and paired perfusions to assess the effect of antimiR-21 treatment (**B**). Kidneys from BRNMP05 in **A** were not perfused as part of this work but end perfusion tissue was used to optimise single-cell digest after cryopreservation. Kidneys from donors HMIR21-17 to 19 were used for single kidney perfusions to optimise 24-hour normothermic machine perfusion. In **A**, whether the left (L) or right (R) kidney was used is indicated. Paired perfusions used both kidneys. Cold ischaemic time (CIT) at the start of perfusion is given in hours to the nearest half hour. Kidneys within a pair were staggered by no more than 10 minutes and CIT is given for the first kidney to be perfused. Age is recorded in years. Kidneys from donors donating after brainstem death (DBD) and circulatory death (DCD) were included. Normothermic regional perfusion was not used. Whether the donor was known to have hypertension (HTN), peripheral vascular disease (PVD), cardiovascular disease (CVD) or diabetes is indicated. Where known, treatment for type 2 diabetes (T2DM) is categorised as insulin, diet or other medication (med). Cause of death (COD) was hypoxic brain damage following cardiac arrest (HBD) or intracranial haemorrhage (ICH). The reason the kidney was declined for clinical transplantation is given. Summary shows the mean ± standard deviation (to the nearest integer) for numerical variables or the % in the most frequent categorical variable for **B**. Weight is recorded in kg. BMI, body mass index; Cr, serum creatinine in μmol/L; F, female; M, male. *Resolving acute kidney injury with previous reading of 219 μmol/L.

Study ID	Kidney weight (grams)		Kidney that received antimiR-21	Minutes between kidneys
	AntimiR-21	Control		
HMIR21-20	164	161	Left	9
HMIR21-21	232	233	Right	6
HMIR21-22	238	225	Left	7
HMIR21-23	195	192	Left	9
HMIR21-24	159	157	Right	10
Mean ± SD	197.6 ± 36.9	193.6 ± 35.2		

Table 7-3 Kidney pair weights and randomisation.
Weights of human kidneys within pairs used for 24-hour normothermic machine perfusion to assess the effect of antimiR-21 vs control treatment. Kidneys were weighed before perfusion. The kidney that received antimiR-21 treatment is indicated with the contralateral, control kidney, receiving scrambled antimiR. The start of perfusions was staggered with the left kidney perfused first. The interval before the right kidney commenced is provided. There was no difference in kidney starting weights between those assigned the two treatments (*P*=.166, paired t test). SD, standard deviation (SD)

7.3.2 Biochemical improvement within optimisation

Maintaining a stable volume and sodium concentration was challenging during the first single kidney perfusion. Sodium concentrations rose to supraphysiological levels of >180 mmol/L and supplementation with crystalloid boluses was required to ensure the reservoir volume was adequate to avoid air being pulled through the circuit. The difficulties with volume maintenance were attributed to water loss through the evaporation that occurs from maintaining a circuit that is not fully enclosed at 37^{o}C for an extended period. Additionally, 8.4% sodium bicarbonate was administered to balance pH and has a sodium concentration of 1000 mmol/L, therefore contributing to the rising sodium levels. Adaptations to the perfusate composition, infusion rates and circuit to reduce sodium delivery and compensate for and limit water evaporation achieved more physiological sodium levels and maintained the perfusate volume (**Figure 7-2**). Perfusate osmolarity was supraphysiological but not dissimilar from commercially available perfusates.

The oxygenator used for these perfusions is only recommended for 6 hours use but was able to maintain adequate oxygenation and carbon dioxide clearance throughout the 24 hours of perfusion (**Figure 7-2**). Metabolic activity was maintained in the kidney as shown by steady oxygen consumption rates (**Figure 7-2**).

Perfusion parameters appeared stable through the perfusion for all three kidneys and urine output continued to 24 hours. There was an initial period of increased

resistance on starting perfusion but from approximately 2 hours onwards this had resolved and the pump speed required little adjustment to maintain perfusion pressures around 75 mmHg (**Figure 7-2**).

H&E staining on core biopsies taken before, after and during perfusion confirmed the use of a shallow angle when collecting these biopsies was capturing cortex, as intended (**Figure 7-3**). Tubules showed evidence of injury with vacuolation, thinning and loss of brush border (**Figure 7-3**). In the kidney subjected to high sodium levels (HMIR21-17) the extend of vacuolation was severe and may be in part the result of osmolar damage (**Figure 7-3**). The tubular appearance was improved in HMIR21-18 and HMIR21-19 which were exposed to more physiological sodium levels (**Figure 7-3**).

Perfusion parameters

Haemodynamics

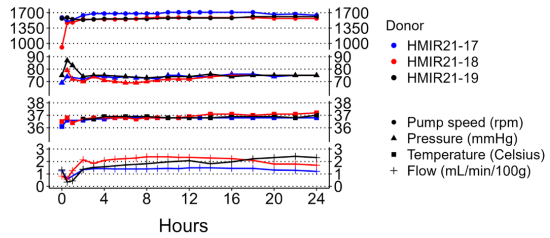

Resistance index

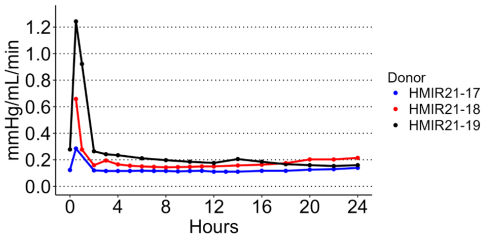

Volume

Infusion rate

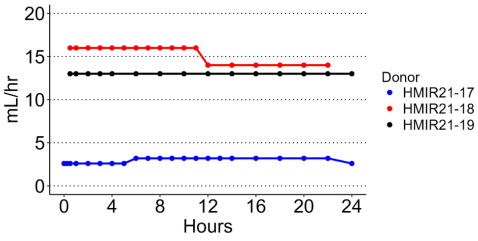

Reservoir volume

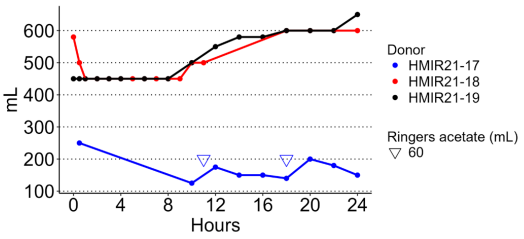

Gas delivery and metabolic activity

Oxygen and carbon dioxide partial pressures

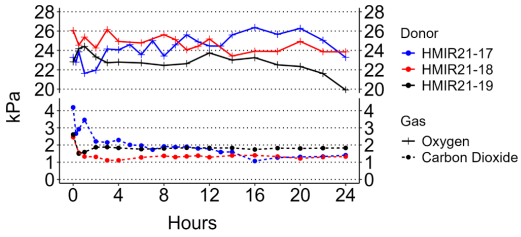

Oxygen consumption

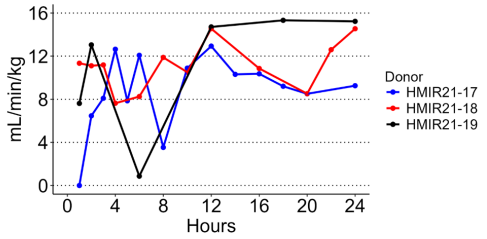

Perfusate glucose

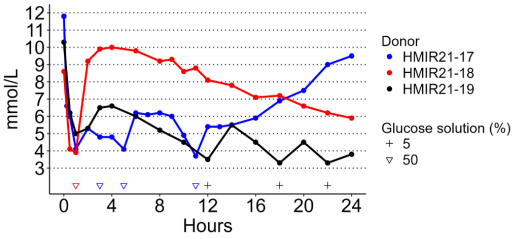

Perfusate biochemistry

Perfusate lactate and potassium

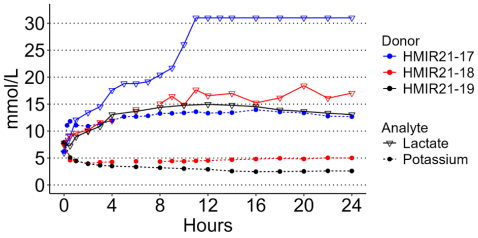

Perfusate sodium

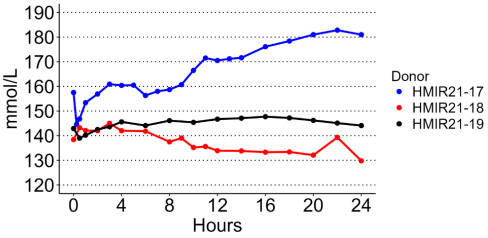

pH stability

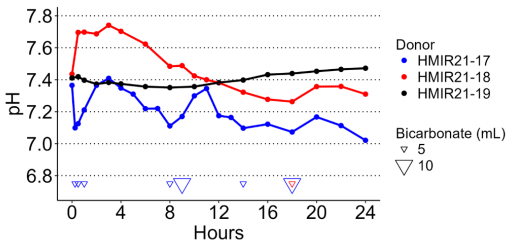

Perfusate Osmolality

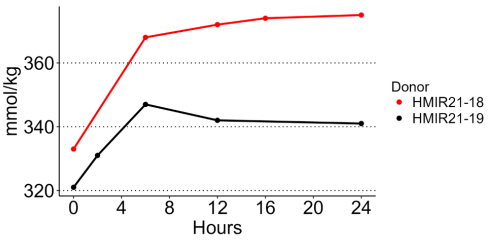

Function

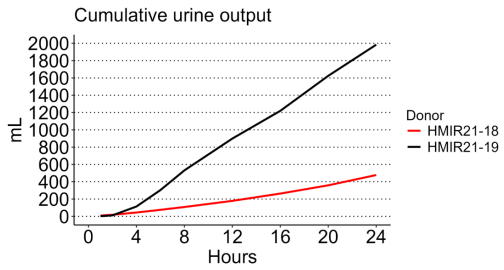

Figure 7-2 Kidney perfusion parameters in optimisation perfusions. Measurements from three single kidneys (HMIR21-17, 18 and 19) perfused to optimise the perfusate composition and set up for 24-hour normothermic machine perfusion with urine recirculation. Perfusion parameters gives perfusion pressure, temperature, flow per 100 g of kidney and pump speed in revolutions per minute (rpm). Resistance Index is calculated by dividing pressure by flow with increasing values indicating higher resistance to perfusion. Volume gives the rate of infusions going into the reservoir and the estimated volume in the reservoir. The timing and mL of ringers acetate used to supplement the perfusate for HMIR21-17 is given. Gas delivery and metabolic activity gives the partial pressures of oxygen and carbon dioxide and oxygen consumption per kg of kidney tissue. Glucose concentration in the perfusate is given and the % of the glucose solution used to deliver 600 mg boluses at the indicated time point are given. Perfusate biochemistry displays the concentrations of lactate, potassium and sodium in the perfusate and the osmolality when measured. The pH of the perfusate is displayed with the timing and volume of boluses of 8.4% sodium bicarbonate. Urine output is only displayed for 2 kidneys as there was damage to the ureter of HMIR21-17 making measurements unreliable.

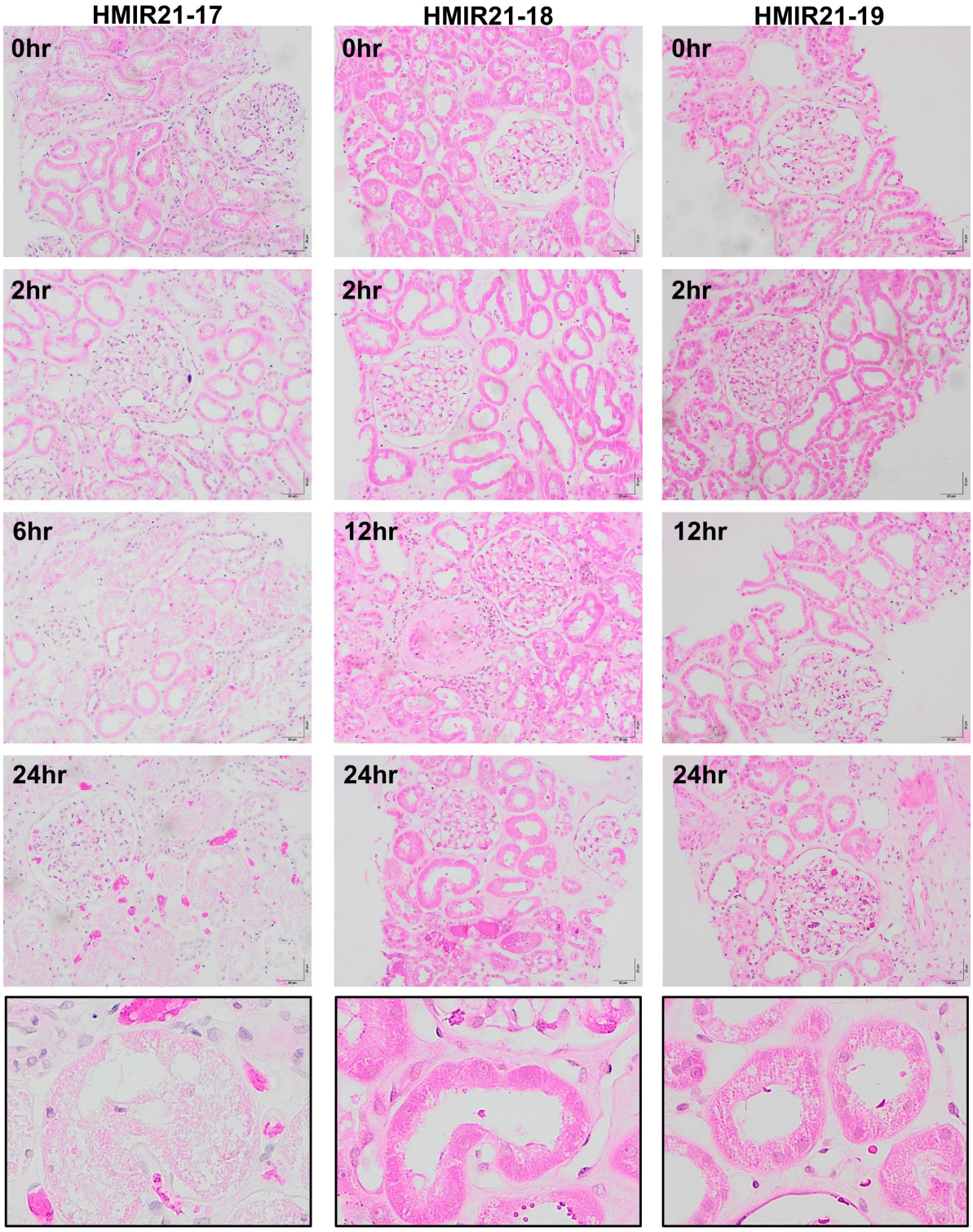

Figure 7-3 Histology of kidneys in optimisation perfusions
Haematoxylin and eosin staining on formalin fixed paraffin embedded core biopsies from human kidneys (HMIR21-17 to 19) perfused for 24 hours using normothermic machine perfusion with urine recirculation. These kidneys were perfused successively for optimisation and as such changes to the perfusate and set up were made between perfusions. Biopsies were taken before perfusion (0hr), during and at the end of perfusion (24hr). Outlined in black are magnified tubules from the end perfusion timepoint showing an improvement in the level of vacuolation in HMIR21-18 and HMIR21-19 compared to HMIR21-17. Images acquired with CMOC colour camera SC50 and Cellsens Standard software using X20 objective.

7.3.3 AntimiR dose optimisation

A further aim of optimisation perfusions was to establish the dose of antimiR required to ensure tubular uptake within the perfusion timeframe. As a concentration of 40 nM was used for *in vitro* work this was first assessed. Administering 40 nM of FAM-labelled antimiR resulted in at least a doubling of fluorescent signal in both the perfusate and urine (**Figure 7-4A**). However, the pattern of fluorescence within tissue sections was not convincing for cellular uptake as although the cytoplasm did appear brighter than the autofluorescence of the pre-antimiR samples, signal was most intense in the basement membrane of the tubules (**Figure 7-4B**). In contrast, a 200 nM dose was associated with an approximately 10-fold increase in perfusate fluorescence and 5-fold increase in urine fluorescence (**Figure 7-4A**). There was clear signal within cells on fluorescent microscopy with the 200 nM dose of antimiR (**Figure 7-4B**). The use of urine recirculation ensured antimiR was not lost from the system and accordingly perfusate fluorescence remained above baseline to the end of perfusion with both doses (**Figure 7-4A**).

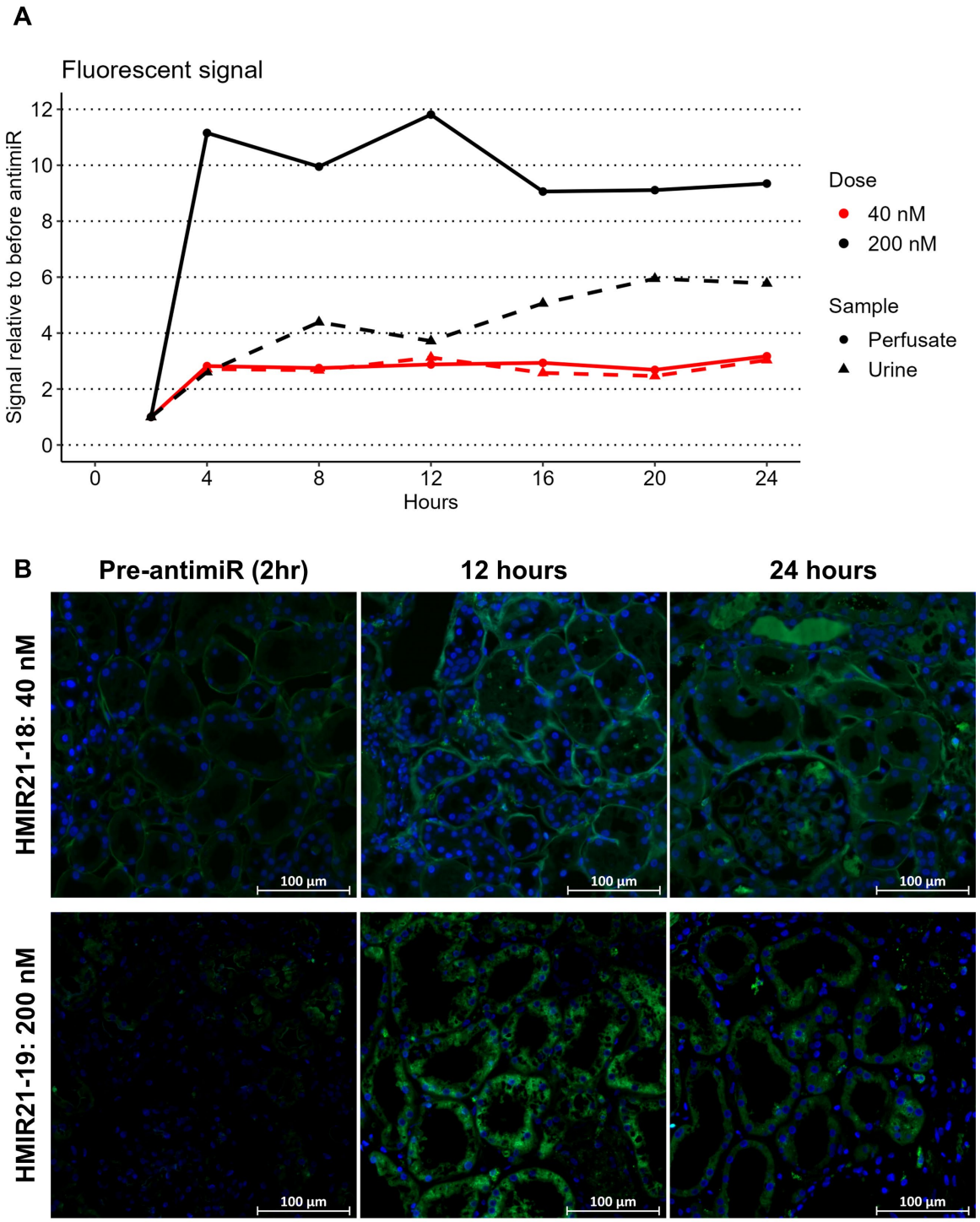

Figure 7-4 AntimiR dose optimisation.
Optimisation of antimiR dose to be administered to human kidneys during 24-hour normothermic machine perfusion with urine recirculation. FAM-labelled antimiR was administered as a bolus after 2 hours of perfusion to achieve a concentration of 40 nM or 200 nM. **A** shows fluorescent signal in the FAM channel in the perfusate and urine, relative to baseline (pre administration) levels of fluorescence. **B** shows widefield fluorescent microscopy of formalin fixed paraffin embedded core biopsies taken 2 hours into perfusion (just prior to antimiR administration) and 12 and 24 hours into perfusion. Nuclei are counterstained with DAPI (blue) and FAM channel signal is shown in green. The kidney IDs and administered antimiR concentrations are given on the left. Images acquired with X40 objective on ZEISS Axio Imager. FAM, fluorescein amidites

7.3.4 Stability of 24-hour paired perfusions

Measurements taken during paired kidney perfusions are shown in **Figure 7-5** with the additions made to the perfusate detailed in **Table 7-4**. Resistance in the kidneys was highest in the first two hours of perfusion after which flows of >100 mL/min/100 g of kidney were generally achieved.

The kidneys maintained metabolic activity throughout perfusion with the oxygen consumption rate remaining relatively stable. All but one kidney (HMIR21-23 control-treated) required glucose boluses, in addition to the continuous glucose infusion, to maintain concentrations above 4 mmol/L (**Table 7-4**). Lactate levels generally rose during perfusion but did not exceed 20 mmol/L and pH levels were maintained above 7.1 by supplementing with no more than 10 mL 8.4% sodium bicarbonate throughout perfusion (**Table 7-4**, **Figure 7-5**). Aside from one reading of 129.3 mmol/L at 24 hours (HMIR21-24 antimiR-21-treated), sodium concentrations were maintained between 130 -155 mmol/L (**Figure 7-5**).

Kidneys were well matched with no significant effect of antimiR treatment on perfusion measures (P>.05, two-way RM-ANOVA). pH, partial pressures, haemoglobin, sodium, potassium, glucose, lactate, urine rate, creatine clearance, perfusion pressure, perfusate flow and reservoir volume varied with time (P<.05, two-way RM-ANOVA with Benjamini-Hochberg adjustment for multiple comparison). However, all parameters remained broadly stable and within acceptable limits (**Figure 7-5**).

Creatinine clearance and fractional excretion of sodium were calculated as commonly used measures of function and were similar between antimiR treatments (**Figure 7-5**). A single kidney perfused in isolation was not expected to produce clinically meaningful values for these measures, particularly given the absence of aldosterone and anti-diuretic hormone in this model which are key for sodium reabsorption.[65]

Urine production continued throughout perfusion and there was no difference in total urine output by antimiR-21 or control treatment (P=.609, paired t test).

Perfusion parameters

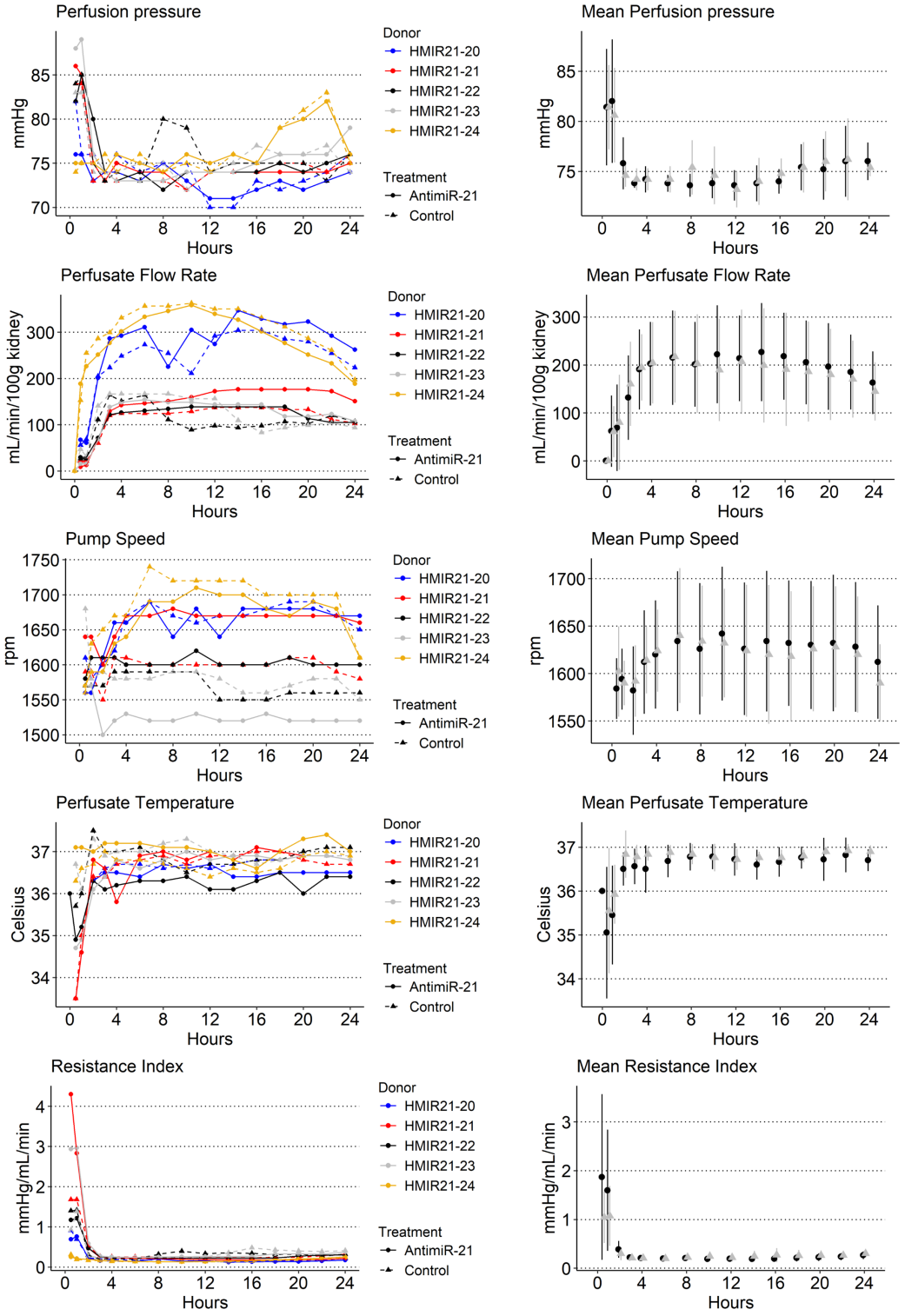

Gas delivery and metabolic activity

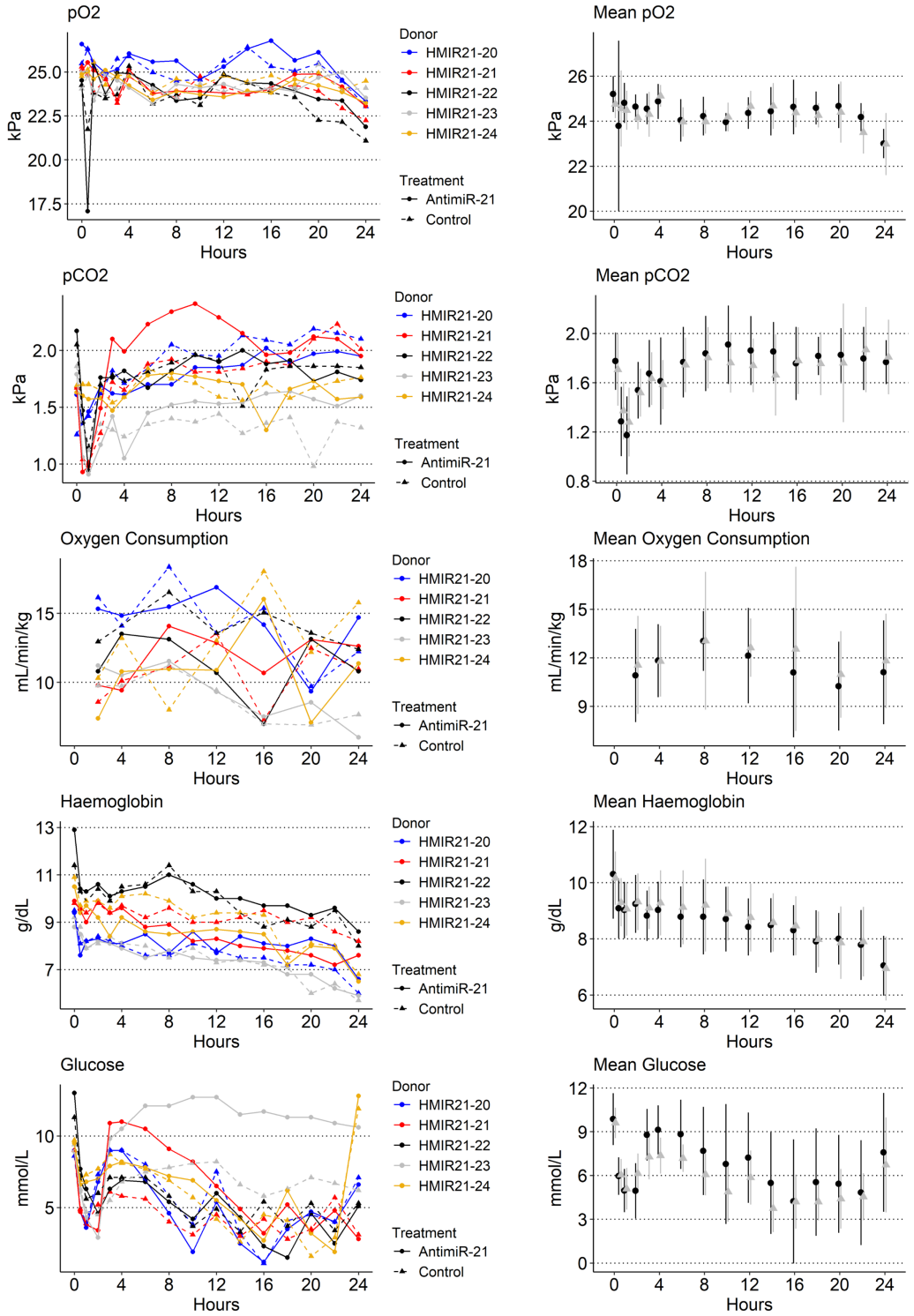

Perfusate biochemistry

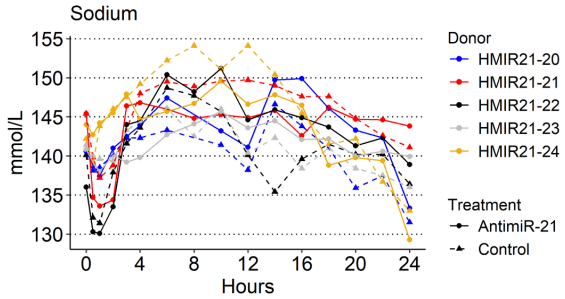

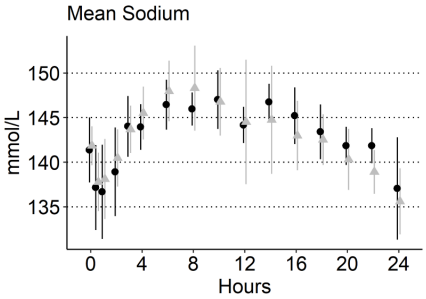

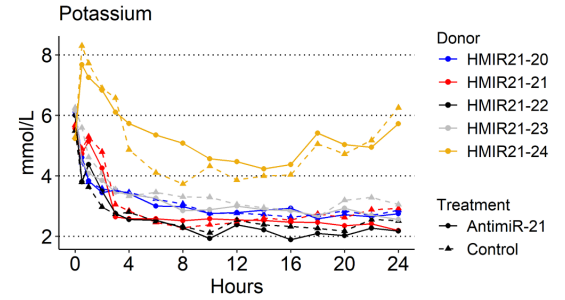

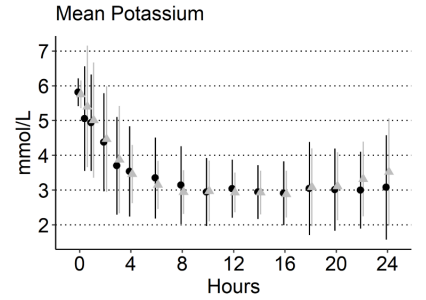

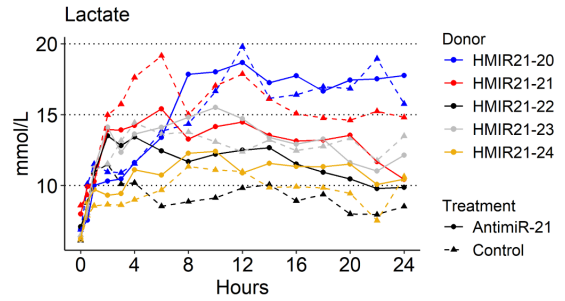

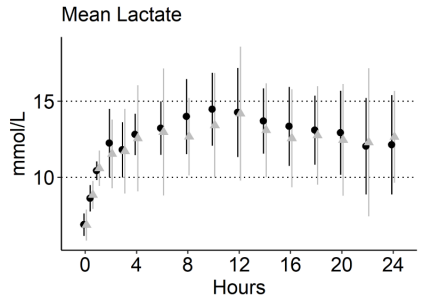

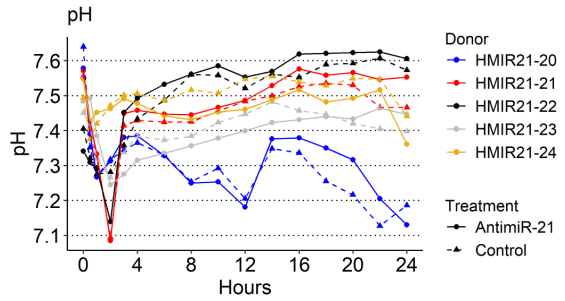

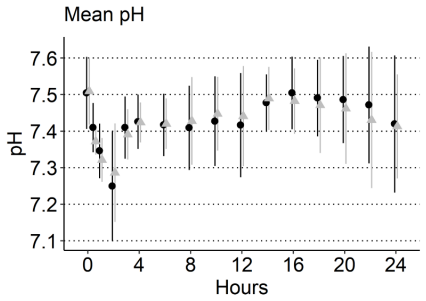

Volume

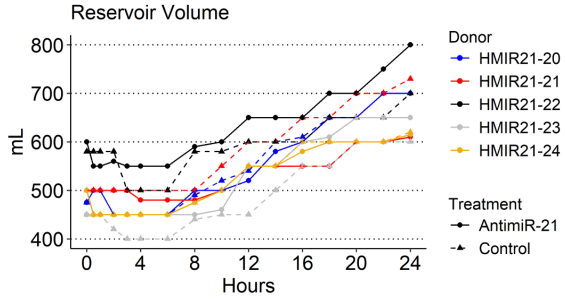

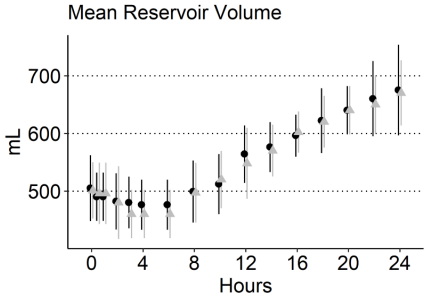

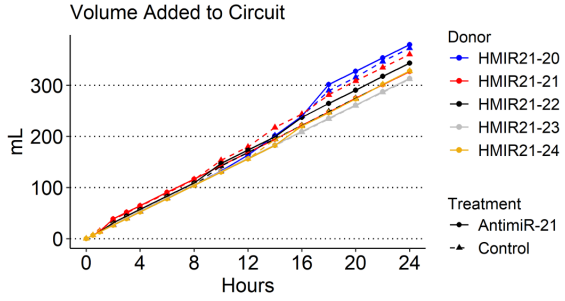

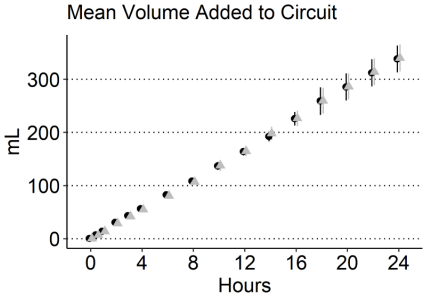

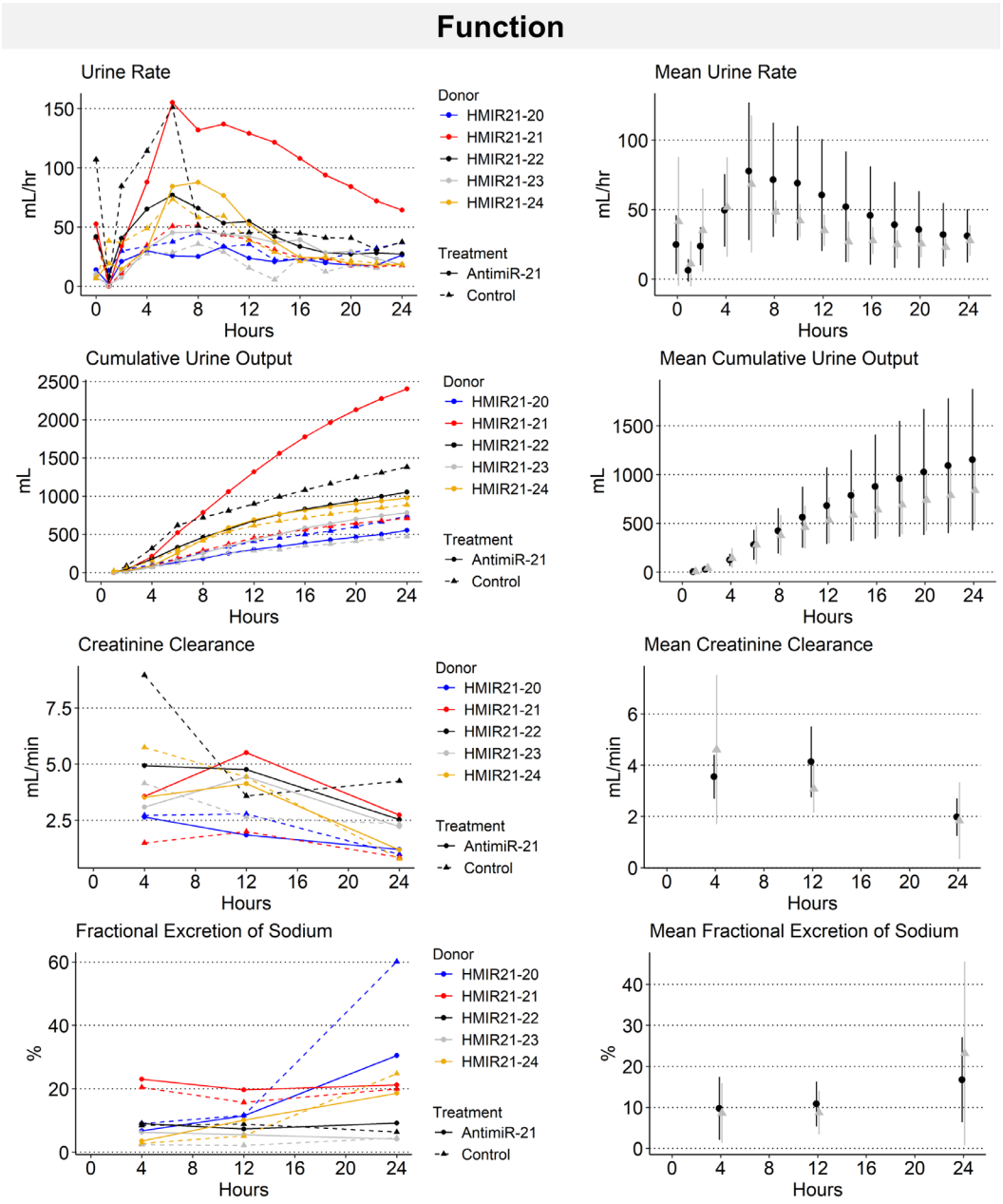

Figure 7-5 Measures from 24-hour paired kidney perfusions.
Measures from 5 pairs of kidneys that underwent 24 hours of normothermic machine perfusions using urine recirculation. The left panel shows the results from each kidney within each pair, with each pair represented by a different colour and the donor study ID given in the legend. The results for each kidney within a pair are labelled by whether that kidney received 200 nM antimiR-21 or control (scrambled) antimiR treatment. The right panel gives the mean ± standard deviation of all kidneys grouped by whether they received antimiR-21 (black circles) or control antimiR (grey triangles) treatment. Oxygen consumption is provided per kg of kidney

	Glucose (mg)		Sodium bicarbonate (mL)		Volume (mL)	
Treatment:	**AntimiR-21**	**Control**	**AntimiR-21**	**Control**	**AntimiR-21**	**Control**
HMIR21-20	4200	3600	5	10	379	372
HMIR21-21	2400	3000	10	10	327	360
HMIR21-22	2400	2400	5	0	343	328
HMIR21-23	600	0	0	0	313	312
HMIR21-24	2400	2400	0	0	328	328
Mean ± SD	2400 ± 1272.79	2280 ± 1368.21	4 ± 4.18	4 ± 5.48	338 ± 25.45	340 ± 25.29
P value	0.621		1		0.830	

Table 7-4 Supplementation of perfusate during 24-hour normothermic machine perfusion of paired kidneys using a circuit involving urine recirculation. One kidney in each pair (listed by donor ID starting HMIR21) was treated with antimiR-21 and the contralateral control kidney received scrambled antimiR. The perfusate was supplemented with glucose and 8.4% sodium bicarbonate during perfusion to maintain glucose and pH levels respectively. The total quantity of glucose and sodium bicarbonate boluses administered during the perfusion are given per kidney. The total volume added to the perfusate per perfusion includes a constant infusion rate of 13 mL/hr in addition to these boluses. Infusions included continuous glucose delivery amounting to 4.8 g in 24 hours. There was no difference in the glucose, sodium bicarbonate or volume added to the perfusate between antimiR-21 and control treated kidneys (paired t test >0.05)

7.3.5 CEUS results

CEUS was used to assess microvascular perfusion of the renal cortex in kidney pairs. There was no significant effect from antimiR treatment on any of the CEUS measures analysed (**Figure 7-6**) suggesting microvascular perfusion was similar between kidneys in each pair.

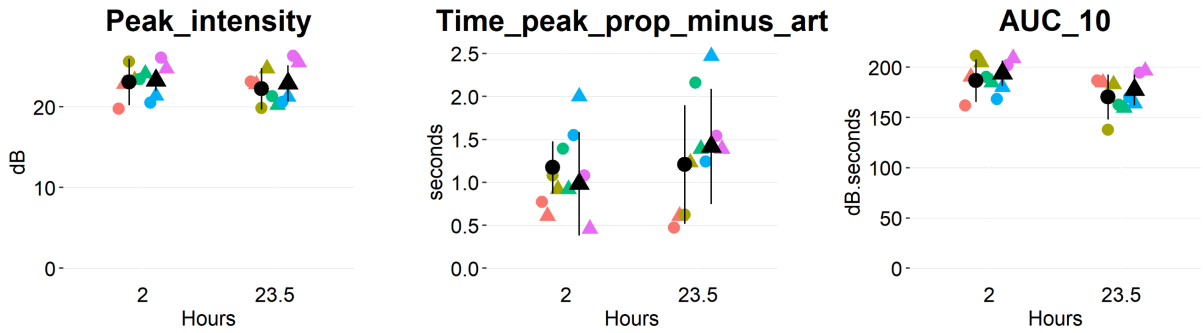

Figure 7-6 Quantification of human kidney cortex microvascular perfusion by contrasted enhanced ultrasound.

Assessment was performed at 2 and 23.5 hours into 24-hour normothermic machine perfusion with urine recirculation. Data presented are from a 5 x 5 mm area of cortex. Data was cropped to start when signal intensity peaked in the artery identified within the same view as the analysed cortex. The maximum cortical intensity (Peak_intensity), time to achieve 90% of this Peak_intensity (Time_peak_prop_minus_art) and the area under the curve for the first 10 seconds of cropped data (AUC_10) are shown. One kidney within each pair was treated with 200 nM antimiR-21 (circles) with the contralateral kidney receiving control (scrambled) antimiR (triangle). Mean ± standard deviation of all kidneys (n=5) within each treatment are overlaid in black. There was no significant effect from antimiR treatment or time of perfusion on any of these perfusion measures and no significant interaction identified between these effects (*P*>.05, two-way repeated measures analysis of variance)

7.3.6 miR-21 suppression

miR-21 levels in kidney tissue before and after perfusion were measured to assess whether antimiR-21 had been effectively delivered and bound its target. AntimiR-21 significantly reduced miR-21 expression relative to baseline levels at the start of perfusion, whereas in control treated kidneys, miR-21 expression increased with perfusion (**Figure 7-7**, **Table 7-5**).

To assess if the composition of core biopsies used for this analysis may have influenced the levels of miR-21 measured, expression of the proximal tubule marker *SLC34A1* and the mRNA housekeeper *HPRT1* were also measured. AntimiR treatment did not have a significant effect on either of these genes, suggesting biopsies were well-matched within pairs (**Figure 7-5**). The timing of biopsy relative to perfusion had a significant effect on C_T values for both these genes so they are likely both modulated by reperfusion. In contrast, the housekeeper (*RNU48*) that miR-21 expression was normalised to was stably expressed (**Table 7-5**). These results support tissue sampling being consistent across kidneys and unlikely to have greatly influenced the measured miR-21 expression levels.

Mean baseline miR-21 expression was higher in the kidneys ultimately selected for antimiR-21 treatment, compared to their control treated contralateral kidneys (*P*<.0001, paired t test **Table 7-5**). The allocation of antimiR treatment was randomised to avoid bias and there is no clear explanation for this observation. Direct comparison of C_T values is in keeping with miR-21 expression reducing during perfusion with antimiR-21 treatment and increasing during control perfusions (**Table 7-5**).

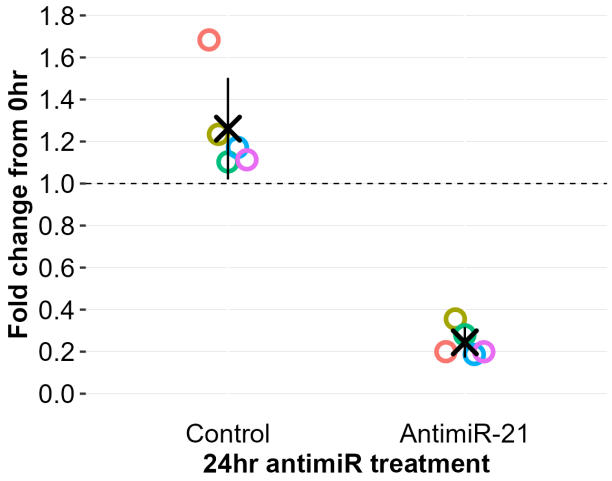

Figure 7-7 miR-21 expression in perfused human kidneys
miR-21 expression in core human kidney biopsies taken after 24 hours of normothermic machine perfusion with urine recirculation and treatment with either 200 nM antimiR-21 or control (scrambled) antimiR. Expression measured by reverse transcription polymerase chain reaction was normalised to RNU48 and expressed as fold change relative to pre-perfusion (0hr) biopsies from the same kidney (indicated by the dashed line). Paired kidneys were used with donor indicated by colour. Two-way repeated measures analysis of variance identified significant variance in miR-21 expression by time (*P*=.009) and antimiR treatment (*P*=.001) with a significant interaction demonstrated (*P*=.001*).*

	Mean C_T				RM-ANOVA (*P*)		
Gene	**AntimiR-21**		**Control**		**AntimiR**	**Hours**	**Interaction**
Time:	0	24	0	24			
SLC34A1	26.67 ± 0.89	28.41 ± 0.67*	27.64 ± 1.55	30.02 ± 1.17#**	0.095	**0.004**	0.488
HPRT1	27.36 ± 0.52	25.95 ± 0.30**	27.26 ± 0.78	26.13 ± 0.73**	0.912	**0.003**	0.333
miR-21	20.38 ± 0.42	22.21 ± 0.70**	24.12 ± 0.74####	23.52 ± 0.81#*	**<0.001**	**0.039**	**<0.001**
RNU48	25.67 ± 0.31	25.42 ± 0.29	25.67 ± 0.35	25.38 ± 0.41	0.938	0.161	0.859

Table 7-5 miR-21 and SLC34A1 expression in perfused human kidneys.
Expression of proximal tubule marker *SLC34A1*, miR-21 and the respective mRNA and small RNA housekeepers of *HPRT1* and *RNU48* measured by reverse transcription polymerase chain reaction and displayed as the mean ± standard deviation threshold cycle number (C_T) from 5 biological repeats. Core biopsies for analysis were taken before (0) and after (24) pairs of human kidneys underwent 24 hours of normothermic machine perfusion with one kidney in each pair receiving antimiR-21 treatment whilst the contralateral kidney was treated with control (scrambled) antimiR. Core biopsies were taken at a shallow angle to target cortex. Two-way repeated measures analysis of variance (RM-ANOVA) explored the effect of antimiR treatment and perfusion (Hours) on C_T values and any interaction between these effects. Where RM-ANOVA was significant (*P* value<.05, underlined in bold) paired t test assessed difference from time 0 (**P*<.05, ***P* <.01) and from matched timepoint in the antimiR-21 treated kidney (#*P*<.05, ##*P* <.01 ###*P* <.001 ####*P* <.0001)

7.3.7 Protein expression changes in reperfusion with antimiR-21

4627 proteins were included for analysis after filtering for missing values, equating to 76% of the input data. Samples separated mostly by whether they were taken at baseline or after perfusion, then clustered by kidney donor more than by the antimiR treatment each kidney was randomised to (**Figure 7-8A**). Reassuringly, there was no differential gene expression at baseline between kidneys that were randomised to antimiR-21 vs control treatment (**Figure 7-8B**).

Within both antimiR-21 and control treated kidneys a high number of genes were differentially expressed at the end of perfusion (400 in control kidneys, 406 in antimiR-21 treated kidneys; **Figure 7-8C**).

Comparing between antimiR treatments at the end of perfusion identified only one differentially expressed protein (**Figure 7-8D**). *MX1* expression was higher in antimiR-21 treated kidneys compared to control treated kidneys (log_2 fold change 0.738, adjusted *P*=.039) at the end of perfusion (**Figure 7-8D**). However, there was no significant difference in *MX1* expression between the start and end of perfusion for either control or antimiR-21 treated kidneys (**Figure 7-8D**), which questions whether the difference in *MX1* expression observed between end-perfusion samples is a true effect of antimiR-21. Furthermore, interaction analysis revealed an effect of time on *MX1* expression (adjusted *P*=.022) but no effect of antimiR treatment (adjusted *P*=.999) or evidence of an interaction between antimiR treatment and time (adjusted *P*=.88).

Of the 400 proteins in the control treated kidneys that were differentially expressed between start and end of perfusion, the two most upregulated proteins were HBD and CA1, encoding for haemoglobin subunit delta and carbonic anhydrase-1 respectively. These proteins are both expressed in erythrocytes so increased detection is likely the results of using a blood based perfusate, rather than upregulation in the kidney, as 0 hour biopsies were taken before perfusion began.[317] Raw counts for other top differentially expressed proteins are displayed in **Figure 7-8E** and show a consistent direction of change with perfusion for each kidney within a pair, regardless of antimiR treatment.

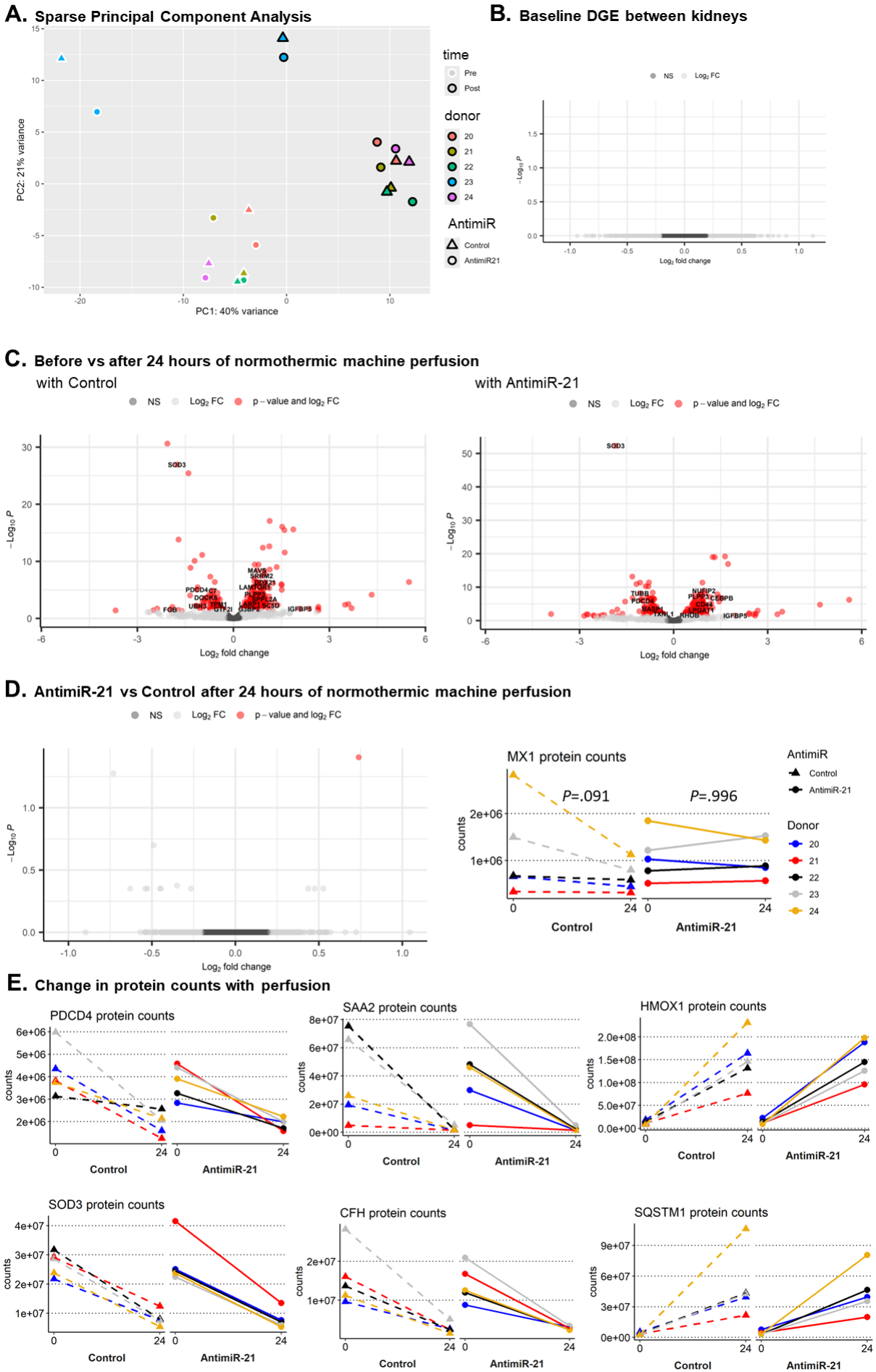
A. Sparse Principal Component Analysis
PC2: 21% variance
PC1: 40% variance
time
Pre
Post
donor
20
21
22
23
24
AntimiR
Control
AntimiR21
B. Baseline DGE between kidneys
NS
Log2 FC
−Log10 P
Log2 fold change
C. Before vs after 24 hours of normothermic machine perfusion
with Control
with AntimiR-21
NS
Log2 FC
p − value and log2 FC
−Log10 P
Log2 fold change
SOD3
D. AntimiR-21 vs Control after 24 hours of normothermic machine perfusion
MX1 protein counts
P=.091
P=.996
counts
Control
AntimiR-21
AntimiR
Donor
E. Change in protein counts with perfusion
PDCD4 protein counts
SAA2 protein counts
HMOX1 protein counts
SOD3 protein counts
CFH protein counts
SQSTM1 protein counts

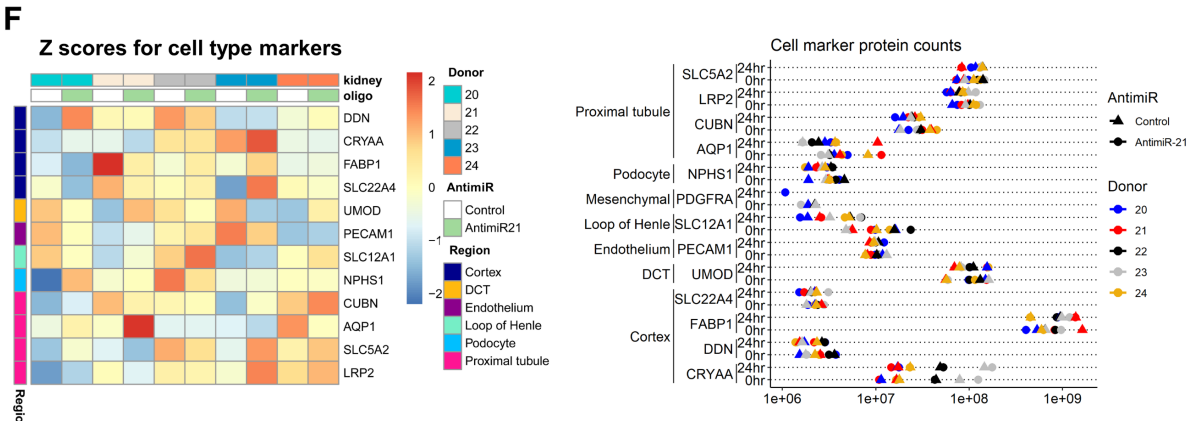

Figure 7-8 Proteomics analysis of perfused human kidney.
Protein expression in pairs of human kidneys treated with 24 hours of normothermic machine perfusion and either control antimiR or antimiR-21. AntimiR treatments were given to contralateral kidneys from each donor (n=5), so all data is paired. Perfusion with an oxygenated red cell-based perfusate was started after a cold ischaemic time of at least 12 hours, to simulate reperfusion at implantation in transplantation. Protein expression was assessed by liquid chromatography mass spectrometry-based proteomics with data independent acquisition (LCMS-DIA). **A** shows sparse principal component analysis with samples separating predominantly by whether they were taken before (pre) or after perfusion (post) perfusion. All pre samples are taken at baseline, before any antimiR treatment. **B.** Samples taken before perfusion were well matched with no differential gene expression (DGE) between kidneys that were randomised to receive antimiR-21 vs control. **C.** Volcano plots displaying DGE in end perfusion samples compared to baseline for kidneys treated with control antimiR or antimiR-21. Annotated genes are limited to miR-21 targets. **D.** Volcano plot to show DGE between antimiR-21 and control treated kidneys at the end of perfusion. The one differentially expressed protein is MX1 and the plot on the right displays the quantification data for each sample at both timepoints (0 and 24 hours) by antimiR treatment. There was no significant DGE between timepoints for either antimiR treatment (adjusted *P* displayed). In volcano plots in **C** and **D** genes meeting both the significance (adjusted *P*<.05) and $\log_2$ fold change (≥0.2) thresholds are highlighted in red with non-significant (NS) values displayed in dark grey. **E** shows raw count of selected genes that were differentially expressed between the start and end of perfusion with kidney donor indicated by colour and results separated by antimiR treatment**. F** Left plot shows z scores (variance from the mean measured in standard deviations) for each sample of different kidney cell markers.[153,318-320] Counts for these proteins are plotted on the right with addition of the mesenchymal marker PDGFRA which was only detected in a subset of samples and at low counts. DGE analysis was performed with DESeq2. DCT, distal convoluted tubule.

Variability in sample composition has the potential to affect the detection of treatment related changes in protein expression.[318] Therefore, markers of selected kidney cell types and nephron segments were assessed for consistency between samples (**Figure 7-8F**). Chosen markers for nephron segments and cell types were selected for being widely published,[153,319,320] with cortex markers identified in analysis by Zhang et al.[318] Proximal tubule, podocyte, endothelium, distal convoluted tubule and loop of henle markers were detected in every sample with counts clustering by gene (**Figure 7-8F**). Z scores to assess variance across the samples generally showed similar trends for a gene in the starting samples from each kidney in a pair (**Figure 7-8F**). Assessment of counts and Z scores supports samples being well matched within the pairs.

As miR-21 expression was higher in antimiR-21 treated kidneys at the end of perfusion, despite significant repression (**Table 7-5**), other approaches were taken to look for subtle modulation of miR-21 targets by antimiR-21 treatment. The 692 miR-21 targets identified were similarly modulated during perfusion regardless of antimiR treatment, as indicated by the positive correlation (Pearson correlation coefficient 0.749, $P<.0001$) between $\log_2$ fold change observed with each treatment. The effect of perfusion on miR-21 targets was particularly well matched between treatment groups for those targets with DGE (
Figure 7-9A-B).

To explore for a signal of antimiR-21 treatment disinhibiting miR-21 target expression, miR-21 targets that were significantly downregulated during control kidney perfusions (
Figure 7-9C) or significantly upregulated in antimiR-21 treated kidney perfusions (
Figure 7-9D) were extracted from the dataset. AntimiR-21 treatment was associated with a small number of downregulated targets loosing significance (
Figure 7-9C) and some upregulated targets gaining significance (
Figure 7-9D) compared to the changes in control treated kidneys. However, the majority of proteins were concordant (
Figure 7-9C-D) so this approach did not elucidate a clear downstream effect from antimiR-21 treatment.

Gene set enrichment analysis confirmed similar negative enrichment of miR-21 targets with reperfusion for both antimiR-21 and control treated kidneys (
Figure 7-9E).

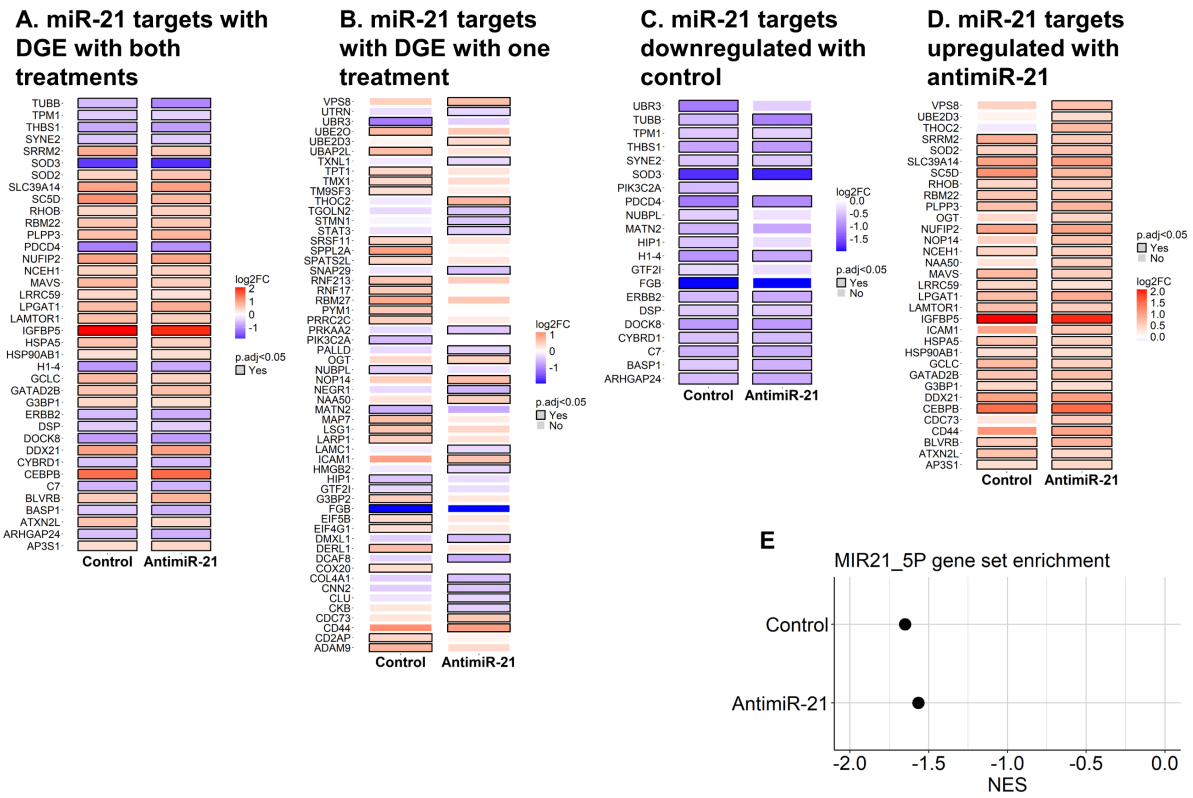

Figure 7-9 Differential gene expression (DGE) analysis for miR-21 targets. Data from human kidneys perfused ex vivo with 24 hours of normothermic machine perfusion and control antimiR or antimiR-21. Protein expression in core biopsies taken before and after perfusion was assessed with liquid chromatography mass spectrometry-based proteomics with data independent acquisition. DGE between start and end biopsies was analysed with DESeq2 for each treatment. Each kidney had at least 12 hours of cold ischaemia before perfusion and antimiR treatment. miR-21 targets were regulated in the same direction during perfusion for both antimiR treatments, as shown by the matched colours (representing $\log_2$ fold change) regardless of whether DGE was present with both antimiR treatments (**A**) or significance was only achieved with one (**B**). miR-21 targets that were significantly downregulated with perfusion in the control kidneys are shown in **C** with those significantly upregulated with antimiR-21 treatment during perfusion shown in **D**. **E** shows normalised enrichment scores (NES) from enrichment analysis for a gene set of miR-21 targets (MIR21_5P), 31 of which were identified in this dataset. There was significant negative enrichment with perfusion for both antimiR treatments, indicating targets were generally downregulated by reperfusion. p.adj, adjusted *P* value; log2FC, $\log_2$ fold change.

7.3.8 Cytokine release

Cytokine release into the perfusate was measured for pairs of kidneys to assess for effects of antimiR-21 treatment on the inflammatory responses to reperfusion. As perfusate volume varied with time (**Figure 7-5**) and was not identical between kidneys, concentrations were converted to total amount to normalise for perfusate volume. The amount of IFNγ, IL-12p70, IL-13, IL1β, IL-2, IL-4, IL-6 and IL-8 all increased significantly with time whereas IL-10 and TNFα did not (**Figure 7-10**). It should be noted that most IL-6 and IL-8 concentrations were above the limit of

detection so, although it is clear these factors were secreted by the kidneys, the assessment of how they varied by time of perfusion will be less accurate. AntimiR treatment had no significant effect on the concentrations or amounts of any of the cytokines measured (**Figure 7-10**).

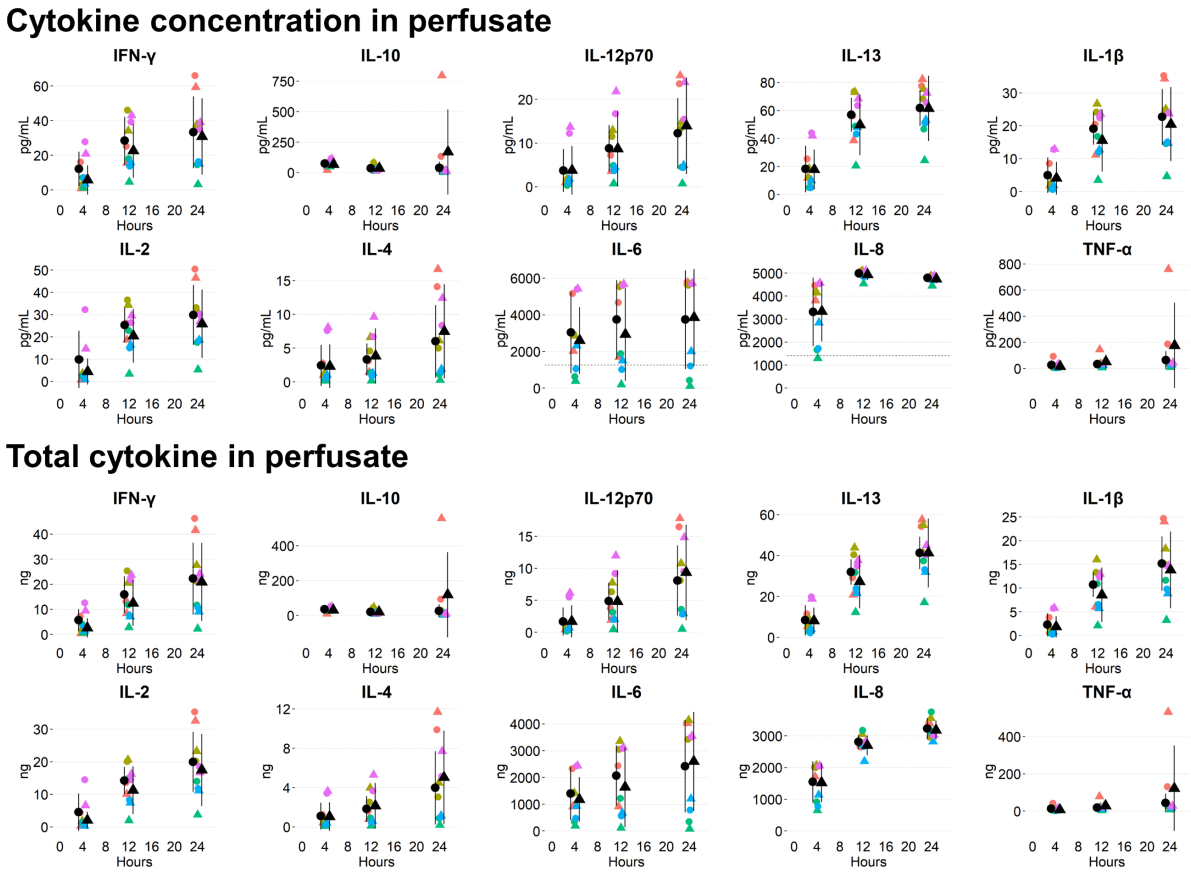

RM-ANOVA: Time	Concentration		Total amount	
Cytokine	p	p.adj	p	p.adj
IFN-γ	**0.0090**	**0.0150**	**0.0080**	**0.0133**
IL-10	0.4910	0.4910	0.4920	0.4920
IL-12p70	**0.0190**	**0.0271**	**0.0130**	**0.0186**
IL-13	**0.0000**	**0.0000**	**0.0000**	**0.0000**
IL-1β	**0.0001**	**0.0004**	**0.0001**	**0.0004**
IL-2	**0.0010**	**0.0025**	**0.0008**	**0.0021**
IL-4	**0.0440**	0.0550	**0.0370**	**0.0463**
IL-6	**0.0030**	**0.0060**	**0.0030**	**0.0060**
IL-8	**0.0000**	**0.0000**	**0.0000**	**0.0000**
TNF-α	0.2410	0.2678	0.2460	0.2733

Figure 7-10 Perfusate cytokine levels.

Cytokine levels in perfusate of 24-hour normothermic machine perfusion of human kidneys using urine recirculation. Levels are reported 4, 12 and 24 hours into perfusion. One kidney within each pair received antimiR-21 treatment (circle) with the contralateral kidney from the same donor receiving control (scrambled) antimiR treatment (triangle). Cytokine levels in perfusate are expressed as concentrations in the top panel whilst the lower panel gives the total quantity of cytokine based on the volume of perfusate for that kidney at that time point. Some IL-6 and IL-8 concentrations were above the upper limit of detection (dashed line) so should be interpreted with caution. Two-way repeated measured analysis of variance (RM-ANOVA) found no significant effect of antimiR treatment on cytokine levels. Time had a significant effect on some cytokine levels but there was no significant interaction between the effects of time and antimiR treatment. The table shows unadjusted (p) and adjusted (p.adj) *P* values for the effect of perfusion time on cytokine levels reported either as concentration or as total amount to normalise for volume. *P* <.05 are in bold. The Benjamini-Hochberg method was used to adjust for multiple comparisons

7.3.9 Levels of apoptosis

To assess the effect of antimiR-21 treatment on the level of apoptosis during IRI, a TUNEL assay was performed. Baseline (mean ± SD) levels of apoptosis at the end of cold ischaemia (before NMP) were 0.53% ± 0.40% for kidneys allocated to receive control antimiR (n=5) and 0.76% ± 0.76% for those allocated to receive antimiR-21. At the end of perfusion the percent of apoptotic cells was numerically higher in both groups at 1.45% ± 0.85% for controls and 1.30% ± 0.79% after antimiR-21, but the effect of perfusion time was not statistically significant. AntimiR-21 treatment did not significantly change the proportion of apoptotic cells compared to controls (**Figure 7-11**).

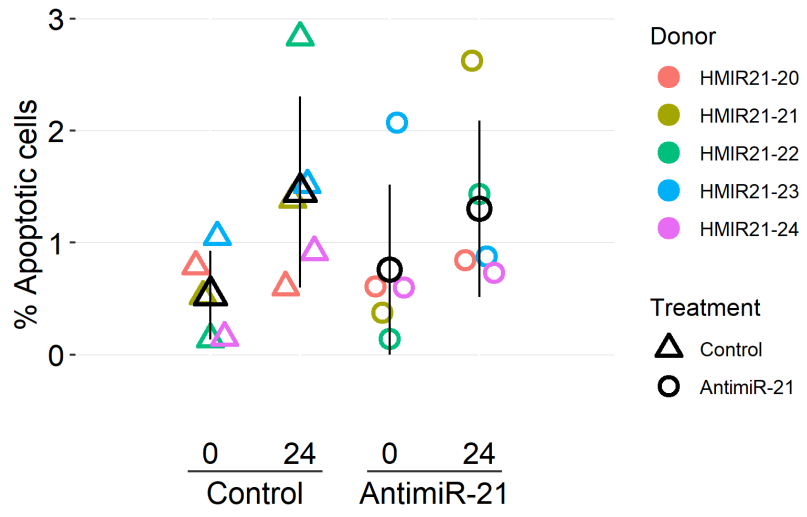

Figure 7-11 Quantifying apoptosis in perfused human kidneys.

The proportion of apoptotic cells in biopsies taken from human kidneys before (0) and after (24) 24 hours of normothermic machine perfusion with urine recirculation. One kidney in each pair was treated during perfusion with 200 nM antimiR-21 whilst the contralateral kidney from the same donor received control (scrambled) antimiR. Sections of formalin fixed paraffin embedded kidney tissue were prepared with TdT-mediated dUTP Nick-End Labelling (TUNEL) assay to identify the DNA fragmentation associated with apoptosis. Nuclei were counterstained with DAPI. Standardised widefield fluorescent microscopy image acquisition was performed with X10 objective on ZEISS Axio Imager. For each treatment, the mean ± standard deviation (n=5) is shown in black with the results for each kidney in colour. Two-way repeated measures analysis of variance found no effect of time (*P*=.18) or antimiR treatment (*P*=.859) on % apoptotic cells and no significant interaction between these two effects was revealed (*P*=.546).

7.3.10 Kidney injury marker assessment

NGAL is a commonly used experimental marker of kidney injury that is released from tubular cells and was found to increase in the urine and perfusate during perfusion (**Figure 7-12**).[15] Particularly in the context of urine recirculation which essentially closes the circuit, this is not an unexpected finding. There was no effect observed from antimiR-21 treatment on NGAL levels (**Figure 7-12**).

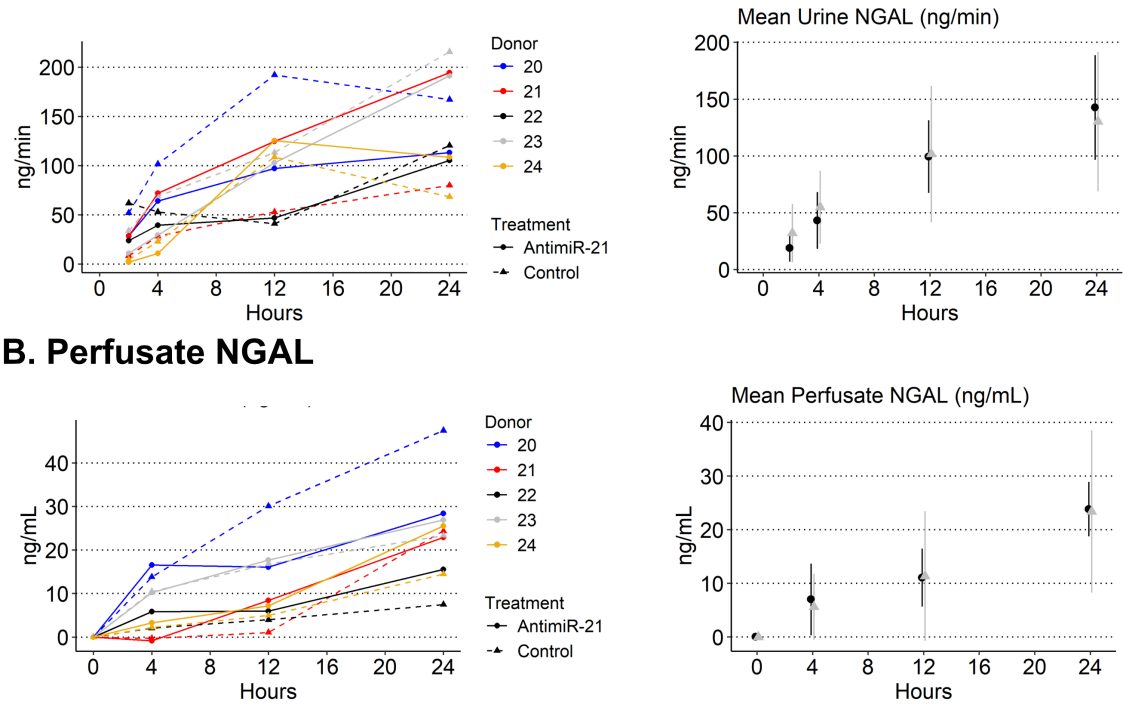

Figure 7-12 Perfusate and urine NGAL levels.
Levels of the kidney injury marker neutrophil gelatinase-associated lipocalin (NGAL) in the urine (**A**) and perfusate (**B**) of human kidneys perfused with normothermic machine perfusion for 24 hours with urine recirculation. All kidneys had at least 12 hours of cold ischaemia on starting perfusion. 5 pairs of kidneys were used with one kidney from each donor receiving control antimiR treatment and the contralateral kidney given 200 nM antimiR-21. Left panels show NGAL levels per kidney with mean ± standard deviation (n=5) on the right panel. Urinary NGAL was normalised for urine flow (**A**). Perfusate concentrations are expressed above baseline to normalise for signal detected in pre-perfusion samples (**B**). Two-way repeated measures analysis of variance (RM-ANOVA) found no significant effect of antimiR treatment on NGAL levels. NGAL levels increase significantly with time (Urine $P<.001$, Perfusate $P<.001$, RM-ANOVA) and no significant interaction was identified between time and antimiR treatment.

7.3.11 Histopathology

Kidneys within a pair were well matched on histology with similar levels of injury demonstrated. Tubular vacuolation and loss of brush border were common findings, with vacuolation in particular appearing more severe at the end of perfusion. There was no clear difference in histological injury by antimiR treatment. Representative images from H&E and PAS stain from one pair of kidneys are shown in **Figure 7-13**. Formal blinded quantification of injury is being conducted by histopathologists but is not yet complete.

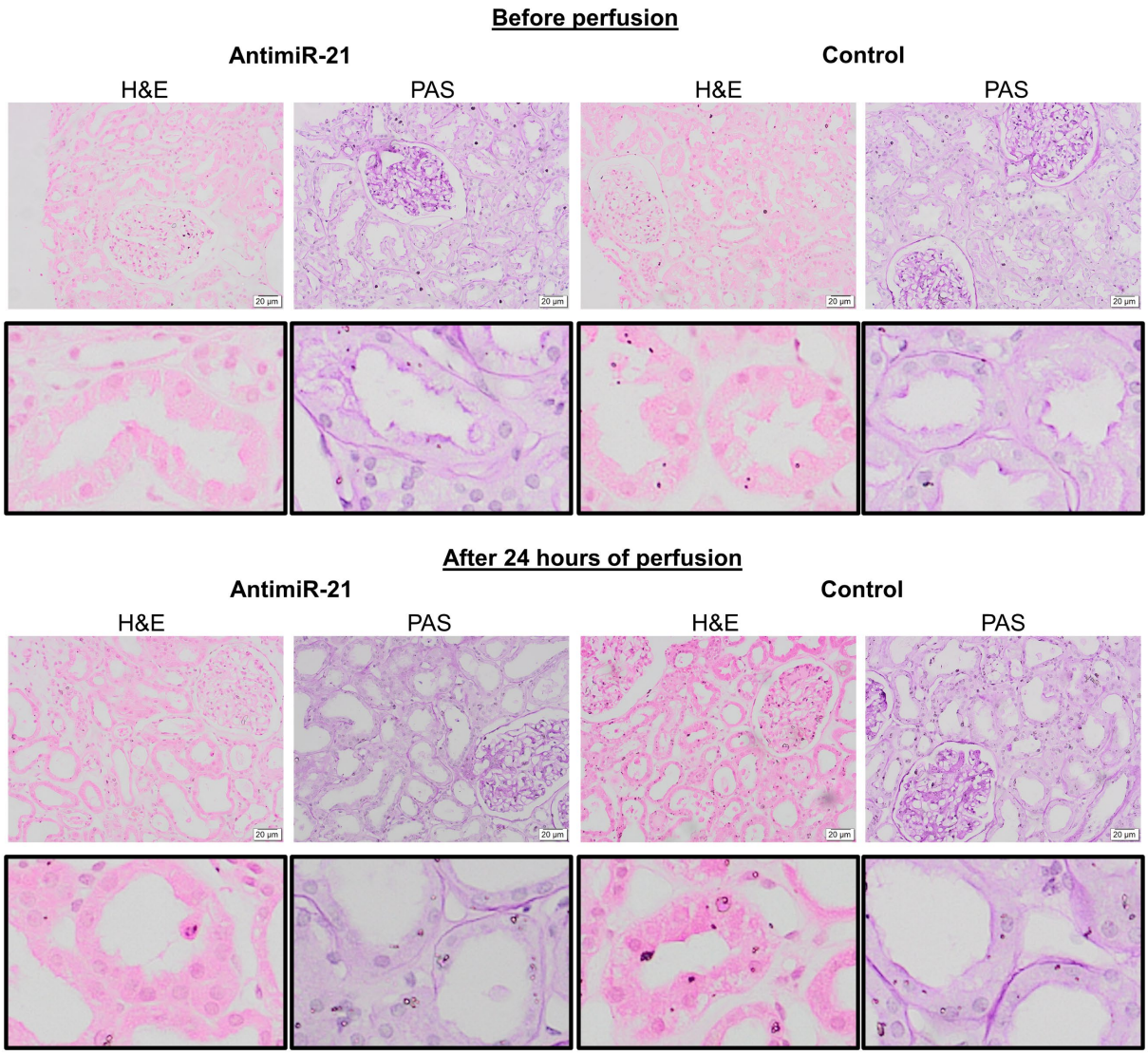

Figure 7-13 Histology before and after perfusion of human kidneys with antimiR-21 or control.
Haemotoxylin and eosin (H&E) and periodic acid schiff (PAS) staining on formalin fixed paraffin embedded human kidney biopsies taken from a pair of human kidneys immediately before (core biopsy) and after (wedge biopsy) 24 hours of normothermic machine perfusion with a blood based perfusate using urine recirculation. Kidneys were donated after circulatory death and had a cold ischaemic time of 18 hours before machine perfusion commenced. 200 nM of antimiR-21 or control antimiR were delivered during perfusion. Framed images demonstrate a magnified area of tubule from the image directly above it. Images acquired with CMOC colour camera SC50 and Cellsens Standard software using X20 objective.

7.3.12 Single cell suspension

Single-cell RNA sequencing has the potential to better dissect the effects of antimiR-21 treatment by cell type within the kidney and unlike single-nuclear RNA sequencing allows assessment of changes to mRNA in the cytoplasm. The use of cryopreserved tissue increases the feasibility of using this method on tissue collected during extended perfusion experiments. The aim was to sequence at least 15000 cells and it is recommended to have a minimum of 70% viability within this, but ideally >80%. As

such, these parameters were first assessed on single cell suspensions generating from core kidney biopsies collected from kidneys in cold storage. Manual cell counts and viability assessment were validated by flow cytometry and found to be comparable (**Table 7-6A**). Flow cytometry confirmed the presence of endothelial cells, mesenchymal cells and immune cells in these suspensions and that the suspension was predominantly composed of single cells rather than doublets (**Table 7-6A**).

The digest protocol was performed on tissue samples taken after NMP to compare to paired samples taken at the end of cold storage. Viability of suspensions generated from post-perfusion samples remained adequate but was noted to be slightly less than for pre perfusion counterparts. In contrast, the cell yield was higher for the post-perfusion samples (**Table 7-6B**).

Cryopreserved tissue is expected to be more fragile so the effect of digest time on cell yields and viability was assessed. Although shortening the digest time to 15 or 20 minutes increased the cell viability, this was at the cost of lower cell yields. When a 30-minute digest was used, cell yield was adequate but only 27% of the cell yield achieved from matched fresh tissue. On balance, a digest time of 30 minutes seems optimum for cryopreserved tissue as further approaches to exclude dead cells can be undertaken during the analysis phase.

A. Validation of cell count and composition

	Values
Manual results	
Cell count (mean ± SD with individual results below)	57333 ± 14843 (70000, 61000, 41000)
Viability (mean ± SD)	98.37% ± 2.8%
Flow cytometry	
Cell count (mean ± SD with individual results below)	70961 ± 27255 (92789, 79682, 40413)
Viability by flow (mean ± SD)*	94.9 ± 1.9%
Single cells (% of cells)	92.8 ± 0.87%
Viability of single cells (mean ± SD)*	96.5 ± 1.48%
CD31 positive	2.64% (396 in 15000)
PDGFRA positive	0.13% (20 in 15000)
PDGFRB positive	0.02% (3 in 15000)
CD45 positive	0.14% (21 in 15000)

B. Cold storage vs perfused kidney

Kidney	HMIR21-17		HMIR21-18		HMIR21-19	
Hours of perfusion	0	22	0	22.5	0	21.5
Initial yield		190800	145500	238000	156450	175200
Initial viability		88%	94%	85%	74%	78%
Post wash yield	86400	184000	26460	163500	62400	77000
Post wash viability	97%	79%	100%	86%	86%	83%
Volume of wash (mL)		1	1	2	2	2
End yield relative to pre-perfusion	2.12		6.12		1.23	

C. Cryopreservation of perfused kidney

Storage	Fresh	Cryopreserved		
Digest time (mins)	30	30	15	20
Initial yield	375600	91450	73700	19950
Initial viability	83.07%	45.76%	58.21%	66.67%
Yield post wash	254800	68600	16000	16500
Viability post wash	92.35%	69.39%	84.38%	93.94%
Yield relative to fresh	1.0	0.27	0.06	0.06
Volume of wash (mL)	2	2	2	1

Table 7-6 Single-cell digest optimisation on human kidney biopsies.

Optimisation and validation of digest method for generating single cell suspension suitable for single-cell RNA sequencing from human kidney core biopsies. **A** shows results from 3 core biopsies taken from the same kidney (HMIR21-16) after 16 hours of cold ischaemia. Cell count and viability assessment was performed both manually (with trypan blue exclusion) and by flow cytometry with DAPI. The number of endothelial (CD31 positive), mesenchymal (PDGFRA or PDGFRB positive) and immune (CD45 positive) cells were estimated by the % of single cells in each positive gate. This was extrapolated to predict the number of each cell type per 15000 cells, as the intended number to analyse by single-cell RNA sequencing. Flow cytometry cell counts were performed by running the sample dry. *As the cells from one biopsy were used as an unstained control for flow cytometry gating, mean ± standard deviation (SD) viability is reported for n=2 by flow cytometry. **B** shows manually acquired cell yield and viability of single cell suspensions produced from freshly taken human kidney core biopsies collected before and after 22 hours of normothermic machine perfusion with urine recirculation. The digest protocol includes a wash step to remove debris and dead cells and counts are reported before (initial) and after (post-wash) this step. **C** gives initial and post-wash manually acquired cell yields and viability in cell suspensions generated from freshly collected or cryopreserved human kidney core biopsies after 13 hours of normothermic machine perfusion with urine recirculation. A 30-minute digest was used as standard, with shorter durations assessed in cryopreserved tissue (**C**).

7.4 Discussion

Work in this chapter further supports the feasibility of using 24-hour NMP as a model of IRI in which to assess potential therapeutics. AntimiR-21 delivery was effective in downregulating miR-21 and although no clear changes in miR-21 targets were identified at a protein level, there is scope to further assess downstream effects at an RNA level. Furthermore, the DIA approach to LCMS-based proteomics was found to be a viable technique for exploring protein expression changes during reperfusion. This data has the potential to guide further research in the field.

The optimised perfusion protocol established in this chapter ensured perfusion was maintained in all kidneys for 24 hours and with limited intervention required after the initial 2 hours. Metabolic activity of the kidneys was preserved with oxygen consumption rates broadly in the region of 5-20 mL/min/kg. Renal oxygen consumption is closely linked to tubular sodium reabsorption so as urinary sodium loss was high in this system, it is not unexpected that renal oxygen consumption was lower than the documented 10 mL/min in post-op ventilated patients.[65]

In terms of appropriately modelling the stress of IRI, the reperfusion that occurs as part of NMP triggered an appropriate cytokine response. Similarly, as expected, there was a trend for increased apoptosis noted at the end of perfusion.

Kidneys were well matched within pairs as demonstrated by similar weights, perfusion parameters, urine output and microvascular perfusion as measured by CEUS. On proteomics analysis samples clustered by whether they were taken before or after perfusion. Within these timepoints samples separated by donor, supporting that paired kidneys were similar but also indicating a benefit in using pairs to account for biological variability.

Fluorescence microscopy of kidney tissue demonstrated antimiR uptake most clearly with the higher dose of 200 nM. AntimiRs are recognised to be filtered at the glomerulus and, in keeping with this, there was a clear increase in urinary fluorescence after antimiR administration.[210,211] As the urine was recirculated, there was no loss of antimiR from the system and, as such, fluorescence remained high in the perfusate. The 200 nM dose is approximately two thirds of the antimiR dose used in 6-hour non-recirculating perfusions by Thompson et al.[97] and further dose reductions may well be feasible with preservation of perfusate antimiR levels when recirculating urine.

There was no convincing effect of antimiR-21 on protein expression after 24 hours of treatment, despite clearly achieving downregulation of miR-21. Higher baseline miR-21 expression in the kidneys randomised to antimiR-21 treatment may have masked changes in miR-21 target expression, as C_T values indicated higher end-perfusion miR-21 expression in kidneys treated with antimiR-21 rather than control. It is difficult to give a biological reason why baseline levels of miR-21 would differ between kidneys of a pair in this way. To account for differing baseline miR-21 expression levels, differences in how miR-21 targets were modulated during perfusion by antimiR treatment were also assessed. Although with this method, there was a signal that a small number of miR-21 targets might be regulated differently during reperfusion in the presence of antimiR-21 treatment, it was not a convincing finding with results being concordant for the vast majority. As such, it seems most likely that 24 hours is not long enough to see changes in protein expression downstream of antimiR-21 in this model.

Given the lack of differential protein expression downstream of antimiR-21, it is not unsurprising that there was no difference in injury detected by either NGAL production, tubular function or levels of apoptosis between antimiR treatments.

Downregulation of miR-21 would be expected to derepress target mRNA, so although no changes were identified from these samples at a protein level, it is still worth looking at mRNA expression. Single-cell RNA sequencing also has the added benefit of allowing different cell types to be looked at individually, thus greatly enhancing the resolution of the technique compared to the bulk proteomics approach used in this chapter. Single-cell RNA sequencing is increasingly being recognised as a viable technique that can be conducted on cryopreserved tissue.[321-326] Expanding from only using freshly collected tissue increases the logistical feasibility of the technique and my preliminary work has shown the potential to generate a suitable single-cell suspension from thawed perfused tissue. I plan to process the stored samples for single-cell RNA sequencing as part of a collaboration but this analysis has not yet been conducted due to time constraints.

The DIA approach to LCMS-based proteomics is recognised to suffer less from the bias towards more abundant proteins that is known to be a problem with the DDA method.[327] As such, DIA is appealing for its potential to recognise more subtle changes in protein expression. However, it is an evolving technique for which there is no consensus on analysis pipeline.[131,327,328] Despite the increased resolution offered by DIA, as the input tissue is a core biopsy in which the composition by cell type is likely to vary, there remain limitations on what differences you might expect to detect. Despite these concerns, sampling appeared to be reasonably consistent when assessed by cell type marker. The intention was to sample cortex so it was reassuring that none of the 7 medulla specific genes identified by Zhang et al.[318] were detected. In contrast, 14 out of 47 cortex markers were detected. The gene panel identified by Zhang et al.[318] included some non-coding RNAs which would be inherently absent from proteomics data.

Designation of any identified proteins as contaminants is a process that requires optimisation for each experiment and again, there are differing approaches. Some would argue there is no need to remove contaminants during analysis as you would expect them to be the same between samples and so not produce misleading DGE results. However, in the setting of perfusion experiments, post-perfusion samples are likely to be contaminated with components of the blood-based perfusate, which pre-perfusion samples have not been exposed to. This is important to consider when interpreting DGE as the interesting question is which proteins have changed in expression within the kidney, rather than which proteins from perfusate components

are contaminating the post-perfusion sample. Although efforts were made to appropriately designate proteins as contaminants from the cRAP library[132] before DGE expression analysis, the library used did not list HBD as a potential contaminant. HBD was the protein in which the greatest difference in levels noted between pre- and post-perfusion samples. It seems most likely this is an artefact of erythrocytes remaining in the post-perfusion samples after washing, rather than a true upregulation of this protein within the kidney.

CA1 displayed the next largest increase in expression with perfusion. Given the scale of the increase and the abundance of expression in erythrocytes, this again seems more likely to reflect the presence of perfusate in the sample.[317] CA1 was not excluded in initial contaminant screening as carbonic anhydrase activity exists in the kidney, however, this is generally attributed to the isoforms encoded by CA2, CA4 and CA12.[329] Interestingly, Weissenbacher et al.[308] found CA1 expression to be increased in kidneys perfused with urine recirculation relative to those perfused with the urine replacement method, despite both using blood-based perfusate. Preservation of CA1 expression in kidneys perfused with urine recirculation was hypothesised to contributed to better pH stability with this method.[308] Overall, the potential for DGE during reperfusion to represent contamination from the perfusate is important to consider before proceeding to pathway analysis.

LCMS-based proteomics on core biopsies from models of kidney IRI has been published previously but has not focused on changes that occur during the reperfusion phase and has not used the DIA approach.[308,330] McEvoy et al.[330] used a DDA approach to unbiased proteomics on samples from a pig model of kidney IRI to assess the difference between storage methods. Weissenbacher et al.[308] used DDA LCMS-based proteomics to explore differences between urine recirculation and urine replacement methods of NMP of human kidneys. Again, the focus of the published analysis was a comparison between methods.[308] However, samples from 16 kidneys were collected at both end-ischaemia and at end of 24-hour NMP, in addition to some interim timepoints.[308] If combined with my data, the results from this study could inform a comparison between DDA and DIA methods.[308]

Only preliminary analysis has so far been conducted on the DGE that occurs during reperfusion of ischaemic human kidneys in this chapter. Given the ongoing development of the DIA approach to LCMS-proteomics, it is reassuring to note

consistencies between my data and published findings on responses to ischaemia-reperfusion.

Of the 400 proteins differentially expressed during reperfusion, HMOX1 was one of the most upregulated. HMOX1 encodes heme oxygenase 1 which is thought to form part of a protective response to ischaemia.[331] Weissenbacher et al. also demonstrated increased protein expression of HMOX1 by 24 hours of reperfusion with NMP.[308] There was also a trend for increased HMOX1 during 6-hour perfusions of human kidneys by Thompson et al. but this upregulation was only significant with the addition of antimiR-24.[97]

Three of the most downregulated proteins during perfusion were CFH, SAA2 and SOD3. CFH encodes complement Factor H and as a negative regulator of the alternative complement pathway, this is in keeping with the understanding that complement activity is increased with ischaemia-reperfusion.[332,333] SAA2 encodes serum amyloid A2 and has been considered both a marker of kidney injury[334] and a molecule able to promote repair after renal IRI.[335] It will be interesting to see what biological pathways are predicted to interact with SAA2 from this data given the consequences of downregulation are not clear in existing literature. Superoxide dismutases are more consistently reported as protective against oxidative stress and are thought to have a role in recovery of blood flow after ischaemia.[336,337] The extracellular isoform SOD3 is considered the most abundant in the kidney and in mice, is rapidly downregulated after IRI.[337] My data showed a similar response with SOD3 expression being reduced during reperfusion.

Different cell types have been shown to respond differently to ischaemia-reperfusion so incorporating single-cell RNA sequencing data has great potential to enhance the understanding given by bulk proteomics approaches.[320] There is limited existing single-cell and single-nuclei RNA sequencing data on the gene expression changes that occur in human kidney IRI.[320,338] Although there is high quality single-cell transcriptomics data from mouse models of kidney injury, including IRI, the comparison made is between sham-operated and injured kidneys.[339] Much like the human data comparing AKI to healthy controls, this analysis does not allow exploration of changes that are occurring specifically during the reperfusion phase.[320,338,339] The paired end-ischaemia and end-perfusion samples from the human kidneys in my work will allow understanding specifically of the changes occurring

during reperfusion. Arguably, this period of injury is the more logistically feasible to target therapeutically.

The work in this chapter supports the feasibility of using high throughput approaches to study the effects of potential therapeutics when modelling ischaemia-reperfusion with NMP of human kidneys. Single-cell transcriptomics remains to be conducted and is an important next step to assess if antimiR-21 treatment modulated miR-21 targets. More broadly, this human data on gene expression changes during kidney reperfusion will be a valuable resource for identifying other potential therapeutic targets in transplantation and AKI, with the optimised DIA proteomics analysis pipeline being transferrable to the wide research community.

Chapter 8. Summary

8.1 Conclusion

The work in this thesis has demonstrated the ability to deliver and study the effects of antimiR-21 in relevant *in vitro* and ex vivo human models of kidney IRI.

Chapter 4 validates the model of using primary human PTEC isolated from human kidneys declined for transplant to model IRI *in vitro*. The isolated cells were characterised and low levels of endothelial and mesenchymal contamination demonstrated. Hypoxia on incubation in 1% oxygen was confirmed by stabilisation of HIF1α and allowing the isolated cells to settle in culture before treatments was found to be an important consideration for maintaining viability. Despite being able to produce a biological response, antimiR-21 did not consistently reduced miR-21 expression or lead to upregulation of selected miR-21 targets.

Chapter 5 demonstrates the ability of primary human PTEC to take up antimiR *in vitro* without the use of transfection reagents. Endocytic entry was confirmed with macropinocytosis identified as the dominant mechanism. Concentrations as low as those commonly used with transfection reagents were effective.

Chapter 6 explores the downstream effects of antimiR-21 using PTEC to model IRI *in vitro* and found antimiR-21 delivery at reoxygenation to be effective in causing differential gene expression at both the RNA and protein level. Bulk RNA sequencing and LCMS-proteomic approaches were used and predicted the downstream effects of antimiR-21 treatment in IRI to be one that encouraged repair.

Chapter 7 confirmed the stability of 24-hr NMP of human kidneys declined for transplantation and demonstrated that effective miR-21 repression could be achieved with antimiR-21 delivery in this model. There was no differential protein expression identified downstream of antimiR-21 treatment but a protocol for establishing single-cell suspensions suitable for single-cell RNA sequencing was optimised on cryopreserved samples to further explore downstream target modulation. Additionally, core biopsies from perfused human kidneys were shown to be a suitable sample for LCMS-based proteomics to explore the changes that occur during reperfusion.

8.2 Strengths and Limitations

A key strength of my work is the use of primary human PTEC and whole human kidneys to provide data that is likely most translatable to people. Biological variability was demonstrated to be an important contributor to differences between samples for both models and the acquisition of paired data has aided the identification of changes secondary to treatments, rather than differences between donors. The use of paired assessment of RNA and protein expression also comes with the benefit of allowing some validation of the proteomics approached used.

Although NMP in my work was for an extended period of 24-hours, the *in vitro* data suggests this may not be long enough to identify changes in protein expression downstream of antimiR-21 treatment when analysing a bulk sample. A much longer duration of at least 48 hours is likely necessary to detect protein level changes and subsequent changes in severity of injury. One way in which monitoring treatment effect could be extended without the inherent logistical challenges of longer perfusion, would be to take tissue slices from kidneys at the end of perfusion to maintain in culture. Such tissue slices could feasibly be maintained for a further few days to assess longer term consequences of antimiR-21 response.[340]

Machine perfusion of whole kidneys remains one of the most relevant models available for kidney IRI but is not without limitations. The use of urine recirculation to allow stability for extended perfusions results in recirculation of secreted cytokines and leukocytes, which are important effectors of injury and repair, are a clear omission from the circuit. The addition of exogenous leukocytes to the circuit would allow greater assessment of the immune consequences of reperfusion. The surgical and post-operative course in transplantation is not always smooth and can include multiple episodes of ischaemia-reperfusion. To better model this tumultuous time, once stabilised on the perfusion circuit for several hours, pump speed could be lowered to reduce perfusion pressure and so model a second hit. Adjusting the timing of such an intervention would allow exploration of when the kidney is most vulnerable to ischaemic insults in the recovery period.

8.3 Future direction

The reperfusion phase of IRI is predictable in the case of transplant, but also in other settings such as major surgery, so offering a window in which therapeutics to target the ensuing injury pathways can be delivered. The samples I have collected from the start and end of control kidney perfusions offer the ability to better unpick what

processes are occurring and so elucidate other potential therapeutic targets. The ability to perform unbiased high throughput techniques such as single-cell RNA sequencing and LCMS-based proteomics on cryopreserved samples makes these techniques feasible to access with unpredictable human samples and has the potential to generate a wealth of data to support future research in the field. In data from the kidney perfusion model, careful consideration is needed when interpreting results for proteins identified as being upregulated during perfusion given the potential for contamination from the blood based perfusate. As experience in the DIA approach to LCMS-based proteomics expands, confidence in results will increase and these techniques are likely to be become staples for predicting downstream effects of interventions to guide relevant functional assessments.

In the domain of antagomirs, such unbiased techniques are key for identifying which of the numerous miR targets are of relevance in a particular cell type and disease state. To further assess for downstream effects from antimiR-21 treatment in the human kidney perfusions presented in this thesis, cryopreserved core kidney biopsies will be processed for single-cell RNA sequencing. If differential expression is identified with this approach, it will be interesting to dissect out the proximal tubule component and see how this data correlates with the changes identified within primary human PTEC *in vitro*, to better understand the transferability of *in vitro* and whole organ results.

Extended kidney perfusions offer a human model in which to assess potential therapeutics without risking harm. The time these perfusions can be maintained for is rapidly lengthening, generating greater opportunity to assess the downstream effects of interventions including impact on injury and fibrosis markers. AntimiR-21 has been found to be safe in systemic use in humans (NCT02855268) outside of transplantation, and if further work supported a potential benefit for kidney reconditioning, it is feasible that delivery could be with a much shorter period of NMP. Further work would be needed to establish the speed of delivery during perfusion and consideration of potential consequences of concomitant immunosuppression.

Bibliography

1. Moss R, Thomas SR. Hormonal regulation of salt and water excretion: a mathematical model of whole kidney function and pressure natriuresis. *Am J Physiol-Renal*. 2014;306(2):F224-F248. doi:10.1152/ajprenal.00089.2013
2. Steddon S, Ashman N. *Oxford Handbook of Nephrology and Hypertension*. 2 ed. Oxford University Press; 2018.
3. Edwards A, Long KR, Baty CJ, Shipman KE, Weisz OA. Modelling normal and nephrotic axial uptake of albumin and other filtered proteins along the proximal tubule. *J Physiol*. Apr 2022;600(8):1933-1952. doi:10.1113/JP282885
4. Faivre A, Verissimo T, Auwerx H, Legouis D, de Seigneux S. Tubular Cell Glucose Metabolism Shift During Acute and Chronic Injuries. *Front Med (Lausanne)*. 2021;8:742072. doi:10.3389/fmed.2021.742072
5. Chaudhry D, Chaudhry A, Peracha J, Sharif A. Survival for waitlisted kidney failure patients receiving transplantation versus remaining on waiting list: systematic review and meta-analysis. *BMJ*. Mar 1 2022;376:e068769. doi:10.1136/bmj-2021-068769
6. Kaballo MA, Canney M, O'Kelly P, Williams Y, O'Seaghdha CM, Conlon PJ. A comparative analysis of survival of patients on dialysis and after kidney transplantation. *Clinical Kidney Journal*. 2017;11(3):389-393. doi:10.1093/ckj/sfx117
7. Wang Y, Hemmelder MH, Bos WJW, et al. Mapping health-related quality of life after kidney transplantation by group comparisons: a systematic review. *Nephrol Dial Transplant*. Dec 2 2021;36(12):2327-2339. doi:10.1093/ndt/gfab232
8. Kerr M, Bray B, Medcalf J, O'Donoghue DJ, Matthews B. Estimating the financial cost of chronic kidney disease to the NHS in England. *Nephrol Dial Transplant*. Oct 2012;27 Suppl 3:iii73-80. doi:10.1093/ndt/gfs269
9. NHS Blood and Transplant. Factsheet 7: Cost-effectiveness of Transplantation. Accessed 04.12.2024, 2024. https://nhsbtmediaservices.blob.core.windows.net/organ-donation-assets/pdfs/Organ_Donation_Registry_Fact_Sheet_7_21337.pdf
10. NHS Blood and Transplant. *Annual Report on Kidney Transplantation Report 2022/2023*. 2024. Accessed 24/08/2024. https://nhsbtdbe.blob.core.windows.net/umbraco-assets-corp/32738/nhsbt-kidney-transplantation-report-2223.pdf

11. Zhao H, Alam A, Soo AP, George AJT, Ma D. Ischemia-Reperfusion Injury Reduces Long Term Renal Graft Survival: Mechanism and Beyond. *EBioMedicine*. Feb 2018;28:31-42. doi:10.1016/j.ebiom.2018.01.025
12. Salvadori M, Rosso G, Bertoni E. Update on ischemia-reperfusion injury in kidney transplantation: Pathogenesis and treatment. *World J Transplant*. Jun 24 2015;5(2):52-67. doi:10.5500/wjt.v5.i2.52
13. Kalogeris T, Baines CP, Krenz M, Korthuis RJ. Cell biology of ischemia/reperfusion injury. *Int Rev Cell Mol Biol*. 2012;298:229-317. doi:10.1016/B978-0-12-394309-5.00006-7
14. Parekh DJ, Weinberg JM, Ercole B, et al. Tolerance of the human kidney to isolated controlled ischemia. *J Am Soc Nephrol*. Feb 2013;24(3):506-17. doi:10.1681/ASN.2012080786
15. SMITH T, ZAIDI A, BROWN CVM, et al. Robust Rat and Mouse Models of Bilateral Renal Ischemia Reperfusion Injury. *In Vivo*. 2024;38(3):1049-1057. doi:10.21873/invivo.13538
16. Tullius SG, Reutzel-Selke A, Egermann F, et al. Contribution of prolonged ischemia and donor age to chronic renal allograft dysfunction. *J Am Soc Nephrol*. Jul 2000;11(7):1317-1324. doi:10.1681/ASN.V1171317
17. Summers DM, Johnson RJ, Hudson A, Collett D, Watson CJ, Bradley JA. Effect of donor age and cold storage time on outcome in recipients of kidneys donated after circulatory death in the UK: a cohort study. *Lancet*. Mar 2 2013;381(9868):727-34. doi:10.1016/S0140-6736(12)61685-7
18. van der Vliet JA, Warle MC, Cheung CL, Teerenstra S, Hoitsma AJ. Influence of prolonged cold ischemia in renal transplantation. *Clin Transplant*. Nov-Dec 2011;25(6):E612-6. doi:10.1111/j.1399-0012.2011.01510.x
19. Tennankore KK, Kim SJ, Alwayn IP, Kiberd BA. Prolonged warm ischemia time is associated with graft failure and mortality after kidney transplantation. *Kidney Int*. Mar 2016;89(3):648-58. doi:10.1016/j.kint.2015.09.002
20. Erecinska M, Thoresen M, Silver IA. Effects of hypothermia on energy metabolism in Mammalian central nervous system. *J Cereb Blood Flow Metab*. May 2003;23(5):513-30. doi:10.1097/01.WCB.0000066287.21705.21
21. Pushpakumar S, Kundu S, Weber G, Sen U. Exogenous hydrogen sulfide and miR-21 antagonism attenuates macrophage-mediated inflammation in ischemia reperfusion injury of the aged kidney. *Geroscience*. Jun 2021;43(3):1349-1367. doi:10.1007/s11357-020-00299-6

22. Wong G, Teixeira-Pinto A, Chapman JR, et al. The Impact of Total Ischemic Time, Donor Age and the Pathway of Donor Death on Graft Outcomes After Deceased Donor Kidney Transplantation. *Transplantation*. Jun 2017;101(6):1152-1158. doi:10.1097/TP.0000000000001351

23. Hosszu A, Fekete A, Szabo AJ. Sex differences in renal ischemia-reperfusion injury. *Am J Physiol Renal Physiol*. Aug 1 2020;319(2):F149-F154. doi:10.1152/ajprenal.00099.2020

24. Willicombe M, Rizzello A, Goodall D, Papalois V, McLean AG, Taube D. Risk factors and outcomes of delayed graft function in renal transplant recipients receiving a steroid sparing immunosuppression protocol. *World J Transplant*. Feb 24 2017;7(1):34-42. doi:10.5500/wjt.v7.i1.34

25. Aufhauser DD, Jr., Wang Z, Murken DR, et al. Improved renal ischemia tolerance in females influences kidney transplantation outcomes. *J Clin Invest*. May 2 2016;126(5):1968-77. doi:10.1172/JCI84712

26. de Kok MJ, McGuinness D, Shiels PG, et al. The Neglectable Impact of Delayed Graft Function on Long-term Graft Survival in Kidneys Donated After Circulatory Death Associates With Superior Organ Resilience. *Ann Surg*. Nov 2019;270(5):877-883. doi:10.1097/SLA.0000000000003515

27. Summers DM, Johnson RJ, Allen J, et al. Analysis of factors that affect outcome after transplantation of kidneys donated after cardiac death in the UK: a cohort study. *Lancet*. Oct 16 2010;376(9749):1303-11. doi:10.1016/S0140-6736(10)60827-6

28. Shamali A, Kassimatis T, Phillips BL, Burton H, Kessaris N, Callaghan C. Duration of delayed graft function and outcomes after kidney transplantation from controlled donation after circulatory death donors: a retrospective study. *Transpl Int*. Jun 2019;32(6):635-645. doi:10.1111/tri.13403

29. Chen R, Wang H, Song L, et al. Predictors and one-year outcomes of patients with delayed graft function after deceased donor kidney transplantation. *Bmc Nephrol*. Dec 4 2020;21(1):526. doi:10.1186/s12882-020-02181-1

30. Yarlagadda SG, Coca SG, Formica RN, Jr., Poggio ED, Parikh CR. Association between delayed graft function and allograft and patient survival: a systematic review and meta-analysis. *Nephrol Dial Transplant*. Mar 2009;24(3):1039-47. doi:10.1093/ndt/gfn667

31. Coca SG, Singanamala S, Parikh CR. Chronic kidney disease after acute kidney injury: a systematic review and meta-analysis. *Kidney Int*. Mar 2012;81(5):442-8. doi:10.1038/ki.2011.379
32. Wald R, Quinn RR, Luo J, et al. Chronic dialysis and death among survivors of acute kidney injury requiring dialysis. *JAMA*. Sep 16 2009;302(11):1179-85. doi:10.1001/jama.2009.1322
33. Nieuwenhuijs-Moeke GJ, Pischke SE, Berger SP, et al. Ischemia and Reperfusion Injury in Kidney Transplantation: Relevant Mechanisms in Injury and Repair. *J Clin Med*. Jan 17 2020;9(1)doi:10.3390/jcm9010253
34. Bonventre JV, Yang L. Cellular pathophysiology of ischemic acute kidney injury. *J Clin Invest*. Nov 2011;121(11):4210-21. doi:10.1172/JCI45161
35. Chaudhry R, Varacallo M. *Biochemistry, Glycolysis*. 2022. *StatPearls*. Accessed 24/08/2024. https://www.ncbi.nlm.nih.gov/pubmed/29493928
36. Alberts B JA, Lewis J, Raff M, Roberts K and Walter P. Chapter 14 - Energy Conversion: Mitochondria and Chloroplasts. *Molecular biology of the cell 5th Edition*

Garland Science, Taylor & Francis Group, LLC, an informa business 2008.
37. Murphy MP, Hartley RC. Mitochondria as a therapeutic target for common pathologies. *Nat Rev Drug Discov*. Dec 2018;17(12):865-886. doi:10.1038/nrd.2018.174
38. Ye Z, Wang S, Zhang C, Zhao Y. Coordinated Modulation of Energy Metabolism and Inflammation by Branched-Chain Amino Acids and Fatty Acids. *Front Endocrinol (Lausanne)*. 2020;11:617. doi:10.3389/fendo.2020.00617
39. Li X, Zheng S, Wu G. Amino Acid Metabolism in the Kidneys: Nutritional and Physiological Significance. *Adv Exp Med Biol*. 2020;1265:71-95. doi:10.1007/978-3-030-45328-2_5
40. Chouchani ET, Pell VR, James AM, et al. A Unifying Mechanism for Mitochondrial Superoxide Production during Ischemia-Reperfusion Injury. *Cell Metab*. Feb 9 2016;23(2):254-63. doi:10.1016/j.cmet.2015.12.009
41. Beach TE, Prag HA, Pala L, et al. Targeting succinate dehydrogenase with malonate ester prodrugs decreases renal ischemia reperfusion injury. *Redox Biol*. Sep 2020;36:101640. doi:10.1016/j.redox.2020.101640
42. Fritz KS, Petersen DR. Exploring the Biology of Lipid Peroxidation-Derived Protein Carbonylation. *Chemical Research in Toxicology*. 2011/09/19 2011;24(9):1411-1419. doi:10.1021/tx200169n

43. Baines CP. The mitochondrial permeability transition pore and ischemia-reperfusion injury. *Basic Res Cardiol*. Mar 2009;104(2):181-8. doi:10.1007/s00395-009-0004-8
44. Wang S, Zhang C, Hu L, Yang C. Necroptosis in acute kidney injury: a shedding light. *Cell Death Dis*. Mar 3 2016;7:e2125. doi:10.1038/cddis.2016.37
45. Sanz AB, Sanchez-Niño MD, Ramos AM, Ortiz A. Regulated cell death pathways in kidney disease. *Nature Reviews Nephrology*. 2023/05/01 2023;19(5):281-299. doi:10.1038/s41581-023-00694-0
46. Jun W, Benjanuwattra J, Chattipakorn SC, Chattipakorn N. Necroptosis in renal ischemia/reperfusion injury: A major mode of cell death? *Arch Biochem Biophys*. Aug 15 2020;689:108433. doi:10.1016/j.abb.2020.108433
47. Li C, Yu Y, Zhu S, et al. The emerging role of regulated cell death in ischemia and reperfusion-induced acute kidney injury: current evidence and future perspectives. *Cell Death Discov*. May 4 2024;10(1):216. doi:10.1038/s41420-024-01979-4
48. Pefanis A, Ierino FL, Murphy JM, Cowan PJ. Regulated necrosis in kidney ischemia-reperfusion injury. *Kidney Int*. Aug 2019;96(2):291-301. doi:10.1016/j.kint.2019.02.009
49. von Massenhausen A, Tonnus W, Himmerkus N, et al. Phenytoin inhibits necroptosis. *Cell Death Dis*. Mar 2 2018;9(3):359. doi:10.1038/s41419-018-0394-3
50. Yang J, Liu X, Bhalla K, et al. Prevention of apoptosis by Bcl-2: release of cytochrome c from mitochondria blocked. *Science*. Feb 21 1997;275(5303):1129-32. doi:10.1126/science.275.5303.1129
51. Qian S, Wei Z, Yang W, Huang J, Yang Y, Wang J. The role of BCL-2 family proteins in regulating apoptosis and cancer therapy. *Front Oncol*. 2022;12:985363. doi:10.3389/fonc.2022.985363
52. Garrido C, Galluzzi L, Brunet M, Puig PE, Didelot C, Kroemer G. Mechanisms of cytochrome c release from mitochondria. *Cell Death Differ*. Sep 2006;13(9):1423-33. doi:10.1038/sj.cdd.4401950
53. Smith SF, Hosgood SA, Nicholson ML. Ischemia-reperfusion injury in renal transplantation: 3 key signaling pathways in tubular epithelial cells. *Kidney Int*. Jan 2019;95(1):50-56. doi:10.1016/j.kint.2018.10.009
54. Koh MY, Powis G. Passing the baton: the HIF switch. *Trends Biochem Sci*. Sep 2012;37(9):364-72. doi:10.1016/j.tibs.2012.06.004

55. Conde E, Alegre L, Blanco-Sanchez I, et al. Hypoxia inducible factor 1-alpha (HIF-1 alpha) is induced during reperfusion after renal ischemia and is critical for proximal tubule cell survival. *PLoS One*. 2012;7(3):e33258. doi:10.1371/journal.pone.0033258
56. Robson MG. Toll-Like Receptors and Renal Disease. *Nephron Exp Nephrol*. 2009;113(1):E1-E7. doi:10.1159/000228077
57. Wu H, Chen G, Wyburn KR, et al. TLR4 activation mediates kidney ischemia/reperfusion injury. *J Clin Invest*. Oct 2007;117(10):2847-59. doi:10.1172/JCI31008
58. Leemans JC, Stokman G, Claessen N, et al. Renal-associated TLR2 mediates ischemia/reperfusion injury in the kidney. *J Clin Invest*. Oct 2005;115(10):2894-903. doi:10.1172/JCI22832
59. Raza Z, Saleem U, Naureen Z. Sphingosine 1-phosphate signaling in ischemia and reperfusion injury. *Prostaglandins & Other Lipid Mediators*. 2020/08/01/ 2020;149:106436. doi:https://doi.org/10.1016/j.prostaglandins.2020.106436
60. Hu M, Wang YM, Wang Y, et al. Regulatory T cells in kidney disease and transplantation. *Kidney Int*. 2016/09/01/ 2016;90(3):502-514. doi:https://doi.org/10.1016/j.kint.2016.03.022
61. Bejugama K, Guditi S. Role of Regulatory T cells in Prognosis, Diagnosis, and Treatment of Kidney Transplant Recipients. *Journal of Cellular Immunology*. 2023;5(5):162-7. doi:https://doi.org/10.33696/immunology.5.181
62. Muczynski KA, Ekle DM, Coder DM, Anderson SK. Normal Human Kidney HLA-DR–Expressing Renal Microvascular Endothelial Cells: Characterization, Isolation, and Regulation of MHC Class II Expression. *Journal of the American Society of Nephrology*. 2003;14(5)
63. Zhou Y, Luo Z, Liao C, et al. MHC class II in renal tubules plays an essential role in renal fibrosis. *Cell Mol Immunol*. Nov 2021;18(11):2530-2540. doi:10.1038/s41423-021-00763-z
64. Zhu D, Tang Q, Yu B, et al. Major histocompatibility complexes are up-regulated in glomerular endothelial cells via activation of c-Jun N-terminal kinase in 5/6 nephrectomy mice. *British Journal of Pharmacology*. 2020;177(22):5131-5147. doi:https://doi.org/10.1111/bph.15237
65. Ricksten S-E, Bragadottir G, Redfors B. Renal oxygenation in clinical acute kidney injury. *Critical Care*. 2013/03/19 2013;17(2):221. doi:10.1186/cc12530

66. Tian Z, Liang M. Renal metabolism and hypertension. *Nat Commun*. Feb 11 2021;12(1):963. doi:10.1038/s41467-021-21301-5
67. Wen L, Li Y, Li S, Hu X, Wei Q, Dong Z. Glucose Metabolism in Acute Kidney Injury and Kidney Repair. *Front Med (Lausanne)*. 2021;8:744122. doi:10.3389/fmed.2021.744122
68. Bonventre JV, Zuk A. Ischemic acute renal failure: an inflammatory disease? *Kidney Int*. Aug 2004;66(2):480-5. doi:10.1111/j.1523-1755.2004.761_2.x
69. Alsahli M, Gerich JE. Renal glucose metabolism in normal physiological conditions and in diabetes. *Diabetes Res Clin Pract*. Nov 2017;133:1-9. doi:10.1016/j.diabres.2017.07.033
70. Situmorang GR, Sheerin NS. Ischaemia reperfusion injury: mechanisms of progression to chronic graft dysfunction. *Pediatr Nephrol*. Jun 2019;34(6):951-963. doi:10.1007/s00467-018-3940-4
71. Thomas MJ, Fraser DJ, Bowen T. Biogenesis, Stabilization, and Transport of microRNAs in Kidney Health and Disease. *Non-Coding RNA*. 2018;4(4):30.
72. Baumann V, Winkler J. miRNA-based therapies: strategies and delivery platforms for oligonucleotide and non-oligonucleotide agents. *Future Med Chem*. 2014;6(17):1967-84. doi:10.4155/fmc.14.116
73. Ribas J, Ni X, Castanares M, et al. A novel source for miR-21 expression through the alternative polyadenylation of VMP1 gene transcripts. *Nucleic Acids Res*. Aug 2012;40(14):6821-33. doi:10.1093/nar/gks308
74. Kumarswamy R, Volkmann I, Thum T. Regulation and function of miRNA-21 in health and disease. *RNA Biol*. Sep-Oct 2011;8(5):706-13. doi:10.4161/rna.8.5.16154
75. Larrue R, Fellah S, Van der Hauwaert C, et al. The Versatile Role of miR-21 in Renal Homeostasis and Diseases. *Cells*. Nov 7 2022;11(21)doi:10.3390/cells11213525
76. Lin Z, Liu Z, Wang X, Qiu C, Zheng S. MiR-21-3p Plays a Crucial Role in Metabolism Alteration of Renal Tubular Epithelial Cells during Sepsis Associated Acute Kidney Injury via AKT/CDK2-FOXO1 Pathway. *Biomed Res Int*. 2019;2019:2821731. doi:10.1155/2019/2821731
77. Choo KB, Soon YL, Nguyen PNN, Hiew MSY, Huang C-J. MicroRNA-5p and -3p co-expression and cross-targeting in colon cancer cells. *Journal of Biomedical Science*. 2014/10/05 2014;21(1):95. doi:10.1186/s12929-014-0095-x

78. Denby L, Ramdas V, Lu R, et al. MicroRNA-214 antagonism protects against renal fibrosis. *J Am Soc Nephrol*. Jan 2014;25(1):65-80. doi:10.1681/ASN.2013010072
79. Chung AC, Dong Y, Yang W, Zhong X, Li R, Lan HY. Smad7 suppresses renal fibrosis via altering expression of TGF-beta/Smad3-regulated microRNAs. *Mol Ther*. Feb 2013;21(2):388-98. doi:10.1038/mt.2012.251
80. Bautista-Sánchez D, Arriaga-Canon C, Pedroza-Torres A, et al. The Promising Role of miR-21 as a Cancer Biomarker and Its Importance in RNA-Based Therapeutics. *Molecular Therapy - Nucleic Acids*. 2020/06/05/ 2020;20:409-420. doi:https://doi.org/10.1016/j.omtn.2020.03.003
81. Moore LD, Le T, Fan G. DNA Methylation and Its Basic Function. *Neuropsychopharmacology*. 2013/01/01 2013;38(1):23-38. doi:10.1038/npp.2012.112
82. Kosek DM, Banijamali E, Becker W, Petzold K, Andersson Emma R. Efficient 3′-pairing renders microRNA targeting less sensitive to mRNA seed accessibility. *Nucleic Acids Research*. 2023;51(20):11162-11177. doi:10.1093/nar/gkad795
83. Koenig AB, Barajas JM, Guerrero MJ, Ghoshal K. A Comprehensive Analysis of Argonaute-CLIP Data Identifies Novel, Conserved and Species-Specific Targets of miR-21 in Human Liver and Hepatocellular Carcinoma. *Int J Mol Sci*. Mar 14 2018;19(3)doi:10.3390/ijms19030851
84. Valinezhad Orang A, Safaralizadeh R, Kazemzadeh-Bavili M. Mechanisms of miRNA-Mediated Gene Regulation from Common Downregulation to mRNA-Specific Upregulation. *Int J Genomics*. 2014;2014:970607. doi:10.1155/2014/970607
85. Fang Z, Rajewsky N. The impact of miRNA target sites in coding sequences and in 3'UTRs. *PLoS One*. Mar 22 2011;6(3):e18067. doi:10.1371/journal.pone.0018067
86. Linsen SEV, Tops BBJ, Cuppen E. miRNAs: small changes, widespread effects. *Cell Research*. 2008/12/01 2008;18(12):1157-1159. doi:10.1038/cr.2008.311
87. Stenvang J, Petri A, Lindow M, Obad S, Kauppinen S. Inhibition of microRNA function by antimiR oligonucleotides. *Silence*. Jan 9 2012;3(1):1. doi:10.1186/1758-907X-3-1
88. Chau BN, Xin C, Hartner J, et al. MicroRNA-21 promotes fibrosis of the kidney by silencing metabolic pathways. *Sci Transl Med*. Feb 15 2012;4(121):121ra18. doi:10.1126/scitranslmed.3003205

89. Obad S, dos Santos CO, Petri A, et al. Silencing of microRNA families by seed-targeting tiny LNAs. *Nat Genet*. Mar 20 2011;43(4):371-8. doi:10.1038/ng.786
90. Godwin JG, Ge X, Stephan K, Jurisch A, Tullius SG, Iacomini J. Identification of a microRNA signature of renal ischemia reperfusion injury. *Proc Natl Acad Sci U S A*. Aug 10 2010;107(32):14339-44. doi:10.1073/pnas.0912701107
91. Khalid U, Jenkins RH, Andrews R, et al. Determination of a microRNA signature of protective kidney ischemic preconditioning originating from proximal tubules. *Sci Rep-Uk*. 2021/05/10 2021;11(1):9862. doi:10.1038/s41598-021-89195-3
92. Denby L, Ramdas V, McBride MW, et al. miR-21 and miR-214 are consistently modulated during renal injury in rodent models. *Am J Pathol*. Aug 2011;179(2):661-72. doi:10.1016/j.ajpath.2011.04.021
93. Zununi Vahed S, Omidi Y, Ardalan M, Samadi N. Dysregulation of urinary miR-21 and miR-200b associated with interstitial fibrosis and tubular atrophy (IFTA) in renal transplant recipients. *Clin Biochem*. Jan 2017;50(1-2):32-39. doi:10.1016/j.clinbiochem.2016.08.007
94. Khalid U, Newbury LJ, Simpson K, et al. A urinary microRNA panel that is an early predictive biomarker of delayed graft function following kidney transplantation. *Sci Rep*. Mar 5 2019;9(1):3584. doi:10.1038/s41598-019-38642-3
95. Khalid U, Ablorsu E, Szabo L, et al. MicroRNA-21 (miR-21) expression in hypothermic machine perfusate may be predictive of early outcomes in kidney transplantation. *Clinical Transplantation*. 2016;30(2):99-104. doi:https://doi.org/10.1111/ctr.12679
96. Connor KL, Teenan O, Cairns C, et al. Identifying cell-enriched miRNAs in kidney injury and repair. *JCI Insight*. Dec 17 2020;5(24)doi:10.1172/jci.insight.140399
97. Thompson ER, Sewpaul A, Figuereido R, et al. MicroRNA antagonist therapy during normothermic machine perfusion of donor kidneys. *Am J Transplant*. Apr 2022;22(4):1088-1100. doi:10.1111/ajt.16929
98. Mace TA, Collins AL, Wojcik SE, Croce CM, Lesinski GB, Bloomston M. Hypoxia induces the overexpression of microRNA-21 in pancreatic cancer cells. *J Surg Res*. Oct 2013;184(2):855-60. doi:10.1016/j.jss.2013.04.061
99. Xu X, Kriegel AJ, Liu Y, et al. Delayed ischemic preconditioning contributes to renal protection by upregulation of miR-21. *Kidney Int*. Dec 2012;82(11):1167-75. doi:10.1038/ki.2012.241

100. Bao H, Hu S, Zhang C, et al. Inhibition of miRNA-21 prevents fibrogenic activation in podocytes and tubular cells in IgA nephropathy. *Biochem Biophys Res Commun*. Feb 21 2014;444(4):455-60. doi:10.1016/j.bbrc.2014.01.065
101. Loboda A, Sobczak M, Jozkowicz A, Dulak J. TGF-beta1/Smads and miR-21 in Renal Fibrosis and Inflammation. *Mediators Inflamm*. 2016;2016:8319283. doi:10.1155/2016/8319283
102. Bian Z, Wang X, Zhu R, Chen S. miR-21-5p in extracellular vesicles obtained from adipose tissue-derived stromal cells facilitates tubular epithelial cell repair in acute kidney injury. *Cytotherapy*. 2023/03/01/ 2023;25(3):310-322. doi:https://doi.org/10.1016/j.jcyt.2022.08.002
103. Chan JA, Krichevsky AM, Kosik KS. MicroRNA-21 is an antiapoptotic factor in human glioblastoma cells. *Cancer Res*. Jul 15 2005;65(14):6029-33. doi:10.1158/0008-5472.CAN-05-0137
104. Gomez IG, MacKenna DA, Johnson BG, et al. Anti-microRNA-21 oligonucleotides prevent Alport nephropathy progression by stimulating metabolic pathways. *J Clin Invest*. Jan 2015;125(1):141-56. doi:10.1172/JCI75852
105. Huang T, Cao Y, Wang H, et al. Circular RNA YAP1 acts as the sponge of microRNA-21-5p to secure HK-2 cells from ischaemia/reperfusion-induced injury. *J Cell Mol Med*. Apr 2020;24(8):4707-4715. doi:10.1111/jcmm.15142
106. Li X, Xin S, He Z, et al. MicroRNA-21 (miR-21) post-transcriptionally downregulates tumor suppressor PDCD4 and promotes cell transformation, proliferation, and metastasis in renal cell carcinoma. *Cell Physiol Biochem*. 2014;33(6):1631-42. doi:10.1159/000362946
107. Liu XJ, Lv JL, Zou X, et al. MiR-21 alleviates renal tubular epithelial cells injury induced by ischemia by targeting TLR4. *Heliyon*. May 2023;9(5):e15818. doi:10.1016/j.heliyon.2023.e15818
108. Song N, Zhang T, Xu X, et al. miR-21 Protects Against Ischemia/Reperfusion-Induced Acute Kidney Injury by Preventing Epithelial Cell Apoptosis and Inhibiting Dendritic Cell Maturation. *Front Physiol*. 2018;9:790. doi:10.3389/fphys.2018.00790
109. Lin L, Gan H, Zhang H, et al. MicroRNA21 inhibits SMAD7 expression through a target sequence in the 3' untranslated region and inhibits proliferation of renal tubular epithelial cells. *Mol Med Rep*. Aug 2014;10(2):707-12. doi:10.3892/mmr.2014.2312

110. Wang K, Bei WJ, Liu YH, et al. miR21 attenuates contrastinduced renal cell apoptosis by targeting PDCD4. *Mol Med Rep*. Nov 2017;16(5):6757-6763. doi:10.3892/mmr.2017.7426
111. Sun Q, Miao J, Luo J, et al. The feedback loop between miR-21, PDCD4 and AP-1 functions as a driving force for renal fibrogenesis. *J Cell Sci*. Mar 26 2018;131(6)doi:10.1242/jcs.202317
112. Hu H, Jiang W, Xi X, Zou C, Ye Z. MicroRNA-21 attenuates renal ischemia reperfusion injury via targeting caspase signaling in mice. *Am J Nephrol*. 2014;40(3):215-23. doi:10.1159/000368202
113. Zhao S, Li W, Yu W, et al. Exosomal miR-21 from tubular cells contributes to renal fibrosis by activating fibroblasts via targeting PTEN in obstructed kidneys. *Theranostics*. 2021;11(18):8660-8673. doi:10.7150/thno.62820
114. Rubel D, Boulanger J, Craciun F, et al. Anti-microRNA-21 Therapy on Top of ACE Inhibition Delays Renal Failure in Alport Syndrome Mouse Models. *Cells*. Feb 9 2022;11(4)doi:10.3390/cells11040594
115. Ma X, Conklin DJ, Li F, et al. The oncogenic microRNA miR-21 promotes regulated necrosis in mice. *Nat Commun*. May 20 2015;6:7151. doi:10.1038/ncomms8151
116. Kolling M, Kaucsar T, Schauerte C, et al. Therapeutic miR-21 Silencing Ameliorates Diabetic Kidney Disease in Mice. *Mol Ther*. Jan 4 2017;25(1):165-180. doi:10.1016/j.ymthe.2016.08.001
117. Thompson ER, Bates L, Ibrahim IK, et al. Novel delivery of cellular therapy to reduce ischemia reperfusion injury in kidney transplantation. *Am J Transplant*. Apr 2021;21(4):1402-1414. doi:10.1111/ajt.16100
118. Brown CD, Sayer R, Windass AS, et al. Characterisation of human tubular cell monolayers as a model of proximal tubular xenobiotic handling. *Toxicol Appl Pharmacol*. Dec 15 2008;233(3):428-38. doi:10.1016/j.taap.2008.09.018
119. Bajaj P, Chung G, Pye K, et al. Freshly isolated primary human proximal tubule cells as an in vitro model for the detection of renal tubular toxicity. *Toxicology*. Sep 2020;442:152535. doi:10.1016/j.tox.2020.152535
120. Newbury LJ, Simpson K, Khalid U, et al. miR-141 mediates recovery from acute kidney injury. *Sci Rep-Uk*. 2021/08/13 2021;11(1):16499. doi:10.1038/s41598-021-94984-x

121. Zack GW, Rogers WE, Latt SA. Automatic measurement of sister chromatid exchange frequency. *Journal of Histochemistry & Cytochemistry*. 1977;25(7):741-753. doi:10.1177/25.7.70454
122. Rogers-Broadway KR, Karteris E. Amplification efficiency and thermal stability of qPCR instrumentation: Current landscape and future perspectives. *Exp Ther Med*. Oct 2015;10(4):1261-1264. doi:10.3892/etm.2015.2712
123. Goeminne LJ, Gevaert K, Clement L. Peptide-level Robust Ridge Regression Improves Estimation, Sensitivity, and Specificity in Data-dependent Quantitative Label-free Shotgun Proteomics. *Mol Cell Proteomics*. Feb 2016;15(2):657-68. doi:10.1074/mcp.M115.055897
124. Goeminne LJE, Sticker A, Martens L, Gevaert K, Clement L. MSqRob Takes the Missing Hurdle: Uniting Intensity- and Count-Based Proteomics. *Anal Chem*. May 5 2020;92(9):6278-6287. doi:10.1021/acs.analchem.9b04375
125. Sticker A, Goeminne L, Martens L, Clement L. Robust Summarization and Inference in Proteome-wide Label-free Quantification. *Mol Cell Proteomics*. Jul 2020;19(7):1209-1219. doi:10.1074/mcp.RA119.001624
126. Ritchie ME, Phipson B, Wu D, et al. limma powers differential expression analyses for RNA-sequencing and microarray studies. *Nucleic Acids Res*. Apr 20 2015;43(7):e47. doi:10.1093/nar/gkv007
127. Gatto LV, Christophe. QFeatures: Quantitative features for mass spectrometry data. https://bioconductor.org/packages/QFeatures
128. Gatto L, Lilley KS. MSnbase-an R/Bioconductor package for isobaric tagged mass spectrometry data visualization, processing and quantitation. *Bioinformatics*. Jan 15 2012;28(2):288-9. doi:10.1093/bioinformatics/btr645
129. Gatto L, Gibb S, Rainer J. <kbd>MSnbase</kbd>, efficient and elegant R-based processing and visualisation of raw mass spectrometry data. *bioRxiv*. 2020:2020.04.29.067868. doi:10.1101/2020.04.29.067868
130. Soneson C, Marini F, Geier F, Love MI, Stadler MB. ExploreModelMatrix: Interactive exploration for improved understanding of design matrices and linear models in R. *F1000Res*. 2020;9:512. doi:10.12688/f1000research.24187.2
131. Demichev V, Messner CB, Vernardis SI, Lilley KS, Ralser M. DIA-NN: neural networks and interference correction enable deep proteome coverage in high throughput. *Nat Methods*. Jan 2020;17(1):41-44. doi:10.1038/s41592-019-0638-x
132. Dawson CS, Tom. camprotR: Processing, analysing and visualising CCP proteomics data. R package version 0.0.0.9000.

133. Wang S, Li W, Hu L, Cheng J, Yang H, Liu Y. NAguideR: performing and prioritizing missing value imputations for consistent bottom-up proteomic analyses. *Nucleic Acids Research*. 2020;48(14):e83-e83. doi:10.1093/nar/gkaa498
134. Oba S, Sato M-a, Takemasa I, Monden M, Matsubara K-i, Ishii S. A Bayesian missing value estimation method for gene expression profile data. *Bioinformatics*. 2003;19(16):2088-2096. doi:10.1093/bioinformatics/btg287
135. Rohart F, Gautier B, Singh A, Lê Cao K-A. mixOmics: An R package for 'omics feature selection and multiple data integration. *PLOS Computational Biology*. 2017;13(11):e1005752. doi:10.1371/journal.pcbi.1005752
136. Blighe KR, Sharmila; Lewis, Myles. EnhancedVolcano: Publication-ready volcano plots with enhanced colouring and labeling. https://bioconductor.org/packages/EnhancedVolcano
137. Ru Y, Kechris KJ, Tabakoff B, et al. The multiMiR R package and database: integration of microRNA-target interactions along with their disease and drug associations. *Nucleic Acids Res*. 2014;42(17):e133. doi:10.1093/nar/gku631
138. Korotkevich GS, Vladimir; Sergushichev, Alexey Fast gene set enrichment analysis. *bioRxiv*. 2019;doi:10.1101/060012
139. Liberzon A, Birger C, Thorvaldsdóttir H, Ghandi M, Mesirov JP, Tamayo P. The Molecular Signatures Database (MSigDB) hallmark gene set collection. *Cell Syst*. Dec 23 2015;1(6):417-425. doi:10.1016/j.cels.2015.12.004
140. Milacic M, Beavers D, Conley P, et al. The Reactome Pathway Knowledgebase 2024. *Nucleic Acids Research*. 2024;52(D1):D672-D678. doi:10.1093/nar/gkad1025
141. Dolgalev I. msigdbr: MSigDB Gene Sets for Multiple Organisms in a Tidy Data Format. https://CRAN.R-project.org/package=msigdbr
142. Durinck S, Moreau Y, Kasprzyk A, et al. BioMart and Bioconductor: a powerful link between biological databases and microarray data analysis. *Bioinformatics*. Aug 15 2005;21(16):3439-40. doi:10.1093/bioinformatics/bti525
143. Chen Y, Wang X. miRDB: an online database for prediction of functional microRNA targets. *Nucleic Acids Res*. Jan 8 2020;48(D1):D127-d131. doi:10.1093/nar/gkz757
144. Krämer A, Green J, Pollard J, Jr., Tugendreich S. Causal analysis approaches in Ingenuity Pathway Analysis. *Bioinformatics*. Feb 15 2014;30(4):523-30. doi:10.1093/bioinformatics/btt703

145. Wickham H. ggplot2: Elegant Graphics for Data Analysis. Springer-Verlag New York. https://ggplot2.tidyverse.org
146. Kassambara A. rstatix: Pipe-Friendly Framework for Basic Statistical Tests. https://CRAN.R-project.org/package=rstatix
147. van den Brand T. ggh4x: Hacks for 'ggplot2'. https://CRAN.R-project.org/package=ggh4x
148. Bonventre JV, Vaidya VS, Schmouder R, Feig P, Dieterle F. Next-generation biomarkers for detecting kidney toxicity. *Nat Biotechnol*. May 2010;28(5):436-40. doi:10.1038/nbt0510-436
149. Goujon M, Woszczyk J, Gaudelot K, et al. A Double-Negative Feedback Interaction between miR-21 and PPAR-α in Clear Renal Cell Carcinoma. *Cancers*. 2022;14(3):795.
150. Liu X-J, Lv J-L, Zou X, et al. MiR-21 alleviates renal tubular epithelial cells injury induced by ischemia by targeting TLR4. *Heliyon*. 2023/05/01/ 2023;9(5):e15818. doi:https://doi.org/10.1016/j.heliyon.2023.e15818
151. Ryan MJ, Johnson G, Kirk J, Fuerstenberg SM, Zager RA, Torok-Storb B. HK-2: an immortalized proximal tubule epithelial cell line from normal adult human kidney. *Kidney Int*. Jan 1994;45(1):48-57. doi:10.1038/ki.1994.6
152. Eshbach ML, Weisz OA. Receptor-Mediated Endocytosis in the Proximal Tubule. *Annu Rev Physiol*. Feb 10 2017;79:425-448. doi:10.1146/annurev-physiol-022516-034234
153. Agarwal S, Sudhini YR, Polat OK, Reiser J, Altintas MM. Renal cell markers: lighthouses for managing renal diseases. *Am J Physiol-Renal*. 2021;321(6):F715-F739. doi:10.1152/ajprenal.00182.2021
154. Stewart BJ, Ferdinand JR, Young MD, et al. Spatiotemporal immune zonation of the human kidney. *Science*. Sep 27 2019;365(6460):1461-1466. doi:10.1126/science.aat5031
155. Liao J, Yu Z, Chen Y, et al. Single-cell RNA sequencing of human kidney. *Sci Data*. Jan 2 2020;7(1):4. doi:10.1038/s41597-019-0351-8
156. Moll R, Divo M, Langbein L. The human keratins: biology and pathology. *Histochem Cell Biol*. Jun 2008;129(6):705-33. doi:10.1007/s00418-008-0435-6
157. Djudjaj S, Papasotiriou M, Bulow RD, et al. Keratins are novel markers of renal epithelial cell injury. *Kidney Int*. Apr 2016;89(4):792-808. doi:10.1016/j.kint.2015.10.015

158. Adler M, Ramm S, Hafner M, et al. A Quantitative Approach to Screen for Nephrotoxic Compounds In Vitro. *J Am Soc Nephrol*. Apr 2016;27(4):1015-28. doi:10.1681/ASN.2015010060
159. Qi W, Johnson DW, Vesey DA, Pollock CA, Chen X. Isolation, propagation and characterization of primary tubule cell culture from human kidney. *Nephrology (Carlton)*. Apr 2007;12(2):155-9. doi:10.1111/j.1440-1797.2007.00779.x
160. Yang X, Zhang D, Chong T, Li Y, Wang Z, Zhang P. Expression of CK19, CD105 and CD146 are associated with early metastasis in patients with renal cell carcinoma. *Oncol Lett*. Apr 2018;15(4):4229-4234. doi:10.3892/ol.2018.7871
161. Tornavaca O, Chia M, Dufton N, et al. ZO-1 controls endothelial adherens junctions, cell-cell tension, angiogenesis, and barrier formation. *J Cell Biol*. Mar 16 2015;208(6):821-38. doi:10.1083/jcb.201404140
162. Shi Y, Li R, Yang J, Li X. No tight junctions in tight junction protein-1 expressing HeLa and fibroblast cells. *Int J Physiol Pathophysiol Pharmacol*. 2020;12(2):70-78.
163. Slusser A, Bathula CS, Sens DA, et al. Cadherin Expression, Vectorial Active Transport, and Metallothionein Isoform 3 Mediated EMT/MET Responses in Cultured Primary and Immortalized Human Proximal Tubule Cells. *PLOS ONE*. 2015;10(3):e0120132. doi:10.1371/journal.pone.0120132
164. Verkman AS. Aquaporin water channels and endothelial cell function. *J Anat*. Jun 2002;200(6):617-27. doi:10.1046/j.1469-7580.2002.00058.x
165. Chabardes-Garonne D, Mejean A, Aude JC, et al. A panoramic view of gene expression in the human kidney. *Proc Natl Acad Sci U S A*. Nov 11 2003;100(23):13710-5. doi:10.1073/pnas.2234604100
166. Pohl M, Shan QX, Petsch T, et al. Short-Term Functional Adaptation of Aquaporin-1 Surface Expression in the Proximal Tubule, a Component of Glomerulotubular Balance. *Journal of the American Society of Nephrology*. Jun 2015;26(6):1269-1278. doi:10.1681/Asn.2014020148
167. Young MD, Mitchell TJ, Vieira Braga FA, et al. Single-cell transcriptomes from human kidneys reveal the cellular identity of renal tumors. *Science*. Aug 10 2018;361(6402):594-599. doi:10.1126/science.aat1699
168. Lawson JS, Syme HM, Wheeler-Jones CPD, Elliott J. Characterisation of feline renal cortical fibroblast cultures and their transcriptional response to transforming growth factor beta1. *BMC Vet Res*. Mar 9 2018;14(1):76. doi:10.1186/s12917-018-1387-2

169. LeBleu VS, Taduri G, O'Connell J, et al. Origin and function of myofibroblasts in kidney fibrosis. *Nat Med*. Aug 2013;19(8):1047-53. doi:10.1038/nm.3218
170. Senbanjo LT, Chellaiah MA. CD44: A Multifunctional Cell Surface Adhesion Receptor Is a Regulator of Progression and Metastasis of Cancer Cells. *Front Cell Dev Biol*. 2017;5:18. doi:10.3389/fcell.2017.00018
171. Sherman L, Sleeman J, Herrlich P, Ponta H. Hyaluronate receptors: key players in growth, differentiation, migration and tumor progression. *Curr Opin Cell Biol*. Oct 1994;6(5):726-33. doi:10.1016/0955-0674(94)90100-7
172. Rouschop KM, Roelofs JJ, Claessen N, et al. Protection against renal ischemia reperfusion injury by CD44 disruption. *J Am Soc Nephrol*. Jul 2005;16(7):2034-43. doi:10.1681/ASN.2005010054
173. Xu H, Tian Y, Yuan X, et al. The role of CD44 in epithelial-mesenchymal transition and cancer development. *Onco Targets Ther*. 2015;8:3783-92. doi:10.2147/OTT.S95470
174. Rouschop KM, Roelofs JJ, Sylva M, et al. Renal expression of CD44 correlates with acute renal allograft rejection. *Kidney Int*. Sep 2006;70(6):1127-34. doi:10.1038/sj.ki.5001711
175. Florquin S, Nunziata R, Claessen N, van den Berg FM, Pals ST, Weening JJ. CD44 expression in IgA nephropathy. *Am J Kidney Dis*. Feb 2002;39(2):407-14. doi:10.1053/ajkd.2002.30563
176. Rouschop KM, Sewnath ME, Claessen N, et al. CD44 deficiency increases tubular damage but reduces renal fibrosis in obstructive nephropathy. *J Am Soc Nephrol*. Mar 2004;15(3):674-86. doi:10.1097/01.asn.0000115703.30835.96
177. Roy-Chaudhury P, Khong TF, Williams JH, et al. CD44 in glomerulonephritis: expression in human renal biopsies, the Thy 1.1 model, and by cultured mesangial cells. *Kidney Int*. Jul 1996;50(1):272-81. doi:10.1038/ki.1996.312
178. Lewington AJ, Padanilam BJ, Martin DR, Hammerman MR. Expression of CD44 in kidney after acute ischemic injury in rats. *Am J Physiol Regul Integr Comp Physiol*. Jan 2000;278(1):R247-54. doi:10.1152/ajpregu.2000.278.1.R247
179. Quintanilla RH, Asprer JST, Vaz C, Tanavde V, Lakshmipathy U. CD44 Is a Negative Cell Surface Marker for Pluripotent Stem Cell Identification during Human Fibroblast Reprogramming. *Plos One*. Jan 9 2014;9(1)doi:ARTNe8541910.1371/journal.pone.0085419

180. Floege J, Eitner F, Alpers CE. A new look at platelet-derived growth factor in renal disease. *Journal of the American Society of Nephrology*. Jan 2008;19(1):12-23. doi:10.1681/Asn.2007050532
181. Nakagawa T, Sasahara M, Haneda M, et al. Role of PDGF B-chain and PDGF receptors in rat tubular regeneration after acute injury. *Am J Pathol*. Nov 1999;155(5):1689-99. doi:10.1016/S0002-9440(10)65484-3
182. Chen YT, Chang FC, Wu CF, et al. Platelet-derived growth factor receptor signaling activates pericyte-myofibroblast transition in obstructive and post-ischemic kidney fibrosis. *Kidney Int*. Dec 2011;80(11):1170-1181. doi:10.1038/ki.2011.208
183. Boor P, Ostendorf T, Floege J. PDGF and the progression of renal disease. *Nephrol Dial Transpl*. Feb 2014;29:I45-I54. doi:10.1093/ndt/gft273
184. Ostendorf T, Boor P, van Roeyen CR, Floege J. Platelet-derived growth factors (PDGFs) in glomerular and tubulointerstitial fibrosis. *Kidney Int Suppl (2011)*. Nov 2014;4(1):65-69. doi:10.1038/kisup.2014.12
185. Buhl EM, Djudjaj S, Klinkhammer BM, et al. Dysregulated mesenchymal PDGFR-beta drives kidney fibrosis. *Embo Mol Med*. Mar 6 2020;12(3)doi:ARTNe1102110.15252/emmm.201911021
186. Kuppe C, Ibrahim MM, Kranz J, et al. Decoding myofibroblast origins in human kidney fibrosis. *Nature*. Jan 14 2021;589(7841):281-+. doi:10.1038/s41586-020-2941-1
187. Horikawa S, Ishii Y, Hamashima T, et al. PDGFR alpha plays a crucial role in connective tissue remodeling. *Sci Rep-Uk*. Dec 7 2015;5doi:ARTN 17948

10.1038/srep17948
188. Erez N, Truitt M, Olson P, Arron ST, Hanahan D. Cancer-Associated Fibroblasts Are Activated in Incipient Neoplasia to Orchestrate Tumor-Promoting Inflammation in an NF-kappa B-Dependent Manner (vol 17, pg 135, 2010). *Cancer Cell*. May 18 2010;17(5):523-523. doi:10.1016/j.ccr.2010.04.018
189. Naing Z, Hamilton ST, van Zuylen WJ, Scott GM, Rawlinson WD. Differential Expression of PDGF Receptor-alpha in Human Placental Trophoblasts Leads to Different Entry Pathways by Human Cytomegalovirus Strains. *Sci Rep*. Jan 23 2020;10(1):1082. doi:10.1038/s41598-020-57471-3
190. Lertkiatmongkol P, Liao D, Mei H, Hu Y, Newman PJ. Endothelial functions of platelet/endothelial cell adhesion molecule-1 (CD31). *Curr Opin Hematol*. May 2016;23(3):253-9. doi:10.1097/moh.0000000000000239

191. Al-Ani A, Toms D, Kondro D, Thundathil J, Yu Y, Ungrin M. Oxygenation in cell culture: Critical parameters for reproducibility are routinely not reported. *PLoS One*. 2018;13(10):e0204269. doi:10.1371/journal.pone.0204269
192. Zeitouni NE, Fandrey J, Naim HY, von Kockritz-Blickwede M. Measuring oxygen levels in Caco-2 cultures. *Hypoxia (Auckl)*. 2015;3:53-66. doi:10.2147/HP.S85625
193. Cotton BA, McElroy LA. Oxygen-carrying Capacity. In: Papadakos PJ, Gestring ML, eds. *Encyclopedia of Trauma Care*. 1st 2015. ed. Springer Berlin Heidelberg : Imprint: Springer; 2015.
194. Collins JA, Rudenski A, Gibson J, Howard L, O'Driscoll R. Relating oxygen partial pressure, saturation and content: the haemoglobin-oxygen dissociation curve. *Breathe (Sheff)*. Sep 2015;11(3):194-201. doi:10.1183/20734735.001415
195. Rivera KR, Yokus MA, Erb PD, Pozdin VA, Daniele M. Measuring and regulating oxygen levels in microphysiological systems: design, material, and sensor considerations. *Analyst*. May 13 2019;144(10):3190-3215. doi:10.1039/c8an02201a
196. Place TL, Domann FE, Case AJ. Limitations of oxygen delivery to cells in culture: An underappreciated problem in basic and translational research. *Free Radic Biol Med*. Dec 2017;113:311-322. doi:10.1016/j.freeradbiomed.2017.10.003
197. Pavlacky J, Polak J. Technical Feasibility and Physiological Relevance of Hypoxic Cell Culture Models. *Front Endocrinol (Lausanne)*. 2020;11:57. doi:10.3389/fendo.2020.00057
198. Kann SH, Shaughnessey EM, Coppeta JR, et al. Measurement of oxygen consumption rates of human renal proximal tubule cells in an array of organ-on-chip devices to monitor drug-induced metabolic shifts. *Microsyst Nanoeng*. 2022;8:109. doi:10.1038/s41378-022-00442-7
199. Lever JE. Inducers of mammalian cell differentiation stimulate dome formation in a differentiated kidney epithelial cell line (MDCK). *Proc Natl Acad Sci U S A*. Mar 1979;76(3):1323-7. doi:10.1073/pnas.76.3.1323
200. Bai Y, Wei C, Li P, et al. Primary cilium in kidney development, function and disease. *Front Endocrinol (Lausanne)*. 2022;13:952055. doi:10.3389/fendo.2022.952055
201. Nakamura M, Yamabe H, Osawa H, et al. Hypoxic conditions stimulate the production of angiogenin and vascular endothelial growth factor by human renal proximal tubular epithelial cells in culture. *Nephrol Dial Transpl*. 2006;21(6):1489-1495. doi:10.1093/ndt/gfl041

202. Tang S, Leung JCK, Lam CWK, Lai FM-M, Chan TM, Lai KN. In vitro studies of aquaporins 1 and 3 expression in cultured human proximal tubular cells: Upregulation by transferrin but not albumin. *American Journal of Kidney Diseases*. 2001;38(2):317-330. doi:10.1053/ajkd.2001.26097
203. Kim BS, Chen J, Weinstein T, Noiri E, Goligorsky MS. VEGF expression in hypoxia and hyperglycemia: reciprocal effect on branching angiogenesis in epithelial-endothelial co-cultures. *J Am Soc Nephrol*. Aug 2002;13(8):2027-36. doi:10.1097/01.asn.0000024436.00520.d8
204. Nakagawa T, Lan HY, Zhu HJ, Kang DH, Schreiner GF, Johnson RJ. Differential regulation of VEGF by TGF-beta and hypoxia in rat proximal tubular cells. *Am J Physiol Renal Physiol*. Oct 2004;287(4):F658-64. doi:10.1152/ajprenal.00040.2004
205. El Awad B, Kreft B, Wolber EM, et al. Hypoxia and interleukin-1beta stimulate vascular endothelial growth factor production in human proximal tubular cells. *Kidney Int*. Jul 2000;58(1):43-50. doi:10.1046/j.1523-1755.2000.00139.x
206. Nakamura M, Yamabe H, Osawa H, et al. Hypoxic conditions stimulate the production of angiogenin and vascular endothelial growth factor by human renal proximal tubular epithelial cells in culture. *Nephrol Dial Transplant*. Jun 2006;21(6):1489-95. doi:10.1093/ndt/gfl041
207. Rogg EM, Abplanalp WT, Bischof C, et al. Analysis of Cell Type-Specific Effects of MicroRNA-92a Provides Novel Insights Into Target Regulation and Mechanism of Action. *Circulation*. Nov 27 2018;138(22):2545-2558. doi:10.1161/CIRCULATIONAHA.118.034598
208. Nallet-Staub F, Yin X, Gilbert C, et al. Cell density sensing alters TGF-beta signaling in a cell-type-specific manner, independent from Hippo pathway activation. *Dev Cell*. Mar 9 2015;32(5):640-51. doi:10.1016/j.devcel.2015.01.011
209. Winkle M, El-Daly SM, Fabbri M, Calin GA. Noncoding RNA therapeutics — challenges and potential solutions. *Nature Reviews Drug Discovery*. 2021/08/01 2021;20(8):629-651. doi:10.1038/s41573-021-00219-z
210. Juliano RL. The delivery of therapeutic oligonucleotides. *Nucleic Acids Res*. Aug 19 2016;44(14):6518-48. doi:10.1093/nar/gkw236
211. Carton-Garcia F, Saande CJ, Meraviglia-Crivelli D, Aldabe R, Pastor F. Oligonucleotide-Based Therapies for Renal Diseases. *Biomedicines*. Mar 16 2021;9(3)doi:10.3390/biomedicines9030303

212. Juliano RL. Intracellular Trafficking and Endosomal Release of Oligonucleotides: What We Know and What We Don't. *Nucleic Acid Ther*. Jun 2018;28(3):166-177. doi:10.1089/nat.2018.0727
213. Koller E, Vincent TM, Chappell A, De S, Manoharan M, Bennett CF. Mechanisms of single-stranded phosphorothioate modified antisense oligonucleotide accumulation in hepatocytes. *Nucleic Acids Res*. Jun 2011;39(11):4795-807. doi:10.1093/nar/gkr089
214. Stein CA, Hansen JB, Lai J, et al. Efficient gene silencing by delivery of locked nucleic acid antisense oligonucleotides, unassisted by transfection reagents. *Nucleic Acids Res*. Jan 2010;38(1):e3. doi:10.1093/nar/gkp841
215. Christensen EI, Birn H, Storm T, Weyer K, Nielsen R. Endocytic receptors in the renal proximal tubule. *Physiology (Bethesda)*. Aug 2012;27(4):223-36. doi:10.1152/physiol.00022.2012
216. Gao S, Hein S, Dagnaes-Hansen F, et al. Megalin-mediated specific uptake of chitosan/siRNA nanoparticles in mouse kidney proximal tubule epithelial cells enables AQP1 gene silencing. *Theranostics*. 2014;4(10):1039-51. doi:10.7150/thno.7866
217. Molitoris BA, Dagher PC, Sandoval RM, et al. siRNA targeted to p53 attenuates ischemic and cisplatin-induced acute kidney injury. *J Am Soc Nephrol*. Aug 2009;20(8):1754-64. doi:10.1681/ASN.2008111204
218. Cordier C, Boutimah F, Bourdeloux M, et al. Delivery of antisense peptide nucleic acids to cells by conjugation with small arginine-rich cell-penetrating peptide (R/W)9. *PLoS One*. 2014;9(8):e104999. doi:10.1371/journal.pone.0104999
219. Juliano RL, Carver K, Cao C, Ming X. Receptors, endocytosis, and trafficking: the biological basis of targeted delivery of antisense and siRNA oligonucleotides. *J Drug Target*. Jan 2013;21(1):27-43. doi:10.3109/1061186X.2012.740674
220. Rennick JJ, Johnston APR, Parton RG. Key principles and methods for studying the endocytosis of biological and nanoparticle therapeutics. *Nat Nanotechnol*. Mar 2021;16(3):266-276. doi:10.1038/s41565-021-00858-8
221. Juliano RL, Ming X, Nakagawa O. Cellular uptake and intracellular trafficking of antisense and siRNA oligonucleotides. *Bioconjug Chem*. Feb 15 2012;23(2):147-57. doi:10.1021/bc200377d
222. Zhuang ZJ, Marshansky V, Breton S, Brown D. Is caveolin involved in normal proximal tubule function? Presence in model PT systems but absence in situ. *Am J Physiol-Renal*. Jan 2011;300(1):F199-F206. doi:10.1152/ajprenal.00513.2010

223. Krawczyk KM, Hansson J, Nilsson H, Krawczyk KK, Sward K, Johansson ME. Injury induced expression of caveolar proteins in human kidney tubules - role of megakaryoblastic leukemia 1. *Bmc Nephrol*. Oct 24 2017;18doi:ARTN 320

10.1186/s12882-017-0738-8

224. Manzanares D, Cena V. Endocytosis: The Nanoparticle and Submicron Nanocompounds Gateway into the Cell. *Pharmaceutics*. Apr 17 2020;12(4)doi:10.3390/pharmaceutics12040371

225. Rennick JJ, Johnston APR, Parton RG. Key principles and methods for studying the endocytosis of biological and nanoparticle therapeutics. *Nat Nanotechnol*. Mar 2021;16(3):266-276. doi:10.1038/s41565-021-00858-8

226. Christensen EI, Birn H. Megalin and cubilin: Multifunctional endocytic receptors. *Nat Rev Mol Cell Bio*. Apr 2002;3(4):258-268a. doi:10.1038/nrm778

227. De S, Kuwahara S, Saito A. The endocytic receptor megalin and its associated proteins in proximal tubule epithelial cells. *Membranes (Basel)*. Jul 11 2014;4(3):333-55. doi:10.3390/membranes4030333

228. Nielsen R, Christensen EI, Birn H. Megalin and cubilin in proximal tubule protein reabsorption: from experimental models to human disease. *Kidney Int*. Jan 2016;89(1):58-67. doi:10.1016/j.kint.2015.11.007

229. Crooke ST, Wang S, Vickers TA, Shen W, Liang XH. Cellular uptake and trafficking of antisense oligonucleotides. *Nat Biotechnol*. Mar 2017;35(3):230-237. doi:10.1038/nbt.3779

230. Roberts TC. The MicroRNA Biology of the Mammalian Nucleus. *Mol Ther Nucleic Acids*. Aug 19 2014;3:e188. doi:10.1038/mtna.2014.40

231. Meister G, Landthaler M, Patkaniowska A, Dorsett Y, Teng G, Tuschl T. Human Argonaute2 mediates RNA cleavage targeted by miRNAs and siRNAs. *Mol Cell*. Jul 23 2004;15(2):185-97. doi:10.1016/j.molcel.2004.07.007

232. Lorenz P, Misteli T, Baker BF, Bennett CF, Spector DL. Nucleocytoplasmic shuttling: a novel in vivo property of antisense phosphorothioate oligodeoxynucleotides. *Nucleic Acids Res*. Jan 15 2000;28(2):582-92. doi:10.1093/nar/28.2.582

233. Li M, Balamuthusamy S, Simon EE, Batuman V. Silencing megalin and cubilin genes inhibits myeloma light chain endocytosis and ameliorates toxicity in human renal proximal tubule epithelial cells. *Am J Physiol-Renal*. Jul 2008;295(1):F82-F90. doi:10.1152/ajprenal.00091.2008

234. Zhai XY, Nielsen R, Birn H, et al. Cubilin- and megalin-mediated uptake of albumin in cultured proximal tubule cells of opossum kidney. *Kidney Int*. Oct 2000;58(4):1523-1533. doi:DOI 10.1046/j.1523-1755.2000.00314.x
235. Bajaj P, Chung G, Pye K, et al. Freshly isolated primary human proximal tubule cells as an in vitro model for the detection of renal tubular toxicity. *Toxicology*. Sep 2020;442doi:ARTN 152535

10.1016/j.tox.2020.152535
236. Hori Y, Aoki N, Kuwahara S, et al. Megalin Blockade with Cilastatin Suppresses Drug-Induced Nephrotoxicity. *J Am Soc Nephrol*. Jun 2017;28(6):1783-1791. doi:10.1681/ASN.2016060606
237. Onodera A, Tani M, Michigami T, et al. Role of megalin and the soluble form of its ligand RAP in Cd-metallothionein endocytosis and Cd-metallothionein-induced nephrotoxicity in vivo. *Toxicol Lett*. Jul 20 2012;212(2):91-6. doi:10.1016/j.toxlet.2012.05.012
238. Long KR, Rbaibi Y, Kashlan OB, Weisz OA. Receptor-associated protein impairs ligand binding to megalin and megalin-dependent endocytic flux in proximal tubule cells. *Am J Physiol Renal Physiol*. Oct 1 2023;325(4):F457-F464. doi:10.1152/ajprenal.00165.2023
239. Sun Y, Goes Martini A, Janssen MJ, et al. Megalin: A Novel Endocytic Receptor for Prorenin and Renin. *Hypertension*. May 2020;75(5):1242-1250. doi:10.1161/HYPERTENSIONAHA.120.14845
240. Vercauteren D, Vandenbroucke RE, Jones AT, et al. The use of inhibitors to study endocytic pathways of gene carriers: optimization and pitfalls. *Mol Ther*. Mar 2010;18(3):561-9. doi:10.1038/mt.2009.281
241. Morgan K, Martucci N, Kozlowska A, et al. Chlorpromazine toxicity is associated with disruption of cell membrane integrity and initiation of a pro-inflammatory response in the HepaRG hepatic cell line. *Biomed Pharmacother*. Mar 2019;111:1408-1416. doi:10.1016/j.biopha.2019.01.020
242. Bouley R, Yui N, Terlouw A, Cheung PW, Brown D. Chlorpromazine Induces Basolateral Aquaporin-2 Accumulation via F-Actin Depolymerization and Blockade of Endocytosis in Renal Epithelial Cells. *Cells*. Apr 23 2020;9(4)doi:10.3390/cells9041057
243. Francia V, Reker-Smit C, Boel G, Salvati A. Limits and challenges in using transport inhibitors to characterize how nano-sized drug carriers enter cells. *Nanomedicine (Lond)*. Jun 2019;14(12):1533-1549. doi:10.2217/nnm-2018-0446

244. Kuhn DA, Vanhecke D, Michen B, et al. Different endocytotic uptake mechanisms for nanoparticles in epithelial cells and macrophages. *Beilstein Journal of Nanotechnology*. // 2014;5:1625-1636. doi:10.3762/bjnano.5.174
245. Schuh CD, Polesel M, Platonova E, et al. Combined Structural and Functional Imaging of the Kidney Reveals Major Axial Differences in Proximal Tubule Endocytosis. *J Am Soc Nephrol*. Nov 2018;29(11):2696-2712. doi:10.1681/ASN.2018050522
246. Li L, Wan T, Wan M, Liu B, Cheng R, Zhang R. The effect of the size of fluorescent dextran on its endocytic pathway. *Cell Biol Int*. May 2015;39(5):531-9. doi:10.1002/cbin.10424
247. Humphries WHIV, Szymanski CJ, Payne CK. Endo-Lysosomal Vesicles Positive for Rab7 and LAMP1 Are Terminal Vesicles for the Transport of Dextran. *PLOS ONE*. 2011;6(10):e26626. doi:10.1371/journal.pone.0026626
248. Koivusalo M, Welch C, Hayashi H, et al. Amiloride inhibits macropinocytosis by lowering submembranous pH and preventing Rac1 and Cdc42 signaling. *J Cell Biol*. Feb 22 2010;188(4):547-63. doi:10.1083/jcb.200908086
249. Ivanov AI. Pharmacological inhibition of endocytic pathways: is it specific enough to be useful? *Methods Mol Biol*. 2008;440:15-33. doi:10.1007/978-1-59745-178-9_2
250. Gekle M, Drumm K, Mildenberger S, Freudinger R, Gassner B, Silbernagl S. Inhibition of Na+-H+ exchange impairs receptor-mediated albumin endocytosis in renal proximal tubule-derived epithelial cells from opossum. *J Physiol*. Nov 1 1999;520 Pt 3:709-21. doi:10.1111/j.1469-7793.1999.00709.x
251. Rolver MG, Elingaard-Larsen LO, Andersen AP, Counillon L, Pedersen SF. Pyrazine ring-based Na(+)/H(+) exchanger (NHE) inhibitors potently inhibit cancer cell growth in 3D culture, independent of NHE1. *Sci Rep*. Apr 2 2020;10(1):5800. doi:10.1038/s41598-020-62430-z
252. Aredia F, Czaplinski S, Fulda S, Scovassi AI. Molecular features of the cytotoxicity of an NHE inhibitor: Evidence of mitochondrial alterations, ROS overproduction and DNA damage. *BMC Cancer*. Nov 5 2016;16(1):851. doi:10.1186/s12885-016-2878-9
253. Lee EC, Valencia T, Allerson C, et al. Discovery and preclinical evaluation of anti-miR-17 oligonucleotide RGLS4326 for the treatment of polycystic kidney disease. *Nature Communications*. 2019/09/12 2019;10(1):4148. doi:10.1038/s41467-019-11918-y

254. Chau BN, Xin C, Hartner J, et al. MicroRNA-21 Promotes Fibrosis of the Kidney by Silencing Metabolic Pathways. *Science Translational Medicine*. 2012/02/15 2012;4(121):121ra18-121ra18. doi:10.1126/scitranslmed.3003205
255. Williams DM, Gungordu L, Jackson-Crawford A, Lowe M. Assessment of endocytic traffic and Ocrl function in the developing zebrafish neuroepithelium. *J Cell Sci*. Sep 15 2022;135(18)doi:10.1242/jcs.260339
256. miRCURY® LNA® miRNA Inhibitors and Target Site Blockers Handbook. Qiagen; 2017. Accessed 04/07/2024. https://www.qiagen.com/gb/resources/resourcedetail?id=c035dbe7-933f-4b11-b36f-b99c8e93aad9&lang=en
257. Yarwood R, Hellicar J, Woodman PG, Lowe M. Membrane trafficking in health and disease. *Dis Model Mech*. Apr 30 2020;13(4)doi:10.1242/dmm.043448
258. Krieger SE, Kim C, Zhang L, Marjomaki V, Bergelson JM. Echovirus 1 entry into polarized Caco-2 cells depends on dynamin, cholesterol, and cellular factors associated with macropinocytosis. *J Virol*. Aug 2013;87(16):8884-95. doi:10.1128/JVI.03415-12
259. Ha KD, Bidlingmaier SM, Liu B. Macropinocytosis Exploitation by Cancers and Cancer Therapeutics. Review. *Frontiers in Physiology*. 2016-September-12 2016;7doi:10.3389/fphys.2016.00381
260. Kumari S, Mg S, Mayor S. Endocytosis unplugged: multiple ways to enter the cell. *Cell Res*. Mar 2010;20(3):256-75. doi:10.1038/cr.2010.19
261. Lin XP, Mintern JD, Gleeson PA. Macropinocytosis in Different Cell Types: Similarities and Differences. *Membranes (Basel)*. Aug 3 2020;10(8)doi:10.3390/membranes10080177
262. Long KR, Rbaibi Y, Bondi CD, et al. Cubilin-, megalin-, and Dab2-dependent transcription revealed by CRISPR/Cas9 knockout in kidney proximal tubule cells. *Am J Physiol Renal Physiol*. Jan 1 2022;322(1):F14-F26. doi:10.1152/ajprenal.00259.2021
263. Takahashi M, Contu VR, Kabuta C, et al. SIDT2 mediates gymnosis, the uptake of naked single-stranded oligonucleotides into living cells. *RNA Biol*. Nov 2 2017;14(11):1534-1543. doi:10.1080/15476286.2017.1302641
264. Ren Q, Weyer K, Rbaibi Y, et al. Distinct functions of megalin and cubilin receptors in recovery of normal and nephrotic levels of filtered albumin. *Am J Physiol Renal Physiol*. May 1 2020;318(5):F1284-F1294. doi:10.1152/ajprenal.00030.2020

265. Gilleron J, Querbes W, Zeigerer A, et al. Image-based analysis of lipid nanoparticle-mediated siRNA delivery, intracellular trafficking and endosomal escape. *Nat Biotechnol*. Jul 2013;31(7):638-46. doi:10.1038/nbt.2612
266. Goldaracena N, Spetzler VN, Echeverri J, et al. Inducing Hepatitis C Virus Resistance After Pig Liver Transplantation-A Proof of Concept of Liver Graft Modification Using Warm Ex Vivo Perfusion. *Am J Transplant*. Apr 2017;17(4):970-978. doi:10.1111/ajt.14100
267. Alam MR, Ming X, Dixit V, Fisher M, Chen X, Juliano RL. The biological effect of an antisense oligonucleotide depends on its route of endocytosis and trafficking. *Oligonucleotides*. Apr 2010;20(2):103-9. doi:10.1089/oli.2009.0211
268. Subramanian A, Tamayo P, Mootha VK, et al. Gene set enrichment analysis: A knowledge-based approach for interpreting genome-wide expression profiles. *Proceedings of the National Academy of Sciences*. 2005/10/25 2005;102(43):15545-15550. doi:10.1073/pnas.0506580102
269. GSEA User Guide. Accessed 07-10-2024, https://www.gsea-msigdb.org/gsea/doc/GSEAUserGuideFrame.html
270. Yang CH, Yue J, Pfeffer SR, Handorf CR, Pfeffer LM. MicroRNA miR-21 Regulates the Metastatic Behavior of B16 Melanoma Cells *. *Journal of Biological Chemistry*. 2011;286(45):39172-39178. doi:10.1074/jbc.M111.285098
271. Yang CH, Yue J, Fan M, Pfeffer LM. IFN induces miR-21 through a signal transducer and activator of transcription 3-dependent pathway as a suppressive negative feedback on IFN-induced apoptosis. *Cancer Res*. Oct 15 2010;70(20):8108-16. doi:10.1158/0008-5472.Can-10-2579
272. Palmyre A, Lee J, Ryklin G, et al. Collective epithelial migration drives kidney repair after acute injury. *PLoS One*. 2014;9(7):e101304. doi:10.1371/journal.pone.0101304
273. Kumar S. Cellular and molecular pathways of renal repair after acute kidney injury. *Kidney Int*. 2018/01/01/ 2018;93(1):27-40. doi:https://doi.org/10.1016/j.kint.2017.07.030
274. Le Jan S, Amy C, Cazes A, et al. Angiopoietin-like 4 is a proangiogenic factor produced during ischemia and in conventional renal cell carcinoma. *Am J Pathol*. May 2003;162(5):1521-8. doi:10.1016/s0002-9440(10)64285-x
275. Fernández-Hernando C, Suárez Y. ANGPTL4: a multifunctional protein involved in metabolism and vascular homeostasis. *Curr Opin Hematol*. May 2020;27(3):206-213. doi:10.1097/moh.0000000000000580

276. Wang X, Chang H-c, Gu X, et al. Renal lipid accumulation and aging linked to tubular cells injury via ANGPTL4. *Mechanisms of Ageing and Development*. 2024/06/01/ 2024;219:111932. doi:https://doi.org/10.1016/j.mad.2024.111932
277. Qin L, Zhang R, Yang S, Chen F, Shi J. Knockdown of ANGPTL-4 inhibits inflammatory response and extracellular matrix accumulation in glomerular mesangial cells cultured under high glucose condition. *Artificial Cells, Nanomedicine, and Biotechnology*. 2019/12/04 2019;47(1):3368-3373. doi:10.1080/21691401.2019.1649274
278. Li S, Nagothu K, Ranganathan G, et al. Reduced kidney lipoprotein lipase and renal tubule triglyceride accumulation in cisplatin-mediated acute kidney injury. *Am J Physiol-Renal*. 2012;303(3):F437-F448. doi:10.1152/ajprenal.00111.2012
279. Chugh SS, Macé C, Clement LC, Del Nogal Avila M, Marshall CB. Angiopoietin-like 4 based therapeutics for proteinuria and kidney disease. *Front Pharmacol*. 2014;5:23. doi:10.3389/fphar.2014.00023
280. Al Shawaf E, Abu-Farha M, Devarajan S, et al. ANGPTL4: A Predictive Marker for Diabetic Nephropathy. *J Diabetes Res*. 2019;2019:4943191. doi:10.1155/2019/4943191
281. Calabrese V, Zirino F, Vienna FG, Siligato R, Cernaro V, Santoro D. Insight into the role of angiopoietin-like protein 4 in podocypopathies (Review). *World Acad Sci J*. 2024/07/01 2024;6(4):29. doi:10.3892/wasj.2024.244
282. Zhang M, Yang J, Liang G, et al. FOXA1-Driven pathways exacerbate Radiotherapy-Induced kidney injury in colorectal cancer. *International Immunopharmacology*. 2024/04/20/ 2024;131:111689. doi:https://doi.org/10.1016/j.intimp.2024.111689
283. Lu S, Wu H, Xu J, He Z, Li H, Ning C. SIKIAT1/miR-96/FOXA1 axis regulates sepsis-induced kidney injury through induction of apoptosis. *Inflammation Research*. 2020/07/01 2020;69(7):645-656. doi:10.1007/s00011-020-01350-0
284. Zheng C, Huang L, Luo W, et al. Inhibition of STAT3 in tubular epithelial cells prevents kidney fibrosis and nephropathy in STZ-induced diabetic mice. *Cell Death & Disease*. 2019/11/07 2019;10(11):848. doi:10.1038/s41419-019-2085-0
285. Park JY, Yoo KD, Bae E, et al. Blockade of STAT3 signaling alleviates the progression of acute kidney injury to chronic kidney disease through antiapoptosis. *Am J Physiol-Renal*. 2022;322(5):F553-F572. doi:10.1152/ajprenal.00595.2020

286. Pace J, Paladugu P, Das B, He JC, Mallipattu SK. Targeting STAT3 signaling in kidney disease. *Am J Physiol Renal Physiol*. Jun 1 2019;316(6):F1151-f1161. doi:10.1152/ajprenal.00034.2019
287. Lee S-H, Kim KH, Lee SM, et al. STAT3 blockade ameliorates LPS-induced kidney injury through macrophage-driven inflammation. *Cell Communication and Signaling*. 2024/10/04 2024;22(1):476. doi:10.1186/s12964-024-01841-1
288. Xu MJ, Feng D, Wang H, Guan Y, Yan X, Gao B. IL-22 ameliorates renal ischemia-reperfusion injury by targeting proximal tubule epithelium. *J Am Soc Nephrol*. May 2014;25(5):967-77. doi:10.1681/asn.2013060611
289. Chai Z, Gong J, Zheng P, Zheng J. Inhibition of miR-19a-3p decreases cerebral ischemia/reperfusion injury by targeting IGFBP3 in vivo and in vitro. *Biological Research*. 2020/04/20 2020;53(1):17. doi:10.1186/s40659-020-00280-9
290. Chang R-L, Lin J-W, Hsieh DJ-Y, et al. Long-term hypoxia exposure enhanced IGFBP-3 protein synthesis and secretion resulting in cell apoptosis in H9c2 myocardial cells. *Growth Factors*. 2015/07/04 2015;33(4):275-281. doi:10.3109/08977194.2015.1077824
291. Lee W-L, Chen J-W, Ting C-T, Lin S-J, Wang PH. Changes of the Insulin-Like Growth Factor I System during Acute Myocardial Infarction: Implications on Left Ventricular Remodeling1. *The Journal of Clinical Endocrinology & Metabolism*. 1999;84(5):1575-1581. doi:10.1210/jcem.84.5.5676
292. Zhou L, Koh H-W, Bae U-J, Park B-H. Aggravation of post-ischemic liver injury by overexpression of insulin-like growth factor binding protein 3. *Sci Rep-Uk*. 2015/06/15 2015;5(1):11231. doi:10.1038/srep11231
293. Allard JB, Duan C. IGF-Binding Proteins: Why Do They Exist and Why Are There So Many? Review. *Frontiers in Endocrinology*. 2018-April-09 2018;9doi:10.3389/fendo.2018.00117
294. Grellier P, Sabbah M, Fouqueray B, et al. Characterization of insulin-like growth factor binding proteins and regulation of IGFBP3 in human mesangial cells. *Kidney Int*. 1996;49(4):1071-1078. doi:10.1038/ki.1996.156
295. Yang CH, Yue J, Pfeffer SR, et al. MicroRNA-21 Promotes Glioblastoma Tumorigenesis by Down-regulating Insulin-like Growth Factor-binding Protein-3 (IGFBP3) *. *Journal of Biological Chemistry*. 2014;289(36):25079-25087. doi:10.1074/jbc.M114.593863
296. Oikonomopoulos A, Sereti K-I, Conyers F, et al. Wnt Signaling Exerts an Antiproliferative Effect on Adult Cardiac Progenitor Cells Through IGFBP3.

Circulation Research. 2011/12/09 2011;109(12):1363-1374. doi:10.1161/CIRCRESAHA.111.250282
297. Cheung CW, Vesey DA, Nicol DL, Johnson DW. The roles of IGF-I and IGFBP-3 in the regulation of proximal tubule, and renal cell carcinoma cell proliferation. *Kidney Int*. 2004;65(4):1272-1279. doi:10.1111/j.1523-1755.2004.00535.x
298. Peters I, Tossidou I, Achenbach J, et al. IGF-Binding Protein-3 Modulates TGF-β/BMP-Signaling in Glomerular Podocytes. *Journal of the American Society of Nephrology*. 2006;17(6)
299. Upadhya SR, Ryan CJ. Experimental reproducibility limits the correlation between mRNA and protein abundances in tumor proteomic profiles. *Cell Rep Methods*. Sep 19 2022;2(9):100288. doi:10.1016/j.crmeth.2022.100288
300. Nicholson ML, Hosgood SA. Renal Transplantation After Ex Vivo Normothermic Perfusion: The First Clinical Study. *American Journal of Transplantation*. 2013;13(5):1246-1252. doi:10.1111/ajt.12179
301. Hosgood SA, Callaghan CJ, Wilson CH, et al. Normothermic machine perfusion versus static cold storage in donation after circulatory death kidney transplantation: a randomized controlled trial. *Nat Med*. Jun 2023;29(6):1511-1519. doi:10.1038/s41591-023-02376-7
302. Hosgood SA, Barlow AD, Hunter JP, Nicholson ML. Ex vivo normothermic perfusion for quality assessment of marginal donor kidney transplants. *British Journal of Surgery*. 2015;102(11):1433-1440. doi:10.1002/bjs.9894
303. Zhang P, Sun C, Mo S, et al. Salvaging donated kidneys from prolonged warm ischemia during ex vivo hypothermic oxygenated perfusion. *Kidney Int*. 2024;106(2):273-290. doi:10.1016/j.kint.2024.04.018
304. Abraham N, Gao Q, Kahan R, et al. Subnormothermic Oxygenated Machine Perfusion (24 h) in DCD Kidney Transplantation. *Transplant Direct*. Jun 2024;10(6):e1633. doi:10.1097/txd.0000000000001633
305. Husen P, Boffa C, Jochmans I, et al. Oxygenated End-Hypothermic Machine Perfusion in Expanded Criteria Donor Kidney Transplant: A Randomized Clinical Trial. *JAMA Surgery*. 2021;156(6):517-525. doi:10.1001/jamasurg.2021.0949
306. Jochmans I, Nicholson ML, Hosgood SA. Kidney perfusion: some like it hot others prefer to keep it cool. *Curr Opin Organ Transplant*. Jun 2017;22(3):260-266. doi:10.1097/mot.0000000000000405

307. Weissenbacher A, Lo Faro L, Boubriak O, et al. Twenty-four-hour normothermic perfusion of discarded human kidneys with urine recirculation. *Am J Transplant*. Jan 2019;19(1):178-192. doi:10.1111/ajt.14932
308. Weissenbacher A, Huang H, Surik T, et al. Urine recirculation prolongs normothermic kidney perfusion via more optimal metabolic homeostasis-a proteomics study. *Am J Transplant*. May 2021;21(5):1740-1753. doi:10.1111/ajt.16334
309. Messner F, Soleiman A, Öfner D, Neuwirt H, Schneeberger S, Weissenbacher A. 48 h Normothermic Machine Perfusion With Urine Recirculation for Discarded Human Kidney Grafts. Original Research. *Transplant International*. 2023-October-13 2023;36doi:10.3389/ti.2023.11804
310. Pool MBF, Hamelink TL, van Goor H, van den Heuvel MC, Leuvenink HGD, Moers C. Prolonged ex-vivo normothermic kidney perfusion: The impact of perfusate composition. *PLoS One*. 2021;16(5):e0251595. doi:10.1371/journal.pone.0251595
311. Fard A, Pearson R, Lathan R, Mark PB, Clancy MJ. Perfusate Composition and Duration of Ex-Vivo Normothermic Perfusion in Kidney Transplantation: A Systematic Review. *Transpl Int*. 2022;35:10236. doi:10.3389/ti.2022.10236
312. Lodhi S, Stone JP, Entwistle TR, Fildes JE. The Use of Hemoglobin-Based Oxygen Carriers in Ex Vivo Machine Perfusion of Donor Organs for Transplantation. *ASAIO J*. Apr 1 2022;68(4):461-470. doi:10.1097/MAT.0000000000001597
313. Dumbill R. ISRCTN13292277, Investigation of the safety and feasibility of preservation of kidneys for up to 24 hours at normal body temperature prior to transplant. London: BioMed Central2021.
314. Alfonzo A, Harrison A, Baines R, Chu A, Mann A, MacRury M. *Clinical Practice Guidelines Treatment of Acute Hyperkalaemia in Adult. UK Kidney Association*. 2023.
315. Ferdinand JR, Hosgood SA, Moore T, et al. Cytokine absorption during human kidney perfusion reduces delayed graft function-associated inflammatory gene signature. *Am J Transplant*. Jun 2021;21(6):2188-2199. doi:10.1111/ajt.16371
316. POL186/19 – Kidney Transplantation: Deceased Donor Organ Allocation. NHS Blood and Transplant; 2023.
317. Hogeback J, Schwarzer M, Wehe CA, Sperling M, Karst U. Investigating the adduct formation of organic mercury species with carbonic anhydrase and hemoglobin from human red blood cell hemolysate by means of LC/ESI-TOF-MS and LC/ICP-MS. *Metallomics*. 2015;8(1):101-107. doi:10.1039/c5mt00186b

318. Zhang R, Trotter PB, McCaffrey J, et al. Assessment of biological organ age using molecular pathology in pre-transplant kidney biopsies. *Kidney Int*. 2024/08/01/ 2024;106(2):302-316. doi:https://doi.org/10.1016/j.kint.2024.03.028
319. Lu Y-A, Liao C-T, Raybould R, et al. Single-Nucleus RNA Sequencing Identifies New Classes of Proximal Tubular Epithelial Cells in Kidney Fibrosis. *Journal of the American Society of Nephrology*. 2021;32(10):2501-2516. doi:10.1681/asn.2020081143
320. Hinze C, Kocks C, Leiz J, et al. Single-cell transcriptomics reveals common epithelial response patterns in human acute kidney injury. *Genome Medicine*. 2022/09/09 2022;14(1):103. doi:10.1186/s13073-022-01108-9
321. Stamper CT, Marchalot A, Tibbitt CA, et al. Single-cell RNA sequencing of cells from fresh or frozen tissue reveals a signature of freezing marked by heightened stress and activation. *European Journal of Immunology*. 2024:2350660. doi:https://doi.org/10.1002/eji.202350660
322. Shi T, Burg AR, Caldwell JT, et al. Single-cell transcriptomic analysis of renal allograft rejection reveals insights into intragraft TCR clonality. *The Journal of Clinical Investigation*. 07/17/ 2023;133(14)doi:10.1172/JCI170191
323. Mirizio E, Tabib T, Wang X, et al. Single-cell transcriptome conservation in a comparative analysis of fresh and cryopreserved human skin tissue: pilot in localized scleroderma. *Arthritis Research & Therapy*. 2020/11/09 2020;22(1):263. doi:10.1186/s13075-020-02343-4
324. Menon R, Otto EA, Sealfon R, et al. SARS-CoV-2 receptor networks in diabetic and COVID-19–associated kidney disease. *Kidney Int*. 2020/12/01/ 2020;98(6):1502-1518. doi:https://doi.org/10.1016/j.kint.2020.09.015
325. Menon R, Otto EA, Hoover P, et al. Single cell transcriptomics identifies focal segmental glomerulosclerosis remission endothelial biomarker. *JCI Insight*. Mar 26 2020;5(6)doi:10.1172/jci.insight.133267
326. Der E, Suryawanshi H, Morozov P, et al. Tubular cell and keratinocyte single-cell transcriptomics applied to lupus nephritis reveal type I IFN and fibrosis relevant pathways. *Nature Immunology*. 2019/07/01 2019;20(7):915-927. doi:10.1038/s41590-019-0386-1
327. Pino LK, Just SC, MacCoss MJ, Searle BC. Acquiring and Analyzing Data Independent Acquisition Proteomics Experiments without Spectrum Libraries. *Mol Cell Proteomics*. Jul 2020;19(7):1088-1103. doi:10.1074/mcp.P119.001913

328. Zhu Y, Orre LM, Zhou Tran Y, et al. DEqMS: A Method for Accurate Variance Estimation in Differential Protein Expression Analysis *Molecular & Cellular Proteomics*. 2020;19(6):1047-1057. doi:10.1074/mcp.TIR119.001646
329. Purkerson JM, Schwartz GJ. The role of carbonic anhydrases in renal physiology. *Kidney Int*. Jan 2007;71(2):103-15. doi:10.1038/sj.ki.5002020
330. McEvoy CM, Clotet-Freixas S, Tokar T, et al. Normothermic Ex-vivo Kidney Perfusion in a Porcine Auto-Transplantation Model Preserves the Expression of Key Mitochondrial Proteins: An Unbiased Proteomics Analysis. *Mol Cell Proteomics*. 2021;20:100101. doi:10.1016/j.mcpro.2021.100101
331. Lever JM, Boddu R, George JF, Agarwal A. Heme Oxygenase-1 in Kidney Health and Disease. *Antioxid Redox Signal*. Jul 20 2016;25(3):165-83. doi:10.1089/ars.2016.6659
332. Santarsiero D, Aiello S. The Complement System in Kidney Transplantation. *Cells*. Mar 2 2023;12(5)doi:10.3390/cells12050791
333. Goetz L, Laskowski J, Renner B, et al. Complement factor H protects mice from ischemic acute kidney injury but is not critical for controlling complement activation by glomerular IgM. *Eur J Immunol*. May 2018;48(5):791-802. doi:10.1002/eji.201747240
334. Schmidt IM, Surapaneni AL, Zhao R, et al. Plasma proteomics of acute tubular injury. *Nature Communications*. 2024/08/27 2024;15(1):7368. doi:10.1038/s41467-024-51304-x
335. Kelly KJ, Kluve-Beckerman B, Zhang J, Dominguez JH. Intravenous cell therapy for acute renal failure with serum amyloid A protein-reprogrammed cells. *Am J Physiol-Renal*. 2010;299(2):F453-F464. doi:10.1152/ajprenal.00050.2010
336. Kim HW, Lin A, Guldberg RE, Ushio-Fukai M, Fukai T. Essential Role of Extracellular SOD in Reparative Neovascularization Induced by Hindlimb Ischemia. *Circulation Research*. 2007/08/17 2007;101(4):409-419. doi:10.1161/CIRCRESAHA.107.153791
337. Schneider MP, Sullivan JC, Wach PF, et al. Protective role of extracellular superoxide dismutase in renal ischemia/reperfusion injury. *Kidney Int*. 2010/08/02/ 2010;78(4):374-381. doi:https://doi.org/10.1038/ki.2010.141
338. Tang R, Jin P, Shen C, et al. Single-cell RNA sequencing reveals the transcriptomic landscape of kidneys in patients with ischemic acute kidney injury. *Chin Med J (Engl)*. May 20 2023;136(10):1177-1187. doi:10.1097/CM9.0000000000002679

339. Chen Z, Li Y, Yuan Y, et al. Single-cell sequencing reveals homogeneity and heterogeneity of the cytopathological mechanisms in different etiology-induced AKI. *Cell Death & Disease*. 2023/05/11 2023;14(5):318. doi:10.1038/s41419-023-05830-z

340. Stribos EGD, Luangmonkong T, Leliveld AM, et al. Precision-cut human kidney slices as a model to elucidate the process of renal fibrosis. *Translational Research*. 2016/04/01/ 2016;170:8-16.e1. doi:https://doi.org/10.1016/j.trsl.2015.11.007